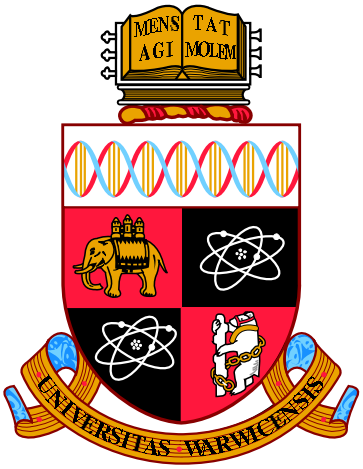

Numerical study on patient-specific haemodynamics subjected to embolisation and wall-distensibility

by

Vasit Sirilapanan

Thesis

Submitted to the University of Warwick

for the degree of

Doctor of Philosophy

School of Engineering

April 2019

THE UNIVERSITY OF WARWICK

To my parents and my grandmother.

Contents

List of Tables **iv**

List of Figures **vii**

Acknowledgments **xviii**

Declarations **xx**

Abstract **xxi**

Chapter 1 Introduction **1**

Chapter 2 Literature Review **4**

2.1 Blood vessel structure 5

2.2 Cerebral aneurysms 5

2.2.1 Aneurysm initiation 8

2.2.2 Aneurysm progression 13

2.2.3 Aneurysm rupture 16

2.3 Endovascular coiling of cerebral aneurysms 17

2.3.1 Blood residence time and thrombus formation 22

2.3.2 Aneurysm recurrence 25

2.3.3 Fluid-structure interactions (FSI): Coiled Aneurysms . 27

2.4 Arteriovenous fistulas 30

2.4.1 Fistula maturation 31

2.4.2 Maturation failure 33

2.4.3 Neo-intimal hyperplasia 34

2.4.4 Fluid-structure interactions (FSI): Fistula 36

2.5 Opportunities of CFD in the present study 37

Chapter 3 Methodology **41**

3.1 Medical Images Acquisition 42
3.2 Geometry Segmentation 42
3.2.1 Segmentation of the Cerebral Aneurysm 44
3.2.2 Aneurysm size and rupture status 47
3.2.3 Coil modelling 50
3.2.4 Segmentation of brachial artery and vein for AVF creation 53
3.3 Boundary conditions and pulsation effects 58
3.4 Fluid governing equations 63
3.4.1 Continuity and Navier-Stokes equations 63
3.4.2 Modeling passive scalar transport 64
3.5 Hemodynamic properties 65
3.5.1 Blood flow regime 65
3.5.2 Blood viscosity and rheology 66
3.6 Validation of the Carreau-Yasuda non-Newtonian model . . . 70
3.7 Eurelian multiphase blood modelling 74
3.8 Mechanical properties of the vessel wall 76
3.8.1 Aneurysm wall thickness and constraints 76
3.8.2 AVF wall thickness and constraints 77
3.8.3 Mechanical properties of the vessel walls 79
3.9 FSI equations and Rayleigh damping 80
3.9.1 Two-way partition method 81
3.9.2 Rayleigh damping model 82
3.9.3 Systematic study on Rayleigh damping coefficients . . 84
3.10 WSS-based parameters 87
3.10.1 Proposed metrics 91

Chapter 4 Validation of Ultrasound-based CFD **95**

4.1 Abstract 95
4.2 Introduction 96
4.3 MRI and ultrasound models 100
4.4 MRI and ultrasound results comparison 103
4.4.1 Mass flow rates 104

4.4.2 Wall shear rates 104
4.4.3 Wall shear rates parameters 105
4.4.4 Low and oscillating wall shear stress 106
4.4.5 Directional wall shear stress 107
4.4.6 Volume fractions and velocities of red and white blood cells 107
4.5 Discussion 115
4.6 Conclusion 119

Chapter 5 Independence Studies 120
5.1 Independence tests for FSI cases 132

Chapter 6 Effects of coil packing density, leukocyte adhesion, and wall compliance on aneurysm flow reduction and recurrence 138
6.1 Flow and WSS reduction 140
6.2 Flow occlusion and thrombus formation 147
6.3 Rupture risk and leukocyte migration 156
6.4 Aneurysm recurrence 163

Chapter 7 Effects of wall compliance and non-Newtonian haemodynamics on fistula maturation failure 186
7.1 Non-Newtonian and wall complaint AVF 187
7.2 Mechanisms of maturation failure 197

Chapter 8 Conclusion 210

List of Tables

2.1 Summary of coiled and rigid aneurysm studies. For rheology, Newt. and non-N denote Newtonian and non-Newtonian flows with the corresponding models used in bracket. CY and CS denotes Carreau-Yasuda and Casson models, respectively. For aneurysm location, CO, ICA, PcommA, and MCA denotes carotid-ophthalmic, internal carotid artery, posterior communication artery, and middle cerebral artery. For pulsatile conditions, 'No' indicates a steady flow simulation. * denotes a study with passive scalar transport 21

2.2 Summary of rigid and pulsatile aneurysm studies with passive scalar applications. For rheology, Newt. and non-N denoted Newtonian and non-Newtonian flows with the corresponding models used in bracket. For aneurysm location, BA indicates basilar artery and MCA indicates middle cerebral artery. . . . 25

2.3 Summary of recent FSI cerebral aneurysm studies with pulsatile flow but no coil treatment and passive scalar analysis. For rheology, Newt. and non-N denotes Newtonian and non-Newtonian flows with the corresponding models used in bracket. CY and C denotes Carreau-Yasuda and Carreau models, respectively. For aneurysm type, B and F indicates bifurcation and fusiform aneurysms. For aneurysm location, MCA, ICA, AcommA detontes middle cerebral artery, internal carotid artery, and anterior communicating artery. 29

2.4 Summary of recent FSI fistula studies. For rheology, Newt. and non-N denote Newtonian and non-Newtonian flows. CS denotes Casson model. For imaging, NPS and US denote the use of non-patient specific and idealised geometry and ultrasound, respectively. 37

3.1 Geometrical aspects of the aneurysm. 48
3.2 Comparison of the present geometric aspects to that of ruptured (RAs) and unruptured (URAs) aneurysms from Nader-Sepahi et al. (2004); Weir (2005); Jou and Britz (2016). + and - Signs indicates that the value of the present geometry is lower and higher than that founded in the literature, respectively. * Symbol indicates rupture status with lower difference. 49
3.3 Coil volumes and packing densities for each cases. 51
3.4 Newtonian blood viscosity of patients with different blood abnormality. 67
3.5 Non-Newtonian blood viscosity of patients with different blood conditions. * and ** indicate parameter set obtained from curve fitting and not used due to insufficient data, respectively. References A17 = (Akherat et al., 2017), V08 = (Valencia et al., 2008), C18 = Clarion et al., (2018), M15 = (Moreno et al., 2015), G17 = (Grechy et al., 2017). Other abbreviations: Chol. = cholesterol and Aneurysm = patient with cerebral aneurysm 69
3.6 Bended pipe mesh summary for the grid independence test. . . 72
3.7 Multiphase blood volume fractions of each phase. 75
3.8 Multiphase blood density (kg/m^3) of each phase. 75
3.9 Carreau-Yasuda non-Newtonian parameters for red and white blood cells. 76
3.10 Wall thickness of the artery and vein used in previous FSI-AVF studies. 78
3.11 Mechanical properties for blood vessel wall 80

4.1 Volumes and diameters of each subject's MRI and ultrasound models. Some subjects do not have a second inlet or outlet their respective diameters are indicated by the - sign. 102

4.2 MRI-ultrasound differences in averaged outlet mass flow rates. 104
4.3 MRI-ultrasound differences in the surface-averaged wall shear stress (SAWSS) averaged throughout the fourth cardiac cycle. 104
4.4 WSS, TAWSS, and OSI thresholds associated with different endothelial changes. IH denotes intimal hyperplasia 106
4.5 Percentage of surface area associated with each range of TAWSS, OSI, LOWSSI, WSS duty factors (DF) measured by MRI and ultrasound 108
4.6 MRI-ultrasound differences in the haematocrit (hct), discharged haematocrit (hct_D), and leukocyte volume fraction (ϵ_{WBC}) . . 112
4.7 MRI-ultrasound differences in averaged velocity of erythrocytes and leukocytes. 114

7.1 AVF case studies 187
7.2 Radial wall displacement conditions for inward and outward wall remodelling. 198

List of Figures

2.1 Schematic structure of the arterial and venous walls. Sections A-B, C-D, and E-F belong to the Tunica intimal (innermost), Tunica media (middle), and Tunica externa (outermost) layers of both artery and vein, respectively. The tissue layers containing the lumen (blood) consists of A. endothelial cells lining, B. Endothelium, C. internal elastin, D. smooth muscle, E. external elastin, F. external wall, G. plaques, H. venous valve. 6

2.2 Two major configurations of cerebral aneurysms; saccular and fusiform aneurysms. (Adapted from Withers et al. 2013) . . . 7

2.3 Different mechanisms of aneurysm formation. Blue, red, black, and green circles represent high velocity, low velocity, flow recirculation, and wall damage respectively. Red blocks emphasise major events upstream of aneurysm formation. 12

2.4 Different mechanisms of aneurysm growth presented by two major theories. Blue and red circles indicate stenosis formation and wall degeneration, respectively. 15

2.5 Angiography of a coil inside an aneurysm (Andrade et al., 2012) 19

3.1 (a) System of cerebral arteries segmented from a CT-scanned image in 3DSlicer. (b) Smoothed model of the Circle of Willis and its proximal arteries in Blender; ACA - Anterior Cerebral Artery, ACommA - Anterior Communicating Artery, MCA - Middle Cerebral Artery, ICA - Internal Carotid Artery, PCommA - Posterior Communicating Artery, PCA - Posterior Cerebral Artery, SCA - Superior Cerebellar Artery, (L) and (R) denotes left and right, respectively. 43

3.2 Detailed view of the Circle of Willis (CoW) from different views. Green and blue arrows show ICAs and basilar arteries inlet sections. 45
3.3 Orientation of the coronal, sagittal, and axial planes over the cerebral anatomy. Segmentation along the black line will produce the respective planes. (Reconstructed from Human Anatomy Atlas, (VisibleBody, 2019)) 45
3.4 a) The right MCA anerysm and the Circle of Willis from in 2D axial view. b) 3D visualisation of the Circle of Willis, the aneurysm, and the proximal arteries. c) The region of interest which includes the target aneurysm. The green box shows the location of the aneurysm, the upstream M1 branch and the the downstream M2 bifurcation. 46
3.5 A comparison between the region of interest from the (a) original CT-scan and (b) the reconstructed region of interest with white arrows showing the directions of blood flow. Two-headed arrows indicate uncertain flow directions. White dashed lines show the plane section used to truncate the vessels. 47
3.6 Geometry of the middle cerebral artery aneurysm used in the present study from the a. coronal, b. axial, and c. sagittal view. Abbreviations used in this figure is explained in Table 3.1. 48
3.7 Coil models of all seven coiled cases. 52
3.8 Orientation of the coronal, sagittal, and axial planes over the forearm anatomy. Segmentation along the black line will produce the respective planes. (Reconstructed from Human Anatomy Atlas, (VisibleBody, 2019)) 53
3.9 A slice of the ultrasound image in (a) the axial, (b) sagittal, and (c) coronal views. Grey contour surrounded by white contours (tissues and muscles) are blood vessels (lumen spaces). Other grey contours not surrounded by white contours are outside the region of interest. The artery and vein surfaces are highlighted with green and red arrows, respectively. (d) A bifurcation is highlighted with a black arrow, proximal to the artery. 54

3.10 The segmented artery and vein in (a) the coronal view and (b) axial view, featuring an arterial bifurcation. (c) Construction of the end-to-end fistula from the arterial end. 56
3.11 Geometry of the AV fistula joining the brachial artery and vein, featuring an arterial bifurcation in the sagittal view. White arrows show the blood flow direction. 57
3.12 Surface averaged mass flow rate measured on a cross-section of the artery upstream of the bifurcation (artery), the bifurcation, and the vein, normalised by 0.01 kg/s. 57
3.13 Smoothed geometry of the AV fistula and the proximal artery and vein without the bifurcation. White dashed lines in (a) shows the original boundary of the artery and vein. White arrows in (b) show the blood flow direction. 58
3.14 Mass flow rate waveform applied at the inlet of the aneurysm (left) and AVF (right) models. (Reproduced from (Xiang et al., 2014) and (Ene-Iordache and Remuzzi, 2012)) 59
3.15 Streamwise velocity profiles at different locations upstream of the pipe inlet across the pipe radius R after three cardiac cycles. 61
3.16 Centreline velocity profiles at different cross sections along the entrance length through multiple cardiac cycles, showing flow periodicity after three cycles (In this case, 0.04s = 1 cycle). . . 61
3.17 30D extension pipe upstream of the artery inlet in the aneurysm (top) and AVF (bottom) models. 62
3.18 Variation of blood viscosity due to changes in the shear rate (Reproduced from Secomb 2016). Plot shows the process of shear thinning until shear rate reaches 100 s^{-1} where the Newtonian flow regime dominates (green arrow), followed by a plateau of infinite-shear viscosity beyond a shear rate of 200 s^{-1} (blue arrow). 67
3.19 Variations of non-Newtonian viscosities corresponding to four patient types presented in Table 3.5 at different shear rates. . 69

3.20 Computational mesh of the bended pipe (cross sectional view included) (left) and inlet velocity profile (right). The mesh in the cross sectional view is also included and the three measuring sections are marked by the numbers 0, 45, 90, corresponding to the degrees they are oriented with respect to section 0. The digitized inlet velocity profile is marked in red and superimposed on the original profile from Gijsen et al. (1999a). 72
3.21 Velocity profiles measured along different measuring sections during peak diastole measured by Gijsen et al. (1999a) (black circles) superimposed by velocity profiles from the four meshes of the present study; base size 0.5mm (red), base size 0.4mm (green), base size 0.2mm (bold blue), and base size 0.15mm (dashed blue). 73
3.22 a. Elastic aneurysm wall with uniform thickness (in blue), b. superimposed onto the MCA and its aneurysm (in red). White lines represent free wall boundaries constrained by fixed displacement. Thickness is clearly shown in Figure c. 77
3.23 a. Elastic AVF wall (in blue) from the axial view, b. showing the slightly non-uniform thickness of the anastomosis. White dashed lines surround the region where arterial thickness is transformed into the venous thickness. The AVF (in red) is superimposed by the wall in Figure c, where the white lines represent free wall boundaries constrained by fixed displacement. 79
3.24 Temporal variation of the maximum displacement of the outer vessel wall for various (α, β) values. 85
3.25 Temporal variation of the maximum displacement of the outer vessel wall for various (α, β) values 86
3.26 Variations of TAWSS and OSI at different LOWSSI levels. . . 92
3.27 A schematic diagram of the compression-tension line on the wall of an aneurysm. Arrows indicate direction of tangent wall movement. 93

4.1 MRI and ultrasound (US) segmented vessels of all four subjects. I1 and 12 denote the inlet boundaries while O1 and O2 denote the outlet boundaries. Red point indicates location of flow split in the ultrasound model of subject 1. 103
4.2 Temporal variations of outlet mass flow rate over a cardiac cycle of MRI and ultrasound models. 105
4.3 Bland-Altman plots comparing MRI and ultrasound measurements of the percentage areas associated with different ranges of TAWSS, OSI, LOWSSI and WSS duty factors in four subjects. 109
4.4 Low and oscillating wall shear stress index (LOWSSI) contours mapped on the MRI and ultrasound models of all four subjects. Numbers 1 to 4 indicate subjects 1 to 4, respectively. 110
4.5 Temporal variations of surface-averaged DWSS in LOWSS, healthy regions of subject 2 and the time taken for DWSS to initiate oscillation as predicted by MRI and ultrasound. 111
4.6 Bland-Altman plot comparing the timestep associated with zero and extreme DWSSs and the temporal variations of averaged DWSSs of subject 1 and 2 and Franzoni et al. (2016) 112
4.7 Comparison of hematocrit variations in a cardiac cycle between MRI and ultrasound. 113
4.8 Comparison of blood cells velocity in a cardiac cycle between MRI and ultrasound 114

5.1 Temporal variations of (a) plane-averaged aneurysmal velocity magnitude at seven different planes 1-7 aligned parallel to the ostium plane and (b) surface-averaged WSS on the aneurysm wall for three mesh densities: 4, 6, and 8 million elements. Each mesh consisting of 4 (red), 6 (green), and 8 (blue) million elements are denoted as 4M, 6M , and 8M, respectively, during the fourth cardiac cycle. (1 seconds per 1 cardiac cycle) 122

5.2 Temporal variations of the percentage differences in the plane-averaged velocity magnitude at the (a) ostium-plane and (b) plane 4 between 4 and 6 million elements mesh (red) and 6 and 8 million elements (green) mesh during the fourth cardiac cycle. (1 seconds per 1 cardiac cycle) 124
5.3 Temporal variations of the percentage differences in the surface averaged WSS between 4 and 6 million elements mesh (red) and 6 and 8 million elements (green) mesh during the fourth cardiac cycle. (1 seconds per 1 cardiac cycle) 125
5.4 Temporal variations of velocity magnitude during the fouth cardiac cycle at (a) arterial bifurcation, (b) inner wall of the fistula entry, (c) venous bend, and (d) venous-fistula anastomosis with different grid densities of 3.5 million (red), 5 million (green), 6 million (blue), 7 million (purple), and 8 million (black) elements. (1 second per 1 cardiac cycle) 127
5.5 Temporal variations of the (a) spatially averaged WSS on the aneurysm wall and (b) plane-averaged velocity magnitude of the planes 1-7 inside the aneurysm at different timestep sizes of 10 ms (red), 5 ms (green), and 2 ms (blue). (1 second per 1 cardiac cycle) 129
5.6 Temoral variations of the velocity magnitude during the fouth cardiac cycle at the (a) arterial bifurcation, (b) inner wall of the fistula entry, (c) venous bend, and (d) venous-fistula anastomosis, at timestep sizes of 20 ms (pale blue), 2.5 ms (red), 1.25 ms (dark blue), and 0.5 ms (black dotted). (1 second per 1 cardiac cycle) 131
5.7 Temoral variations of the maximum aneurysmal wall displacement with different mesh densities and timestep sizes. 134
5.8 Temoral variations of a local radial displacement of the AVF wall with different mesh densities and timestep sizes. 135
5.9 Mesh representation of the aneurysm model. 136
5.10 Mesh representation of the AVF model. 137

6.1 Variation of aneurysmal volume-averaged velocity magnitude with different packing densities in one cardiac cycle (1 second = 1 cycle). 141
6.2 Variation of aneurysmal surface-averaged wall shear stress (SAWSS) with different packing densities in one cardiac cycle (1 second = 1 cycle). Constantly dashed line represents surface-averaged wall shear stress on the bifurcation on which the aneurysm would be initiated. 141
6.3 Ratio of aneurysmal surface-averaged wall shear stress (SAWSS) of each coiling cases to that of the untreated case. 143
6.4 Isosurface of mean velocity (v = 0.69 m/s) in the aneurysm and proximal outlet arteries in (a) the untreated case and treated cases with (b) 3 coils, (c) 4 coils, (d) 5 coils, (e) 6 coils, and (f) 7 coils at peak systole. Arrows show regions of flow recanalisation. 144
6.5 Probability distribution function (PDF) of time-averaged velocity magnitude (TAVEL) for different packing densities (0C-7C) normalsied by the standard deviation of TAVEL of the untreated case, SD($TAVEL_{0C}$), in log-scale. The horizontal axis, representing TAVEL/SD($TAVEL_{0C}$), spans (a) from 0.0 to 4.86 and (b) from 0.0 to 0.25. 146
6.6 Standard deviation of the PDF of TAVEL for different packing densities and their difference from that of the preceeding coil (i.e. 2C-1C means difference between the TAVEL/SD($TAVEL_{0C}$) of the 2 coil and 1 coil cases). 147
6.7 (a) Probability distribution function of time-averaged passive scalar concentration, TAPS/SD($TAPS_{0C}$), (range 1.8 to 2.2) and the difference between the PDF of TAPS of a coiling case TAPS/SD($TAPS_{0C,C}$) and that of the precceding coil case TAPS/SD($TAPS_{0C,C}$) spanning (b) from. 1.85 to 2.15 and (c) 2.0 to 2.1. 150
6.8 Maximum PDF of the time-averaged passive scalar concentration, TAPS/SD($TAPS_{0C}$), of each coiling case. 151

6.9 Spatial distribution of passive scalar transport inside the aneurysm and proximal outlet arteries for different packing densities at time t=0.32T, t=0.44T (peak systole), and t=0.75T where T is duration in one cardiac cycle (T=1s). 153
6.10 Time-density curve of passive scalar concentration on the ostium plane and blood residence time calculated using the thresholds of b. 0.2 and c. 0.02 of maximum concentration (normalised by the blood residence time of the 7 coil case). 155
6.11 Oscillatory shear index (OSI) distributions with different packing densities. 157
6.12 Regions of low and oscillating WSS induced by different packing densities. 158
6.13 Flow impingement highlighted by abnormal low TAWSS (less than 2 Pa) region on the untreated aneurysm. 159
6.14 Normalised impingement ratio (NIR) on the (a) front and (b) back sides of the aneurysm and WSS vectors on the (c) front and (d) back sides of the aneurysm. Black lines enclose region of low WSS (WSS $<$ 1 Pa) and flow impingement in both figures. Pink lines in Figure c-d enclose area of high impingement ratio (NIR $>$ 0.1). 160
6.15 Prediction of thrombus formation and leukocyte activation based on changes in the time-averaged wall shear stresses (TAWSS) for different coiling cases. Colour labels in relation to TAWSS (Pa): HI - high WSS regions that are not prone to thrombus (TAWSS $>$ 2Pa), HE - healthy state (0.45 $<$ TAWSS $<$ 2.0Pa), LA - leukocyte adhesion (0.35 $<$ TAWSS $<$ 0.45 Pa), TF - Regions prone to thrombosis (0.2 $<$ TAWSS $<$ 0.35 Pa), T2 - thrombus induction (0.15 $<$ TAWSS $<$ 0.2 Pa), and T1- potential thrombus formation (0 $<$ TAWSS $<$ 0.15 Pa). Coloured arrows indicate locations referred to in the text. 162
6.16 (a) Local packing densities of different cross sections along the aneurysm depth of the 6 and 7 coil case from the neck (0 mm) to the tip (7.4 mm) as shown in (b) 164

6.17 Cross-sectional area averaged velocity magnitude along aneurysm depth at end diastole (dashed) and peak systole (bold) and local packing densities (bold with symbol) of the (a) 6 and (b) 7 coil case. 165
6.18 Cross-sectional area averaged velocity magnitude along aneurysm depth at end diastole of the 6 and 7 coils cases. The plot near the aneurysm tip is zoomed in as shown by the right figure. . . 165
6.19 Cross-sectional area averaged velocity magnitude along aneurysm depth at peak systole of the 6 and 7 coils cases. The plot near the aneurysm tip is zoomed in as shown by the right figure. . . 166
6.20 Cross-sectional area averaged velocity magnitude of white blood cells (leukocytes) along aneurysm depth at end diastole (left) and peak systole (right) of the 6 and 7 coils cases. 168
6.21 Each figure consists of three sections; Wall shear stress magnitude (bold lines in the top section), Directional wall shear stress (dashed lines in the middle section), and location of leukocyte adhesion to the wall (bold lines in the bottom section) along the circumference of cross-sectional planes 1-7 inside the aneurysm dome. Black and red lines for wall shear stresses represent the 6 and 7 coil cases, respectively. In the bottom section, grey and orange lines represent leukocyte volume fraction of 1% in the 6 and 7 coil cases. The black and red lines represent leukocyte volume fraction above % in the 6 and 7 coil cases. 172
6.22 Cross-sectional area averaged velocity magnitude along aneurysm depth at end diastole of the 6 and 7 coils RIGID and FSI cases. 175
6.23 Cross-sectional area averaged velocity magnitude along aneurysm depth at peak systole of the 6 and 7 coils RIGID and FSI cases. 175
6.24 Radial displacement and location of leukocyte adhesion to the wall along the circumference of cross-sectional planes 1-7 inside the aneurysm dome with 6 (black) and 7 (red) coils. 180
6.25 Displacement of the compliant coil in the streamwise (left) and transverse (right) directions inside the rigid-walled aneurysm at peak systole. 183
6.26 Temporal variations of coil displacements over a cardiac cycle. 183

6.27 Temporal variations of wall shear stresses of the aneurysm and coil in rigid coil case and compliant coil case. 184
6.28 Temporal variations of plane-averaged velocity magnitude of different planes in the aneurysm in rigid coil case and compliant coil case. 185

7.1 Distribution of diastolic wall shear stress in all four cases. Red and blue arrows indicate regions of major WSS overestimation and underestimation by the rigid wall assumption, respectively. White line contours encircle regions of WSS below 1 Pa. . . . 192
7.2 Isosurface of flow recirculation (negative streamwise velocity) in all four cases. 193
7.3 Isosurface of local normalised helicity (LNH) showing clockwise (dark purple) and anticlockwise (red) rotating vortical structures in all four cases. 194
7.4 Low and oscillating wall shear stress index showing reions prone to maturation failure in all four cases. Red and blue arrows indicate regions of major WSS overestimation and underestimation by the rigid wall assumption, respectively. 196
7.5 Locations of all six arterial and venous planes investigated. . . 198
7.6 Circumferential radial displacements of the inner (red) and outer (black) walls, red blood cells viscosity, wall shear stresses, von-Mises stresses on the inner and outer walls, and flow recirculation regions (blue) on arterial plane 1. 201
7.7 Circumferential radial displacements of the inner (red) and outer (black) walls, red blood cells viscosity, wall shear stresses, von-Mises stresses on the inner and outer walls, and flow recirculation regions (blue) on arterial plane 2. 202
7.8 Circumferential radial displacements of the inner (red) and outer (black) walls, red blood cells viscosity, wall shear stresses, von-Mises stresses on the inner and outer walls, and flow recirculation regions (blue) on arterial plane 3. 203

7.9 Circumferential radial displacements of the inner (red) and outer (black) walls, red blood cells viscosity, wall shear stresses, von-Mises stresses on the inner and outer walls, and flow recirculation regions (blue) on venous plane 4. 204
7.10 Circumferential radial displacements of the inner (red) and outer (black) walls, red blood cells viscosity, wall shear stresses, von-Mises stresses on the inner and outer walls, and flow recirculation regions (blue) on venous plane 5. 205
7.11 Circumferential radial displacements of the inner (red) and outer (black) walls, red blood cells viscosity, wall shear stresses, von-Mises stresses on the inner and outer walls, and flow recirculation regions (blue) on venous plane 6. 206

Acknowledgments

First of all, I would like to thank my PhD supervisor, Dr. Yongmann Chung. Throughout my four-year course, he has given me insightful advise and encouragement that has inspired and strengthened my knowledge of CFD and hemodynamics. Although there have been difficult times during my PhD, they did not last long with his motivating support that brought me back on track. There was one sentence he said that always kept me going; "Never regret and move on". Besides academic support, he also cared about my health and well-being during the times of my sleepless nights. A cup of hot carmomile tea a day he recommended to someone who rarely drinks tea like me did helped brighten up the days. I admire his passion for research and will always be thankful to him for still believing in me when I lost hope. This thesis would never have been completed without his support and encouragement.

I would also like to thank my parents and family for their ever-lasting support during my tiring times. Despite having been abroad for 3 years prior to my PhD, I still admit that living and studying far away from home is never an easy thing. But the smile on their face kept me fighting and never gave up on hard work.

The four years I spent at the University of Warwick would not have been as enjoyable without the following people whom I would like to give my

special thanks to: Dr. Qiang Yang and Dr. Zhixin Wang, my senior colleagues in our research group from whom I have learned useful computational and presentation skills from, especially through our group's weekly seminars. Dr. Wang and I spent two years together and he has always been a good example of dilligence to me and other group members; Dr. Minsuok Kim, who has given me insights into the biomedical field before he left; Dr. Masashi Yamakawa from Kyoto Institute of Technology who paid a one year visit to our university for his experiences in coding, his kindness, and delicious snacks from Japan he shared with me; Samuel Dunstan, Selcuk Sever, Xue Chen, Adam Nawaz, Jacqueline Mifsud, my PhD colleagues who have made my times in the office enjoyable; Dr. Julia Choe, Dr. Yuanwei Xu, Dr. Jasmine Desmond, Dr. Chimie Gamot, Dr. Chinedu Nwaigwe, and Dr. Aaron Finney, who were members of the laboratory next door to us when we were still based in the Department of Computer Sciences, for organising the FATNODE monthly dinner which I really enjoyed; Dr. Dugan Whiterick, from the Centre for Scientific Computing for setting up Star-CCM+ on our high performance computing machines towards the end of my PhD course. The weekly fluid seminar at the School of Engineering also provided a lot of inspiration to new but relevant research fields.

Declarations

This thesis, and the materials in it, is my own work. It has not been submitted for a degree at any other university.

Abstract

Computational fluid dynamics (CFD) simulations have been peformed to investigate the hemodynamics of patient-specific cerebral aneurysm treated with endovascular coils; and arteriovenous fistula (AVF) using Star-CCM+. Fluid-structure interactions (FSI) between the elastic vessel walls and the blood flow within were also taken into account to provide a more realistic environment and better understanding of haemodynamic effects on wall remodelling. The blood in both studies was modelled as non-Newtonian fluid and comprises of three phases to fully incorporate the effects of shear-thinning and distributions of blood cells, respectively. The use of a less invasive ultrasonic imaging texhnique for CFD simulations is shown to be a viable alternative to magnetic resonance imaging (MRI). This has proven to be beneficial especially for haemodialysis patients who require fistula check-up on a regular basis.

Excessively enlarged sections of arteries, called aneurysms, are vulnerable to vessel wall degradation. When blood flows into a cerebral aneurysm, it causes abnormal haemodynamic changes, which increases the risk of aneurysm rupture and strokes. Patients diagnosed with a cerebral aneurysm are therefore treated by stenting the parent artery or aneurysmal coiling to achieve occlusion. Despite high coiling packing density, aneurysm may recanalise, which consequently leads to aneurysm recurrence. Our understanding of the relationship between coiling density and aneurysmal occlusion and aneurysm recurrence in a non-Newtonian environment are limited.

The effects of coil packing density on aneurysmal haemodynamics and the mechanism behind aneurysmal recurrence are discussed in this thesis. In the present aneurysm study, the aneurysm dome was embolised with seven different coil configurations of different packing densities. A time-dependent passive scalar was added to the multiphase blood inflow to represent medical dyes which allows for the visualisation of blood flow penetrating into the coils.

The observed relationship between passive scalar visualisations, white blood cells distribution, and hemodynamic quantities will be beneficial for clinical evaluation of aneurysm occlusion. It is shown that a packing density of 31% (7 coils) is the optimal coil density that can supress the aneurysmal volume-averaged velocity and wall shear stress. Furthermore, the temporal variation in streamwise velocity inside the aneurysm dome does not nescessarily decrease with coiling packing density during peak systole. Local packing density, distribution of red and white blood cells, and wall compliance have been correlated with aneurysm recurrence. Circumferential wall shear stress, radial wall displacement, adhesion of white blood cells on the wall, and whole blood velocity magnitude in the six and seven coils cases are compared. These two coiling cases are chosen to represent an event of aneurysm recurrence as unexpected increase in the mean inflow into the aneurysm is observed despite higher coil packing densities. To the best of the author's knowledge, the present aneurysm study is the first to investigate the effects of coil packing densities and blood cells distribution on non-Newtonian aneurysmal flow reduction and aneurysm recurrence in both rigid and compliant cerebral aneurysms. Additionally, the effects of aneurysmal haemodynamics on coil movement and vice versa are investigated in a study featuring a compliant coil in a rigid aneurysm. Overestimation in aneurysmal velocity and wall shear stress at multiple locations by the rigid coil model has been observed.

An arteriovenous fistula (AVF) is a connection between a brachial artery and vein that is surgically created to provide haemodialysis patients with matured vascular access points. AVF maturation failure, however, often occurs and its underlying mechanisms still remain controversial. The present AVF study investigates the effects of the compliant wall and non-Newtonian blood viscosity in an end-to-end AVF. Four simulations were performed to compare Newtonian and non-Newtonian haemodynamics in both rigid and wall-compliant fistulas. Different ranges of wall shear stress parameters corresponding to certain endothelial changes are compared among the four cases. It is found that the effects of wall compliance is more significant than that of non-Newtonian rheology. Furthermore, non-Newtonian effects are more clear when the AVF walls are compliant. Volumetric quantities like flow recirculations and helicity, which are related to abnormal endothelial changes, are also found to be overestimated by the rigid wall assumption. The study also investigates the effects of multiphase haemodynamics on inward wall remodelling and thus AVF maturation failure. Low and oscillating wall shear stress index is introduced as a tool for predicting the risk of maturation failure. Wall shear stresses, both directional and magnitude, red blood cell viscosity, flow recirculations are correlated with wall remodelling and endothelial damages derived from von-Mises stresses.

Glossary

Aneurysm - a bulge in a blood vessel due to excessive dilatation of the wall.
Atherosclerosis (plaque) - accumulation of fats and cholesterol in or on the arterial wall which can limit blood flow.
Cerebral - related to the brain.
Coil - a type of flow diverter, made of platinum, inserted inside an aneurysm to induce aneurysmal occlusion.
Endothelium - the innermost layer of blood vessels where endothelial cells are located.
Endothelial cells (EC) - cells on the innermost layer of blood vessels. These cells interact with the blood flow.
Erythrocytes - red blood cells (RBC).
Fistula - an artificial connection between an artery and a vein of a haemodialysis patient.
Intimal hyperplasia - inward remodelling of a blood vessel wall due to smooth muscle cells migration to the endothelium to form new cell layers.
Leukocytes - White blood cells (WBC).
Lumen - the space inside blood vessels through which blood flows.
Platelets (thrombocytes) - a type of cell which aggregates to one another to form thrombus (blood clots).
Smooth muscle cells (SMC) - a network of muscle cells that lies in the intimal layer of the blood vessel. When endothelial cells are damaged, they migrate to the endothelium to protect the endothelial cells.
Stenosis - inward remodelling of a blood vessel wall as a result of atherosclerosis or thrombus formation.
Thrombosis - the process of thrombus (blood clots) formation.

Chapter 1

Introduction

Haemodynamics, the dynamics of blood flow, plays an important part in the initiation and progression of cardiovascular diseases. Hypertension (high blood pressure), coronary heart diseases, kidney diseases, and strokes following the rupture of cerebral aneurysms are among the main causes of high mortality rate worldwide (Vorp, 2007). Previous studies have investigated the mechanisms behind these pathological lesions, but some causes still remain inconclusive. Changes in haemodynamic quantities, especially wall shear stress (WSS), can be related to the formation of atherosclerotic plaques (Chaichana et al., 2013a), coronary heart diseases (Soulis et al., 2006), homeostatic maturation of arteriovenous fistulas (AVF) for haemodialysis (McGah et al., 2013), aneurysm growth (Boussel et al., 2008) and its rupture (He and Ku, 1996; Jou et al., 2008; Byrne et al., 2014; Lauric et al., 2014).

These pathological changes and diseases are related to the interaction between haemodynamics and blood vessel morphology, which can be numerically investigated through computational fluid dynamics (CFD) simulations. In this thesis, patient-specific haemodynamics of coiled cerebral aneurysms and arteriovenous fistulas (AVF) are investigated. Furthermore, the response of the vessel wall to local blood flow is modelled using the fluid-structure interaction technique while non-Newtonian blood viscosity is used to incorporate shear-thinning effects of the multiphase blood. High performance computing (HPC) is used to reduce computational time while maintaining the accuracy of these simulations.

Endovascular coiling in cerebral aneurysm have previously been associated with flow reduction and decreased risk of rupture. However, aneurysm recurrence can be observed despite a high coil packing density and there is a limited understanding on its underlying mechanism. This thesis discusses how aneurysm recurrence can be attributed to local packing density, leukocyte adhesion to the endothelial cells, and wall compliance. Coil movement during a cardiac cycle and its effects of aneurysmal haemodynamics is also studied. Furthermore, haemodynamics in a wall compliant and non-Newtonian end-to-end AVF have been investigated. Red blood cell viscosity, wall shear stress, von-Mises stress, and flow recirculation are linked to AVF maturation failure. The low and oscillating wall shear stress index has been introduced as a prediction tool not only for aneurysm rupture, but also for fistula maturation. To the best of the author's knowledge, these haemodynamic factors attributed to aneurysm recurrence and AVF maturation failure have never been investigated in previous studies. Therefore, they are discussed in the present work.

This thesis consists of eight chapters which include the literature review, methodology, validation of ultrasound-derived CFD, independence tests, and results from the two main studies; coiled aneurysm, and AVF maturation failure, followed by a conclusion. The known mechansims of aneurysm initation, growth, and rupture, coiling, AVF maturation and failure are discusssed in chapter 2. In chapter 3, simulation setup, geometry segmentation, boundary conditions, governing equations of both the blood and vessel walls, wall shear stress derived parameters including the new index proposed are defined. Validation of the Carreau-Yasuda non-Newtonian model used in both studies are also presented in this chapter. Ultrasound-derived CFD is validated against MRI-derived CFD in chapter 4. Grid and timestep sizes independent tests were conducted for both studies and shown in chapter 5. The main findings from the aneurysm and AVF studies are presented in chapter 6 and 7, respectively.

In chapter 6, aneurysmal flow through seven different coil configura-

tions were investigated to find the optimal coil packing density for aneurysmal velocity and wall shear stress reduction. Blood residence time and thrombus formation, both of which are related to aneurysmal occlusion, were predicted based on passive scalar concentration and low and oscillating wall shear stress regions, respectively. FSI simulations have also been performed to study aneurysm wall remodelling during a cardiac cycle. Correlation of leukocyte behaviour during each stage of coiling was observed. However, aneurysm recurrence is evident after the insertion of the seventh coil as shown by the flow recanalisation near the neck and was therefore investigated. Effects of local packing density, leukocyte adhesion, and wall compliance on aneurysm recurrence were examined. Additionally, an FSI simulation of a distensible coil in the same aneurysm was performed to study coil movement and its interaction with local haemodynamics. Another separated retrospective study was also conducted to explain the mechanism behind the formation of this aneurysm.

Chapter 7 discusses the effects of wall compliance and non-Newtonian viscosity in four end-to-end fistula models; compliant wall with Newtonian flow, complaint wall with non-Newtonian flow, rigid wall with Newtonian flow, and rigid wall with non-Newtonian flow. Wall shear stress at the peak diastole, where the minimum of both effects are compared. Regions of low and oscillating wall shear stress, flow recirculations and helicity are also compared between the four cases. The mechanisms behind AVF maturation failure have been investigated using the wall complaint AVF model with non-Newtonian flow as it represents the most realistic blood flow environment. Effects of local wall shear stress, both magnitude and directional, red blood cells viscosity, von Mises stress, and flow recirculation on fistula wall remodelling are studied. Both inward and outward wall remodelling are discussed as the former leads to AVF maturation failure and the latter is related to successful maturation. Conclusion from both studies are presented in chapter 8.

Chapter 2

Literature Review

Reviews of previous computational studies on cerebral aneurysms and arteriovenous fistulas are presented in this chapter. As cardiovascular diseases in both cases are related to specific arterial layers, the structure of the blood vessel is first discussed. Previous findings on the nature of cerebral aneurysms including the known mechanisms behind their initiation, progression, and rupture are then explained. Endovascular coiling as a preventive treatment option for growing aneurysms and the subsequent thrombus formation are reviewed. Similarly for the arteriovenous fistula study, the clinical criteria for undergoing haemodialysis, fistula maturation, neo-neo-intimal hyperplastic maturation failure are explained. Previous uses of fluid-structure interaction in both studies are reviewed.

Aneurysm rupture is a direct cause of strokes, a lethal condition responsible for the majority of death annually and globally. Even if it is treated in time, the aneurysm can still be subjected to recurrence. The causes of both conditions have not yet been fully understood. Patients suffering from chronic kidney disease can only rely on haemodialysis, which depends on the maturity of the venous access point. Like the mortality rate due to strokes, the rate of fistula maturation failure is high. Therefore, it is important for these two conditions to be investigated. The present aneurysm study examines the effects of coil packing density on flow reduction and investigates the mechanisms of aneurysm recurrence. Understanding the previously established haemodynamic conditions for each stage of cerebral aneurysm growth

is therefore nescessary for idenitifying aneurysm recurrence following endovascular coiling. Likewise, understanding the requirement for AVF maturation is nescessary for studying the mechanisms of maturation failure.

2.1 Blood vessel structure

Both aneurysm progression and rupture, and arteriovenous fistula maturation failure are all related to vessel remodelling and degradation of the endothelial layer of the vessel. It is therefore beneficial to give an introduction to each tissue layer of blood vessels and how they responded to haemodynamic changes. A distinct difference between an artery and a vein is that only the latter has a valve which restricts deoxygenated blood from flowing back upstream. The innermost layer of both artery and vein is comprised of endothelial cells as shown by Figure 2.1. These cells are in direct contact with the blood and are responsible for wall remodelling (Baek et al., 2007) and inflammation (Middleton et al., 2007) in response to damages caused by the local haemodynamics (Luscher and Tanner, 1993; Drexler and Hornig, 1999). Smooth muscle cells are located in the tunica media (middle) layer of the vessel wall but can migrate to the intimal (inner) layer in the presence of haemodynamic changes (Hull et al., 2013). Endothelial and smooth muscle cells, like other cells, are filled with intracellular matrix which governs their behaviour. Extracellular matrices, on the contrary, fill the volume of the blood vessel outside the cells. The three tunica layers are each separated by an elastic lamina (called elastin) which regulates elastic deformation of the blood vessel. These elastins and the extracellular matrix are significant components that maintain the integrity of the arterial walls (Sforza et al., 2009). Therefore, elastin degradation may result in permanent remodelling (Menashi et al., 1987) such as an aneurysm.

2.2 Cerebral aneurysms

An aneurysm is an excessive dilataion of an arterial wall, usually in a bulged shape, that can no longer withstand local haemodynamic changes. As a consequence, aneurysms can grow in size and rupture, leading to intracranial

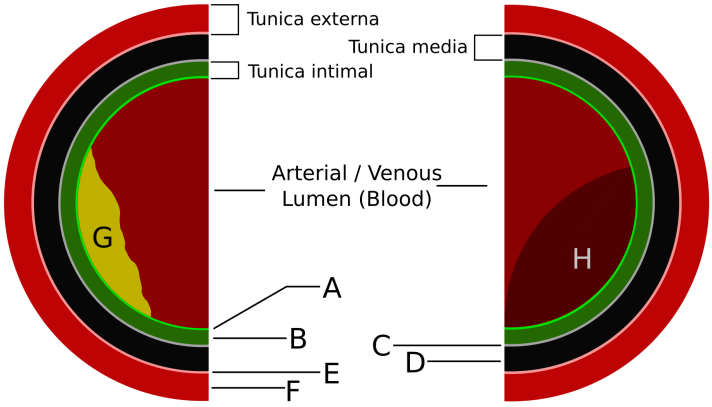

Figure 2.1: Schematic structure of the arterial and venous walls. Sections A-B, C-D, and E-F belong to the Tunica intimal (innermost), Tunica media (middle), and Tunica externa (outermost) layers of both artery and vein, respectively. The tissue layers containing the lumen (blood) consists of A. endothelial cells lining, B. Endothelium, C. internal elastin, D. smooth muscle, E. external elastin, F. external wall, G. plaques, H. venous valve.

haemorrhage (Rinkel et al., 1998; Shamloo et al., 2017) and ischaemic strokes (Pearson et al., 1991). Ten percent of all strokes are known to have been caused by cerebral aneurysm rupture (Bederson et al., 2000). Although only 2-5% of the world population is at risk of harbouring cerebral aneurysm (Rinkel et al., 1998; Curtis et al., 2012), a high mortality rate of up to 40-50% was associated with this pathology (Teunissen et al., 1996; van Gijn and Rinkel, 2001). This is because patients with cerebral aneurysms experience no symptoms far in advance (Shamloo et al., 2017). Some patients may develop a sudden headache, nausea, or loss of consciousness but it would already be too late for treatment as these symptoms occur after aneurysm rupture; up to 8% of these aneurysms rupture before diagnosis. Cererbal aneurysms are commonly found in the Circle of Willis (Humphrey and Taylor, 2008), a system of arteries at the centre of the intracranium. There is a higher possibility of aneurysm formation in female patients (79.7%) than in male patients (20.3%) regardless of age (Jing et al., 2015). Nevertheless, it is still impossible to predict aneurysm behaviour with full confidence (Huberts et al., 2018) and it is crucial to identify one before it ruptures. Additionally, a growing aneurysm does not nescessarily have to rupture (Lee et al., 2013) and those that have already ruptured can re-rupture at any moment (Kataoka et al., 1999). It was reported that among

115 aneurysms, 45% ruptured and 55% did not (Jing et al., 2015). A similar conclusion was made in another study of bifurcation aneurysms where 44 out of 81 aneurysms ruptured (Shamloo et al., 2017). This suggested that the probability of harbouring a stabilised aneurysm is almost identical to that of aneurysm rupture. Moreover, there is a probability of 15-36% for an individual patient to have more than one aneurysm (Ellamushi et al., 2001). In such cases, the aneurysm that is most likely to rupture would be treated first (Jing et al., 2015). Cerebral aneurysms mostly come in two different forms, saccular and fusiform. Saccular aneurysms are mostly found in intracranial arteries, while aortic aneurysms are fusiform. Intracranial aneurysms are less common than abdominal aortic aneurysms (Sharzehee et al., 2018). Eighty five percent of saccular aneurysms are found mostly in the Circle of Willis (Chason and Hindman, 1958), especially in regions with thinner arterial walls (Suzuki and Ohara, 1978) or bifurcations (Shamloo et al., 2017). Haemodynamics is also another significant factor in determining the progress of aneurysm initiation, growth, and rupture (Cebral et al., 2011; Xiang et al., 2014) and it is important to understand their underlying mechanisms (Crompton, 1966). However, these mechanisms were not well-compiled in the literature. Therefore, they are summarised into flowcharts which illustrate the known mechanisms as suggested by different previous studies. The reader is referred to a glossary for the definitions of medical terms used in this thesis.

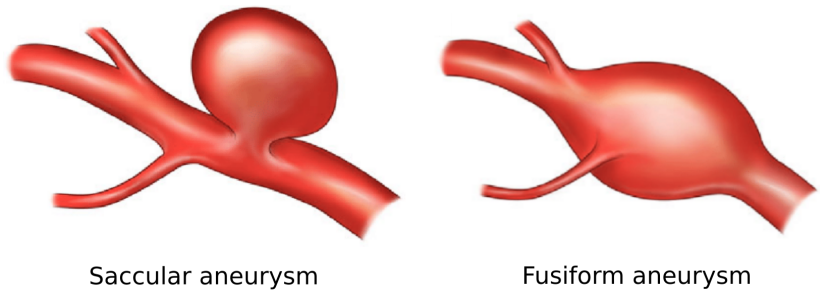

Figure 2.2: Two major configurations of cerebral aneurysms; saccular and fusiform aneurysms. (Adapted from Withers et al. 2013)

2.2.1 Aneurysm initiation

Wall shear stress (WSS) has been regarded as a defining factor for vessel remodelling and aneurysm formation (Luscher and Tanner, 1993; Drexler and Hornig, 1999). Here, wall shear stress is the product of dynamic viscosity and the velocity gradient at the blood vessel wall (see Chapter 3 Section 3.8). It is evident from the literature that both low (Shamloo et al., 2017) and high (Shojima et al., 2004; Hoi et al., 2004) wall shear stresses can independently lead to destructive remodelling of vessel walls (Sforza et al., 2009), and consequently, aneurysm formation (Steiger, 1990). Destructive remodelling is attributed to abnormal endothelial gene expression (Bruno et al., 1998) that weakens the vessel wall and can be traced back to both abnormally high and low wall shear stresses (Fukuda et al., 2000; Georgakarakos et al., 2010). When endothelial genes, or instructions encoded within the endothelial cells, are expressed, the behaviour of the cell changes with local haemodynamic stimulation. In addition, both high (Peerless and Drake, 1982) and low (Soulis et al., 2006; Chaichana et al., 2011) WSS were observed at bifurcations where cerebral aneurysms typically initiate (Shamloo et al., 2017). Figure 2.3 summarises different mechanisms of aneurysm initiation that are understood so far from the literature in details.

High WSS typically originates from accelerated flow (Meng et al., 2007) and high velocity, as wall shear stress is directly proportional to the velocity gradient at the vessel wall. Likewise, proximal cerebral arteriovenous malformations (Peerless and Drake, 1982) and flow impingement (Torii et al., 2010; Lee et al., 2013) have also been observed to raise the blood circulation and wall shear stress downstream of the impingement location, respectively. However, WSS at the location of impingement is theoretically lower than that observed downstream of flow separation. Consequently, wall inflammation was observed at this complex flow region (Cebral et al., 2005, 2011). In the presence of low WSS-induced atherosclerosis (Frosen et al., 2004), proteolytic matrix metalloproteinase (MMP) activity is increased in the region of inflammation (Middleton et al., 2007). Cell damage can propragate deeper into the internal elastic lamina as a result of high WSS (Steiger et al., 1989; Steiger, 1990). MMP gene expression signals the wall to remodel when it is injured,

causing endothelial wall degradation (Menashi et al., 1987; Bruno et al., 1998).

Additionally, oscillatory flow was found to significantly promote endothelial gene expressions (Frosen et al., 2004; Russell et al., 2013). Haemodynamic forces acting on the wall as a result of high velocity can also lead to wall remodelling (Sforza et al., 2009). Endothelial remodelling (Luscher and Tanner, 1993; Kamiya et al., 1988) and malfunction (Fukuda et al., 2000) were found to increase the production of flow-induced nitric oxide. Nitric oxide is released by endothelial cells when they are mechanically stimulated by WSS elevation (Frosen et al., 2004) to dilate the vessel and restore the WSS to its homeostatic range (Lee et al., 2013). However, overproduction of the substance causes excessive remodelling through smooth muscle cells relaxation (Hara et al., 1998). This relaxation process deteriorates the internal wall stress and weakens the arterial structure (Baek et al., 2007). The imbalance between the lumen pressure and the internal wall stress leads to locally destructive wall remodelling (Watton et al., 2009). This process is enhanced by flow impingement which causes local wall remodelling (Sforza et al., 2009). Nitric oxide continues to be overproduced as a result of destructive remodelling and hence, an aneurysm is formed. Unlike the effect of flow impingement, a continuous increase in wall shear stress throughout the wall causes dilatation in all directions. This is due to gene expressions in the endothelial and smooth muscle cells to expand the vessel and reduce the wall shear stress to its homeostatic range. This may be an underlying mechanism specific to fusiform and aortic aneurysms.

Blood velocity usually decreases during hypertension (Lee et al., 2013), which results in low WSS (Chaichana et al., 2011). Under normal circumstances, the intimal layer of blood vessels are atheroprotective, which means they are protected from the formation of atherosclerosis (Stehbens, 1989). However, chronic low and uniform WSS can reverse the endothelial phenotype from atheroprotective to atherogenic and induce the endothelium to atherosclerotic plaque formation (Wasserman and Topper, 2004) in a process called atherogenesis. Recent studies clearly suggested that atherosclerosis is caused by low wall shear stress (Chaichana et al., 2011, 2013a) which originates

from regions of low velocity (Chaichana et al., 2012). Existence of high flow oscillation in low WSS regions can also induce atherosclerosis (Cebral et al., 2019). Atherosclerotic-inflamed endothelium were founded to promote MMP activity which directly contributes to the degradation (He and Roach, 1994) and destructive remodelling (Ross, 1999) of the wall. Aneurysms that form as a result of atherosclerosis typically have a size (maximum diameter) larger than 5 mm (Kataoka et al., 1999). Other aneurysms that are smaller than 5 mm (and presumed to not be formed by atherosclerosis) tend to have 48% thinner walls than usual. This finding agreed with another observation which suggested that atherosclerosis alone only results in wall thickening due to high endothelial cell turnover rate (Ford et al., 2005),

Wall thickening reinforces the parent artery by reducing the risk of aneurysm initiation. This was shown in a study where aneurysms were observed to have thinner and more vulnerable walls (van Gijn and Rinkel, 2001). Additionally, it was also shown that parent arteries with thinner walls (0.05-0.1mm thickness) are more prone to aneurysm initiation (Suzuki and Ohara, 1978). Wall thickening is also observed in low and oscillating flow regions (Dardik et al., 2005). Besides atherosclerosis formation, low WSS elongates and orientates the endothelial cells in the direction of flow (Sforza et al., 2009). However, the insufficiently low shear stress may also reduce the endothelial integrity (Shojima et al., 2004) and consequently weakens the wall (Lee et al., 2013). Atherosclerotic plaques develop into a stenosis which increases the velocity of the flow downstream but can also create regions of recirculating flow. Blood velocity decreases in flow recirculation areas which results in low WSS. Low WSS due to flow recirculation has been reported to be associated with thrombus formation in an oscillating flow environment (Rayz et al., 2010; Meng et al., 2007; Dolan et al., 2013). While low and uniform WSS orientate the endothelial cells to the flow direction, low but oscillating WSS disalign their structure (Dardik et al., 2005; Sforza et al., 2009) which supports thrombus deposition. Apart from thickening the wall, thrombotic plagues may leads to MMP activation (Nakahashi et al., 2002; Hoshina et al., 2003; Sho et al., 2004), which regulates vessel remodelling in response to injury and lead to aneurysm formation. However unlike the atherosclerosis-induced MMP activation, the

process can be reversed for thrombus deposition when the endothelium is inflamed (Ross, 1999).

Arteries are normally straight for efficient blood circulation (Han, 2012) but can deform into a tortuous shape due to their abnormal development (Xie et al., 2013) and cardiovascular diseases (Han, 2009, 2012). Hypertension is also known to develop in older patients with cardiovascular diseases and can cause wall degradation and vessel dilatation (Lee et al., 2013). Patients with cerebral aneurysm were typically found to have twice higher blood pressure than patients without aneurysm. When blood pressure rises and exceeds the critical buckling pressure of the vessel wall, the artery buckles (Hatakeyama et al., 2001; Fillinger et al., 2004) and results in a tortuous artery (Han et al., 2013; Lee et al., 2014; Sharzehee et al., 2018). Tortuous arteries were reported to be prone to aneurysm initiation (Hatakeyama et al., 2001; Fillinger et al., 2004). Once an aneurysm is formed, the axial tension in the aneurysm wall tends to reduce the critical buckling pressure (Liu and Han, 2012), which implies a higher possibility for the parent artery to buckle again (Lee et al., 2014). Like atherosclerotic stenoses, vessel tortousity may lead to higher velocities and wall shear stress (Chaichana et al., 2011; Sun and Cao, 2011; Chaichana et al., 2013a) and the process can continue to iterate until the aneurysm is fully matured. Although there are mutual agreements within the literature on aneurysm formation, the most significant mechanism is still unknown (Torii et al., 2009; Shamloo et al., 2017). High WSS was found to cause direct damages to the endothelium, whereas low WSS requires either flow oscillation or cell inflammation to be present to achieve the same result. Relationships between flow impingement and low oscillating WSS still remain controversial.

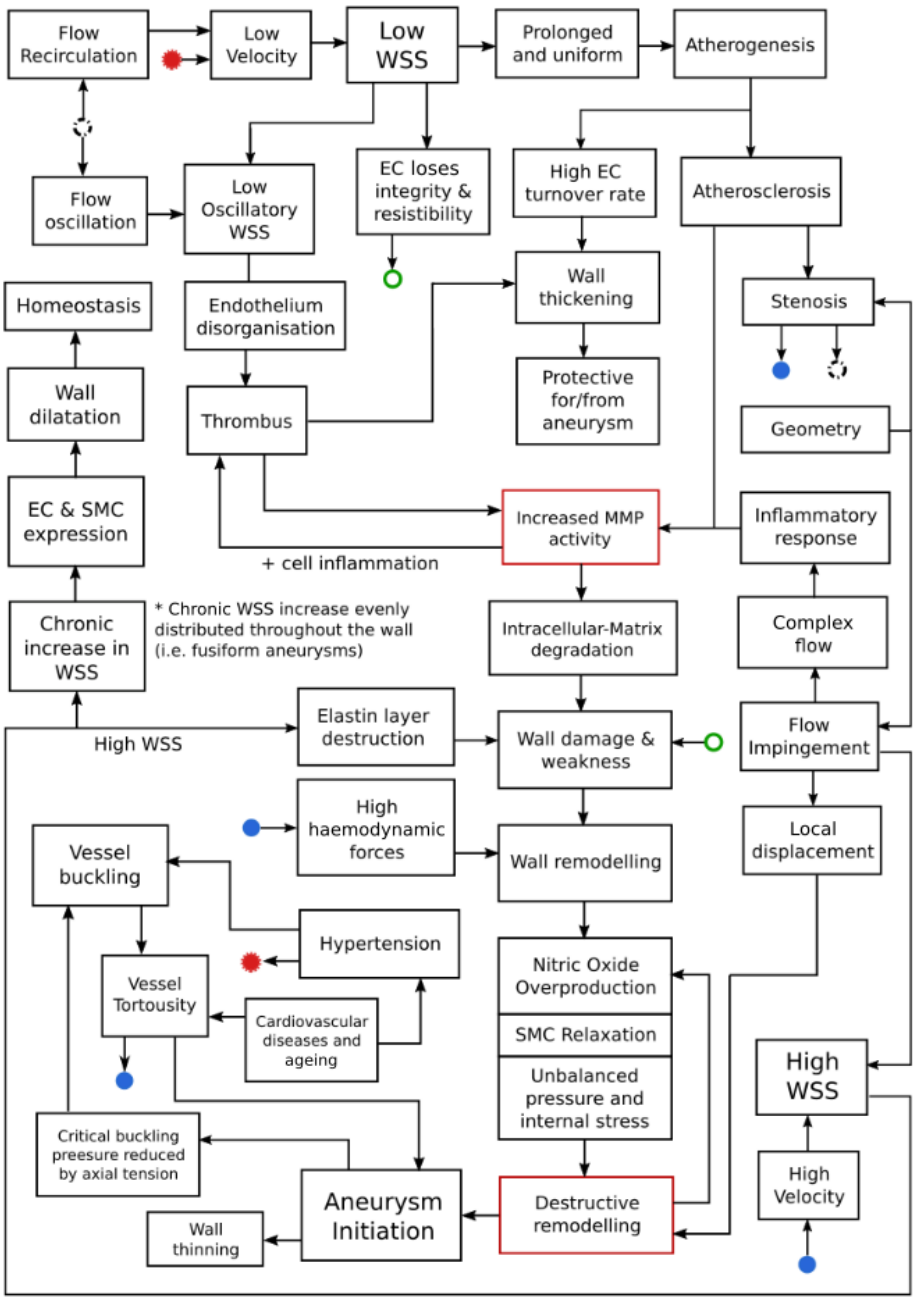

Figure 2.3: Different mechanisms of aneurysm formation. Blue, red, black, and green circles represent high velocity, low velocity, flow recirculation, and wall damage respectively. Red blocks emphasise major events upstream of aneurysm formation.

2.2.2 Aneurysm progression

Shear stress on the aneurysm lumen is still a significant factor in aneurysm growth (Cebral and Raschi, 2013; Otani et al., 2018). High WSS and low flow have been proposed as two independent indicators of aneurysm growth and deformation. Unlike the initiation phase, the mechanisms originating from high WSS and low velocity in the progression phase are clearly different. However, both haemodynamic factors interfere with the cellular structure of the aneurysm (Sforza et al., 2009) which is comprised mainly of collagen, that are responsible for enlargement (Gaetani et al., 1998; Bruno et al., 1998). Figure 2.4 summarises the two main theories that lead to aneurysm growth as suggested by the literature.

The high flow theory suggests that aneurysm growth is maintained by high WSS (Meng et al., 2007). The abnormal increase in WSS, nitric oxide overproduction (endothelial malfunction), and endothelial damage from the initiation phase continue to degrade the wall (Nakatani et al., 1991; Fukuda et al., 2000). Relaxation of smooth muscle cells, despite its apoptosis (death) (Hara et al., 1998) and medial thinning (Kondo et al., 1998), may also promote endothelial degradation. Smooth muscle cell apoptosis is a natural cell-programmed self-destruction that provides a healthy life cycle while the aneurysm progresses. Wall degradation continues to cause destructive wall dilation as the lumen pressure outweighs the deteriorated internal wall stress. Wall-embedded collagens and the elastic lamina layers are stretched as the vessel deforms. This allows the internal wall stress to rise back to its homeostatic range as the wall stiffness increases. However, due to the passive accumulation of lumen blood pressure, the balance between internal wall stress and transmural pressure cannot be maintained and a new level of homeostasis has to be achieved (Steiger et al., 1989). This results in a continuous increase in the internal wall stress which can eventually exceed the critical stress for further deformation and aneurysm growth (Sforza et al., 2009). Oscillatory lumen pressure due to flow pulsation was found to apply periodic loading on the endothelium and enlarge the aneurysm (Watton et al., 2009). Longitudinal flow into the dome may also cause impingement on the wall and enhance WSS elevation (Lee et al., 2013).

The low flow theory differs from the high flow theory in the underlying mechanism of wall degradation which consequently leads to the deformation of a growing aneurysm. Previous studies have shown to support this hypothesis (Shojima et al., 2004; Jou et al., 2005; Rayz et al., 2010). Blood velocity can be reduced after entering the aneurysm sac causing flow stagnation (Baharoglu et al., 2010). In this low flow environment, the aneurysm wall cannot be mechanically stimulated and the production of nitric oxide is dysfunctioned due to WSS insufficiency (Frosen et al., 2004). Consequently, the low concentration of nitric oxide in the aneurysm endothelium disables relaxation of smooth muscle cells and prohibits the artery from restoring its original shape after continuous remodelling, hence promoting aneurysm growth (Lee et al., 2013). Flow stagnation and shear rate reduction (Otani et al., 2017a, 2018) causes the platelets to aggregate and accumulate along the intimal surface of the aneurysm (Sforza et al., 2009). Platelet adhesion damages and inflames the intimal layer, which results in the migration of leukocytes (white blood cells) into the degraded wall to repair it (Crompton, 1966). Patients with leukocyte deficiency may be exposed to higher risk of aneurysm rupture if the inflamed wall is not treated in time. Blood flow was also reported to stagnate due to shear-thining and hence increase in viscosity (Otani et al., 2017a). Wall degeneration due to intimal damage reduces the critical wall tensile force that supports the aneurysm from transmural pressure. The wall tensile force may increase due to pressure variation, especially during hypertension, to reach an equilibrium. However, it can easily exceed the lowered critical tensile force and cause permanent deformation and aneurysm growth. In the presence of low flow and hence thrombus deposition in the aneurysm (Rayz et al., 2010; Zhou et al., 2017), MMP may be reactivated and cause further wall degeneration (Hoshina et al., 2003; Sho et al., 2004). The main causes of high WSS and low flow are high velocity and flow recirculation, respectively. Both hemodynamic changes can be observed at stenotic cross sections (Chaichana et al., 2012), similar to the neck of a saccular aneurysm. Although the two controversial mechanisms of aneurysm progression are different, the formation of a stenotic aneurysm neck may be the only relationship between the two theories.

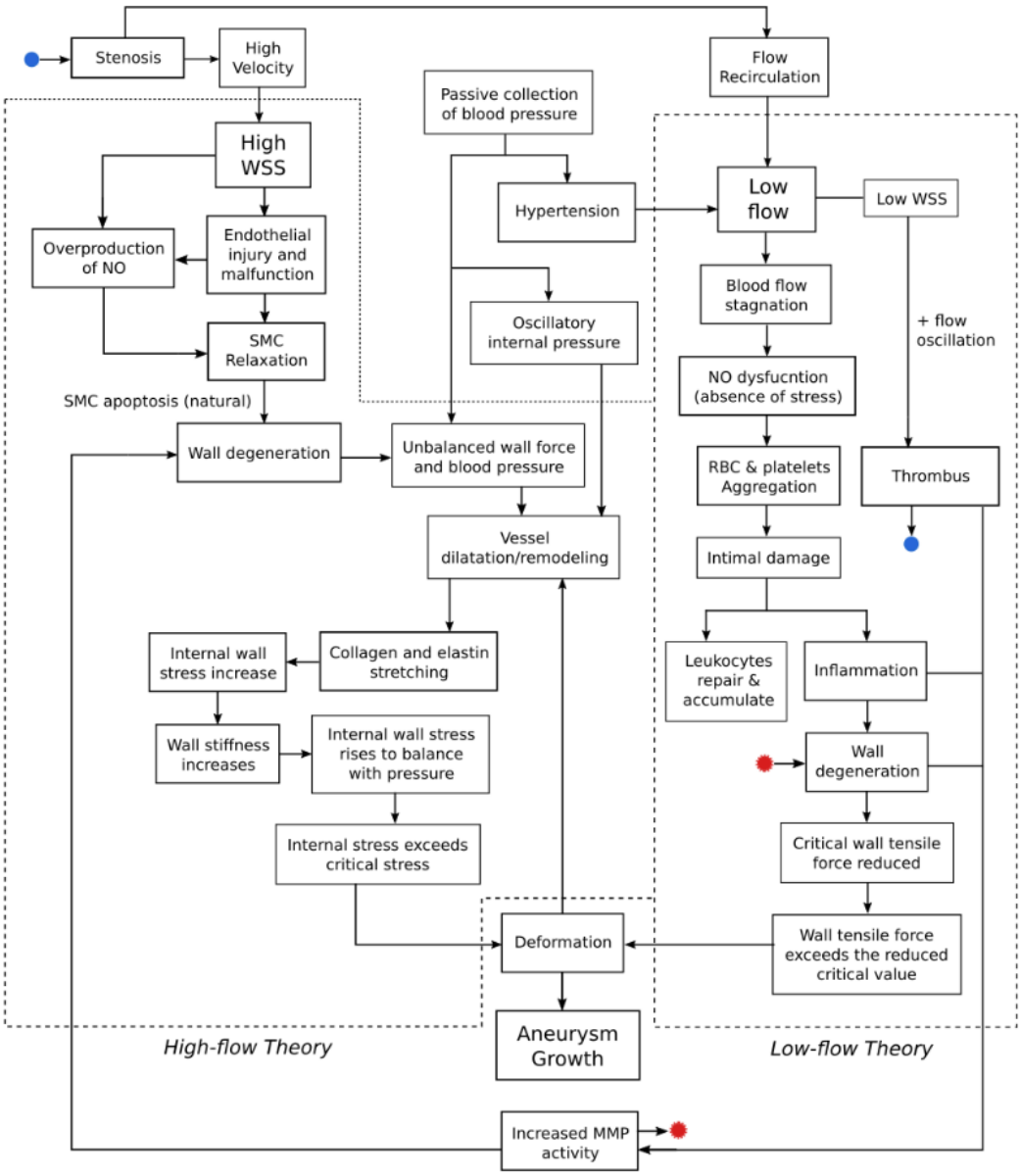

Figure 2.4: Different mechanisms of aneurysm growth presented by two major theories. Blue and red circles indicate stenosis formation and wall degeneration, respectively.

2.2.3 Aneurysm rupture

A growing aneurysm ruptures when it can no longer withstand the transmural pressure (Sforza et al., 2009). Hypertension was reported to contribute to both aneurysm growth and rupture (van Gijn and Rinkel, 2001; Lee et al., 2013) but is not the sole discriminator for rupture (Taylor et al., 1995) as there are many other factors that have proven to be mode relevant. Although maximum aneurysm diameter (Georgakarakos et al., 2010; Sharzehee et al., 2018) and mechanical stress on the aneurysm wall (Lee et al., 2013) were also proposed as rupture predictors, WSS variation is the most significant mechanism of rupture (Sharzehee et al., 2018). However, it is believed that aneurysm morphology and size can still play a major role in aneurysm rupture (Jing et al., 2015). Aneurysm size is defined as its the maximum diameter. Large aneurysms (size greater than 4mm) carry a higher risk of rupture (Vorp, 2007) as 90% of unruptured aneurysms were reported to be smaller than 4mm in size. Although Lee et al. suggested that aneurysm size is the most reliable method for clinical discrimination of rupture, some ruptured aneurysms in the study had a size that is larger than the critical value of 5 mm (Lee et al., 2013). Aneurysmal tortuosity (Hatakeyama et al., 2001; Fillinger et al., 2004; Georgakarakos et al., 2010; Sharzehee et al., 2018) and high aspect ratio (aneurysm height divided by neck width) are also important factors that lead to aneurysm rupture (Ujiie et al., 1999; Nader-Sepahi et al., 2004). Lastly, the thickness of the medial layer decreases during aneurysm growth as a result of smooth muscle cells apoptosis (Kondo et al., 1998; Hara et al., 1998; Stehbens, 1989). It was reported that aneurysm rupture occurs when its wall thickness decreases below 0.05 mm (Abruzzo et al., 1998).

It was also understood that an aneurysm ruptures when its internal wall stress rises beyond the failure strength (Sharzehee et al., 2018), especially in low WSS regions (Rayz et al., 2010) where anti-thrombotic factors are under-produced by endothelial cells (Longest and Kleinstreuer, 2003). In the high-flow theory of aneurysm growth, the internal wall stress increases to exceed the critical stress (Sforza et al., 2009). In the low-flow theory on the other hand, the critical tensile force of the wall is reduced, shortening the process of tensile force increment below the critical value (Lee et al., 2013;

Sharzehee et al., 2018). Once the critical wall stress or wall tensile force is exceeded, regardless of theory, the aneurysm ruptures and subarachnoid hemorrhage follows (Taylor et al., 1995; Teunissen et al., 1996; van Gijn and Rinkel, 2001; Jing et al., 2015; Shamloo et al., 2017). The mechanisms which lead to wall degradation as observed during the aneurysm growth include wall inflammation (Torii et al., 2010) and thrombus formation (Zhou et al., 2017), which is strongly related to local viscosity (Boussel et al., 2008; Morales et al., 2013a), is still in effect. In fact, thrombus formation can also be beneficial to a growing aneurysm, if it does not develop thrombo-embolisms (Rayz et al., 2010). At a low shear rate of 100 s^{-1} where thrombus are usually formed, it can initiate aneurysm occlusion (Otani et al., 2017a). Aneurysm occlusion, naturally by thrombus formation or endovascular intervention, prevents blood inflow into the aneurysm and WSS variation, reducing the rupture risk before wall degradation becomes too severe. Proximal vasospasm, a sudden arterial contraction, was also suggested to be related to hemorrhage after the aneurysm ruptures (Mortimer et al., 2016). Nevertheless, the mechanism of aneurysm rupture still remains controversial (Rayz et al., 2015; Sharzehee et al., 2018) and requires tremendous attention to fully understand its nature.

2.3 Endovascular coiling of cerebral aneurysms

Endovascular treatments of cerebral aneurysms provide a method of isolating an aneurysm sac from its parent artery (Morales et al., 2011) to avoid abnormal haemodynamic changes that can stimulate the endothelial cells (Otani et al., 2017a) and reduce consequent rupture risk (Otani et al., 2018). As prediction of aneurysm growth and rupture is poor, preventive interventions must be conducted to avoid rupture and subarachnoid haemorrhage (Otani et al., 2016). Different treatments have previously been used by clinicians which includes clipping (Kataoka et al., 1999), coiling (Hirashima et al., 2002; Gallas et al., 2005) and stenting (Kaku et al., 2007). Most aneurysm cases were previously treated by coiling in the past 15 years as it resulted in lower mortality rates in aneurysm patients when compared to surgical clipping (Morales et al., 2011). The process of aneurysmal coiling involve inserting a flexible platinum coil inside the aneurysm dome to prevent parent-arterial flow

from entering the sac. In certain circumstances where there is a risk of a coil escaping the aneurysm, a stent can be placed across the aneurysm neck to avoid non-target embolization of the coil (Rayz et al., 2015). Nevertheless, the application of depends on the aneurysm shape, neck width, and its position on the Circle of Willis (Shamloo et al., 2017). If the aneurysm morphology does not allow the catheter carrying the coil to access the aneurysm sac, an alternative method must be employed. Other drawbacks of coiling includes challenges of its usage in ruptured aneurysms due to geometric complications (Zhou et al., 2017) and aneurysm recurrence (Otani et al., 2018). However, endovascular coiling is still in common use as it is less invasive, but more effective than other treatment methods (Otani et al., 2017a). The major effect of coiling is to achieve aneurysmal blood flow stagnation and partial occlusion of the aneurysm sac. In the long term, a complete occlusion can be obtained by the coil-induced thrombus formation (Sforza et al., 2009). Different coil models have been used in previous studies which include the representation of the coil as a straight cylinder (Narracott et al., 2005), helical cylinders (Schirmer and Malek, 2010), large hollow sphere (Byun and Rhee, 2004), and porous medium by assuming unrealistic homogenous occlusion of the aneurysm (Cha et al., 2007; Groden et al., 2003; Kakalis et al., 2008). Although these coiling models have been used in previous studies, they do not resemble the shape and distribution of a real coil and little is known about their effects on aneurysmal haemodynamics (Morales et al., 2011; Levitt et al., 2017). Moreover, coiling patterns in different patients can never be identical due to geometric diversity. Uniform occlusion of an aneurysm is clinically unachievable even when it is heavily packed with real coils (Otani et al., 2018). The only coil configuration that truly represents clinical coiling cases is used by Otani et al., Morales et al., and the present study. Figure 2.5 shows an angiography of an aneurysmal coil during operation (Andrade et al., 2012). The white arrow in the figure points to a coiled aneurysm.

Since coils have different dimensions depending on manufacturers and aneurysm sizes vary with different patients, the volume of the coils inserted alone may not be informative. A more useful measure of the coil volume inside the aneurysm is packing density (PD). It is defined as the ratio between the vol-

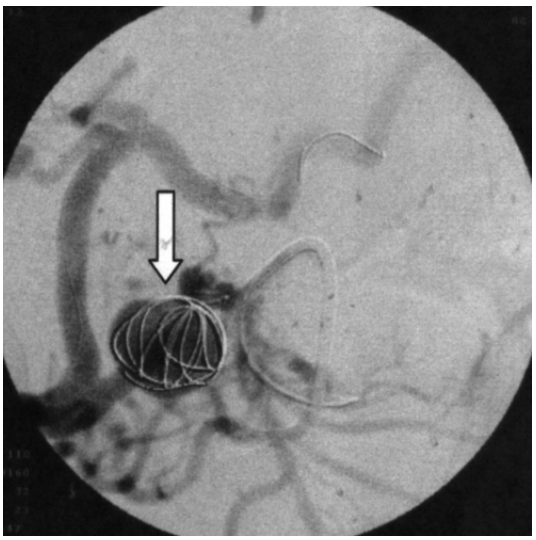

Figure 2.5: Angiography of a coil inside an aneurysm (Andrade et al., 2012)

ume of the coils inserted to the volume of the aneurysm. Coil configurations and packing density used in this study are discussed and defined in Chapter 3. Aneurysmal haemodynamics have been investigated in coiled aneurysms in ten previous studies. Table 2.1 summarises numerical studies on coiled aneurysms to date.

Local packing density is reported to have an inverse relationship with local flow velocity (Otani et al., 2018). Higher packing density can also promote flow stagnation, which was observed from the spatial reduction in both velocity and WSS inside the aneurysm. Generally, a packing density of 30% is high enough to suppress the intra-aneurysmal flows (Morales et al., 2011, 2013b). Other studies reported that a packing density between 25-27% is also sufficient in isolating the aneurysm from extra-aneurysmal flows (Otani et al., 2016, 2018). Although aneurysms are usually packed with the highest coil density (Morales et al., 2011), a complete flow blockage at the aneurysm neck may not be achieved (Otani et al., 2018). This suggested that coiled aneurysms can still be prone to rupture and recurrence regardless of the high packing density.

The effects of packing density on kinetic energy distributions and shear rates in a steady flow environment were investigated to understand flow stagnation and thrombus formation, respectively Otani et al. (2017a). Morales et al. (2013b) studied local coil distribution in the longitudinal (Otani et al. 2018) and radial direction. Otani et al. (2018) investigated the relationship between local packing density, flow kinetic energy (KE), and volume of low shear stress. Flow KE was found to be more evenly distributed prior to coiling and only 20% of the total flow KE dwelled at the neck region as shown by the flow kinetic ratio (FER). After coiling, 80% of the total flow KE was observed at the neck region. This rise in flow KE at the neck created locally disturbed flow and contributed to a risk of recurrence even with high packing density. The negative correlation between FER and local PD weakened as the flow travels into the aneurysm. Flow momentum ratio (FMR) and flow shear rate ratio (FSR) were also devised to investigate the effects of coil density on flow momentum and shear rates (Otani et al., 2017b). Both ratios dramatically decreased by approximately 80% even at a low packing density of 10%. At this same packing density, a reduction in FER of 90% was observed. Only Otani et al. (2017b,a), and Morales et al. (2011) performed packing density independence tests. However, Morales et al. (2011) was the only study that conduct the packing density independence test in an unsteady but Newtonian flow environment. Additionally, they investigated the effects of packing densities on WSS reduction, velocity reduction, and the increase and decrease in area of low and high WSS.

Otani et al. (2017b) and Morales et al. (2013b) compared the use of Newtonian and different Non-Newtonian models of coiled aneurysms. It was concluded that the non-Newtonian features of the blood may be negligible when evaluating time-averaged velocity reduction and the WSS of an untreated aneurysm. However, the differences in WSS and space-averaged velocity magnitude in treated aneurysms cannot be neglected. Therefore, both concluded that Newtonian flow should be used when only the global flow is investigated. Thus, non-Newtonian models must be used in order to investigate local flows near the wall. It was also reported that non-Newtonian flow behaviour may provide insights on the thrombogenic hemodynamics in the vincinity of the

Table 2.1: Summary of coiled and rigid aneurysm studies. For rheology, Newt. and non-N denote Newtonian and non-Newtonian flows with the corresponding models used in bracket. CY and CS denotes Carreau-Yasuda and Casson models, respectively. For aneurysm location, CO, ICA, PcommA, and MCA denotes carotid-ophthalmic, internal carotid artery, posterior communication artery, and middle cerebral artery. For pulsatile conditions, 'No' indicates a steady flow simulation. * denotes a study with passive scalar transport

Study	aneurysm type	Pulsatile flow	Rheology
(Wan et al., 2020)	CO	No	Newt.
(Sheng et al., 2019)	unknown types	Yes	Newt.
(Otani et al., 2018)	ICA	No	Newt.
(Misaki et al., 2017)	PcommA	Yes	Newt.
(Otani et al., 2017b)	ICA	No	non-N (CY).
(Otani et al., 2017a)	ICA	No	Newt.
(Otani et al., 2016)	ICA	No	Newt.
(Morales et al., 2013b)*	5 unknown types	Yes	Newt
(Morales et al., 2013a)	ICA	Yes	non-N (CS)
(Morales et al., 2011)	Right MCA	Yes	Newt.
Present study*	MCA	Yes	non-N (CY).

coils (Otani et al., 2018), whereas a Newtonian model would underestimate the reduction in shear rate and thus the probability of thrombus formation. Additionally, reduction in the kinetic energy due to increased packing density and time-averaged aneurysmal velocity were overestimated in the Newtonian model (Otani et al., 2017a) and may contribute to a misleading conclusion on aneurysm recurrence. The overestimation of intra-aneurysmal velocity was reported to be more significant in treated aneurysms.

Both studies used two different non-Newtonian models for their investigation on coiled aneurysms. Otani et al. (2017b) used the Carreau-Yasuda model while Morales et al. (2013b) used the Casson model. These two models have previously been compared against one another and their corresponding Newtonian model (Boyd et al., 2007). The shear and velocity profiles derived from the Casson model were found to exhibit a larger variation from that of the Newtonian model. Our current understanding on the effects of endovas-

cular coiling on non-Newtonian haemodynamics is attributed to Otani et al. (2017b) and Morales et al. (2013b). However, the causes of aneurysm rupture and recurrence in a non-Newtonian environment were not discussed in these two previous works.

Although all four works of Otani et al. provided an insight into the effects of coil distribution on aneurysmal haemodynamics, their results were concluded based on the assumption that blood flow is steady and aneurysm walls are rigid. Additionally, none of the rigid coiled aneurysm studies conducted by Morales et al. discussed the effects of haemodynamics on aneurysm recurrence. Aneurysm recurrence is a post-coiling condition when flow is allowed to re-enter the aneurysm despite high coil packing density (see Section 2.3.2). Other recent studies on coiled aneurysm since 2017 assumed Newtonian flow but suggested possible mechanisms of aneurysm recurrence (Misaki et al., 2017; Sheng et al., 2019; Wan et al., 2020). However, they did not discuss how blood cells distribution and wall compliance affected aneurysmal haemodynamic and recurrence. Their findings on aneurysm recurrence are further discussed in Section 2.3.2 (Aneurysm Recurrence). The present study uses the Carreau-Yasuda model to investigate aneurysm haemodynamics and the effects of local packing density, leukocyte (white blood cell) re-entry and adhesion, and wall compliance on aneurysm recurrence. These three haemodynamic factors have not been discussed in the literature.

2.3.1 Blood residence time and thrombus formation

While packing density is a good predictor of aneurysm rupture, it is not easily measured by clinicians during an operation so blood flow visualisation using medical contrast agent is preferred. In CFD, contrast agents are modelled as a passive scalar and reduction in its concentration inside the aneurysm sac leads to a successful treatment (Rayz et al., 2015). To the best of the author's knowledge, there is currently only one study that investigated passive scalar transport in coiled aneurysm models (Morales et al., 2013b), in several aneurysms of unknown types. However, non-Newtonian effects were

not investigated in the study. Although a highly sufficient packing density of 30.0% was achieved, a packing density independence test was not performed in each aneurysm so the effect of coil density on flow reduction was not observed. Therefore, the present study is the first to investigate the effects of packing density on aneurysmal flow, WSS reduction, and also the distribution of passive scalar transport in a cerebral aneurysm with non-Newtonian flow regime. Rayz et al. (2010), Rayz et al. (2015), and Vali et al. (2017) also visualised passive scalar transport (in Basilar artery aneurysms) and proposed different methods in determining the residence time. However, coiling was not involved in these studies. Rayz et al. (2010) calculates residence time using a virtual contrast threshold of 0.02 in non-Newtonian blood flow and correlated both residence time and wall shear stress with thrombus and thrombus-free areas. They also observed that high residence time region are usually located near the aneurysm walls. Localisation of high residence time near the inner walls was also observed with coils reducing the inflow into the aneurysm and inducing thrombus within it Morales et al. (2013b). This can also be observed clinically as the amount of contrast trying to enter the aneurysm is blocked by coils.

Increase in the residence time was associated with low WSS, blood cells aggregation, and thrombus deposition in the near-wall region. All current non-Newtonian models does not take account of the red blood cell aggregation, namely the Rouleaux formation (Arzani, 2018). This behaviour of red blood cells is observed in regions of low shear and there is a time scale involved. Blood must enter and reside in this low shear region for a specific amount of time, usually three seconds to a minute, for Rouleaux structures to be formed. Both low shear and time is needed, therefore, the current non-Newtonian models alone cannot be used. Arzani (2018) proposed that for a Largrangian blood particle with a residence time higher than the threshold value for Rouleax formation, the Carreau-Yasuda non-Newtonian viscosity can be used. For other particles with residence time below the threshold value, the Newtonian viscosity is used. This method can be used if Rouleaux formation is of great concern. Otherwise, the use of passive scalar transport is sufficient for predicting blood residence time as shown in Morales et al. (2013b).

Fast filling of the scalar transport was observed in healthy parts of the arteries (Rayz et al., 2010), while slow filling promotes thrombus formation (Vali et al., 2017). In fact, regions that were not filled with the virtual contrast are correlated with increased flow residence time and thrombus deposition. Despite these findings, however, a specific time frame for fast filling, slow filling, and concentration criteria for no filling was not clarified. Two percent of the maximum contrast concentration was proposed only because a zero threshold value would also include the outlet regions which were setted to be contrast-free and cause confusion. Morales et al. (2013b) used Turnover Time (TOT) to describe the time taken to refill an standardised aneurysm with equivalent volume with new blood. It was defined by the quotient of the aneurysm volume and mean inflow rate through the aneurysm neck over one cycle. Higher values of TOT was observed in all treated cases as expected due to the flow resistance induced by the coils. However, the index only considers the global aneurysmal flow and does not capture localised residence times or flow oscillations. Vali et al. (2017) compared scalar transport into a basilar artery aneurysm with agent contrast clinically used in pre-coiling X-ray angiography. The aneurysmal flow characteristics in both cases were found to be equally preserved when using either contrast model.

Flow residence time visualised by virtual contrast is also in good agreement to MR data (Rayz et al., 2015), suggesting that medical images, and thus passive scalar, can be used to predict operation outcomes in cerebral aneurysms. Like that of Morales et al. (2013b), the time-density curve of passive scalar was shown to describe residence time and thrombosis probabilities. Table 2.2 summarised the rheology configuration used in previous studies with passive scalar applications. Only Morales et al. (2013b) studied aneurysmal haemodynamics using passive scalar in a coiled, but Newtonian, aneurysm. To the best of the author's knowledge, the present study is the first to investigate non-Newtonian passive scalar transport inside coiled aneurysms.

Low flow regions in coiled aneurysms increase blood residence time and activate platelets that enters the dome, allowing them to initiate thrombus formation (Ouared et al., 2008; Sforza et al., 2009). During thrombosis (the

process of thrombus formation), activated platelets aggregate to form blood clots which eventually occlude the aneurysm sac, reducing the risk of rupture. However, the aggregated platelets that forms the thrombus can cause damage to and inflame the aneurysm wall, which again increases the rupture risk. Therefore the stability of the aneurysm depends not only on the occlusion rate, but also on the rate at which the inflamed wall is healed. In response to the wall inflammation, cytokines (a type of protein) are released into the bloodstream to enable leukocyte adhesion to the endothelial lining of the aneurysm wall (Lindemann et al., 2001). These leukocytes (white blood cells) migrate to the aneurysm wall where they adhere to and infiltrate the endothelial lining to reach the inflamed regions (Swystun and Liaw, 2016). When they reach the inflamed region, leukocytes begin to heal the degrading wall. Consequently, the risk of aneurysm rupture, and hence recurrence, is reduced.

Table 2.2: Summary of rigid and pulsatile aneurysm studies with passive scalar applications. For rheology, Newt. and non-N denoted Newtonian and non-Newtonian flows with the corresponding models used in bracket. For aneurysm location, BA indicates basilar artery and MCA indicates middle cerebral artery.

Study	aneurysm type	Rheology	Coiling
(Vali et al., 2017)	BA	Newt.	No
(Rayz et al., 2015)	BA	Newt.	No
(Morales et al., 2013b)	unknown type	Newt.	Yes
(Rayz et al., 2010)	thrombolised BA	non-N	No
Present study	MCA	Non-N	Yes

2.3.2 Aneurysm recurrence

Aneurysm rupture risk can be reduced by thrombus formation and leukocyte migration and adhesion to the aneurysm wall. However, occluding aneurysms can still be subjected to flow recanalisation despite a high coil packing density (Otani et al., 2016; Liu et al., 2016; Otani et al., 2018). Flow recanalisation is when blood is allowed to re-enter the occluding aneurysm due to aneurysm regrowth (Hoppe et al., 2015) or coil compaction (Morales

et al., 2013b; Otani et al., 2018; Greve et al., 2020). This leads to aneurysm recurrence. Coil compaction causes the disintegration of the thrombus formation (Sluzewski et al., 2004), preventing the aneurysm from being completely occluded (Greve et al., 2020). This decrease in the percentage of aneurysm occlusion, which results in an abnormal increase in flow velocity and thus contrast filling (Greve et al., 2020), have been associated with aneurysm recurrence (Chalouhi et al., 2014). Increase in the contrast filling is clinically represented by opacification on the angiography (Misaki et al., 2017). Therefore, aneurysm recurrence can be identified when aneurysmal velocity abnormally increases with increasing coil density. A reduction in leukocyte migration into the occluding aneurysm (as a response to thrombus-induced wall inflammation) can also lead to aneurysm recurrence (Swystun and Liaw, 2016). Therefore, aneurysm recurrence can also be observed when there is a decrease in leukocyte inflow and adhesion to the aneurysm wall. Other factors like high pressure difference on the coil (Uno et al., 2020) and rupture status have been suggested to cause aneurysm recurrence. Aneurysm size and location also play a significant role in determining the probability of recurrence (Ferns et al., 2009). Aneurysm recurrence has already been observed in 15-25% of coiling cases that were thought to be successful (Sluzewski et al., 2003), but there is currently no unified mechanism or a global prediction method for aneurysm recurrence (Morales et al., 2013b; Otani et al., 2018).

(Misaki et al., 2017) and (Sheng et al., 2019) compared wall shear stress, velocity, and coil packing density in a group of patients with recurrent and stable aneurysms. Misaki et al. (2017) found that wall shear stress, regions of low coil packing density, aneurysm size, and neck in the recurrence group were not significantly different from those of the stable group. Only the aneurysmal velocity and flow rate are significantly different; velocity in the recurrence group is lower. They suggested that the decreased velocity due to wall impingement in the recurrence cases are converted into static pressure, a factor they believed to be a possible mechanism of aneurysm recurrence. On the other hand, (Sheng et al., 2019) founded that the peak systolic and post-treatment WSS, high near-wall flow oscillation, and high blood velocity were associated with aneurysm recurrence. (Wan et al., 2020) found that aneurysm recurrence

can be reduced if the aneurysm neck is densly coiled. However, they did not take into account the fact that local coil packing densities at the neck, and elsewhere inside the aneurysm, can be unevenly distributed. The additional coil in some regions of the aneurysm neck may not be as densly packed as other neck regions. Relatively lower coil density in the neck region can still provoke aneurysm recurrence (Otani et al., 2017a). Otani et al. (2018) showed that lower coil packing density in the neck region induced higher flow kinetic energy. Increase in local flow and abnormal changes in WSS promote aneurysm regrowth, and consequently recurrence. They suggested that coil compaction was an unlikely cause of aneurysm recurrence as the thrombotic blood clots inside the aneurysm tends to support the coils against flow impingement rather than being destroyed by it. Blood clots are known to have solid and viscoelastic structures (Weisel, 2008), so they have the ability to reinforce the coils. All these studies assumed Newtonian viscosity and did not take into account wall compliance and the multiphase characteristic of blood. The present study proposes new haemodynamic factors which can contribute to aneurysm recurrence; local coil packing density, leukocyte re-entry and adhesion, and wall compliance.

2.3.3 Fluid-structure interactions (FSI): Coiled Aneurysms

Interactions between the aneurysmal flow and the wall can provide insights on the flow-induced wall motion and effects of such displacement on the flow that cannot be accurately acquired in vivo (Lee et al., 2013). More importantly, the ability to investigate wall movements will lead to a better understanding of aneurysm growth and hence rupture. Prediction of aneurysm rupture in the past relied only on statistics of aneurysm size and location. FSI simulations of coil compaction and deformation due to aneurysmal flow can also be an important tool in determining the mechanisms of aneurysm recurrence (Otani et al., 2016). Recent CFD studies have implemented fluid-structure interactions to investigate the effect of intra-aneurysmal flows on the walls and vice versa.

Jahed et al. (2018) conducted the first FSI study of MCA and BA aneurysms with the completed Circle of Willis included to investigate its effect on aneurysm

stability. The Circle of Willis is a system of cerebral arteries in which most cerebral aneurysms are located. The aneurysm neck was concluded to be prone to rupture as WSS was higher at the location compared to the fundus. However, non-Newtonian effects across the Circle of Willis were not investigated, while mesh and time-step size independence tests were not performed to justify accuracy. Shamloo et al. (2017) and Torii et al. (2010) investigated the effects of wall thickness variations on treated and untreated cerebral aneurysms, respectively. In the former study, a completed occlusion was modelled to represent coil treatment in a wall-compliant aneurysm with Carreau-Yasuda non-Newtonian flow (Shamloo et al., 2017). Although the occlusion reduced the flow entering the sac, the proposed coil model does not truly represent real clinical coils as packing density would never reach 100% and coil distribution is not uniform (Otani et al., 2018). Additionally, an idealised geometry with an insufficient extrusion of the inlet was used in that study even though they claimed that the an inlet section of 5 times the diameter is sufficient for pulsatile condition. Besides, there was another attempt to model endovascular coil as one hugh sphere in a wall-compliance aneurysm (Ahmed et al., 2011), which also did not represent a realistic clinical case. Torii et al. (2010) founded that modelling ruptured aneurysms (which normally have thin walls) with thicker walls underestimated wall displacement. This underestimation can be explained by results obtained from Lee et al. (2013), which suggested that ruptured aneurysms have larger displacement than unruptured aneurysms.

Aneurysmal Von-Mises stress on aneurysm walls was reported in Fu and Qiao (2011). There is a good agreement in the maximum wall stresses (0.0-0.3 MPa) in all previous studies except in Shamloo et al. (2017). The values reported in Shamloo et al. (2017) are higher and fall in the range of 0.0-0.9 MPa. The difference in aneurysm type, inlet entrance length, the use of idealised geometry, and wall elasticity model may contribute to this overestimation. Near-wall flow oscillations, relatve residence time and time-averaged WSS in a wall-compliant aneurysm were presented only in Shamloo et al. (2017). Table 2.3 summarises what aspects of simulations have been investigated by recent FSI aneurysm studies. To the best of the author's knowledge,

there is no FSI study on coiled aneurysm, especially with non-Newtonian rheology and the use of passive scalar.

Interactions between elastic coils and the aneurysm wall were considered only in coil deployment simulations Morales et al. (2013b); Otani et al. (2016). In these studies, there is no interaction between the flow haemodynamics, the coils, and the aneurysm wall. The present study investigates the interaction between the compliant aneurysm wall and haemodynamic, the effects of wall compliance on aneurysm recurrence, and the effects of compliant coils on aneurysmal haemodynamics. The present study is the first to investigate the haemodynamics of a wall compliant aneurysm subjected to coil embolisation and passive scalar.

Table 2.3: Summary of recent FSI cerebral aneurysm studies with pulsatile flow but no coil treatment and passive scalar analysis. For rheology, Newt. and non-N denotes Newtonian and non-Newtonian flows with the corresponding models used in bracket. CY and C denotes Carreau-Yasuda and Carreau models, respectively. For aneurysm type, B and F indicates bifurcation and fusiform aneurysms. For aneurysm location, MCA, ICA, AcommA detontes middle cerebral artery, internal carotid artery, and anterior communicating artery.

Study	aneurysm type	Rheology	Coiling	PS.
(Jahed et al., 2018)	MCA (B) and BA	Newt.	No	No
(Helthuis et al., 2018)	MCA (F)	non-N (C)	No	No
(Sharzehee et al., 2018)	Idealised	Newt.	No	No
(Shamloo et al., 2017)	Idealised	non-N (CY)	No	No
(Eken and Sahin, 2017)	unknown (B)	Newt.	No	No
(Fu and Qiao, 2011)	ICA (S)	Newt.	No	No
(Torii et al., 2010)	MCA (B)	Newt.	No	No
(Valencia et al., 2008)	unknown (B)	non-N (C)	No	No
Present study	MCA (B)	non-N (CY)	Yes	Yes

2.4 Arteriovenous fistulas

Chronic kidney disease can lead to a severe dysfunction of the human blood purification system in the final stages of the pathological condition (Iori et al., 2015). Patients suffering from end-stage renal (kidney) diseases therefore rely on haemodialysis (Jodko et al., 2014), if they are not eligible for a kidney transplant. Haemodialysis, the process of purifying blood, can only be performed through successful vascular access (Sigovan et al., 2013). The process requires an exchange of the patient's blood (contaminated with metabolic wastes) for purified blood from the dialysis machine. Two needles are injected into the arm to provide vascular access to the patient's vein from which the blood can be withdrawn at a typical flow rate of 500 ml/min (Kharboutly et al., 2010). However, at this high volumetric flow rate, the vein can be at risk of collapsing which would result in a haemodialysis failure. To avoid such an event from occuring, the venous wall needs to be thicker to withstand this high withdrawal rate. In order to achieve this, an excess volume of blood is required to enter the vein in order to increase the flow rate and thus the wall shear stress. As a natural response to this abnormal increase in WSS, the vein dilates and its thickness is increased to reduce the WSS back to its physiological range and maintain homeostasis. This process is called maturation. The only local source of this additional blood supply is the proximal artery. Through a minor vascular surgery, an artificial connection between the artery and the vein of the patient, called a fistula, can be created to allow blood from the artery to supply the vein.

Different configurations of these two vessels can be arranged which includes a side-to-side, a side-to-end, an end-to-side, and an end-to-end anastomoses. The name given to these anastomoses depends on the direction of blood transfer from one vessel to the other. A fistula connecting the end of a vein to the side of an artery would be called a side-to-end arteriovenous fistula (AVF) as the blood leaves the side of the artery and enters the end of the vein. In the event of a fistula failure (i.e. when a vascular access point cannot be created), only the use of arteriovenous grafts (AVG) with a tunneled dialysis catheter can be provided as an alternative trial for patients who did not suc-

ceed in fistula hemodialysis (Astor et al., 2005). Although there is a possibility of surviving despite its higher risk of infection (Asif et al., 2006), the mortality rate associated to AVG is relatively higher than that of AVF (Grechy et al., 2017) by a factor of 1.5. Higher cost and complications involved in the administration of AV grafts also resulted in higher usage of AV fistulas (Leermakers et al., 2013). However, despite 50 years of clinical practice and development since the first fistula was created (Brescia et al., 1966), the success rate is still as high as the failure rate. There have not been any significant findings in the last 30 years that can improve the outcome of hemodialysis (Boghosian et al., 2014). The main reason behind this slow advancement revolves around several controversies of the actual mechanisms of fistula maturation failure that have not yet been understood (Pike et al., 2017b; Drost et al., 2017; Ene-Iordache and Remuzzi, 2017).

The present study is the first to investigate the underlying mechanism in an end-to-end AV fistula. To the best of the author's knowledge, there have been very limited studies on the failure of fistula with end-to-end configuration, all of which conducted grid independence tests based on steady simulations rather than using realisitic flow conditions (McGah et al., 2013). In addition, none of these studies used patient-specific images acquired from ultrasound images. Although unsteady grid independence tests and ultrasound images have previously been used with other types of fistulas, the outcome of different AVF configurations are not identical (Malovrh, 2009; Ene-Iordache et al., 2013). This reflects the opportunity of this study not only to investigate the mechanism of AVF maturation and failure, but to use a higher mesh accuracy and alternative imaging modality to empathises or argue against the difference in the performance of an end-to-end fistula.

2.4.1 Fistula maturation

When the arterial blood flow (with high and pulsating pressure) is directed into the vein, which originally had low and steady pressure, the pressure gradient and flow rate immediately increase across the AVF (Browne et al.,

2015). The resulting variation in WSS promotes endothelial gene expression to stimulate wall remodelling (Sho et al., 2002) through nitric oxide overproduction. Post-surgery increase in venous pressure initiate smooth muscle cell migration into the intimal layer to prevent further compression of the endothelial cells induced by the pressure (Gusic et al., 2005). The proliferation of smooth muscle cells results in media-layer thickening and wall weakening. High lumen pressure can also cause endothelium dilatation and outward remodelling of the lumen, which on the contrary may lead to maturation success. The imbalance between the high lumen pressure and the deteriorated internal wall stress force the circumferential tension to increase (Corpataux et al., 2002) during homeostatis. High and low WSS were reported to cause wall dilatation and intimal thinning, respectively (Gusic et al., 2005). Lumen dilatation is an endothelial response to decrease the WSS to its homeostatic level. On the other hand, intimal thinning is related to insufficient endothelial stimulation, dysfunction of nitric oxide production, and consequent wall degradation in this order. After 6 weeks, endothelium dilatation and WSS reduction may still be observed if homeostatis has not yet been reached. However, WSS in regions proximal to the anastomosis may still be high despite the decrease in flow rate during this period.

The criteria for a matured fistula is a vein diameter of 6 millimetres, a volumetric flow rate of 600 ml/min, and a 6 mm offset from the skin surface (Shenoy, 2009). Other studies suggested that a higher blood flow rate of up to 800 ml/min may be required for hemodialysis (Jodko et al., 2014). The maturation process usually takes 6 to 8 weeks after which vein cannulation can be observed. Some studies suggested that AVF are matured 2-4 weeks (Robbin et al., 2016), 4-6 weeks or 12-16 weeks after operation (Shenoy, 2009). Longitudinal studies of fistula maturation have been conducted in previous studies Beathard et al. (2019); Leotta et al. (2003) to find a common agreement in the maturation time, but it remains inconclusive. The generalised guidelines for justifying fistula maturation have also proved to be misleading and out of date (Beathard et al., 2019).

Present controversies also include the mechanism behind the maturation

of AV fistulas. Throughout the entire process, the venous segment experiences outward remodelling in order to maintain a homeostatic range of wall shear stress (McGah et al., 2013). The increased blood flow (McGah et al., 2014) and pressure (Browne et al., 2015) have independently been reported to elevate the wall shear stress (WSS) in the anastomotic regions. The endothelial cells (EC) on the inner lining of the vein respond to this stimulation by remodelling outward to decrease the wall shear stress. Although several haemodynamic quantities have shown to be related to AVF failure and can be use to interpret the opposite phenomenon, a direct relationship between these variables and successful maturation have not yet been established.

2.4.2 Maturation failure

There are three possible outcomes for fistula maturation; outward remodelling of the vessel wall, inward remodelling of the vessel wall, or both simultaneously. Outward remodelling is favourable and would result in successful maturation while any presence of inward remodelling will increase the risk of maturation failure. The latter is also associated with neo-intimal hyperplasia and stenosis development (Ene-Iordache and Remuzzi, 2012; Geenen et al., 2016). Media-layer thickening induced by the proliferation of smooth muscle cells was found to cause remodelling in both directions (Rothuizen et al., 2013). On the other hand, high-WSS-induced dilatation results in outward remodelling only. However, lumen dilatation was observed to be associated with progressive intimal and medial thickening during the first 6 weeks of maturation. Direction of remodelling is therefore determined by the more influential mechanism (between dilatation and intimal-medial thickening), which is still unknown. The non-uniform increase in the endothelium cross-sectional area along the vessel due to dilatation can only approximate locations prone to and safe from inward remodelling, but not the underlying mechanism.

The AVF failure rate spans in a very large range from 18% to 53% with a mean rate of 25% (Asif et al., 2006) and up to 60% (Grechy et al., 2017; Pike et al., 2017b) when failing AVF requires surgical intervention after one year (McGah et al., 2014). Similarly, the success rate considered at a one-year

patency mark is 60% to 70 % (Roy-Chaudhury et al., 2007). Neo-intimal hyperplasia (impaired outward remodelling) and inadequate maturation are two mechanisms briefly known to be responsible for maturation failure (Pike et al., 2017b), both leading to occlusive inward remodelling also known as a stenosis. Neo-intimal hyperplasia is well documented to have a direct relationship to the formation of stenosis (Geenen et al., 2016; Ene-Iordache and Remuzzi, 2012). The blockage of blood flow leads to insufficient volumetric blood flow, which is not ideal for haemodialysis. Other similar lesions including hand ischemia, thrombosis, and cardiac output failure can also lead to unsuccessful maturation (Pike et al., 2017b). All of these causes are related to endothelium dysfunction (Geenen et al., 2016).

2.4.3 Neo-intimal hyperplasia

Intimal hyperplasia (IH) is a morphological disorder of the vessel wall in which the intimal layer of the blood vessel thickens. Instead of remodelling outwards, the innermost layer grows in size and decreases the local lumen diameter and possible stenosis. IH-induced stenoses and atherosclerosis may lead to insufficient oxygen supply to nearby tissues and cardiac failure (Almasri et al., 2016). The consequent lack of oxygen supply supresses the remodelling of both the fistula and vein. IH develops as a result of endothelial cell activation by the local multi-directional flows near the wall (Flores et al., 2016). The blood vessel responds to this invasive haemodynamics by migrating the smooth muscle cells from the media layer to the intimal layer where the endothelial cells are located (Hull et al., 2013). The smooth muscle cells (SMC) proliferate over the activated cells in order to prevent them from being injured (Jia et al., 2015), in the same manner as the formation of scar tissue. Like what is observed in a growing aneurysm, the activated endothelial cells reduce the production of nitric oxide that promote vascular dilation, resulting in an adequate outward remodelling. Every stage of haemodialysis from the creation of the fistula through vascular surgery (Genek et al., 2015), the possible incompatibility of the newly created AVF with native vessels (Niemann et al., 2010), and the lesion resulting from dialysis needle injection (Kharboutly et al., 2007) can all lead to IH. High wall shear stress induced by turbulence during

hemodialysis can also injure the endothelial cells causing further SMC proliferation (Kharboutly et al., 2007). Additionally, low WSS (Yamamoto et al., 2015), disturbed flow relative to long residence time (McGah et al., 2011; Caroli et al., 2013; Beathard et al., 2019), cell inflammation due to surgery (Genek et al., 2015) and repetitive venous cannulation (Metry et al., 2011) have also shown to be related to IH formation and stenosis. This inward remodelling of the wall is an endothelial response to the initial vessel wall deterioration and is directly proportional to the level of vascular lesions experienced by the endothelial cells. Arterial and venous calcification, the deposition of calcium substances on the inner lining of the wall, can also cause inward remodelling, like atherosclerosis and stenosis (Browne et al., 2015). This pathological lesion eventually hardens the blood vessel, disabling further remodelling regardless of direction. The formation of the new cells due to SMC proliferation on the intimal layer is called neo-intimal hyperplasia (NH). In wall compliant CFD, it can be observed as inward remodelling of the arterial wall. The present study correlates AVF maturation failure due to neo-intimal hyperplasia with wall shear stress, red blood cell viscosity, von-Mises stress, and flow recirculation.

2.4.4 Fluid-structure interactions (FSI): Fistula

Previous investigations on the wall-compliant effects on arteriovenous fistulas were limited only to four studies as listed in Table 2.4. All four studies used a patient-specific model except for Ngoepe et al. (2011), the first FSI study for AV grafts, which also function like a fistula. Additionally, only the side-to-end or end-to-side AVF configurations were investigated in the four studies. Ngoepe et al. (2011) studied the effects of flow-induced wall tension, shear stress, and wall deformation on graft failure. An end-to-side anastomosis with perpendicular and acute angulations was formed on the artery in one case, and the vein in another case. Highest wall displacement was observed in the acute arterial anastomosis (135 degrees) where graft failure was expected due to its circumferential deformation. Decorato et al. (2014) is the only FSI-AVF study to model blood as a non-Newtonian fluid. Regions of low oscillatory and high shear stresses that are prone to intimal hyperplasia were identified over the entire venous segment. Newtonian simulation was also conducted and showed that the WSS can be overestimated from the Non-Newtonian findings by 15%. The artery was modelled to have a greater wall thickness than the vein to avoid under- or over-estimation of the internal wall stress. McGah et al. (2014) and de Villiers et al. (2018) developed their own algorithms for FSI simulations which have also been validated with MRI in-vivo experiments. The FSI results in McGah et al. (2014) were compared to a rigid case and found that the time-averaged wall shear stress is overestimated by the rigid model. Also, WSS at the anastomosis was overestimated by 15% in the rigid model. The identical overestimation of WSS by Newtonian flow in Decorato et al. (2014) and the rigid model in McGah et al. (2014) could also be attributed to the significantly larger venous segment compared to the proximal artery in both studies. Although, the AVF geometry used in McGah et al. (2014) was also acquired using 3D ultrasound, the present study is the first to investigate both wall-compliance and non-Newtonian effects in an ultrasound-derived end-to-end arterioveneous fistula.

Table 2.4: Summary of recent FSI fistula studies. For rheology, Newt. and non-N denote Newtonian and non-Newtonian flows. CS denotes Casson model. For imaging, NPS and US denote the use of non-patient specific and idealised geometry and ultrasound, respectively.

FSI Study	Fistula type	Rheology	Imaging
(Ngoepe et al., 2011)	End-to-side	Newt.	NPS
(Decorato et al., 2014)	End-to-side	non-N (CS)	CT
(McGah et al., 2014)	End-to-side	Newt.	US
(de Villiers et al., 2018)	End-to-side	Newt.	MRI

2.5 Opportunities of CFD in the present study

Intra-aneurysmal haemodynamics and the mechanisms of aneurysm growth and rupture, or the rupture time were studied and understood with the use of computational fluid dynamics (Jing et al., 2015; Shamloo et al., 2017). Aneurysm size and shape alone still cannot discriminate ruptured aneurysm from unruptured ones due to existing contradictions (Jing et al., 2015). Therefore, CFD is used to assist clinicians and researchers to identify haemodynamic factors and distribution that cannot be obtained from angiography (Chaichana et al., 2013a). In AVF studies, CFD has also been an important tool for the investigation haemodynamics and intimal hyperplasia (Ene-Iordache and Remuzzi, 2017), regardless of geometric complications that were involved. It also allows researchers to study the interactions between haemodynamics and vascular leison development in realistic geometries that cannot be obtained through in vivo measurements. Despite many findings in recent studies, there are several issues that have not been investigated in previous aneurysm and fistula studies. The following list explains how the present study addresses these issues.

For the aneurysm study:

1. Although there are several agreements among results from previous aneurysm studies, none of them have conducted independence tests for the time-step size used. The senstivity of aneurysmal haemodynamic to the timestep size is discussed in Chapter 5.

2. The distribution of passive scalar, which can be used to interpret blood residence time inside an aneurysm, have previously been studied in a Newtonian environment (Morales et al., 2013b). The present study investigates non-Newtonian blood residence time and thrombus formation by observing passive scalar transport as shown by the results in Chapter 6 Section 6.X.

3. The relationship between low and oscillating WSS with aneurysmal atherosclerosis and plaque-free regions in a non-Newtonian coiled aneurysm is still poorly understood (Otani et al., 2017a). This issue is investigated in Chapter 3 Section 6.X.

4. Areas of low and high WSS in coiled aneurysms have been investigated (Morales et al., 2011) but areas of low and oscillating WSS, which can be prone to atherosclerotic development, have not been studied. They are investigated in Chapter 6 Section 6.X.

5. Aneurysmal tortuosity has been suggested to not significantly affect FSI results (Shamloo et al., 2017). However, the aneurysm geometry used in Shamloo et al. (2017) is idealised and symmetric. Therefore, it may be possible for aneurysmal tortuosity to affect results obtained from a patient-specific aneurysm with compliant wall like that of the present study. The effects of aneurysmal tortuosity can be seen in Chapter 6.

6. Although packing density can predict coiling success to a certain level (Morales et al., 2013b), more indices to predict clinical outcomes need to be discovered (Otani et al., 2018). In Chapter 6 Section 6.X, the low and oscillating wall shear stress index is introduced and used as a prediction tool for aneurysm rupture.

7. Effects of local packing densities on aneurysmal flow have been studied by (Otani et al., 2018). However, they did not take into account the multiphase characteristics and flow pulsatility of blood. In Chapter 6 Section 6.X, blood is modelled blood as a multiphase fluid and the effects of local packing density on the distribution of red and white blood cells, as well as that of the aneurysmal flow, are investigated.

8. The effects of local packing density, leukocyte distribution and adhesion to the aneurysm wall, and wall compliance on aneurysm recurrence are investigated in the present study. These haemodynamic factors have never been related to aneurysm recurrence in the literature. Previous studies which discussed the role of haemodynamics on aneurysm recurrence all assumed Newtonian flow and did not investigated the contributions of these proposed factors (Misaki et al., 2017; Otani et al., 2018; Sheng et al., 2019; Wan et al., 2020). Results from the present aneurysm recurrence study are presented in Chapter 6 Section 6.X.

9. Although previous studies have simulated the deployment of elastic coils into an aneurysm, they did not show how the compliant coil affected aneurysmal haemodynamics (Morales et al., 2013b; Otani et al., 2017a). The present compliant coil study in Chapter 6 Section 6.X addresses this issue.

For the fistula study:

1. It is clear that studies on rigid end-to-end fistula are rather limited (Ene-Iordache et al., 2001; Kharboutly et al., 2010; Ene-Iordache and Remuzzi, 2012; Jodko et al., 2014), especially with geometry acquired by ultrasound imaging (Niemann et al., 2012b). Since ultrasound imaging are rarely used for CFD-based fistula studies due to the complicated image segmentaion involved, they have been never been validated in detail. Therefore, ultrasound-derived haemodynamics have been validated against those derived from the already well-established MRI as presented in Chapter 4. Different wall shear stress derived parameters and multiphase haemodynamics have been used for the validation.

2. Among some of the previous rigid end-to-end AVF studies, either an inappropriate pulsatile inflow (Jodko et al., 2014) or a Newtonian flow (Kharboutly et al., 2010; Niemann et al., 2012b) was used. The inlet waveform used by Jodko et al. (2014) was claimed to be time-dependent but it was generated by velocity data from multiple steady simulations. Additionally, it was unclear whether an unsteady simulation was performed. Appropriate boundary conditions have been used in the present study as discussed in Chapter 3.

3. Large time step sizes of 100 ms (Jodko et al., 2014), 40 ms (Kharboutly et al., 2010) and 20 ms (Ene-Iordache and Remuzzi, 2012) were used in previous studies. Some studies did not discuss the sensitivity of their mesh (Ene-Iordache et al., 2001; Ene-Iordache and Remuzzi, 2012; Jodko et al., 2014). Mesh and timestep size independence tests have been conducted for this study and are discussed in Chapter 5.

4. In terms of 3D flow structures, only the localised normalised helicity (LNH) have previously been observed (Browne et al., 2015). Further investigation on other 3D structures in the AVF may be beneficial to our understanding of AVF maturation. The present study investigates 3D contours of LNH, flow recirculation regions, and wall shear stress in four conditions; rigid wall with Newtonian flow, rigid wall with non-Newtonian flow, compliant wall with Newtonian flow, and compliant wall with non-Newtonian flow. These contours are presented in Chapter 7.

5. There is currently a limited understanding on the relationship between wall shear stress and AVF maturation failure (Ene-Iordache and Remuzzi, 2017). Chapter 7 of this thesis also investigates the contributions of wall shear stress, red blood cell viscosity, von-Mises stress, and flow recirculation to AVF maturation failure.

Chapter 3

Methodology

Computational fluid dynamics (CFD) simulations were performed to numerically solve the 3D Navier-Strokes equations for both wall surface and volumetric hemodynamic quantities. Numerical simulations heavily rely on geometries, so the method used to obtain them are important. In the case of the present study, the geometry used are obtained from anonymous patients. 3D images of their blood vessels were acquired and segmented so a model can be reconstructed for the CFD solver. Moreover, the type and rupture status of the aneurysm can be identified using criteria from the literature. Virtual coils of seven different packing density have also been created to perfectly fit the aneurysm sac. This process is important as the study investigates the effects of coil packing density on aneurysmal haemodynamics and recurrence in Chapter 6. For the AVF study, the brachial artery and vein were connected with a fistula, forming an end-to-end AVF. This process allows arterial blood flow to enter the vein, and for the study on fistula maturation to be conducted in Chapter 7. For both studies, computational meshes were generated and independence tests were conducted as explicitly discussed in Chapter 5. The boundary conditions and governing equations, including that of the passive scalar transport, the multiphase blood, and the fluid-structure interactions are presented. Lastly, haemodynamic properties, including the proposed low and oscillating wall shear stress index, investigated in this thesis are defined.

3.1 Medical Images Acquisition

Most CFD packages comes with a 3D-CAD modelling interface which allows users to create their own geometry. However, simulations which involve the human cardiovascular system require an accurate representation of blood vessels in the region of interest. It is very likely that these blood vessels do not hold a regular pipe-like shape due to vascular abnormality and may contain geometric complications like stenosis and thrombus deposition (Niemann et al., 2010) that are unique to every patient. Only a number of major flow characteristics found in a straight pipe flow like the Dean vortices can still be observed occasionally (Ene-Iordache and Remuzzi, 2012) in straight sections. Dean vortices are two counter-rotating vortices observed in pipe flows.

The geometry used for most blood flow simulations is obtained using computed tomography (CT) (Otani et al., 2016), magnetic resonance imaging (MRI) (Niemann et al., 2012b), and only a few studies using ultrasound imaging. This may be due to the additional complications involved in differentiating image artifacts from the actual vessel morphology during segmentation of ultrasound images when compared to the other two techniques. CT and MRI scans typically produce images with higher resolution but can be more harmful to patients compared to ultrasound imaging. Although it is more portable and safer to operate, ultrasound imaging is not regularly used to capture systems of narrower blood vessels like cerebral arteries due to its own limitations. To the best of the author's knowledge, only three studies on AVF and none of cerebral aneurysms used medical images acquired by ultrasound scanning. In the present study, the cerebral aneurysm geometry was segmented from a CT scan. The AVF geometry used is comprised of a brachial artery and vein pair obtained from ultrasound scanning.

3.2 Geometry Segmentation

Due to the complicated geometry of the blood vessels obtained and the intention to use patient-specific geometries for realistic results, the AVF and aneurysm geometry cannot be modelled nor directly imported into Star-

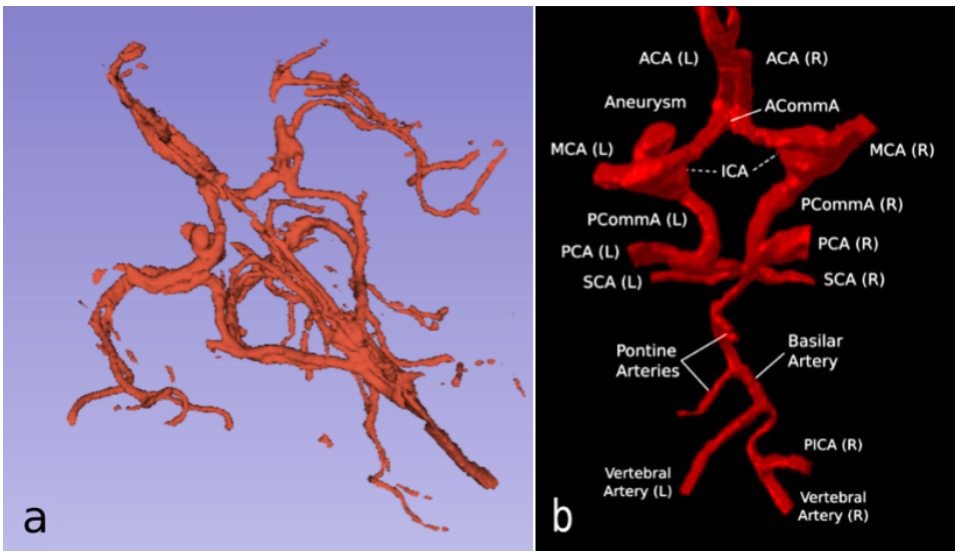

Figure 3.1: (a) System of cerebral arteries segmented from a CT-scanned image in 3DSlicer. (b) Smoothed model of the Circle of Willis and its proximal arteries in Blender; ACA - Anterior Cerebral Artery, ACommA - Anterior Communicating Artery, MCA - Middle Cerebral Artery, ICA - Internal Carotid Artery, PCommA - Posterior Communicating Artery, PCA - Posterior Cerebral Artery, SCA - Superior Cerebellar Artery, (L) and (R) denotes left and right, respectively.

CCM+ as would have normally be done in simulations of regular geometry. The raw images received from the source are instead imported into an open-source medical image segmentation software 3dSlicer 4.8 (Fedorov et al., 2012). The region of interest is specified, segmented, and exported to another 3D rendering software, Blender 2.79 (Blender Institute, Netherlands). In Blender, the imported .STL (stereolithography) model is reconstructed (Chaichana et al., 2013a) through face subdivision and triangulation. Further refinement and surface smoothing can done in this stage. A balanced level of smoothing of the surface is important: over-smoothing may distort the lumen shape and size while insufficient smoothing may leave in the geometry, sharp edges and surfaces, which do not exist in a real blood vessel. Both can lead to artificial results as mass flow rate can directly be affected by an underestimation of the lumen diameter and shear stresses can be abnormally high at sharp edges. These risks have been taken into consideration so that the geometrical aspects of the model are preserved. This was achieved by applying additional subdi-

vision to all surfaces until vertex smoothing only smooth the local surface and does not alter the size of the model. Finally the geometry with completed surface finishing is exported to Star-CCM+ for simulation setup to be prepared. As geometry segmentation is a crucial step towards a realistic simulation, a lot of effort has equally been put into it. The Circle of Willis (CoW) can be considered as one of the most complicated system of arteries in the human body and the blood vessels in this area can be tortuous when affected with diseases (Han, 2012). It is also where cerebral aneurysms typically grow (Humphrey and Taylor, 2008; Schievink, 1997).

In order to enhance the understanding of the CoW structure and extend the ability in image segmentation, a patient-specific geometry of a Circle of Willis was segmented in 3DSlicer as shown in Figure 3.1a and was exported to Blender where imaging artifacts were removed and the region of interest was smoothed (Figure 3.1b). Every aspect of the Circle of Willis was captured and its proximal arteries are labelled in the caption. Figure 3.2 shows the details of the CoW from different angles, an MCA aneurysm and an ACommA (a), a tortuous pair of the ACAs (b) with possible formation of an arterial malfunction, two ICAs (green arrows), and a pair of vertebral arteries (blue arrows) which allows blood inflow into the CoW (c), and a side view of the model showing the inclined structure of the CoW (d).

3.2.1 Segmentation of the Cerebral Aneurysm

Another CT-scan of the the brain which belongs to a patient diagnosed with a cerebral aneurysm was imported into 3DSlicer for segmentation. Like most 3D medical images, the medical scan was comprised of a series of 2D images, taken consecutively in three directions. These three directions are normal to three different planes that are orthogonal to one another as shown in Figure 3.3. The coronal plane divides the head into the front and back halves, while the sagittal plane divides the head into the left and right halves. The axial plane divides the head into the upper and lower halves and typically provides the best view of the Circle of Willis due to the orientation of the

latter. The 3D image was observed thoroughly and the aneurysm was located as shown in the axial view by Figure 3.4a. The 3D image was segmented parallel to the axial plane in order to confirm the location of the aneurysm as illustrated by the green box in Figure 3.4b.

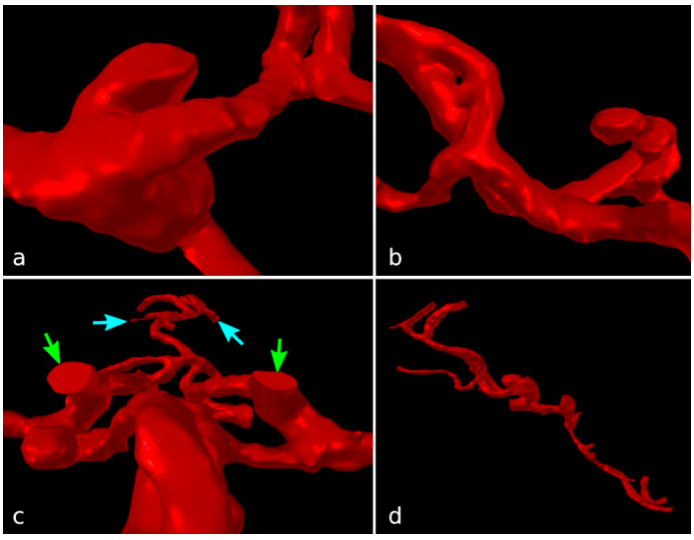

Figure 3.2: Detailed view of the Circle of Willis (CoW) from different views. Green and blue arrows show ICAs and basilar arteries inlet sections.

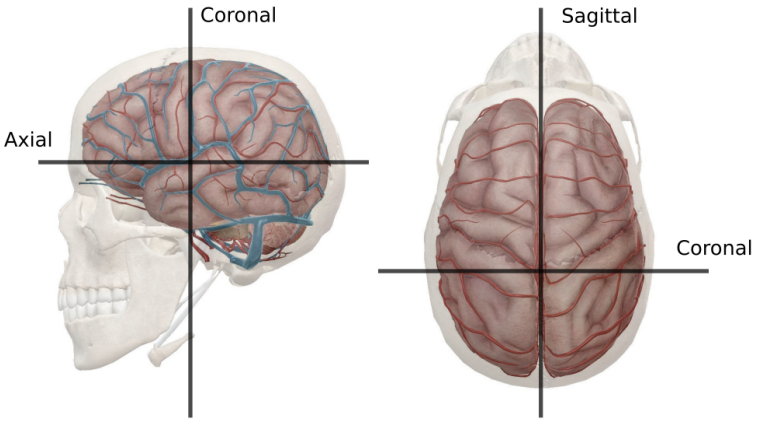

Figure 3.3: Orientation of the coronal, sagittal, and axial planes over the cerebral anatomy. Segmentation along the black line will produce the respective planes. (Reconstructed from Human Anatomy Atlas, (VisibleBody, 2019))

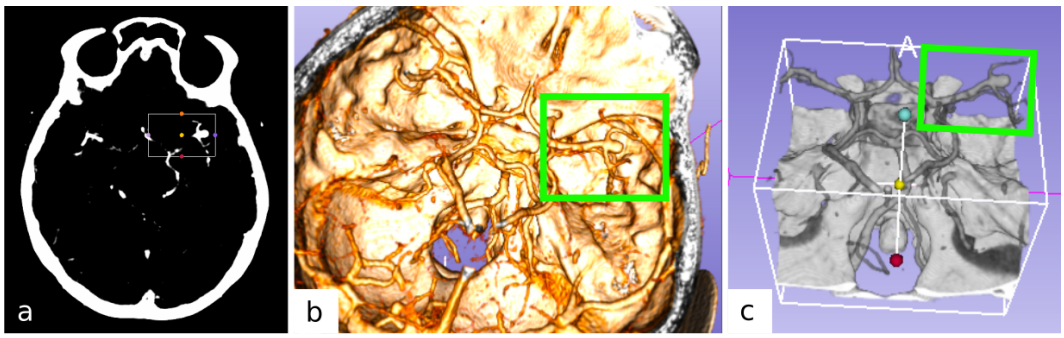

Figure 3.4: a) The right MCA anerysm and the Circle of Willis from in 2D axial view. b) 3D visualisation of the Circle of Willis, the aneurysm, and the proximal arteries. c) The region of interest which includes the target aneurysm. The green box shows the location of the aneurysm, the upstream M1 branch and the the downstream M2 bifurcation.

A right MCA aneurysm was located on the bifurcation of the M2 segment. For clarification, the MCA is frequently categorised into three connected segments M1, M2, and M3 with the M1 segment attached to the CoW (nearer to the centre of the head) and M3 segment further away from the CoW (away from the centre of the head). Blood leaves the Circle of Willis and flows into the M1 segment of the MCA before approaching a bifurcation that leads to a pair of M2 segments. This is where the present aneurysm is located. It was observed that 63% of 1,309 middle cerebral artery aneurysms occur at this M2 bifurcation (Elsharkawy et al., 2013). The region of interest was specified as shown in Figure 3.4c, and exported to Blender for further segmentation and surface finishing. The image imported into Blender contained a lot of artificial fragments of vessel tissues that were incorrectly identified by 3DSlicer as illustrated in Figure 3.5a. It is possible to adjust the segmentation threshold to split the image by non-contiguous but that will also destroy the surface of the targeted arteries and aneurysm, Figure 3.5b shows the smoothed model of the MCA aneurysm and its proximal arteries. According to the angle and orientation of the aneurysm, it is evident that blood flows from the Circle of Willis towards the aneurysm through the right MCA and follow the bifurcated M2 segments before it leaves the domain through the four outlets. However, the flow directions in the upstream ACA and PCommA are not certain and no supporting literature can be found to provide clarification on this matter. Therefore, the geometry was truncated by a section plane through the

MCA, separating the aneurysm from the Circle of Willis. Since the present study is focused on aneurysmal hemodynamics, the problem size can be reduced by truncating both M2 segment to isolate the M2 bifurcations and the four outlets. This would also minimise any errors that may occur as a result of implementing inappropriate flow split as each outlet varies significantly in diameter. Although a considerable amount of time and effort was put into surface finishing, it is more important to preserve the accuracy of the boundary conditions of the model. The segmented MCA aneurysm is used for the present study.

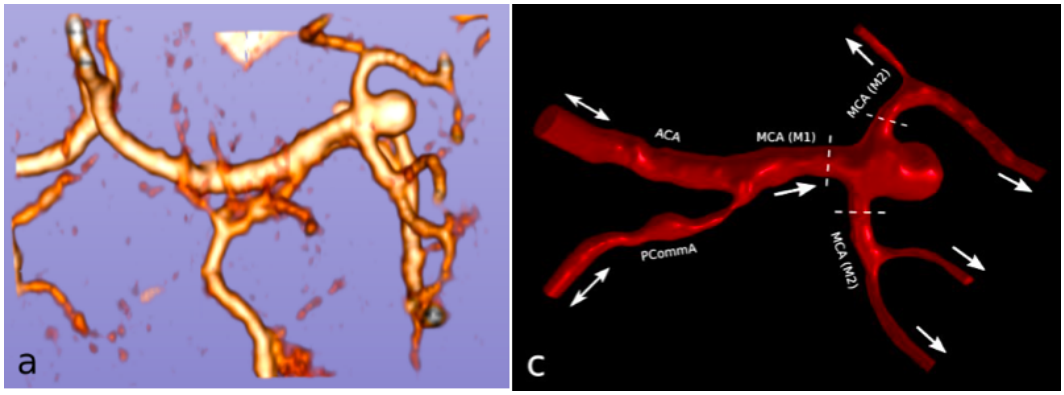

Figure 3.5: A comparison between the region of interest from the (a) original CT-scan and (b) the reconstructed region of interest with white arrows showing the directions of blood flow. Two-headed arrows indicate uncertain flow directions. White dashed lines show the plane section used to truncate the vessels.

3.2.2 Aneurysm size and rupture status

The geometrical aspects of the segmented aneurysm are listed in Table 3.1 and explained graphically in Figure 3.6. Aneurysm depth, d, is the distance measured from the fundus to the aneurysm neck, perpendicular to the ostium plane. Aneurysm width in the coronal w_{cor} and sagittal view w_{sag} are measured across the neck parallel to the its respective view. The aspect ratio (AR) of the aneurysm is the ratio between the dome length (L) and the minimum neck width (Ujiie et al., 2001), which in this case is w_{sag}. The size ratio is the quotient of the aneurysm size (maximum aneurysm depth or width) and the parent's artery diameter (Rahman et al., 2010). Both aspect ratio and size

ratio are significant in determining the rupture status of an aneurysm. The inlet cross section is modified into a circular shape to allow for a parabolic inlet boundary condition to be initiated, and the inlet diameter was obtained.

Table 3.1: Geometrical aspects of the aneurysm.

Parameters	Values
Aneurysm depth (d)	7.41 mm
Neck width in Coronal view (w_{cor})	8.33 mm
Neck width in sagittal view (w_{sag})	6.14 mm
Aspect ratio (AR)	1.20
Size ratio (SR)	2.52
Ostium area (A_{ostium})	34.3 mm^2
Inlet diameter (d_{IN})	3.3 mm
Outlet 1 diameter (d_{Hout1})	2.6 mm
Outlet 2 diameter (d_{Hout1})	3.2 mm

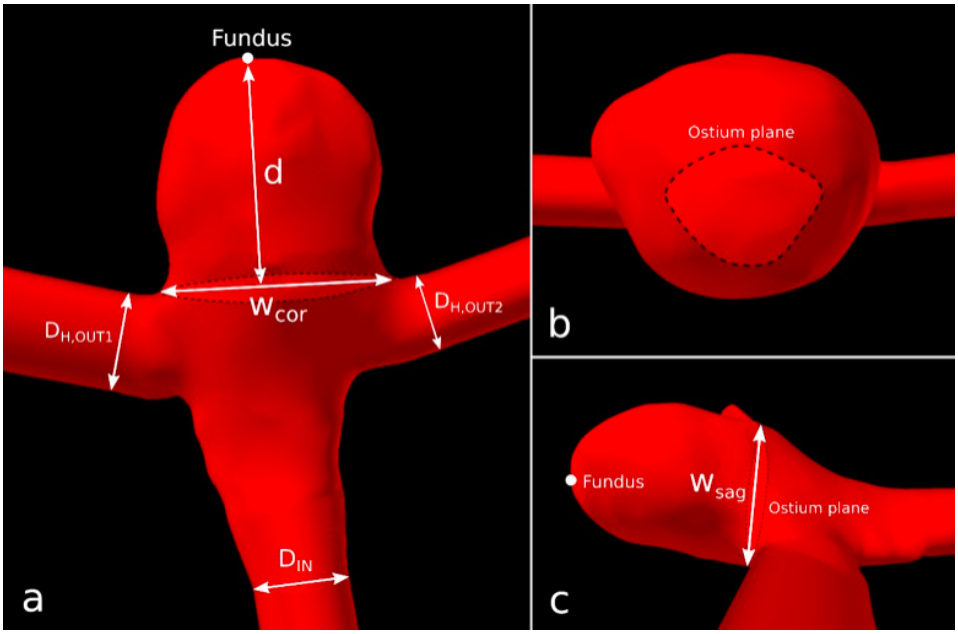

Figure 3.6: Geometry of the middle cerebral artery aneurysm used in the present study from the a. coronal, b. axial, and c. sagittal view. Abbreviations used in this figure is explained in Table 3.1.

However, the two outlets remained in their original non-circular shapes as there is no need for them to be circular. Their hydraulic diameters were obtained instead from the equation $D_H = 4A/P$, where A and P are the cross sectional area and the perimeter, respectively. Aneurysm size is defined as the maximum dimension among the depth and the neck width from any view. In this study, the neck width in the coronal view w_{cor} has the largest length and is the size of the aneurysm. Therefore, the present aneurysm is categorised as a medium-sized aneurysm since its size falls in the range of 5 to 15 mm (Cebral et al., 2005).

Table 3.2: Comparison of the present geometric aspects to that of ruptured (RAs) and unruptured (URAs) aneurysms from Nader-Sepahi et al. (2004); Weir (2005); Jou and Britz (2016). + and - Signs indicates that the value of the present geometry is lower and higher than that founded in the literature, respectively. * Symbol indicates rupture status with lower difference.

Parameters	%Difference from RAs	%Difference from URAs
Aneurysm depth (d)	+3.7%*	-45.0%
Aneurysm size (w_{cor})	-4.1%*	-19.0%
Aspect Ratio (AR)	+55.5 to +64.7%	+33.3%*
Size ratio (SR)	+37.0%	-0.8%*

As illustrated by Table 3.2, the present aneurysm depth and size are significantly closer to the averaged values for ruptured aneurysms reported in (Nader-Sepahi et al., 2004) than for unruptured aneurysms. Therefore, depth and size of the present aneurysm suggests that the aneurysm is ruptured. However, the aspect ratio and size ratio of this aneurysm suggests that it is an unruptured aneurysm (Weir, 2005; Jou and Britz, 2016). This is because the present values for AR and SR fall closer to the typical values for unruptured aneurysms than to that of ruptured aneurysms. Although the aneurysm status cannot be firmly concluded by these three studies, there is a higher probability that this aneurysm is unruptured. As the neck width, which is derived from aneurysm size in this case, is not a significant factor in determining the rupture status (Nader-Sepahi et al., 2004). There is a majority among the parameters which suggests that the aneurysm is not ruptured. Moreover, it was founded that 66% of aneurysms located in the MCA and 54% of aneurysms located in

other locations are unruptured. Therefore, it can be concluded only from the geometric point of view that the aneurysm is unruptured, and may be on the verge of rupturing. The flow patterns and impingement sizes can be used to confirm this rupture status (Cebral et al., 2005).

3.2.3 Coil modelling

A virtual platinum coil was modelled and placed inside the aneurysm to perform numerical treatments. The coil is modelled as a flexed narrow cylinder with a constant diameter of 0.254mm (Morales et al., 2012; Otani et al., 2016, 2017b) with a total length of 100 mm (Morales et al., 2013b). Other coil diameters were used in different literature which includes 0.292mm, 0.355mm, and 0.304mm (Morales et al., 2011). Coil with a diameter of 0.355mm is normally use for aneurysms larger 500mm^3, while smaller aneurysms (i.e. the present one) would be treated with a 0.254mm diameter coil (Morales et al., 2013b). Similarily, other coil lengths of 300mm (Otani et al., 2017b) and 150mm (Otani et al., 2018) were also used. As there are no ultimately preferred coil diameter and length, a standard measure was introduced to quantify the volume of aneurysm taken up by the coil regardless of coil length and diameter (Morales et al., 2011). The coil packing density (PD%) is defined by the ratio between the volume of coil and the volume of the aneurysm or as shown by Equation 3.1.

$$PD\% = \frac{\pi D^2 L}{4V_{aneurysm}} \tag{3.1}$$

where D is the coil diameter and L is the coil length. The aneurysm volume $V_{aneurysm}$ is 116.85 mm^3. Coils were treated as a straight cylinder when their volumes were calculated. Seven different cases of coiling were performed to produce a set of coiled aneurysms with 1-7 coils, respectively. A single coil (L = 100mm) has a volume of 5.067 mm^3 and a packing density of 4.33%. Theorectically, the coil volume and packing density increase proportionally with the number of coils inserted. However, due to the tortuosity of the coils, their volume and thus their packing density can slightly deviate from the theoretical values (Morales et al., 2013b). The first coil inserted was distributed mainly along the aneurysm wall and radial distribution became more uniform upon insertion of additional coils. However, due to the non-triviality in virtual coil

modelling, regions of void may still be present in the aneurysm core as also presented in the previous study. Additionally, coils are typically non-uniformly distributed when deployed manually (Otani et al., 2018) and manual modelling of coils is challenging (Morales et al., 2013b). Table 3.3 shows the actual coil volumes and the respective packing densities. Since these are the actual coil volumes and not the calculated coil volumes, they may not increase linearly with the number of coils. Those minor deviations are attributed to the curvature of the coil. Packing density is often used as a prediction factor for

Table 3.3: Coil volumes and packing densities for each cases.

Number of coil(s)	Coil volume (mm^3)	PD%
1	5.06	4.33%
2	10.13	8.67%
3	15.20	13.0%
4	20.27	17.34%
5	25.33	21.67%
6	30.40	26.02%
7	31.80	30.35%

aneurysm stability (Otani et al., 2017b), coil contraction (Cebral and Lohner, 2005), aneurysm regrowth (Cebral et al., 2005), and coiling success (van Gijn and Rinkel, 2001). A packing density greater than 20-25% is considered as high (Otani et al., 2017b), beyond which the reduction in blood velocity does not change with additional coils (Morales et al., 2011). A packing density of 30-33% was found to be sufficient in suppressing the aneurysmal flow for both ICA aneurysms (Morales et al., 2012, 2013b) and right MCA aneurysm (Morales et al., 2011), which strongly agreed with the optimised packing density of 30.35% found in the present study. Although a previous study (Morales et al., 2011) had investigated coiling effects in the right MCA aneurysm, but unlike the present study, a Newtonian (instead of a non-Newtonian) blood viscosity was used. Nevertheless, patient-specific geometry allows studies with the same type of aneurysm to be different and able to express unique findings. Coils were modelled in Blender with the aneurysm surface on the background to ensure that the surfaces of both parts do not intersect and that the coil

is contained within the aneurysm as shown in Figure 3.7. A circular cross-sectional profile followed a flexible guiding line which dictates the curvature of the coil and mimics the insertion process. Due to the irregular shape in all directions of the aneurysm, there is no way of duplicating coils to easily increase the coil length without major modifications. Therefore, a huge amount of effort was put into modelling each coil model in an independent manner. Additionally, coils were modelled very close and along the curvature of the aneurysm inner surface, similar to what is normally performed by clinicians. The distance between a coil surface and the aneurysm inner wall can be as small as 5% of the coil diameter, or in a two orders of magnitude when measured in millimetres. The coil and aneurysm models were combined into one .STL file and exported to Star-CCM+. The coil did not have to be subtracted from the aneurysm as the volume that lies between both surfaces can directly be assigned as the fluid domain. All coils modelled in the present study reflect real coils used in coiling surgery (Figure 2.5) and have a similar layout to those presented in the study of Morales et al. and Otani et al.

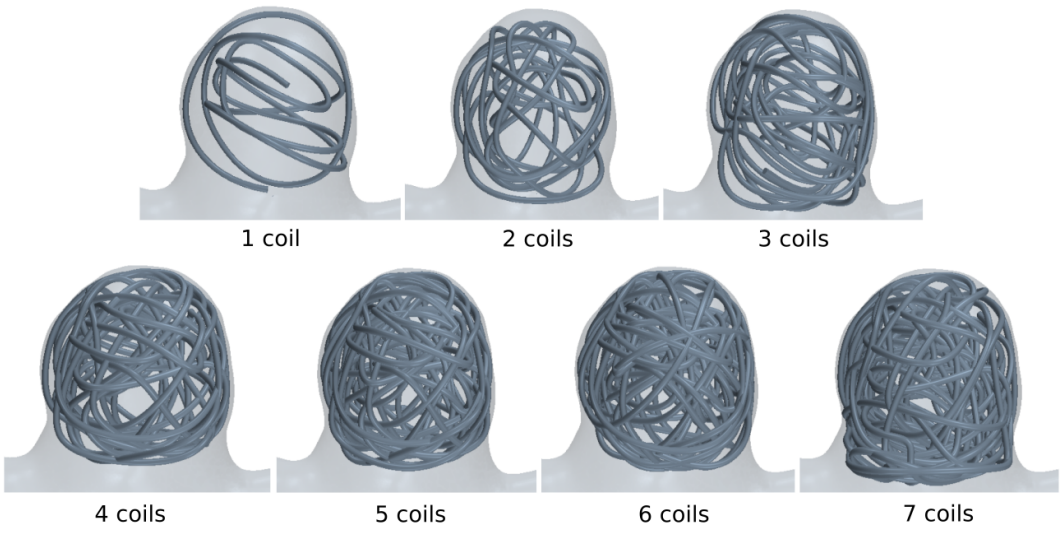

Figure 3.7: Coil models of all seven coiled cases.

3.2.4 Segmentation of brachial artery and vein for AVF creation

A set of ultrasound images of a brachial artery and a vein in a patient's arm was obatained from another anonymous patient. The fistula was not yet created as the patient has not yet undergone haemodialysis. An end-to-end fistula was later created by numerically joining the segmented brachial artery and vein. Similar to the aneurysm image, the three segmentation views are defined as shown in Figure 3.8. This 3D ultrasound series of 2D images consisted of 60, 80, and 60 slices in the axial, sagittal, and coronal view, as shown in Figures 3.9a-c, respectively, and covered a length of 600 mm in the axial direction as reported in the clinical data. It also has to be noted that the ultrasound scanner produces images that are oversized by 20 times, therefore the actual axial length of the image is 3 centimetre. 3DSlicer considered the

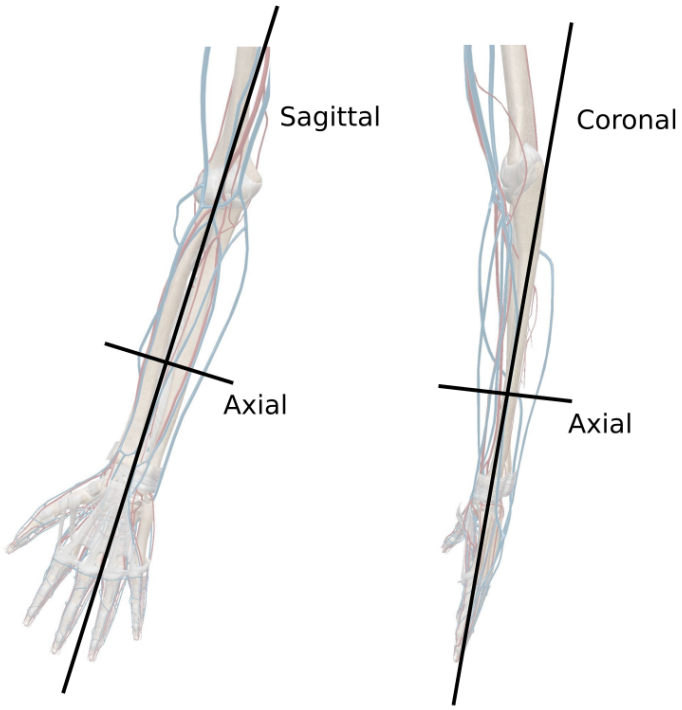

Figure 3.8: Orientation of the coronal, sagittal, and axial planes over the forearm anatomy. Segmentation along the black line will produce the respective planes. (Reconstructed from Human Anatomy Atlas, (VisibleBody, 2019))

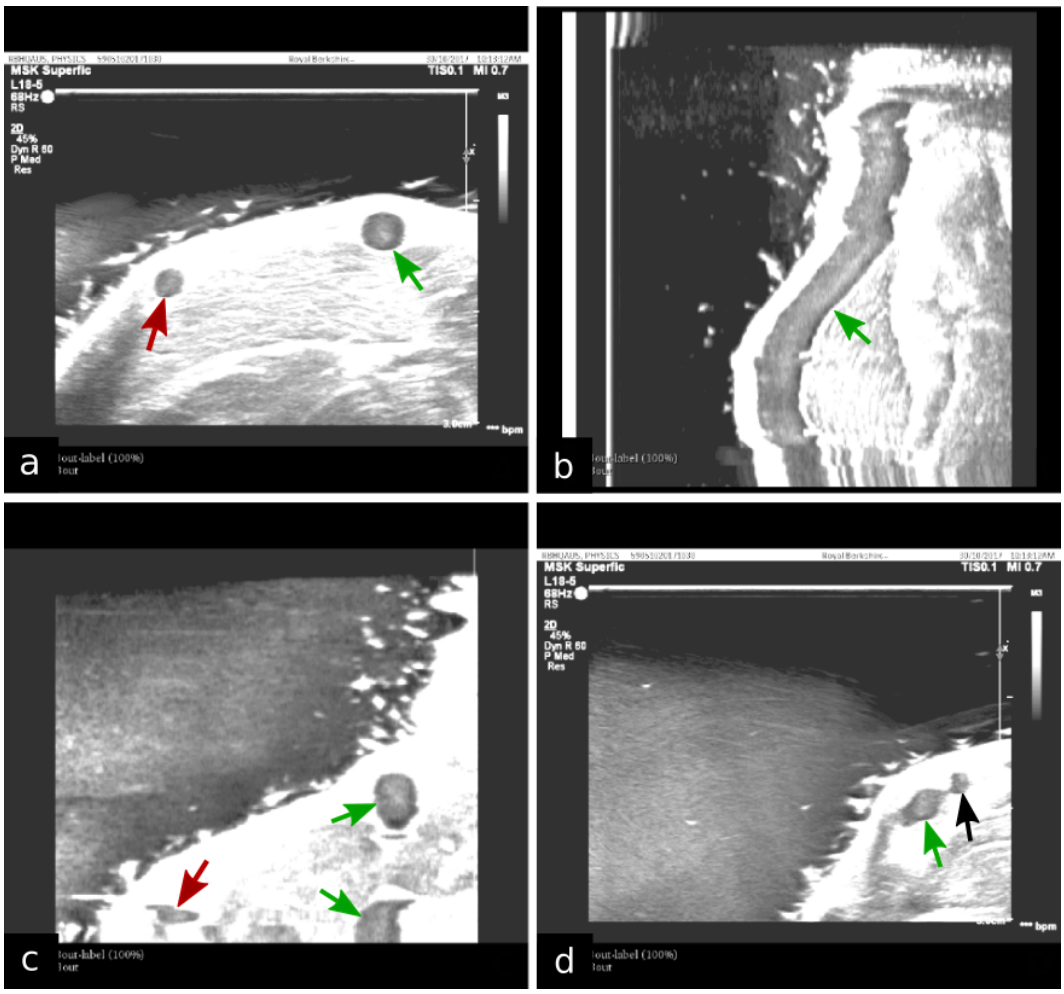

Figure 3.9: A slice of the ultrasound image in (a) the axial, (b) sagittal, and (c) coronal views. Grey contour surrounded by white contours (tissues and muscles) are blood vessels (lumen spaces). Other grey contours not surrounded by white contours are outside the region of interest. The artery and vein surfaces are highlighted with green and red arrows, respectively. (d) A bifurcation is highlighted with a black arrow, proximal to the artery.

acquired image to be of a vector volume type and this prevented the blood vessels from being extracted with normal convention. It is first converted to a scalar volume to allow normal procedure of volume rendering and segmentation to proceed using the Vector to Scalar Volume module. Grow cut and spherical paint effects could be applied to each slices in order to extract the lumen cross-section with minimised error. Fast marching techniques were also used to optimise the segmentation process. Threshold values distinguish the

lumen circumferences by identifying colour contrast in the medical images. Like micro-MRI, ultrasound imaging only captures the innermost endothelial lining of a vessel without presenting information on the composition of its surroundings (Caroli et al., 2013). However, that is insignificant to the modelling of the lumen space and can be ignored. All modalities have their own advantages and drawbacks, but as long as a sufficient amount of quality is maintained, it should serve as a competent imaging technique (Ene-Iordache et al., 2001; Flores et al., 2016). Ultrasound images can be acquired in a short time with minimal effort and harm (Niemann et al., 2012a). Further reconstruction of the model was performed in Blender where imaging artifacts were removed to create a smoothed blood vessel model. Again, surface finishing usually comes at the cost of obtaining slight deviation in the wall shear stress value due to additional shrinkage of the blood vessels. However, this effect is negligible when compared to increased flow instability due to rough surfaces (Caroli et al., 2013). A bifurcation was observed to branch off from the artery, downstream of the lumen profile as shown in Figure 3.9d.

Following such observation, the artery can be distinguished from the vein, which would not have a bifurcation of such orientation. The averaged diameter of the artery (3.35 mm) is slightly larger than that of the vein (2.25 mm). Although venous diameters are usually larger than arterial diameters, the opposite is possible (Perktold and Rappitsch, 1995). An anastomosis was constructed by connecting one end of the artery to the end of the vein to form an end-to-end arteriovenous fistula as shown in Figure 3.10. Although idealised AVF models can be a good representation of a patient-specific model (Robbin et al., 2016; Beathard et al., 2019), the fistula created resembles the latter to represent a real blood vessel pathology observed in clincal surgeries. The cross sections of both the artery and vein vary along its axial directions and the 180 degree fistula bend is not of a regular shape due to the alignment of the end of both the artery and vein as shown by the sagittal view of the fistula model in Figure 3.11. The bifurcation captured from the medical image is also visible but it is very short compared to the total length of the artery and vein by approximately 8.2 times. Since the patient-specific flow split between the artery outlet and this bifurcation was not provided, the flow

rate through this bifurcation is directly defined by pressure at the bifurcation and venous outlets, both of which were set to zero (Niemann et al., 2012a). A preliminary simulation showed that approximately 41% of the artery mass flow is lost through the bifurcation as shown in Figure 3.12. In order to avoid the ambiguity, the bifurcation was discarded in the main study. The reconstructed geometry with no bifurcation is therefore used in the main simulations as shown in Figure 3.13. Since the preliminary and main studies will not be compared in full, a few minor modifications on the new geometry were performed to make the flow more stable and realistic. The surface of both the artery and vein were further smoothed for stability. The artery inlet plane was rotated slightly to ensure that the blood inflow is parallel to the local arterial centreline to prevent unrealistic flow impingement. As a result, the inlet plane is relocated approximately 0.5 diameters upstream of the original inlet plane. However, the majority of the vessel pathology was preserved, including the inclination (θ) of the downstream venous segment of approximately 17 degrees. This process is not responsible for the fully-developed inflow into the artery. It only prevents unrealistic flow impingement. Processes carried out to ensure fully-developed inflows for both the AVF and aneurysm studies are discussed in the next section.

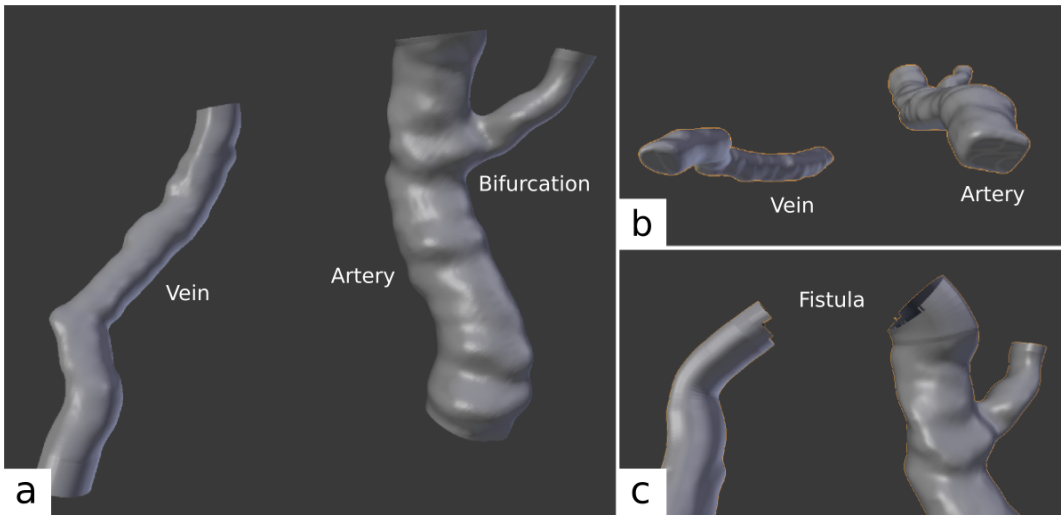

Figure 3.10: The segmented artery and vein in (a) the coronal view and (b) axial view, featuring an arterial bifurcation. (c) Construction of the end-to-end fistula from the arterial end.

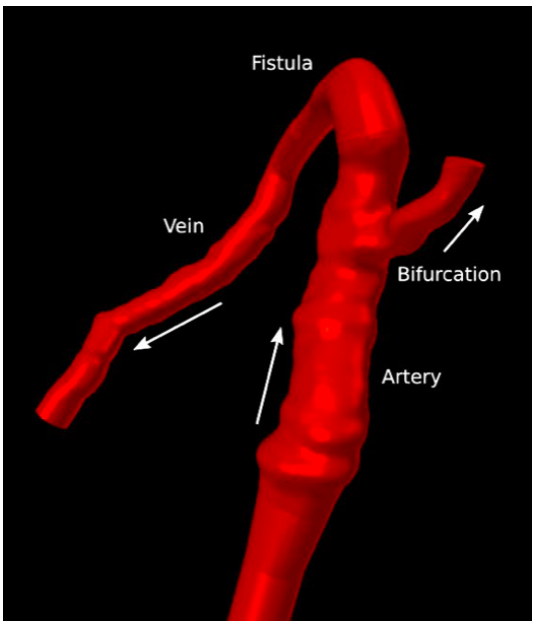

Figure 3.11: Geometry of the AV fistula joining the brachial artery and vein, featuring an arterial bifurcation in the sagittal view. White arrows show the blood flow direction.

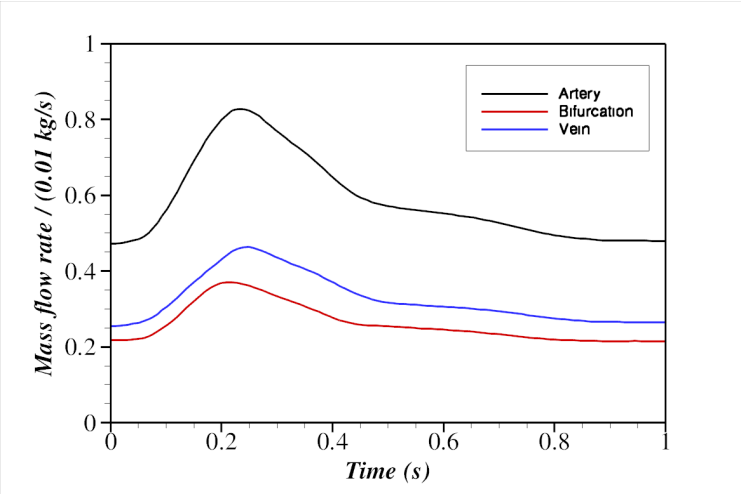

Figure 3.12: Surface averaged mass flow rate measured on a cross-section of the artery upstream of the bifurcation (artery), the bifurcation, and the vein, normalised by 0.01 kg/s.

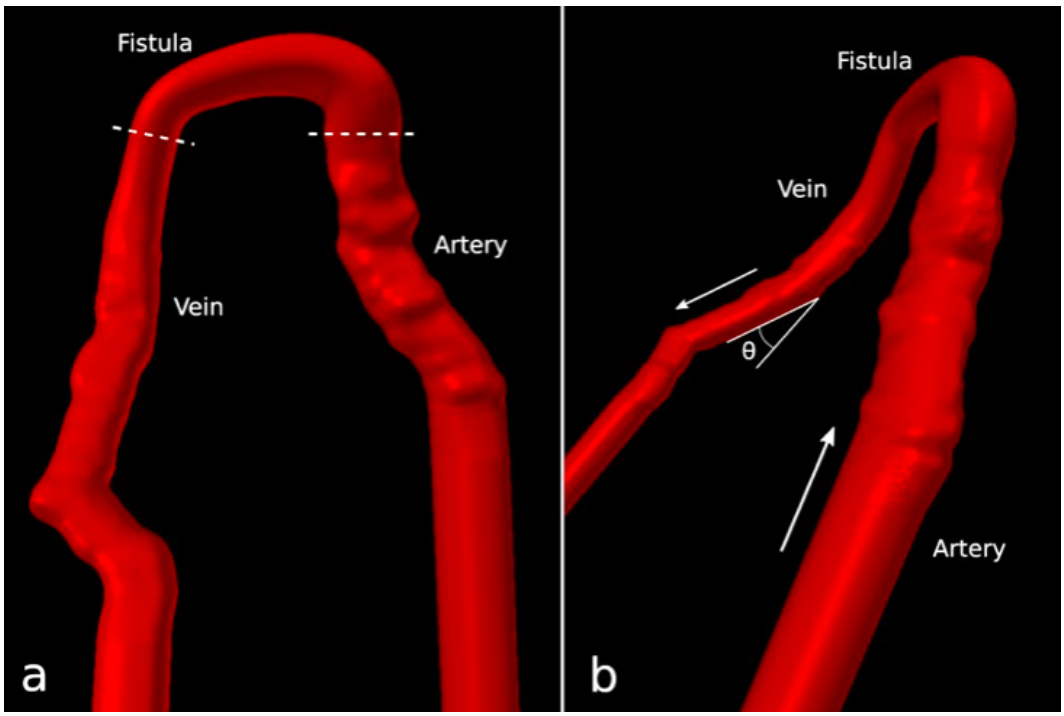

Figure 3.13: Smoothed geometry of the AV fistula and the proximal artery and vein without the bifurcation. White dashed lines in (a) shows the original boundary of the artery and vein. White arrows in (b) show the blood flow direction.

3.3 Boundary conditions and pulsation effects

In the aneurysm study, blood flows into the MCA M1 segment and leaves through the two MCA M2 segment outlets (Figure 3.5c). In the AVF study, blood flows into the brachial artery and leaves through the vein (Figure 3.13b). In both studies, a 3D parabolic mass flow rate profile, pulsating in time, must be applied at the respective inlet plane of both models. To feature a realistic inlet flow like what would be observed clinically, a patient-specific inflow waveform obtained either by MRI (Niemann et al., 2012a) or Doppler ultrasound (Niemann et al., 2010; Bozzetto et al., 2015) scans should be applied (Jodko et al., 2017). Patient-specific waveforms are not frequently obtained, especially for cerebral arteries where surgical intervention for such data is rare (Zhou et al., 2017). The mass flow rate waveform applied at the aneurysm inlet was derived from an ICA volumetric flow rate of a 56 years old female patient diagnosed with an aneurysm (Xiang et al., 2014). The study

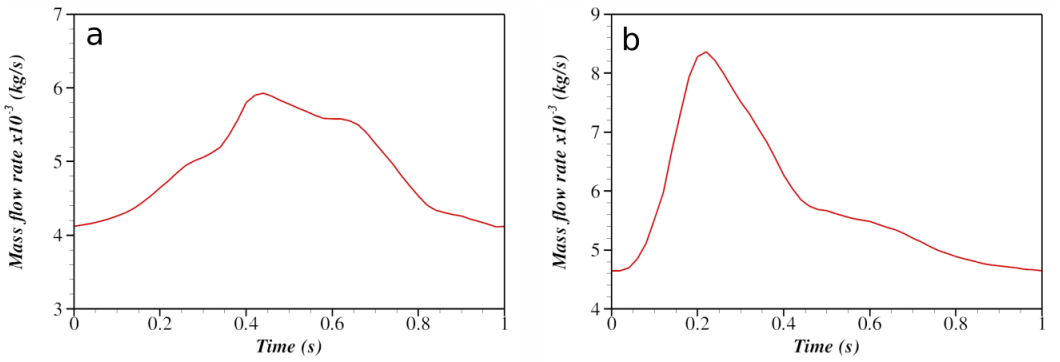

Figure 3.14: Mass flow rate waveform applied at the inlet of the aneurysm (left) and AVF (right) models. (Reproduced from (Xiang et al., 2014) and (Ene-Iordache and Remuzzi, 2012))

investigated effects of applying inlet waveform of normal patients and those diagnosed with an aneurysm so different waveforms presented were normalised by a mean ICA volumetric flow rate of 4.6 mL/s for comparison. The waveform used in the present study is the only one among four that belonged to a patient with aneurysm, therefore it was chosen. The equivalent mass flow rate waveform used for the aneurysm study was calculated and shown in Figure 3.14a. The gradual changes in the magnitude of the waveform are a typical blood characteristic of a patient with aneurysm. Flow waveforms of brachial arteries in the arm, on the other hand, are more available in the literature. The volumetric flow rate waveform used for the AVF study was obtained from a patient undergoing haemodialysis with an end-to-end fistula (Ene-Iordache and Remuzzi, 2012). The waveform was converted into an equivalent mass flow rate waveform and is shown in Figure 3.14b. Zero pressure was prescribed at the outlet(s) of the model in both and other studies, where the flow fields were unaffected by the imposed condition (Kharboutly et al., 2007; McGah et al., 2011; Otani et al., 2017a; Riccardello et al., 2018). In fact, a previous study with passive scalar injected into a cerebral aneurysm suggested that numerical results obtained using a zero-pressure outlet condition are closer to in-vivo measurements (Rayz et al., 2015). Although some studies applied patient-specific pressure waveforms (Jodko et al., 2014) or pressure lost (Niemann et al., 2010) at the outlet, implementations of outlet pressure that do not belong to the specific geometry may be inappropriate. Additionally, the

application of idealised waveform, such as the Womersley profile, may introduce wall shear stress instability in patient-specific geometries (Zhou et al., 2017). Therefore, Womersley profile was not considered in the present study. All fluid wall boundaries in both studies were treated with a no-slip condition (Johnston et al., 2004).

The 3D parabolic mass flow rate profile can be directly imposed at the inlet plane (Chaichana et al., 2011). Alternatively, an extension pipe, which allows a parabolic profile to develop, can be connected upstream of the inlet plane (Otani et al., 2018). In that case, a mass flow rate profile that is constant in space, but still pulsating in time, can be applied at the inlet of the extension pipe to produce the desired pulsating parabolic inflow (Shamloo et al., 2017; Otani et al., 2018). A preliminary simulation of a straight pipe flow was conducted to validate the alternative method. The pipe has a diameter D of 4mm and a length of 50D. A constant velocity profile was applied at the pipe inlet and the velocity profiles at different cross-sections downstream of the inlet were observed as seen in Figure 3.15. It is evident that a fully developed parabolic profile is achieved at 30D downstream of the inlet and an extension pipe of such length can be used as an entry length. Although the pipe diameter does not affect the outcome of this study, its value of 4mm was chosen to represent a typical artery diameter (Krejza et al., 2006). However, a significantly shorter entrance length of 5D was previously used as entrance length (Bozzetto et al., 2015; Shamloo et al., 2017) and may affect the inlet velocity profile as shown. In turbulent pipe flows, an entrance length of up to 40D was used (Wang et al., 2018) to fully develop the inlet flow. In order for the 30D extension pipe to be used as an entry length in the present study, the artery inlet cross sections of both the aneurysm and AVF models were segmented to form a new inlet plane, in each model, that is perpendicular to the local flow direction (Grechy et al. 2017). The new inlet cross sections were transformed into a circular shape of approximately the same diameter. In a similar manner, the outlet(s) of every model in the present study were extruded perpendicular to the local normal axis (Kharboutly et al. 2010, Otani et al. 2018) by a length of five times the local outlet diameter to avoid upstream pertubation.

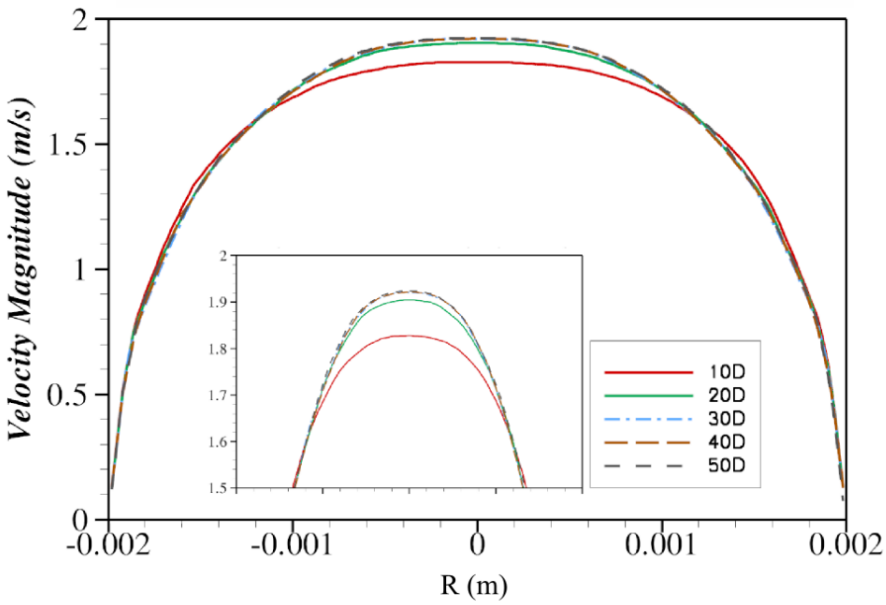

Figure 3.15: Streamwise velocity profiles at different locations upstream of the pipe inlet across the pipe radius R after three cardiac cycles.

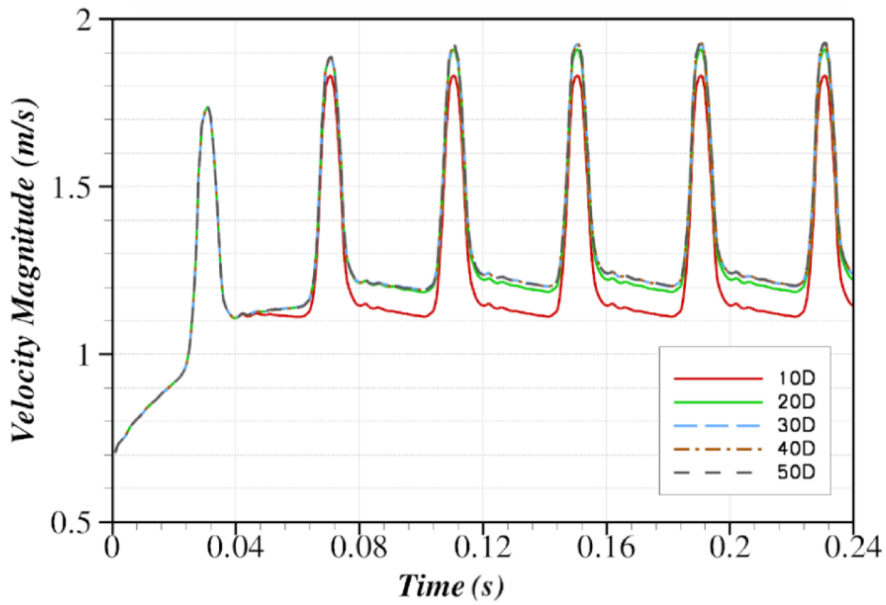

Figure 3.16: Centreline velocity profiles at different cross sections along the entrance length through multiple cardiac cycles, showing flow periodicity after three cycles (In this case, 0.04s = 1 cycle).

Additionally, since the mass flow rates used are varying in time, the pulsation effects were also studied. The mass flow rate profile used in the AVF study (Ene-Iordache and Remuzzi, 2012) was applied at the inlet of the same pipe in the preliminary simulation. The centreline velocity at different locations downstream of the inlet was monitored throughout multiple cardiac cycles. It was found that the centreline velocity was converged by the third cardiac cycle as seen in Figure 3.16. The same conclusion was made in previous studies (Ene-Iordache and Remuzzi, 2012; Pike et al., 2017b; Sharzehee et al., 2018). Since an accurate result is produced by the third cycle, the velocity profiles shown in Figure 3.15 were also obtained at the third cardiac cycle. Moreover, this can only be achieved at a location that is at least 20D downstream of the inlet. To conclude,the inlet of both the aneurysm and AVF models are extended by the length of 30D as shown in Figure 3.17.

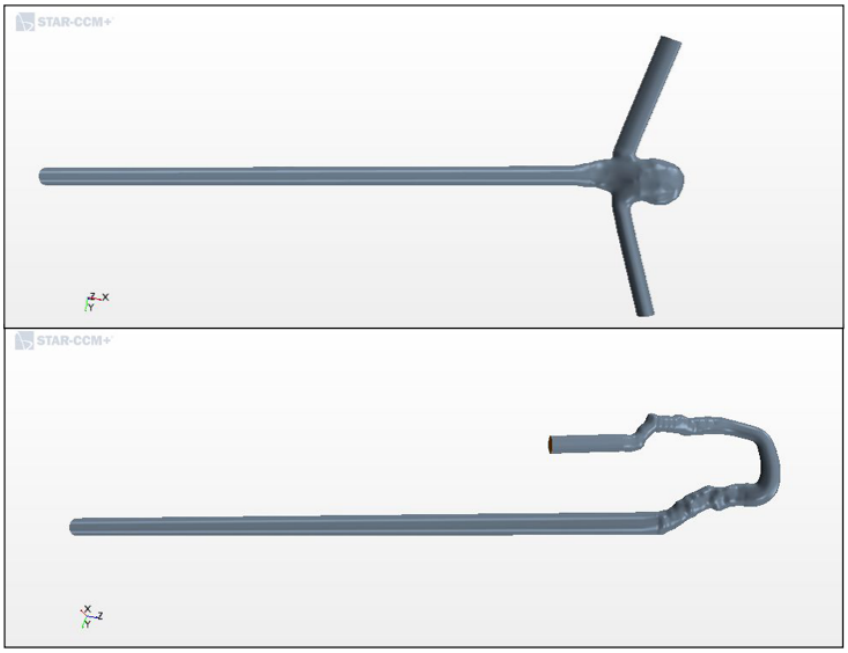

Figure 3.17: 30D extension pipe upstream of the artery inlet in the aneurysm (top) and AVF (bottom) models.

3.4 Fluid governing equations

The fluid in the present study is modelled as blood, which like other fluids, is governed by the Continuity and the Navier-Stokes equations. These equations were solved at each computational node to determine the pressure, p, and the velocities in all three Cartesian components u_x, u_y, u_z.

3.4.1 Continuity and Navier-Stokes equations

As blood moves in a continuum, the Continuity equation shown in Equation 3.2 was solved to account for the law of mass conservation.

$$\frac{\partial u_x}{\partial x} + \frac{\partial u_y}{\partial y} + \frac{\partial u_z}{\partial z} = 0 \tag{3.2}$$

The incompressible form of the Navier-Stokes equations are derived from Newton's laws of motion and describe the viscous flow of incompressible fluids. They can be represented by Equation 3.3 where x, y, z indicate the three directions in the Cartesian coordinate system.

$$\rho(\frac{\partial u_x}{\partial t} + u_x\frac{\partial u_x}{\partial x} + u_y\frac{\partial u_x}{\partial y} + u_z\frac{\partial u_x}{\partial z}) = -\frac{\partial p}{\partial x} + \mu(\frac{\partial^2 u_x}{\partial x^2} + \frac{\partial^2 u_x}{\partial y^2} + \frac{\partial^2 u_x}{\partial z^2}) \tag{3.3}$$

$$\rho(\frac{\partial u_y}{\partial t} + u_x\frac{\partial u_y}{\partial x} + u_y\frac{\partial u_y}{\partial y} + u_z\frac{\partial u_y}{\partial z}) = -\frac{\partial p}{\partial y} + \mu(\frac{\partial^2 u_y}{\partial x^2} + \frac{\partial^2 u_y}{\partial y^2} + \frac{\partial^2 u_y}{\partial z^2})$$

$$\rho(\frac{\partial u_z}{\partial t} + u_x\frac{\partial u_z}{\partial x} + u_y\frac{\partial u_z}{\partial y} + u_z\frac{\partial u_z}{\partial z}) = -\frac{\partial p}{\partial z} + \mu(\frac{\partial^2 u_z}{\partial x^2} + \frac{\partial^2 u_z}{\partial y^2} + \frac{\partial^2 u_z}{\partial z^2})$$

The external force term, including the gravitational effects (Decorato et al., 2014), is neglected in this study since the direction of its vector acting on both the aneurysm and AVF depends on the person's posture which may changes randomly in time. The equations are solved in Star-CCM+ with second order spatial and temporal discretizations. Only the fluid domain of FSI simulations used first order Backward-Euler discretization in time to solve the equations, as is recommended by the software for increased simulation stability. Velocity and pressure solvers were segregated and under-relaxation factors were setted to

0.8 and 0.2, respectively, for simulation stability. The convergence torelances of each velocity and continuity solvers for the fluid domain were set, but were not limited, to 1×10^{-3} (Chaichana et al., 2013a). During diastole, where flows are more stabilised, the residuals of both variables converged at 1×10^{-4}. Nevertheless, the time-step size used was optimised and results were converged.

3.4.2 Modeling passive scalar transport

Phase-contrast agents are frequently used in clinical practices for the purpose of image acquisition (Otani et al., 2017b) and flow measurements (Niemann et al., 2012a). Another significant usage of these contrast agents is for blood flow visualisations. During coiling processes, clinicians may inject medical dyes into the patient's proximal artery to observe the blood flow into the aneurysm. They rely mostly on live images of contrast agents to make decisions on the optimal coil density that will sufficiently suppress the aneurysmal blood flow. However, the relationship between the kinematics of medical dyes and other aneurysmal hemodynamic quantities cannot be observed clinically. The only way of investigating such relationship is through coupling CFD with contrast injections. Medical dyes are modelled in numerical simulations as passive scalar (Rayz et al., 2015; Vali et al., 2017) which does not affect the flow field as the advection-diffusion and Navier-stokes equations are only coupled one-way (Rayz et al., 2010). Passive scalars are governed by molecular diffusivity which is represented by the Schmidt number, Sc, in Equation 3.4. A time-dependent passive scalar waveform of contrast value equal to one was applied at the domain inlet after the fourth cardiac cycle for one second (Morales et al., 2013b).

$$Sc = \frac{\nu}{D} = \frac{\mu}{\rho D_m} \tag{3.4}$$

where D_m is the molecular diffusivity [m^2/s]. The dimensionless Schmidt number used in all simulations that involved passive scalar is 6280 (Evegren et al., 2011). The contrast solver is maintained at second order convection and diffusion transport and an under relaxation factor of 0.9. Residuals for passive scalar are capped below 1×10^{-8}.

3.5 Hemodynamic properties

Blood is modelled as an incompressible (Johnston et al., 2004; Cebral et al., 2005), isotropic, and homogeneous (Decorato et al., 2014) fluid with constant density (Morales et al., 2013b; Ene-Iordache et al., 2015) in a laminar flow regime (Ene-Iordache et al., 2013). From a wide range of blood densities reported in the literature, from 1050 kg/m^3 (Valencia et al., 2008; Otani et al., 2016) to 1130 kg/m^3 (Kharboutly et al., 2010), most studies agreed on 1060 kg/m^3 (Chaichana et al., 2013a; McGah et al., 2014; de Villiers et al., 2018) which was used in this present study.

3.5.1 Blood flow regime

Although blood flows are typically laminar, they can develop into a transitional or turbulent flow in the existence of geometric complications especially in anastomotic regions, like in a fistula. In these circumstances, the endothelial cells may elongate and become disorganised, leading up to neointimal hyperplasia which would rarely develop under its natural condition. The Reynolds number based on the inlet diameter and mean inflow velocity dictates the flow regime and varies at different sites due to the variations in the cross-sectional area. In the fistula study, the Reynolds numbers were 825 to 1020 in the artery, 580 to 870 in the fistula, and 700 - 870 in the venous segment. All of these values are within typical range as reported in previous findings (Browne et al., 2015; Grechy et al., 2017). In other types of AVF, like a side-to-side fistula where there existed proximal and distal veins, the flow split between the two vessels can play a more significant role in determining the flow regime than Reynolds number (Browne et al., 2015). In the same DNS study, it was reported that models with a flow split ratio of 100:0 (proximal vein : distal vein) like an end-to-end AVF experiences no high velocity and pressure oscillations. Blood flow in the present aneurysm study, on the other hand, is less laminarised. The Reynolds number, based on the neck width in coronal view, at the ostium plane is approximately 1010 for the untreated case. As the packing density is increased, the ostium flow becomes dramatically laminarised. The Reynolds numbers at the ostium plane for the treated cases are approximately 757, 350, 63 for 4, 5, and 6 coils model respectively,

which agreed with the literature especially at higher packing densities (Morales et al., 2011; Otani et al., 2016, 2017a). Previous coiled aneurysm studies did not investigated the variation of Reynolds number due to increased packing density so therefore the corresponding packing density for the Reynolds numbers reported could not be determined. On the contrary, it is found in the present study that the aneurysmal flow laminarized with increasing packing density. Nevertheless, the laminar flow model was used in all simulations in this study as the highest Reynolds number still falls in the range of laminar flow regime.

3.5.2 Blood viscosity and rheology

The Newtonian flow regime is regularly assumed for blood transportation as suggested in previous studies (Roy-Chaudhury et al., 2007; Browne et al., 2015). Additionally, the Newtonian assumption has been justified for blood flows in large vessels which include the coronary arteires (Johnston et al., 2004; Chaichana et al., 2013b) and the aorta (Canchi et al., 2018). Different values for the constant dynamic viscosity including 0.00375 Pa-s (Morales et al., 2011) and the most commonly used value of 0.0035 Pa-s (Chaichana et al., 2014; Otani et al., 2018) were used. This viscosity is mostly found in patients with normal blood conditions (Abraham et al., 2005). Blood viscosity is directly affected by the patient's level of cholesterol, haemodialysis status in the case of AVF, and other blood abnormalities. Table 3.4 shows different Newtonian blood viscosity of patient's with varying blood conditions. It is evident that patients diagnosed with higher cholesterol tend to develop a significantly more viscous blood flow due to the nature and presence of the former. However, when the morphology of red blood cells (RBC) are taken into consideration, the blood viscosity can change with local shear rates (Secomb, 2016). This means that blood behave like a non-Newtonian fluid. In an idealised and straight blood vessel, the shear rate is typically above 200 s^{-1}, where the Newtonian flow regime dominates. Nonetheless, since diseased blood vessels are tortuous and irregular (Han, 2012), the shear rate can quickly reduce due to such abnormality. At a low shear rate below 100 s^{-1}, biochemical interactions were observed between endothelial cells which resulted in

Table 3.4: Newtonian blood viscosity of patients with different blood abnormality.

Patient type	Newtonain viscosity [Pa · s]	References
Hemodialysis patient	0.002036, 0.002644	Akherat et al. (2017)
High cholestrol	0.01	Clarion et al., (2018)
Low cholestrol	0.0013	Moreno et al. (2015)

non-Newtonian behaviour in aneurysmal blood flow (Otani et al., 2017a). At lower shear rates (i.e. 0.01 s^{-1}), RBC are able to elongate themselves and align their long axes to the flow. As the shear rate rises to restore its homeostatic condition, RBC continue to aggregate and deform, owing to their low elastic bending modulus. In this process of shear-thining, the blood viscosity decreases and converges back towards its individual Newtonian plateau value as shown in Figure 3.18. A shear rate of 100 s^{-1} was reported to be the threshold value that distinguishes the two flow regimes. Additionally, shear rates may vary as a function of haematocrit and plasma proteins.

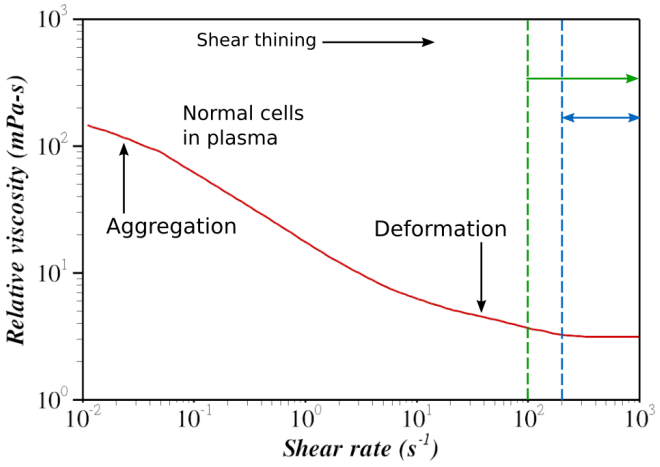

Figure 3.18: Variation of blood viscosity due to changes in the shear rate (Reproduced from Secomb 2016). Plot shows the process of shear thinning until shear rate reaches 100 s^{-1} where the Newtonian flow regime dominates (green arrow), followed by a plateau of infinite-shear viscosity beyond a shear rate of 200 s^{-1} (blue arrow).

The non-Newtonian viscosity can be determined using different models. Johnston et al. (2004) compared five non-Newtonian models, and also the Newtonian viscometry, to see their effects on wall shear stress of coronary arteries. Only three of these models discussed in the study are used widely in the literature and are described by Equations 3.5 - 3.7. Although it was reported that wall shear stresses produced by these three models are higher than other models (Walburn-Schneck and Casson models), the differences in haemodynamic quantities are considered small. This is especially applicable for cases where the centreline velocities are low (0.02 - 0.05 m/s), as found in the present studies.

The Power Law model (Ostwald 1929)

$$\mu = \mu_0(\gamma)^{n-1} \tag{3.5}$$

The Generalised Power Law model (Ballyk et al. 1994)

$$\mu = \lambda|\gamma|^{n-1} \tag{3.6}$$

The Carreau-Yasuda model (Cho and Kensey, 1991)

$$\mu = \mu_0 + (\mu_0 - \mu_\infty)[1 + (\lambda\gamma)^a]^{(n-1)/a} \tag{3.7}$$

where μ, μ_0, n, μ_∞, λ, a, and γ represents the non-Newtonian viscosity, zero-shear viscosity, power constant, infinite-shear viscosity, relaxation time constant, shear thinning control parameter and the shear rate, respectively. However, only the Generalised Power Law and the Carreau-Yasuda models are available in STAR-CCM+. The two models agree well at low shear rates (0.5 - 50 s^{-1}) (Johnston et al., 2004). In this study, the Carreau-Yasuda model is used to model the non-Newtonian blood flow as suggested by previous studies on patients with normal (Grechy et al., 2017) and abnormal (referred to in Table 3.4) blood. In STAR-CCM+, the Carreau-Yasuda model was modified to include a temperature shift factor a_T as an option to model temperature-dependent viscosity. Equation 3.7 is modified into Equation 3.8.

The Modified Carreau-Yasuda model

$$\mu = a_T(\mu_0 + (\mu_0 - \mu_\infty)[1 + (\lambda a_T \gamma)^a]^{(n-1)/a}) \tag{3.8}$$

The original Carreau-Yasuda model can be restored when the temperature shift factor $a_T = 1$. Different non-Newtonian studies used different sets of Carreau-Yasuda parameters as listed in Table 3.5. The data from this table, except for that of an aneurysm patient, are plotted in Figure 3.19 to show the effects of these parameters on the variation of viscosity at different shear rates. Each viscosity profile are normalised by their zero-shear viscosity.

Table 3.5: Non-Newtonian blood viscosity of patients with different blood conditions. * and ** indicate parameter set obtained from curve fitting and not used due to insufficient data, respectively. References A17 = (Akherat et al., 2017), V08 = (Valencia et al., 2008), C18 = Clarion et al., (2018), M15 = (Moreno et al., 2015), G17 = (Grechy et al., 2017). Other abbreviations: Chol. = cholesterol and Aneurysm = patient with cerebral aneurysm

Patient type	μ_0 [Pa · s]	μ_∞ [Pa · s]	λ [s]	a	n	Reference
Haemodialysis	0.008755	0.002036	0.03824	0.5123	0.4645	A17*
Aneurysm	0.056	0.00345	10.976	N/A	-0.3216	V08**
High chol.	0.0987	0.01	1.1111	24.6304	0.3902	C18
Low chol.	0.0054	0.0013	0.6519	17.2712	0.4913	M15
Healthy	0.16	0.0035	8.2	0.64	0.2128	G17

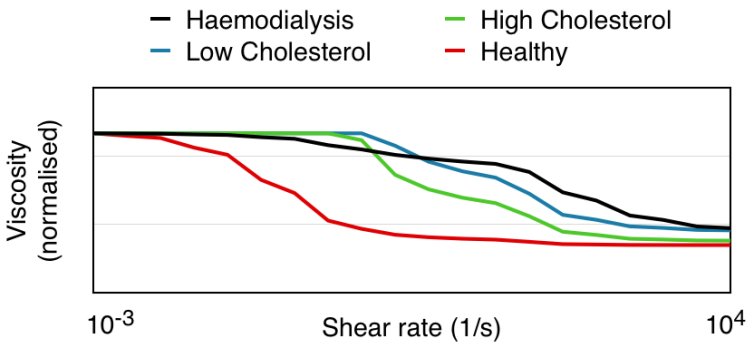

Figure 3.19: Variations of non-Newtonian viscosities corresponding to four patient types presented in Table 3.5 at different shear rates.

The viscometric parameters for a normal and haemodialysis patient was used in all non-Newtonian aneurysm and AVF studies, respectively, for realistic outcomes. The default value of 1.0 for the temperature shift factor was used as it is not given in previous studies. The non-Newtonian blood parameters for haemodialysis patients in Table 3.5 were curve fitted with patient-specific viscosity data. The patients had an considerably low haematocrit level (28% to 32%) as compared to the normal levels of 40% to 50%. This is expected in haemodialysis patients. The literature reported a diverse conclusion on the use of non-Newtonian models. The Carreau-Yasuda model was observed to significantly affect the pressure drop across a coronary artery at Reynolds number below 100 (Cho and Kensey, 1991), which can be rare due to the flow nature in such vessels. Moreover, in the same study, it was suggested that the Newtonian assumption (at shear rate 114 s^{-1}) underestimated wall shear stress (WSS) as compared to all the non-Newtonian models considered, including the Carreau-Yasuda model, especially in flow recirculation areas. Other regions, such as a side-to-end AVF and low-shear dilated vein, experienced WSS underestimation by 10% and 13%, compared to the Casson model (Decorato et al., 2014). Underestimation of Newtonian WSS was more significant in normally-dilated regions (59%) compared to steonotic regions (5%) (Schirmer and Malek, 2007). As the geometries in the present study do not involve stenosis, it is highly likely that Newtonian assumption would introduce unrealistic results. Therefore, the Carreau-Yasuda non-Newtonain model in Star-CCM+ is used in the present study.

3.6 Validation of the Carreau-Yasuda non-Newtonian model

The Carreau-Yasuda (C-Y) model available in the CFD software Star-CCM+ has been validated against a previous experimental study. There are two experimental studies on C-Y non-Newtonian pipe flow in the literature; Gijsen et al. (1999b) and Gijsen et al. (1999a). Both studies compared Newtonian and non-Newtonian flow in a specific carotid bifurcation (Gijsen et al.,

1999b) and a 90 degrees bended pipe Gijsen et al. (1999a). A mixture of KSCN and Xanthan gum was used as working fluid to represent non-Newtonian blood in both studies. The laminar blood was assumed to have a constant density of 1410 kg/m^3. In their Newtonian studies, they assumed a blood viscosity of 2.9 mPa-s.

In order to perform the validation, the geometry and C-Y parameters used in the reference study must be known. A complete set of Carreau-Yasuda parameters was given in Gijsen et al. (1999b), but the geometry used was not reproducible due to insufficient information on the dimensions of the irregular bifurcation. Additionally, steady flow was investigated in this study, whereas unsteady flow was investigated in Gijsen et al. (1999a). Therefore, (Gijsen et al., 1999a) was chosen for validation. The 90 degrees bended pipe geometry used in Gijsen et al. (1999a) is reproducible, but the C-Y parameters given in the study is not completed. Only the relaxation time and the 'a parameter' were given. The relaxation time was assumed by the study to have the same value as the characteristic time constant, which have a value of 0.1s. The 'a parameter' of 0.377 was calculated using equations 3 and 4 and the KSCN-X solution properties in Table 1 of Gijsen et al. (1999a). The zero-shear viscosity, infinite-shear viscosity, and power constant (n) used are from a healthy patient in the presnet study (Table 3.5).

Unsteady simulations of the C-Y non-Newtonian blood flow in a 90 degrees bended pipe have been conducted accordingly. The bended pipe has been modelled according to Figure 1 of Gijsen et al. (1999b). Additionally, the inlet and outlet were extended by 30D and 10D to ensure a fully-developed flow. The pipe used in the reference study was meshed such that there are 16 elements across the pipe diameter. Each square element has a length of 0.5mm and was evenly spaced. When the geometry with this mesh density was reproduced, only 252,609 elements were generated. A grid independence test was conducted for this validation study by systematically decreasing the base size of the bended section. The base size of the 30D entrance length was kept constant at a value of 0.4mm. Four meshes, each with three prism layers, were generated and summarised in Table 3.6.

Table 3.6: Bended pipe mesh summary for the grid independence test.

Mesh	Element count	Base size (bended section)
Gijsen et al. (1999a)	N/A	0.5 mm
Present 0.5mm	252,609	0.5mm
Present 0.4mm	440,178	0.4mm
Present 0.2mm	1,111,746	0.2mm
Present 0.15mm	1,865,719	0.15mm

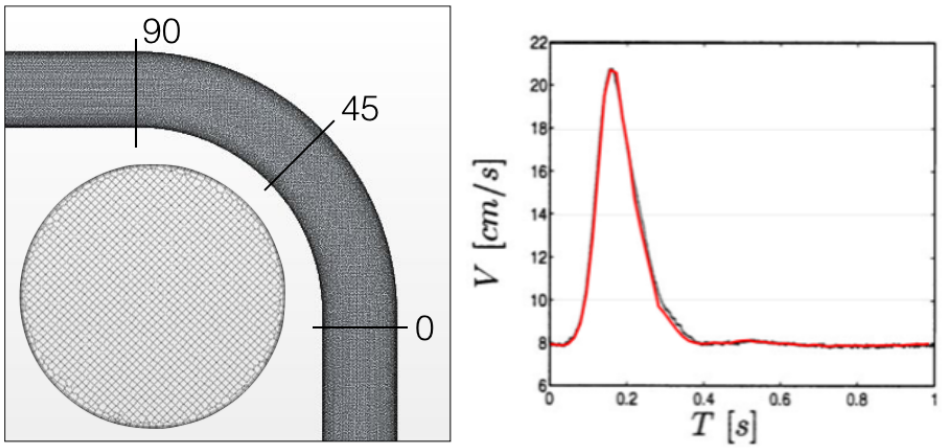

Figure 3.20: Computational mesh of the bended pipe (cross sectional view included) (left) and inlet velocity profile (right). The mesh in the cross sectional view is also included and the three measuring sections are marked by the numbers 0, 45, 90, corresponding to the degrees they are oriented with respect to section 0. The digitized inlet velocity profile is marked in red and superimposed on the original profile from Gijsen et al. (1999a).

The mesh (front view and cross sectional view) and the inlet velocity profile used in the validation study are shown in Figure 3.20. The inlet velocity profile from the reference study was digitised, converted into m/s, and applied at the inlet plane located 30D upstream of the 90 degrees measuring section. Velocity profiles along three measuring sections, as marked in Figure 3.20, are plotted in Figure 3.21. There is a good agreement between the present simulation result (red lines - base size 0.5 mm) and experimental results (black circles - element size 0.5mm). The discrepancies are attributed to the difference in the zero-shear viscosity, infinite-shear viscosity, and the power constant used. Although Figure 3.21 suggest that present results obtained from the mesh with the base size of 0.2 mm is grid independent, present results using the base size of 0.5 mm was used for validated. This is to ensure that the mesh used by both Gijsen et al. (1999a) and the present study are the same. To conclude, the Carreau-Yasuda model in Star-CCM+ has been validated.

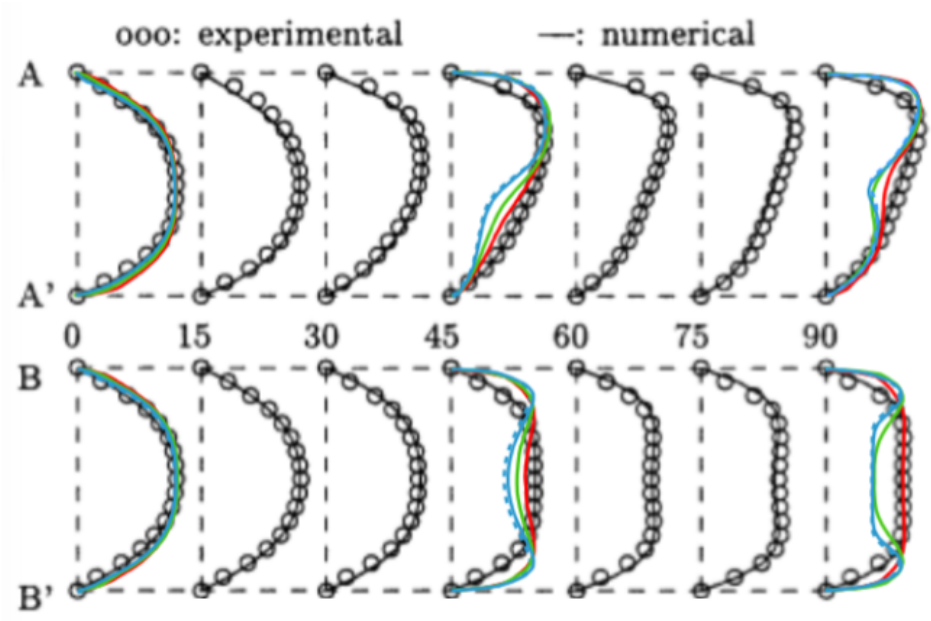

Figure 3.21: Velocity profiles measured along different measuring sections during peak diastole measured by Gijsen et al. (1999a) (black circles) superimposed by velocity profiles from the four meshes of the present study; base size 0.5mm (red), base size 0.4mm (green), base size 0.2mm (bold blue), and base size 0.15mm (dashed blue).

3.7 Eurelian multiphase blood modelling

As the present studies also investigate the role of red and white blood cells on aneurysmal and AVF haemodynamics, additional simulations of multiphase blood flow have been performed for both the aneurysm and AVF studies. Some results in Chapters 6 and 7 that invlove multiphase blood flow are obtained from these additional simulations. Unlike the single-phase blood, the multiphase blood have phase-dependent volume fractions, densities, and Carreau-Yasuda non-Newtonian parameters. Therefore, results from single-phase simulations and multiphase simulations are not compared. When certain haemodynamic properties (i.e. wall shear stress) are compared with multiphase properties (i.e. red blood cell viscosity), they are both obtained from multiphase simulations. Results from multiphase simulations (in chapters 6 and 7) are discussed in separated sections to avoid ambiguity.

In these multiphase simulations, blood is treated as a multiphase mixture and follows the Eurelian-Eurelian multiphase approach (Yilmaz et al., 2011; Mubita et al., 2014; Ou et al., 2016). This approach allows the erythrocytes (red blood cells), leukocytes (white blood cells) and plasma phases to coexist in the same computational element. Each phase is inter-penetrating and possess individual phase-dependent volume fraction, density, and velocity. Volume fraction, $\overline{v^2} - f$, defines the proportion of a computational cell occupied by each phase, and like density, varies with different health conditions. The volume fractions of red (erythrocytes) and white (leukocytes) blood cells used in the present study are 45% (Jung et al., 2006; Buradi and Mahalingam, 2016) and 1% (Ostrowski et al., 2016; Melka et al., 2018). The remaining 54% of the whole blood constitutes the volume fraction of the plasma phase. For reference, the volume fraction of red blood cell is also known as haematocrit.

In the single-phase approach, blood is typically modelled to have a constant density. However, a multiphase approach is used in this study and blood density varies with blood phases. Red blood cells (erythrocyte), white blood cells (leukocyte) and whole blood plasma densities of 1080, 1064, and 1003 kg/m^3 (Wen et al., 2015; Buradi and Mahalingam, 2016) are used. These

properties are specifically chosen such that each phase has different density (Melka et al., 2018) and the leukocyte phase is denser than plasma as would be observed in a typical centrifugal separation of blood components. The multiphase blood volume fractions and densities for each phase are summarised in Table 3.7 and 3.8, respectively.

The erythrocyte and leukocyte phases have Carreau-Yasuda non-Newtonian

Table 3.7: Multiphase blood volume fractions of each phase.

Volume fraction	Value
Red blood cell	0.45
White blood cell	0.01
Plasma	0.54

Table 3.8: Multiphase blood density (kg/m^3) of each phase.

Density	Value
Red blood cell	1,080
White blood cell	1,064
Plasma	1,003

viscosity, while the plasma phase have a Newtonian infinite shear viscosity of 1 mPa-s (Jung et al., 2006; Buradi and Mahalingam, 2016; Mehri et al., 2018). The Carreau-Yasuda parameters for the red and white blood cells used are suggested by Buradi and Mahalingam (2016) and are listed in Table 3.9. The density of the blood mixture is equal to the sum of the volume-fraction-weighted densities of each phase (Jung and Hassanein, 2008). As white blood cells contributes to only 1% of the total volume, its effect on the mixture density, as well as interparticle blood pressure, is neglegible.

Table 3.9: Carreau-Yasuda non-Newtonian parameters for red and white blood cells.

Parameter	Value	Unit
Infinite-shear viscosity (μ_{inf})	0.00345	mPa-s
Zero-shear viscosity (μ_0)	0.056	mPa-s
Relaxation time (λ)	3.313	s
a parameter (a)	2.0	-
Power constant (n)	0.3568	-

3.8 Mechanical properties of the vessel wall

For FSI simulations in the present study, the wall mechanical properties including the wall thickness are shown in this section. The boundary constraints for the distensible wall and the surrounding tissue supports on the blood vessels are also discussed.

3.8.1 Aneurysm wall thickness and constraints

Cerebral artery wall thicknesses are not typically found in the literature and even if found, they may not be accurately acquired (Lee et al., 2013) as cerebral artery thicknesses are too small for CT-scanners to capture (Torii et al., 2010). Therefore, the aneurysmal wall thickness were modelled based on previous FSI simulations. Wall thickness values between 0.35 and 0.41 mm were recently used for MCA aneurysms (Jahed et al., 2018). However like other arteries, cerebral aneurysms do not have a trivial value of wall thickness. Therefore, a theoretical value is preferable when the actual patient-specific wall thickness is not available. It was reported that the thickness of a healthy ICA is approximately 10-15% of the diameter (Riley et al., 1992), while that for the intracranial vertebral arteries is 4.4% of the diameter. Information on the relationship between the wall thickness of MCA and its geometric aspects was not available (Lee et al., 2013), but it is expected to be close to that of the ICA due to their proximity. The averaged diameter of the inlet and outlet of the aneurysm model is 3.03 mm. Taking into consideration the lower bound (Torii et al., 2010) diameter proportion of the typical ICA wall thickness of

10%, the calculated wall thickness for the present model is approximtely 0.3 mm. This wall thickness has been used for MCA (Torii et al., 2009, 2010) and other cerebral arteries, both patient specific (Lee et al., 2013) and idealised (Shamloo et al., 2017). The aneurysm sac was modelled to have the same wall thickness as its parent MCA (Torii et al., 2009) as only a typical wall thickness for ruptured aneurysms (of 0.051 mm) was available (Abruzzo et al., 1998)

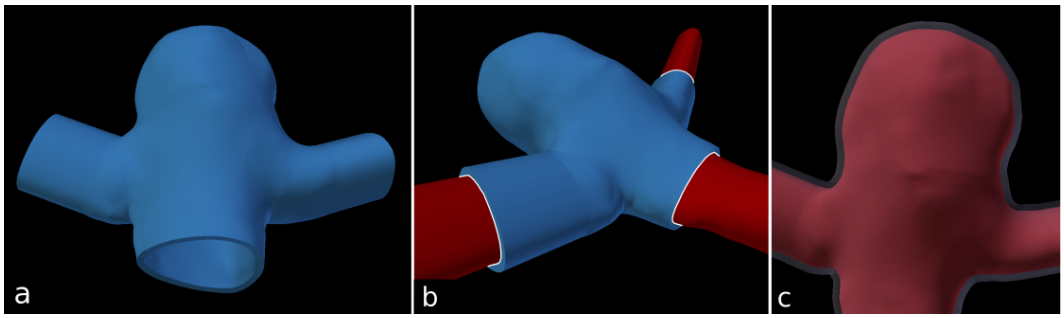

Figure 3.22: a. Elastic aneurysm wall with uniform thickness (in blue), b. superimposed onto the MCA and its aneurysm (in red). White lines represent free wall boundaries constrained by fixed displacement. Thickness is clearly shown in Figure c.

and the present aneurysm model is categorised as unruptured. By using a slightly thinner wall in the present study as compared to that used in previous MCA aneurysms (Jahed et al., 2018), the rupture risk is not underestimated (Torii et al., 2010). Figure 3.22 shows the vessel wall of the MCA aneurysm and the free wall boundaries (marked by white lines) that are constrained with fixed displacement. These constraints represent the tension forces in the vessel sections upstream and downstream of the inlet and outlets, that hold the model in place, respectively. The boundaries of the vessel wall are located approximately 2D away from the aneurysm dome, where D is the respective inlet and outlet diameters, to discriminate the aneurysm stress from the constraint effects (Valencia et al., 2008). This is also applied to the AVF model.

3.8.2 AVF wall thickness and constraints

Unlike FSI aneurysm studies, FSI arteriovenous fistula studies are rather limited if longitudinal studies of fistula remodelling are ignored. Of all four

patient-specific FSI-AVF studies, three provided data on the wall thickness which is not uniform throughout the model, except for Ngoepe et al. (2011), due to the difference in size of the artery and vein (Decorato et al., 2014; McGah et al., 2014), and in some circumstances inflammation (Torii et al., 2010). As the present AVF model also comprised of an artery and a vein, a non-uniform wall thickness was modelled. Table 3.10 summarises the arterial and venous wall thickness used in previous studies.

Table 3.10: Wall thickness of the artery and vein used in previous FSI-AVF studies.

Artery [mm]	Vein [mm]	References
0.5	0.5	(Ngoepe et al., 2011)
0.6	0.4	(Decorato et al., 2014)
0.55	0.51	(McGah et al., 2014)

It is evident that there is no common thickness for an arterial wall. However, a previous study suggested that the arterial wall thickness is typically 0.1 times the diameter (Gutierrez et al., 2002). The arterial wall thickness reported by Decorato et al. (2014) of 0.6 mm was also determined from this principle. Therefore, this method of determining arterial thickness was considered and the arterial wall thickness of the present AVF model is 0.36 mm, one-tenth of the inlet diameter. Although this thickness is smaller than those reported in the literature, it was modelled in accordance to the validated scheme. The venous wall thicknesses used in the literature varied less significantly. However, these values are all patient-specific except for 0.4 mm, which is typically found in vein prior to AVF surgery (Decorato et al., 2014). As the fistula segment of the present model was reconstructed for the simulation, it represents a newly-created AVF which makes this thickness a suitable choice. Additionally, since the fistula segment originally belongs to the vein, it was also modelled with the venous wall thickness. The transformation in wall thickness from the artery to the vein is illustrated in Figure 3.23

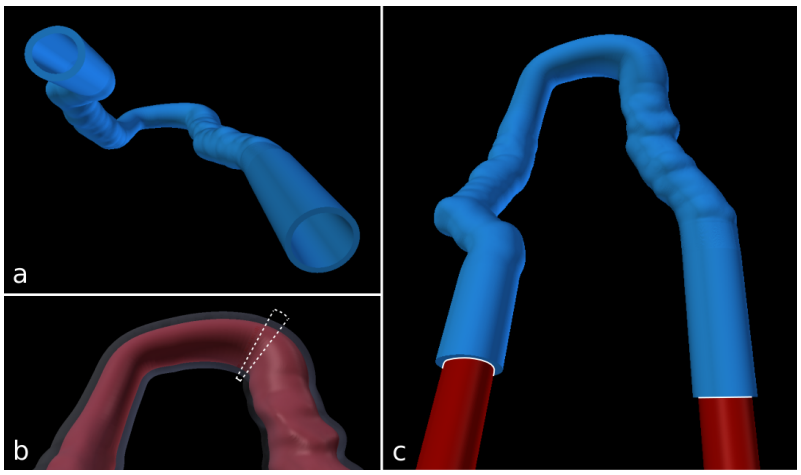

Figure 3.23: a. Elastic AVF wall (in blue) from the axial view, b. showing the slightly non-uniform thickness of the anastomosis. White dashed lines surround the region where arterial thickness is transformed into the venous thickness. The AVF (in red) is superimposed by the wall in Figure c, where the white lines represent free wall boundaries constrained by fixed displacement.

3.8.3 Mechanical properties of the vessel walls

In the present study, the aneurysm and AVF walls share the same Young's modulus, density, and Poisson's ratio as they are made up of the same material. Moreover, there is no preferred choice for all the properties in the literature of both pathologies. Previous studies used different Young's modulus of 1.6 MPa (Helthuis et al., 2018), 2 MPa (Valencia et al., 2008), and 5 MPa (Suzuki and Ohara, 1978). However, to examine the case of maximum deformation, the lowest Young's modulus of 1 MPa, which is also a typical value for normal vessels (Valencia and Solis, 2006), was used in this study. On the contrary, the highest Poisson's ratio was chosen to simulate the extreme case of maximum lateral displacements. Properties used for both models are listed in Table 3.11.

Table 3.11: Mechanical properties for blood vessel wall

Property	Value for vessel wall	References
Young's modulus	1 MPa	Ahmed et al. 2007, Lee et al. 2013
Density	1100 kg/m^3	Lee et al. 2013, Suzuki et al. 2015
Poisson's ratio	0.49	Ngoepe et al. 2011, Torii et al. 2009

3.9 FSI equations and Rayleigh damping

In the present aneurysm and AVF studies, the effects of wall compliance have been investigated. To allow the blood vessel walls to interact with the blood flow, FSI simulations have been performed. These FSI simulations couple the fluid domain and a solid domain (representing the walls) through a fluid-solid interface. The blood flow and shear traction in the fluid domain (calculated using CFD govering equations) and vessel wall deformation in the solid domain (calculated using FEA governing equations) are coupled. There are two methods of performing FSI simulations; the monolithic method (Eken and Sahin, 2017) and partitioned method (Degroote and Vierendeels, 2011). In the monolithic method, the governing equations for the fluid and solid domains are solved simultaneously using one solver and involve higher computational cost. In the more verified and efficient partitioned method, the governing equations of both domains are solved separately in their designated solver.

Wall information is transferred between the domains to allow one domain to use the output of the other as its input value. If the information is transferred only in one direction (i.e. from fluid to solid), it is called a one-way partitioned method. Alternatively, if information is exchanged between the domain in both directions, it is called a two-way partitioned method. FSI simulations in Star-CCM+ use a two-way partitioned method.

3.9.1 Two-way partition method

The two-way partition FSI simulations allow the fluid motion, viscous shear traction, and pressure to cause wall deformation and in turn allows the displaced wall nodes to change the vessel cross-sectional areas. This changes the volume of the fluid region and affects the flow field. For such interaction to occur, the interface between the fluid and solid regions need to be compatible and have an equilibrium tractions. Wall elements of the fluid domain are mapped onto elements on the inner surface of the solid domain to ensure the compatibility of the fluid-solid interface (Valencia et al., 2008). Interface mapping enables information to be exchanged between the two domains. However, interface mapping is usually complicated when the meshes of the two domains are non-coincident. Coupling between these two domains, and the compatibility of the fluid-solid interface, are ensured by internal algorithms of the software. In order to achieve this, the displacement and stress tensors of the fluid and solid domains at the interface needs to be in equilibrium, as shown in Equations 3.9 and 3.10. The parameters δ, σ and $\hat{n}$ denote the displacement, stress tensor (σ=F/A), and normal vector of the interfaces. Interface mapping is responsible for ensuring this equilibrium. During the simulation runtime, the fluid solver calculates the pressure and force on the wall due to fluid flow and transfers this information to the solid solver, which computes the wall displacement. At this stage, it is essential for the fluid mesh to adapt to the deformed solid mesh for the successful transfer of the wall information

$$\delta_{solid} = \delta_{fluid} \tag{3.9}$$

$$\sigma_{solid} \cdot \hat{n_{solid}} = \sigma_{fluid} \cdot \hat{n_{fluid}} \tag{3.10}$$

In a fluid domain with moving boundaries, the Navier-Stokes equations can be discretised using either the space-time methodology (Torii et al., 2006; Takizawa et al., 2010) or the Arbitrary Lagrangian-Eurelian (ALE) formulation (Formaggia et al., 2001; Sun et al., 2020). Although space-time methodology provides higher time accuracy, the ALE method is computationally more effec-

tive and is widely used. Additionally, as its name suggests, the ALE method (Hirt et al. 1974) combines the advantages and overcomes the drawbacks of the Lagragian and Eurelian methods used to describe fluid flow.

In the Lagragian method, the mesh can be expanded or compressed according to the local blood velocity. However, this deformation can potentially lead to mesh distortion (Margolin, 1997). Hemodynamic properties are measured for individual fluid particles in the Lagragian domain. On the other hand, for an Eurelian domain, these properties are measured in a control volume of fixed coordinates. Therefore, the flow fields are visualised as scalar and vector fields. Since Eurelian meshes do not move with the local flow, mesh distortion issues are not commonly observed. However, Eurelain solutions are diffusive. In the ALE method, the continuous mesh adaptation can be defined arbitrarily without affecting the mesh topology. Another requirement for a two-way partioned method is the stabilisation of the numerical solutions. Therefore the Rayleigh damping model was introduced.

3.9.2 Rayleigh damping model

The Rayleigh damping model incoporates the mass-proportional and stiffness-proportional dampings into the finite element method (Langen and Sigbjornsson, 1979). Mass proportional damping is added to provide the arterial dynamics with damping effects from the surrounding exterior tissues (Eken and Sahin, 2017) and elimates high-frequency modes of the vessel deformation (Tezduyar et al., 2007). It is represented by a viscous damping matrix [C] which is defined by Equation 3.11. The damping matrix is the sum of the mass matrix [M] and stiffness matrix [K] weighted, respectively, by the mass proportional damping (α) and stiffness proportional damping (β) coefficients. The mass and stiffness damping coefficients represent thresholds used to damp low and high frequencies, respectively, due to external fluid, shear, and dilation waves (CD-Adapco). These two coefficients are unknowns and can be determined by solving the damping ratio in Equation 3.12. According to this equation, a damping ratio ζ_i is associated with a certain natural frequency ω_i.

If two pairs of ζ_i and ω_i are known, the damping coefficients α and β can be determined by simultaneously solving Equation 3.12 as shown below in Equation 3.13 (Wilson, 2004). The two frequencies ω_1 and ω_2, which provide the upper and lower limits for which the resulting damping effects associated with ζ_1 and ζ_2 do not dramatically change within this frequency range, are chosen.

$$[C] = \alpha[M] + \beta[K] \tag{3.11}$$

$$\zeta_n = \frac{\alpha}{2\omega_n} + \frac{\beta\omega_n}{2} \tag{3.12}$$

$$\begin{pmatrix} \zeta_1 \\ \zeta_2 \end{pmatrix} = \frac{1}{2} \begin{pmatrix} \frac{1}{\omega_1}\omega_1 \\ \frac{1}{\omega_2}\omega_2 \end{pmatrix} \begin{pmatrix} \alpha \\ \beta \end{pmatrix} \tag{3.13}$$

The natural frequencies of soft tissues including blood vessels cannot be obtained directly as their vibration properties vary with patient-specific muscle forces and muscle activities (Formaggia et al., 2001). Furthermore, damping coefficients corresponding to these natural frequencies in soft tissues are subjected to muscle length, contraction history, surrounding fat properties, and the coupling between connective tissues and blood vessels. Although Wakeling and Nigg (2001) provided several choices of natural frequency for leg muscles, estimations of the natural frequency of brachial and cerebral blood vessels are not possible without the knowledge of the number of contractions, tendon (muscle) forces, and other muscle properties. Chowdhury and Dasgupta (2003) presented an insightful procedure for determining the damping coefficients. However, without knowledge of natural frequencies and their corresponding damping ratios of the patient-specifc blood vessel, the procedure is inapplicable (CD-Adapco).

It can be concluded that both damping coefficients cannot be determined through calculation. In this case, damping coefficients from previous FSI studies may be used. There is only one study, among all previous FSI aneurysm and AVF studies, which provided a completed pair of mass and

stiffness proportional damping coefficients of $\alpha = 6000$ Hz and $\beta = 0$ s (Eken and Sahin, 2017). However, unlike in Eken and Sahin (2017), a stiffness proportional damping coefficient of 0s cannot be used in Star-CCM+ as it resulted in simulation instability. Additionally, the study did not justify its use of these damping coefficients. It can be understood from $\beta = 0$ s that they did not take account of the stiffness, but $\alpha = 6000$ Hz was not justified. Therefore, a systematic study is conducted to investigate the effects of Rayleigh damping coefficients on wall displacement and determine the suitable pair of damping coefficients for the present study.

3.9.3 Systematic study on Rayleigh damping coefficients

Ten simulations of a 10D straight pipe with a constant radius of 2mm have been performed to investigate the effects of ten pairs of Rayleigh damping coefficients on wall displacement. The same boundary conditions, non-Newtonian blood properties, and wall thickness of the aneurysm study were used in all 10 simulations. In each simulation, the Rayleigh damping coefficients α and β were changed. Initially, the pair of damping coefficients provided by Eken and Sahin (2017) of $\alpha = 6000$ Hz and $\beta = 0$s were used. However, the simulation stability was compromised when β is set to 0s. In fact, the use of any values of β less than 0.1 resulted in numerical instability. Therefore, the stiffness proportional damping coefficient β was systematically increased from 0.1 while $\alpha = 6000$ Hz remained constant. Figure 3.24 shows the temporal variations of the maximum displacement of the outer wall with different β values during the fourth cardiac cycle. As β increases, the following points was observed:

1. The amount of cardiac cycles required for the displacement waveform to become periodic increases with β. At the fourth cycle, the displacement waveform corresponding to the pair ($\alpha = 6000$, $\beta = 0.1$) has become perioidic, while that of the pair ($\alpha = 6000$, $\beta = 10$) has not yet reached its perioidicity.

2. When the displacements become periodic in time, their waveforms are not nescessarily the same. The periodic displacement waveform due to larger values of β varied less in amplitude during a cardiac cycle due to stronger stiffness proportional damping effects.

3. The difference between the displacement magnitude and radial displacement becomes smaller with increasing β.

4. Therefore, the smallest possible value of β (which does not compromise the simulation stability) is the optimal choice.

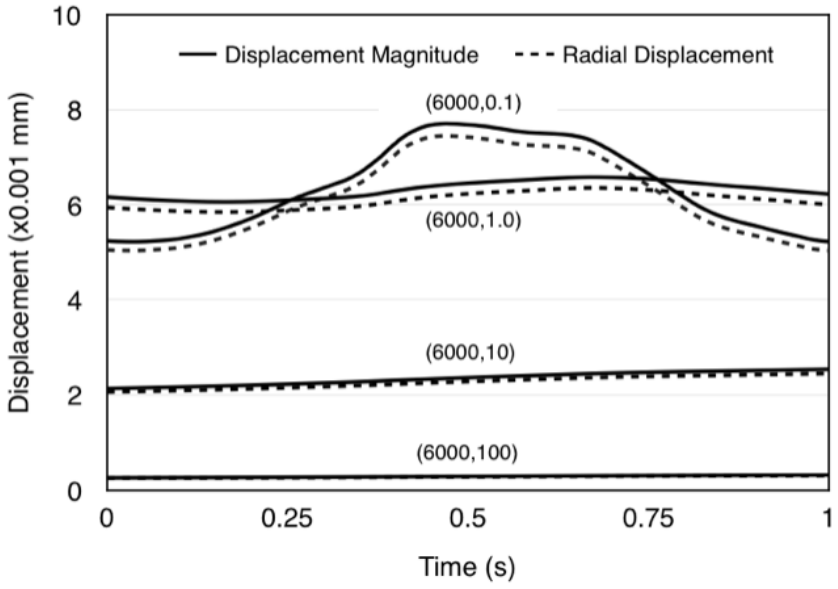

Figure 3.24: Temporal variation of the maximum displacement of the outer vessel wall for various (α, β) values.

Furthermore, the effects of the mass proportional damping coefficient on the wall displacement is also studied. Figure 3.25 shows the temporal variation in the displacement of the outer vessel wall with different α values throughout the fourth cardiac cycle. While α is varied, the stiffness proportional damping coefficient β is kept constant at 0.1s. It is clear that the displacement waveforms are insensitive to changes in the mass proportional damping effects.

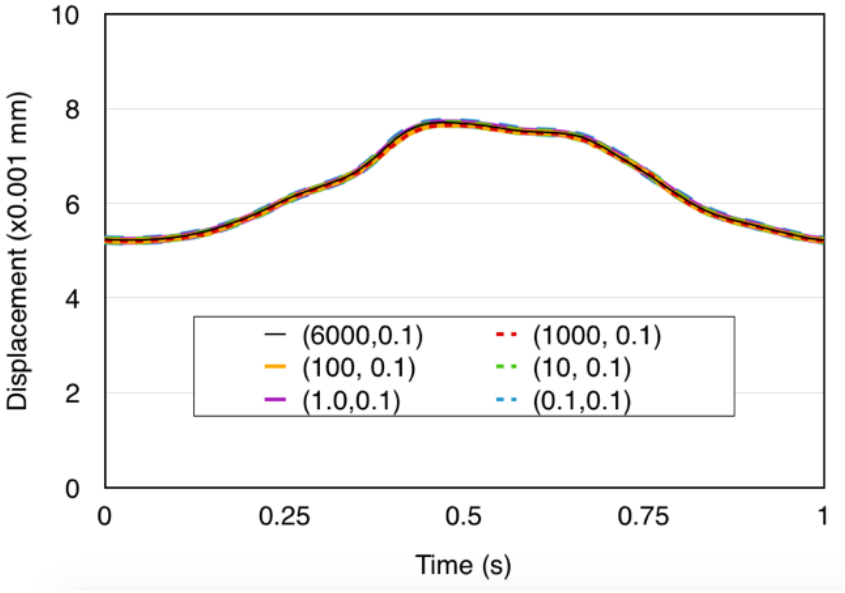

Figure 3.25: Temporal variation of the maximum displacement of the outer vessel wall for various (α, β) values

There is no significant changes in the displacement as α decreases from 6000 Hz, the value used by Eken and Sahin (2017), to 0.1. At $\alpha = 0$ the simulation crashed due to simulation instability, similar to the case of $\alpha = 0$s. Therefore, there is no difference between using $\alpha = 6000$ Hz and $\alpha = 0.1$ Hz under the assumption of the linear elasticity model.

In other cases where the vessel walls are assumed to be hyperelastic, the displacement is significantly higher than that of a linear elastic vessel. This is due to the nature of hyperelastic materials. Eken and Sahin (2017) assumed the Saint Venant-Kirchoff hyperelastic model and, therefore, may have required a larger mass proportional damping coefficient of 6000 Hz. Lower values of α may compromise the stability of their hyperelastic simulation. Additionally, the Saint Venant-Kirchoff hyperelastic model was not used for the present study as it is not available in Star-CCM+. If the model was available, it would have been applied to the present aneurysm and AVF geometries. In that case, the pair of Rayleigh damping coefficients initially suggested by Eken and Sahin (2017) would also have been used.

To conclude, the preferrable mass and stiffness proportional damping coefficients α and β are 6000 Hz and 0.1s, respectively. The mass proportional damping coefficients of 6000 Hz was based on the suggestion of Eken and Sahin (2017). The stiffness proportional damping coefficient of 0.1s is the lowest possible value that can be used without compromising the stability of the straight pipe flow simulation. For simulations of a more complicated geometry, a higher value of β may be nescessary.

In the present aneurysm and AVF studies, FSI simulations were performed using the finite volume method for the fluid domain and the finite volume solid stress model for the solid domain. The first order Backward Euler integration method, which allows for numerical damping, was employed to add the accerelation term into the equation of motion for the solid stress model. Displacement and morphing convergence tolerance was maintained at 1x10-8 and 1x10-7, respectively. The linear isotropic elasticity model was used as a material law for the blood vessel (Torii et al. 2009, Lee et al. 2013). Hyperelastic models including the Mooney-Rivlin (Shamloo et al. 2017), Neo-Hookean, and Ogden (Ngoepe et al. 2011, Sharzehee et al. 2018) models can also be used in Star-CCM+. However, the Saint Venant-Kirchoff hyperelastic model used by Eken and Sahin (2017), where the present damping coefficients used in the present study are based on, is not avaliable in Star-CCM+. Therefore, hyperelastic models were not used.

For the present aneurysm study, the preferrable pair of damping coefficient ($\alpha = 6000$ Hz and $\beta = 0.1$s) are used. In the present fistula study, $\beta = 0.1$s resulted in numerical instability due to the stronger and more disturbed flows. Therefore, the lowest possible β values of 100s was used with $\alpha = 6000$ Hz.

3.10 WSS-based parameters

As wall shear stress significantly contributes to the growth and rupture of aneurysms and maturation of AVF, different metrics related to it have

been proposed in the literature and are defined below. The present study also introduces additional metrics that would improve our understanding of the mechanisms behind these pathologies.

Wall Shear Stress

Wall shear stress (τ) is defined as the product of the time-dependent non-Newtonian dynamic viscosity (μ) and streamwise velocity gradient on the vessel wall (Equation 3.14). In Newtonian simulations, the viscosity remained constant and the wall shear stress is only affected by the near-wall velocity. The streamwise veocity gradient is measured at the first grid point away from the wall. In turbulence modelling, the size of the element on the wall is significantly more important. A dimensionless distance y^+ measured away from the wall is defined in Equation 3.15. It is the product of the streamwise velocity u, and the distance from the first gridpoint from the wall dy, and the fluid kinematic viscosity ν. The turbulent boundary layer near the wall must be captured by the first gridpoint from the wall. This can be ensured by meshing the first gridpoint from the wall such that the y^+, which depends on dy, is kept below a value of 1.0. If this condition is not met, the wall function used by the turbulent solver may miscalculate the velocity at the first gridpoint and the wall shear stress. However, since all flows in the present studies are laminar, y^+ values were not calculated.

$$\tau = \mu \frac{du_{wall}}{dy} \tag{3.14}$$

$$\mathbf{y}^+ = udy\nu \tag{3.15}$$

Time-averaged wall Shear Stress (TAWSS)

Time averaging is often performed for wall shear stress over a cardiac cycle (T) to represent the its overall variation. Systolic and diastolic oscillations are usually captured by instantaneous WSS instead if they are not prolonged. $\overline{\tau_{\mathbf{wall}}}$ is defined by the integral of WSS magnitude divided by the time in one

cardiac cycle.

$$\overline{\tau_{\mathbf{wall}}} = \frac{1}{T}\int_0^T |\tau| dt \tag{3.16}$$

Oscillatory Shear Index (OSI)

Directional variation of WSS from its time-averaged vector is taken into account by the oscillatory shear index (Ku et al., 1985). It is defined by Equation 3.17 and is related to both TAWSS and averaged WSS vector (AWWSV). AWSSV is the magnitude of the time-averaged WSS at a computational node.

$$OSI = \frac{1}{2}\left(1 - \frac{\left|\int_0^T \tau dt\right|}{\int_0^T \mid \tau \mid dt}\right) \tag{3.17}$$

$$= \frac{1}{2}\left(1 - \frac{AWSSV}{TAWSS}\right) \tag{3.18}$$

Unlike TAWSS, OSI describes the oscillatory behaviour of the WSS vectors through its value. The minimum and maximum values for OSI are 0.0 and 0.5, respectively. A WSS vector that does not change direction in time at all will produce an OSI value of 0.0 (no WSS oscillation). On the other hand, a WSS vector that regularly changes direction or completely reverse its direction (180 degree WSS oscillation) will produce a non-zero OSI or a value of 0.5, respectively. However, OSI values will never reach these minimum and maximum boundaries in reality.

Relative residence time (RRT)

Intimal hyperplasia (Meng et al., 2007) and thrombus formation (Dolan et al., 2013) which lead to AVF maturation failure, aneurysm growth and rupture were all reported to be associated with low and oscillatory WSS. In order for the two hemodynamic variables to be coupled, the relative residence time (RRT) [1/Pa] was introduced (Himburg et al., 2004) as presented by Equation 3.19. The equation does not represent an actual blood residence time and is only used to locate regions of low oscillatory WSS.

$$\mathrm{RRT} \sim \frac{1}{[1 - (2 \times \mathrm{OSI})] \times \mathrm{TAWSS}} \tag{3.19}$$

RRT can range from a value of $1/TAWSS$ where flow in unidirectional to infinity. Due to its wide range, RRT is normalised by its value in an equivalent and fully-developed blood flow in a straight vessel (Ene-Iordache and Remuzzi, 2012). In that case, an RRT higher than 1.0 would highlight regions of lower and more oscillating WSS.

Localised normalised helicity (LNH)

Counter-rotating vortices induced by primary and secondary velocities are commonly observed in pipe flows and are associated with helical flow structures. The interaction between these helical vortices and their sources is measured by helicity, which is the product of the instantaneous velocity and vorticity vectors as expressed in Equation 3.20.

$$H = (\nabla \times \mathbf{v}) \cdot \mathbf{v} \tag{3.20}$$

The relationship between helicity and other haemodynamic quantities is rarely studied in both aneurysm and AVF literature but can play a significant role, especially in regards to disturbed shear (Gallo et al., 2012). Helicity magnitude and directions describes the speed and tortuousity of the helical flow, respectively. For helical structure visualisation in patient-specific models, local normalised helicity (LNH) was employed. LNH isosurfaces of -0.9 $\geq$ LNH $\geq$ 0.9 was used in a previous AVF study (Bozzetto et al., 2015).

$$LNH = \frac{H}{\mid \nabla \times \mathbf{v} \mid \cdot \mid \mathbf{v} \mid} \tag{3.21}$$

Von Mises stress

In FSI studies, the internal stress of the vessel wall is determined by von Mises stress as expressed by Equation 3.22

$$\sigma_{VM} = \sqrt{\frac{1}{2}\left[(s_1 - s_2)^2 + (s_1 - s_3)^2 + (s_2 - s_3)^2\right]} \tag{3.22}$$

where s_i denotes the eigenvalues of stress (or principal stresses) where i=1,2,3 represents the maximum, intermediate, and minimum principal stresses, respectively. Plaque burden, wall thinning, and thickening were found to be independently predicted by von Mises stresses in atherosclerotic coronary arteries (Liu et al., 2016). Coronary wall thickness was also found to be inversely proportional to von Mises stress (Tang et al., 2013)

3.10.1 Proposed metrics

Three new metrics are introduced by the present study to further investigate underlying mechanisms of aneurysm rupture, aneurysm recurrence, and fistula maturation failure; Low and oscillating wall shear stress index (LOWSSI), stress divergence line (SDL), flow impingement ratio (IR).

Low and oscillating wall shear stress index (LOWSSI)
Regions of low and oscillating wall shear stress (LOWSS) have previously been indicated by contours of relative residence time (RRT) (Himburg et al., 2004). With TAWSS and OSI coupled, RRT is used to indicate regions of LOWSS as shown in Equation 3.19. However, it does not represent the actual blood residence time and does not define the LOWSS regions based on clinical threshold values of TAWSS and OSI. The low and oscillating wall shear stress index (LOWSSI) is therefore introduced as the relative residence time normalised by the parameter itself but based on the threshold TAWSS and OSI known to be responsible for certain endothelial abnormalities. LOWSSI is expressed as shown in Equation 3.23 where $TAWSS_{th}$ and OSI_{th} are the threshold TAWSS and threshold OSI, respectively.

$$LOWSSI = \frac{TAWSS_{th}([1 - (2 \times OSI_{th})])}{TAWSS([1 - (2 \times OSI)])} \tag{3.23}$$

LOWSSI value of 1.0 means that the TAWSS and OSI of that computational cell is equal to the respective threshold values. This marks the boundary of potential stenosis initiation. As LOWSSI increases from 1.0, the TAWSS required to produce a certain amount of flow oscillation (OSI) lowers linearly

by a factor equivalent to the LOWSSI value as shown in Figure 3.26. For example, LOWSSI = 3.0 indicates that the TAWSS of that cell is three times lower than the threshold WSS. Consequently, three times the TAWSS of the cell is needed to secure the cell itself from experiencing low and oscillating flow when the local flow oscillation is too strong to be changed. Therefore, besides identifying low and oscillating WSS regions, LOWSSI can also be used to indicate the required increase in TAWSS to prevent low and oscillating flows. Regions with LOWSSI lower than 1.0 indicate sufficiently high TAWSS and almost unidirectional flow (low OSI) in that region. Endothelial cells in these regions do not experience LOWSS and hence are unlikely to develop IH. As LOWSSI decreases from 1.0 towards zero, the TAWSS required to produce a certain amount of flow oscillation rises linearly by a factor of the reciprocated LOWSSI value. For example, LOWSSI = 0.25 indicates that the TAWSS of that element is four times that of the threshold WSS. The local TAWSS would have to be reduced by four times for low and oscillating flow to exist. Note that a LOWSSI value of zero only exist in a uni-directional flow.

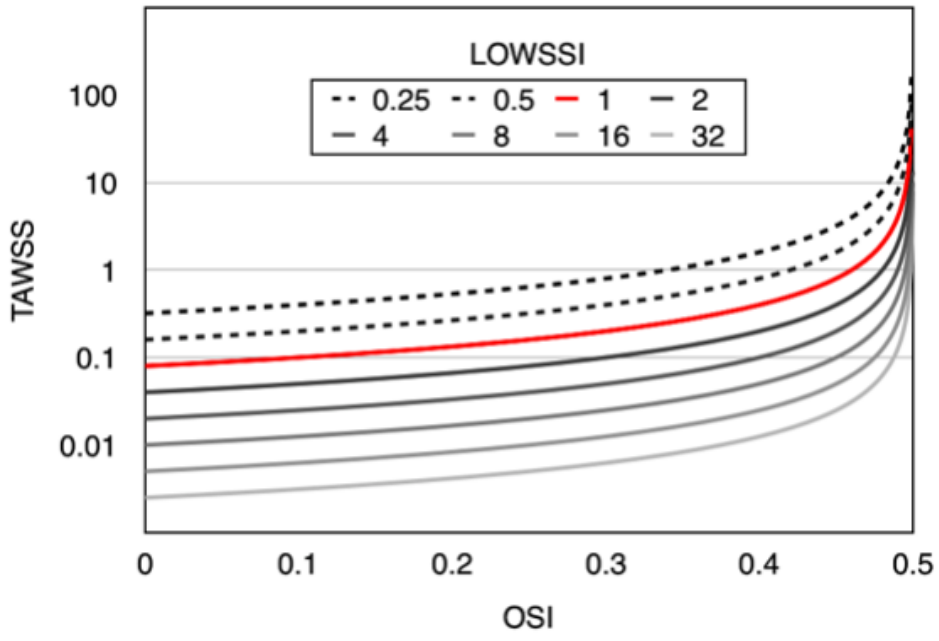

Figure 3.26: Variations of TAWSS and OSI at different LOWSSI levels.

Compression-tension line (CTL)

The compression-tension line separates the wall surface into two regions subjected to either compression or tension. The criteria in defining this isoline is zero wall displacement magnitude or zero wall displacement in the axial and transverse directions. Wall displacement is calculated by the length of the displacement vector on each wall node. Figure 3.27 shows an example of the CTL indicating compression and tension regions on an aneurysm wall.

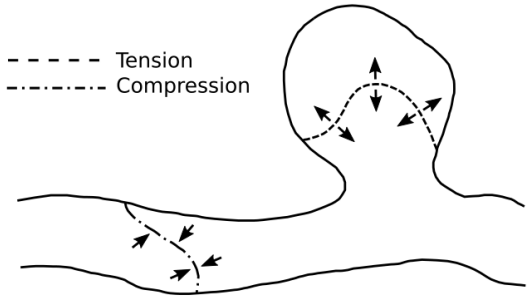

Figure 3.27: A schematic diagram of the compression-tension line on the wall of an aneurysm. Arrows indicate direction of tangent wall movement.

Flow impingement ratio (IR)

Flow impingement has been suggested by previous studies to cause flow stagnation on the wall and high WSS downstream. Both flow stagnation and high WSS have been related to aneurysm growth and intimal hyperplasia in the literature. IR compares the loading on the vessel wall due to pressure and wall shear stress. It is defined by the quotient of the blood pressure and the WSS magnitude at a wall gridpoint as described in Equation 3.24. Both pressure and WSS can be normalised by their respective spatial maximum value in the model for a more physical interpretation. The normalised flow impingement ratio (NIR) is described below.

$$IR = \frac{P_{wall}}{|\tau|} \tag{3.24}$$

$$NIR = \frac{P_{wall} \cdot |\tau|_{max}}{|\tau| \cdot P_{wall,max}} \tag{3.25}$$

Unlike IR which has a wide range, NIR is bounded between 0 and 1. Locations that are subjected to complete shear with no impingement would have NIR =

0, while an NIR value of 1.0 would be observed at locations subjected to complete flow impingement with no shear. The NIR value does not have to reach 1.0 for a flow impingement region to be identified. Locations of flow impingement have been determined without quantitative analyses in most previous studies. Cebral et al. (2005) interpreted the size of flow impingement relative to aneurysm dome size and found that small and changing impingement regions led to rupture. However, the oscillation frequency of the changing impingement region was not discussed. Cornelissen et al. (2015) suggested that flow impingement zone is determined by WSS distribution and velocity streamline. The location of maximum WSS was interpreted as flow impingement zone. However, high WSS is not nescessarily attributed to flow impingement alone, so this interpretation may lead to inconclusive findings.

Riccardello et al. (2018) introduced the isolated impingement indicator (III) which functions in a similar manner as the flow impingement ratio (IR) in the present study. The dynamic pressure normal to the wall was used to calculate the flow energy that impinges onto the wall. As increase in pressure has been suggested as an indicator of flow impingement (Tobe et al., 2014), both III and IR have taken it into account. However, wall shear stress was taken into consideration only by the flow impingement ratio (IR). A strong correlation between flow impingmement and high and less oscillatory WSS have recently been confirmed (Cebral et al., 2019). To take account of the low oscillation among high wall shear stresses, the IR contours presented in this study are interpreted in conjunction with diverging WSS vectors (Tobe et al., 2014) for higher confidence. Nevertheless, the employment of pressure in determining flow impingement may not be appropriate in AVF studies where the pressure drops continuously along the domain length and variations of pressure can be underestimated. This may be the reason why flow impingement indices have not yet been used in previous AVF studies.

Chapter 4

Validation of Ultrasound-based CFD

This chapter validates the use of ultrasound images for CFD simulations. A journal paper will be published based on this chapter of the thesis.

4.1 Abstract

Purpose: Ultrasound imaging is not widely used for computational fluid dynamic (CFD) studies, despite its harmlessness and accessibility, due to the segmentation complications involved. Other imaging modalities, such as magnetic resonance imaging (MRI), have instead been employed to produce 3D vessel geometries for CFD simulations. However, exposure to harmful radiations and access to these imaging techniques may put the patients health at unnescessary risks. This study aims to validate the capability of ultrasound-based CFD in predicting haemodynamic quantites by comparing against the already well-established MRI technique.

Methods: Brachial vessels of four healthy subjects were scanned using both MRI and ultrasound imaging and eight CFD simulations were performed. Non-Newtonian and multiphase blood properties were modelled to mimic the realistic blood behaviours. Statistical analyses, including Bland-Altman plots, were employed to compare ultrasound-derived wall and volumetric haemodynamic quantities against those of MRI-based.

Results: MRI-ultrasound differences in mass flow rates, hematocrit, erythrocytes and leukocyte velocities are sufficiently low and within satisfactory range. Comparison of various wall shear stress (WSS) parameters, including the proposed low and oscillatory wall shear stress index (LOWSSI), derived from MRI and ultrasound are in good agreements ($r2 > 0.95$) and are statistically significant. These findings suggest that ultrasound is capable of predicting haemodialysis patency and intimal hyperplasia due to oscillating WSS ($OSI > 0.42$). Additionally, the proportions of vessel walls experiencing low and oscillating wall shear stress predicted by both the MRI and ultrasound models present no systematic bias and correctly confirms the low possibility of intimal hyperplasia of these healthy blood vessels.

Conclusion: The present validation study is the first to confirm that ultrasound images can be used for multiphase and non-Newtonian CFD simulations. Therefore, the use of the ultrasound image of fistula in the present AVF study has been validated.

4.2 Introduction

The progression of cardiovascular diseases has been related to pathological lesions and abnormal changes in haemodynamic quantities. Atherosclerosis, together with other cardiovascular diseases, have long been responsible for the high mortality rate worldwide (Vorp, 2007). In order to predict haemodynamic changes, especially in arteriovenous fistulas where these changes are rapid (Niemann et al., 2012a), and understand the mechanisms behind these conditions, the use of computational fluid dynamic (CFD) simulations is necessary (Chaichana et al., 2013a; Jing et al., 2015). Different imaging modalities including computed tomography (CT) (Otani et al., 2016; Grechy et al., 2017) and magnetic resonance imaging (MRI) (Sigovan et al., 2013) have been used for previous CFD simulations. Other techniques such as ultrasound scanning (McGah et al., 2014), digital subtraction angiography or X-ray (Ene-Iordache et al., 2001), and 3D rotational angiography imaging (Morales et al., 2016) are also clinically available.

The use of one particular imaging modality instead of another is justified by considering its relative capabilities and limitations. Typical CT and MRI scanning provide images with less artifacts, but are more harmful to patients, compared to ultrasound images. CT and X-ray scanners expose patients to ionizing radiation by an amount of approximately 0.6 mSv/year, equivalent to 20% of the global exposure to ionizing radiation in daily life (Ribeiro et al., 2020). While patients who undergo MRI scanning do not risk being exposed to ionizing radiation, they are instead exposed to both static and time-varying magnetic fields (de Vocht et al., 2012). Additionally, patients with kidney disease were found to be allergic to the gadolinium-based contrast agents which enhances blood contrast in MRI scanning (Gauden et al., 2010).

Ultrasound (US) scanning is a non-invasive imaging technique that is more portable, less expensive, and requires shorter scanning duration compared to CT and MRI (Daoud et al., 2015). However, computational studies on patient-specific haemodynamics using ultrasound images are very limited due to the complications involved in image acquisition and reconstruction. Stable handling of the ultrasound transducer and maintenance of a constant advancement rate, in the case of free-hand scanning, is a major clinical challenge for ultrasound scanning (Niemann et al., 2012a). Reflection delays caused by the different layers of tissue was also known to be responsible for producing image artifacts (Gee et al., 2003). In certain cases where reductant image artifacts prevent vessel reconstruction, idealised vessel geometries were instead constructed based on the outlines of the original US geometry (Pennati et al., 2008), resulting in a loss of patient-specifc wall information. With these complications, reasonable differences between MRI and US-based geometries are unavoidable. Nevertheless, ultrasound scanning is capable of discriminating even the atherosclerotic plagues from CT scans of a coronary artery, in an attempt to reconstruct a healthy vessel from the diseased (Ryou et al., 2012).

Previous studies have attempted to compare the MRI-US differences in flow measurements observed in different blood vessels, mostly the carotid arteries. MRI-US differences in the systolic velocity can range from -12% (Safavi et al.) to 36% (Maier et al., 2018). It should be noted that positive dif-

ference indicates MRI underestimation, while a negative difference indicates MRI overestimation. Similarily, differences in the diastolic velocity ranging from -9% (Harloff et al., 2013) to 28% (Safavi et al.) were reported. Mean velocities were mostly found to be underestimated (30%) by MRI, while the cross-sectional area of a carotid artery can be overestimated (-34%) by MRI (Glor et al., 2003). A wide range of MRI-US difference in the volumetric flow rate from -5 to -115% (Niemann et al., 2012a) previously observed among 6 patients. On the other hand, He et al. (2018) compared the volumetric flow rates acoss 60 patients undergoing arteriovenous fistula surgery and came to a slightly different conclusion. In their study, various flow rates obtained were categorised. Approximately 80% of the MRI and US scan pairs were sorted into the same flow rate categories. It is not clear which modality overestimates or underestimates these haemodynamic properties.

Flow measurements obtained from Doppler ultrasound scanning have frequently been used for CFD boundary conditions by previous studies including Jiang and Strother (2009), Niemann et al. (2010), and Sobkowiak et al. (2018). However, ultrasound scanning has not been extensively used for blood vessel reconstruction. There are only a few US-based CFD studies. These studies investigated haemodynamic properties in femoeral bypass grafts (McGah et al., 2011, 2012), brachial arteriovenous fistulas for haemodialysis (McGah et al., 2013, 2014), and stenosed carotid arteries (Sousa et al., 2016). All these studies assumed Newtonian blood viscosity.

McGah et al. (2013) provided additional evidence of partial restoration of wall shear stress (WSS) after fistula maturation, which contradicted with the concept of complete WSS homeostasis after maturation (Ene-Iordache et al., 2001). Their correlation of determination analysis showed that the vessel WSS were still dependent on the inflow velocity and Reynolds number when they should not if complete restoration of wall shear stress is true. Additionally, the post-maturation WSS in the venous segment was reported to be three times higher than the homeostatic values, indicating potential WSS restoration. This high WSS was further illustrated by the WSS duty factor, which represented the fraction of a cardiac cycle for which WSS rises beyond a threshold of 15

Pa (highly stressed area). The US-based FSI study by McGah et al. (2014), and other non-US based FSI studies (Perktold and Rappitsch, 1995; Bazilevs et al., 2010), suggested that the rigid vessel assumption can overestimate WSS by 20 to 50%. However, it was shown that geometrical precision is more significant than wall-distensibility, and is responsible for up to 40% deviation in WSS estimation (Lee and Steinman, 2007). Using US-based geometry, McGah et al. (2014) overpredicted arterial and venous displacement by 50% and to a factor of 5, respectively, compared to in vivo measurement. The discrepancy in displacement comparison was reported to be partially attributed to the US measurement of the reference diameters, which can vary from cycle to cycle. On the other hand, it is possible that their fluid-structure interaction model was not accurately assumed (McGah et al., 2014). To lower this ambiguity, US imaging needs to be further validated against other extensively used modalities.

There are currently a limited number of studies comparing haemodynamic properties in MRI and ultrasound-derived blood vessels. In Glor et al. (2004), the WSS parameters on the carotid bifurcations were compared across nine healthy subjects. A satisfied correlation in the time-averaged wall shear stress (TAWSS) and oscillatory shear index (OSI) was observed in most cases. However, significantly large differences in the mean WSS and OSI of approximately 50% and 25%, respectively, were also reported. The assumption of Newtonian blood viscosity may contribute to the large MRI-ultrasound difference. McGah et al. (2013) and McGah et al. (2014) compared ultrasound-derived lumen pressure and wall displacement with those obtained from Doppler-ultrasound, respectively. However, they did not compare ultrasound-derived these haemodynamic quantities with another imaging modalities that has widely been used for CFD simulations. The 3D ultrasound scans used by these two studies are also not widely available. Nevertheless, both studies and the present study compliment each other and validated the use of ultrasound images for CFD simulations in their own unique ways.

Wall and volumetric haemodynamics in MRI and US-derived models with non-Newtonian rheology in four healthy subjects have been compared in the present study. Additionally, the effects of vessel morphology on the distribution of red and white blood cells in plasma are investigated. The low and oscillating wall shear stress index (LOWSSI) is introduced and used to validate US prediction of low and oscillating WSS regions prone to intimal hyperplasia and the cause of haemodialysis failure due to stenosis.

4.3 MRI and ultrasound models

Four healthy subjects undergone MRI and ultrasound scanning at the Royal Berkshire Hospital. A total of eight 3D images reassembling each subject's right forearm were obtained in DICOM and BPM formats, respectively. All four sets of MRI images consisted of 337, 337, 350, and 391 consecutive image slices (1mm thick) in the axial direction, respectively. The time of flight for each subject is between 15 to 16 seconds. The corresponding sets of US images consisted of 1188, 1481, 1099, and 1097 consecutive image slices in the axial direction.

Different parts of the forearm vessels were chosen for each subject to compare the haemodynamic quantities in diversified cases. Figure 4.1 shows four pairs of reconstructed MRI and their corresponding ultrasound models for each subject with the proximal side at the top. The model of subject 1 is comprised of two proximal brachial veins. Blood exchange between these two vessels can be observed at two locations along its axial direction where the vessels are joined. Unlike the other three subjects, these two brachial veins are larger in diameter and thus in volume. The MRI scan of subject 2 captures a network of veins but its corresponding US scan only capture a section of the network (marked in red). This is due to the depth of these vessels. Therefore, only the identical vessel was segmented. Subject 3 is represented by a superficial vein with a bifurcation and a junction located towards inlet I1 and outlet O1, respectively. The bifurcated vessel leading to the outlet O2 is relatively short compared to the main vein. However, it cannot be mistaken

for imaging artifact since its vessel structure is clearly visible in both scans. Therefore, outlet O2 was extended by a sufficient length to prevent artificial loss in the blood flow through this outlet due to high pressure difference. This length is equal to the distance between the bifurcation and the junction. The tortuosity of the main vein due to probe movement can be observed in the ultrasound model. Subject 4 is represented by a single bifurcation, with the ultrasound model having a wider bifurcation angle. This geometrical difference, and the vessel tortuosity observed in the ultrasound model of subject 3, is often encountered as a result of using hand-held ultrasound transducer. It was found that vessel centreline curvatures and cross-sectional areas derived from ultrasound scanning did not agree well with MRI images (Glor et al., 2003, 2004).

Previous studies have investigated the effect of bifurcation angles wall shear stress (Chaichana et al., 2011). They have shown that a variation in bifurcation angle of approximately 30 degrees did not significantly affect the haemodynamic property. In the present study, the MRI-ultrasound difference in the angle of the outlet regions of subject 1 and the bifurcation angles of subject 4 is 30 and 17 degrees. Therefore, the haemodynamic differences in these two subjects are unlikely to be attributed to these deviation in geometrical aspects. Furthermore, the MRI and ultrasound models for each subject were segmented such that their volumes, inlet, and outlet diameters are identical as summarised in Table 4.1. Finally, all vessel surfaces were smoothen and triangulated in Blender to eliminate geometrical irregularities that do not exist in real blood vessels while still preserving the original lumen shape. Boundary conditions used for the present AVF study have been applied to this validation study. Blood is modelled as multiphase and non-Newtonian fluid have multiphase volume fractions, densities, and Carreau-Yasuda non-Newtonian viscosity as previously explained. Wall shear stress, wall shear stress duty factor (McGah et al., 2013), oscillatory shear index (OSI), and low and oscillating wall shear stress index (LOWSSI) have been investigated and compared among the eight models. The wall shear stress duty factor measures the porportion of a cardiac cycle for which the wall shear stress at a specific wall gridpoint exceeds a predefined threshold.

Exposure to both high and low WSS have been found to be in relation with wall remodelling and stenosis initiation (Decorato et al., 2014). Nonetheless, intimal-hyperplasia-induced stenoses have been correlate with regions of not only low but also oscillating wall shear stress (McGah et al., 2013). Thus, the LOWSSI is used to compare the risk of stenosis developmnent predicted by the MRI and ultrasound models.

Percentage differences and coefficient of correlation are used to compare MRI and ultrasound-derived flow measurements and wall haemodynamics. The Bland-Altman analysis (Bland and Altman, 1986), a well-established method in the medical statistics literature, has also been used for interpretation alongside the percentage difference. Bland-Altman plots are used to compare the differences between two techniques of clinical measurements; MRI and ultrasound.

Table 4.1: Volumes and diameters of each subject's MRI and ultrasound models. Some subjects do not have a second inlet or outlet their respective diameters are indicated by the - sign.

Geometric aspects	Units	Subject 1	Subject 2	Subject 3	Subject 4
Volume	mm^3	5,962	796	1,412	3,729
Diameter (Inlet 1)	mm	3.02	3.45	2.09	4.09
Diameter (Outlet 1)	mm	5.07	3.90	3.09	3.10
Diameter (Inlet 2)	mm	5.03	-	1.82	-
Diameter (Outlet 2)	mm	4.55	-	2.49	4.40

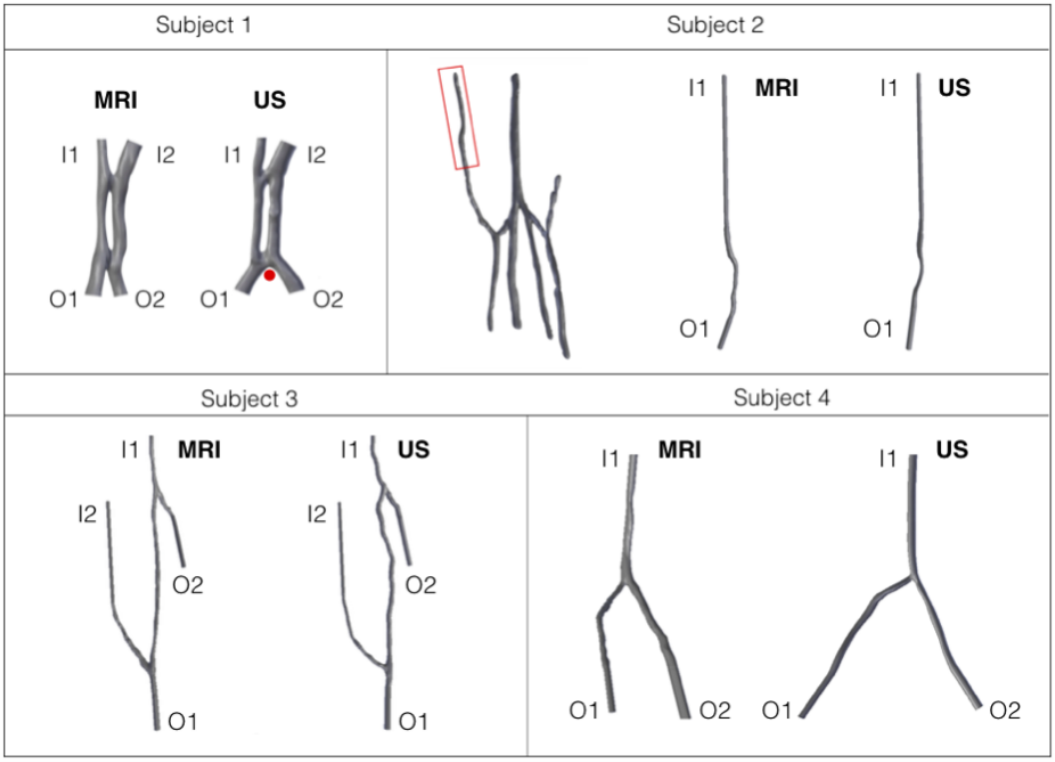

Figure 4.1: MRI and ultrasound (US) segmented vessels of all four subjects. I1 and 12 denote the inlet boundaries while O1 and O2 denote the outlet boundaries. Red point indicates location of flow split in the ultrasound model of subject 1.

4.4 MRI and ultrasound results comparison

Haemodynamic quantities between MRI and ultrasound models for all four subjects are presented in this section. Mass flow rates, WSS, OSI, LOWSSI, blood cells volume fractions and velocities are compared.

4.4.1 Mass flow rates

Volumetric flow rates predicted by the ultrasound models were compared with that predicted by MRI. The outflow from each model are affected by the upstream morphology of the respective vessels. Therefore, the outlet mass flow rates predicted by MRI and ultrasound models are compared and the percentage differences are summarised in Table 4.2. The MRI-ultrasound differences for all subjects, except for subject 1, are well below 20% indicating a good agreement between the measurement methods. Temporal variation of mass flow rates can be observed in Figure 4.2.

Table 4.2: MRI-ultrasound differences in averaged outlet mass flow rates.

% Differences	Subject 1	Subject 2	Subject 3	Subject 4
Outlet O1	39.7%	0.00%	-7.0%	9.2%
Outlet O2	53.6%	-	-18.8%	-3.9%

4.4.2 Wall shear rates

Surface-averaged wall shear stresses (SAWSS) were measured and compared in Table 4.3.

Table 4.3: MRI-ultrasound differences in the surface-averaged wall shear stress (SAWSS) averaged throughout the fourth cardiac cycle.

SAWSS (Pa)	Subject 1	Subject 2	Subject 3	Subject 4
MRI	6.61	7.04	27.24	3.84
Ultrasound	6.99	7.03	33.95	3.61
% Differences	-12.06%	2.89%	-23.15%	5.90%

a

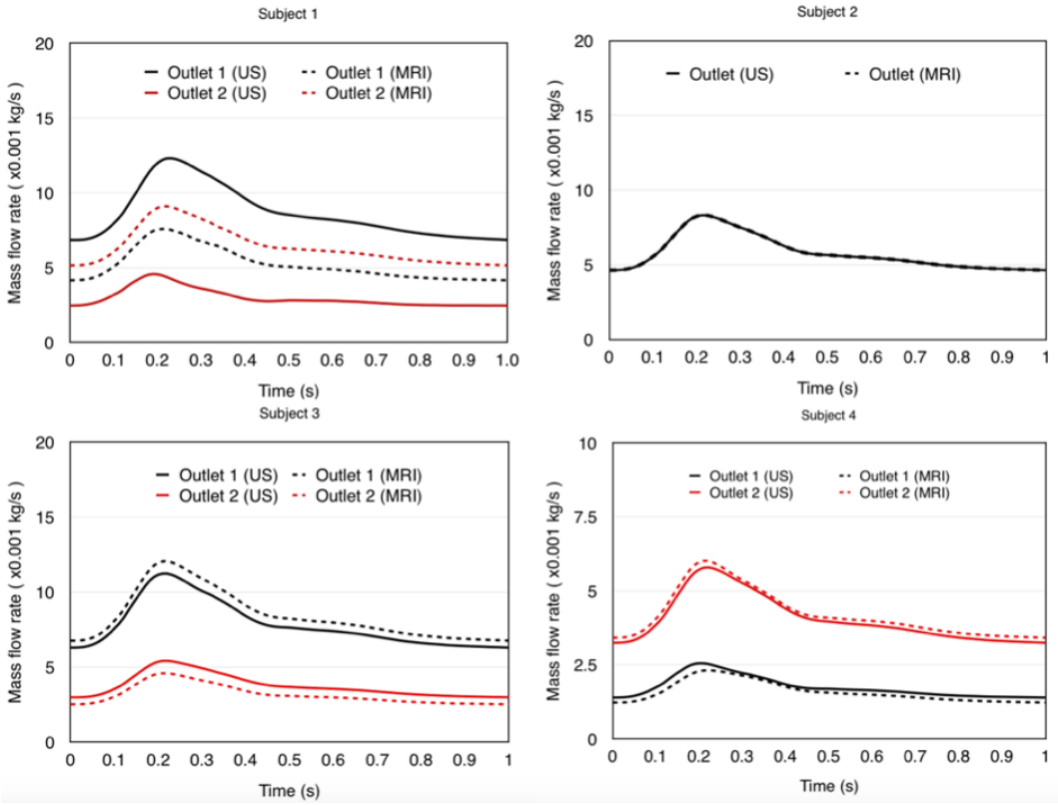

Figure 4.2: Temporal variations of outlet mass flow rate over a cardiac cycle of MRI and ultrasound models.

There are no significant MRI-ultrasound differences in all models, except for that of subject 3 where the percentage difference slightly exceeded -20%. MRI and ultrasound-derived TAWSS have been compared by contour plottings and thresholding in Glor et al. (2004). In that study, TAWSS and OSI contours presented satisfactory comparisons in most cases. Therefore, these contours are not nescessary in the present study. However, numerical comparisons against other WSS parameters, with different thresholds, are still mandatory and discussed in the present study.

4.4.3 Wall shear rates parameters

WSS-derived parameters including TAWSS, OSI, LOWSSI and WSS duty factors were calculated and sorted into different ranges according to their relation with endothelial changes as explained by Table 4.6. For the present

validation study, the threshold WSS and OSI used for calculating LOWSSI is 0.6 Pa and 0.42, respectively (Shintani et al., 2018). Table 4.7 summarises the proportions of surface area associated with different ranges of WSS parameters. The majority of the surface area corresponds to very low LOWSSI (< 0.1). TAWSS, OSI, LOWSSI, and WSS duty factors (DFs) measured by MRI and ultrasound are further compared using the Bland-Altman plots as shown in Figure 4.3.

4.4.4 Low and oscillating wall shear stress

Figure 4.4 shows the LOWSSI contours of all four subjects. The blue contours represent regions with TAWSS at least ten times higher than the threshold WSS (LOWSSI > 0.10). On the other hand, contours representing LOWSSI values of 1.0 and higher only occupy a very small surface area, and is therefore not explicitly shown in Table 4.7. For each gridpoint in the identified region of LOWSS (LOWSSI > 1.0), the temporal variations of wall shear stress vectors parallel to the flow direction are investigated.

Table 4.4: WSS, TAWSS, and OSI thresholds associated with different endothelial changes. IH denotes intimal hyperplasia

Endothelial changes	TAWSS / OSI	References
Healthy ranges	1.0 < WSS < 2.3 Pa	Kamiya et al. (1984)
Atheroprotective	WSS > 1.5 Pa	Malek et al. (1999)
Haemodialysis safe	15 < WSS < 20 Pa	McGah et al. (2013)
IH due to high WSS	WSS > 20 Pa	McGah et al. (2013)
IH due to low WSS	WSS < 1.0 Pa	Ene-Iordache and Remuzzi (2012)
Atherogenesis	WSS < 0.4 Pa	Malek et al. (1999)
High WSS	WSS > 7.0 Pa	Ene-Iordache and Remuzzi (2012)
Low WSS	TAWSS < 0.6 Pa	Shintani et al. (2018)
Wall rupture	OSI > 0.0125	Miura et al. (2013)

4.4.5 Directional wall shear stress

The surface averaged directional WSS (DWSS) in LOWSS and healthy (LOWSS ¡ 1.0) regions were plotted against time for subject 1 and 2 as shown in Figures 4.5 and 4.6, respectively. These two subjects were chosen because their LOWSS regions, comprising of WSS vectors parallel to local flow directions, are significantly larger than that of the other two subjects. The time instant at which zero and local extremes of directional wall shear stresses are observed are compared between MRI and ultrasound, as shown in Figure 9. Additionally, the normalised and averaged waveform of directional WSS from subjects 1 and 2 is compared with that found in reciprocating flow regions of (Franzoni et al., 2016).

4.4.6 Volume fractions and velocities of red and white blood cells

The capability of ultrasound-derived models in predicting volumetric haemodynamic quantities are further validated with blood cells transport taken in consideration. The volume fractions of red (erythrocytes) and white (leukocytes) blood cells in plasma measured by MRI and ultrasound are compared. and summarised in Table 4.6. Hematocrit (hct) variations throughout a cardiac cycle are shown in Figure 4.7. Hematocrit is the volume fraction of erythrocytes suspended in the blood vessel while discharge hematocrit (hct_D) represents the volume fraction of red blood cells leaving through the outlets (Pozrikidis and Davis, 2013). Discharge hematocrit is determined by multiplying the hematocrit with the ratio of erythrocyte velocity and the mean blood flow velocity. The averaged velocity of the erythrocyte and leukocyte phases, in the region where their local volume fractions are equal to the prescribed value, are compared. The MRI-ultrasound differences in the averaged blood cells velocities are summarised in Table 4.7. Temporal variations of the blood cells velocities predicted by MRI and ultrasound models are compared in Figure 4.8.

Table 4.5: Percentage of surface area associated with each range of TAWSS, OSI, LOWSSI, WSS duty factors (DF) measured by MRI and ultrasound

TAWSS (Pa)

Ranges	MRI1	US1	MRI2	US2	MRI3	US3	MRI4	US4
0-1	9.61	7.36	3.16	13.15	1.92	1.57	12.55	4.71
1-7	57.70	56.48	60.80	46.35	23.35	25.79	76.25	88.66
7-15	24.46	25.14	26.37	29.95	23.18	26.21	9.80	5.46
15-20	4.35	5.39	6.12	7.73	8.60	5.48	1.15	0.60
20-max	3.85	5.60	3.52	2.79	42.92	40.93	0.23	0.54

OSI

0-0.0125	86.73	91.79	97.41	91.53	94.54	90.29	92.68	98.92
0.0125-0.2	11.88	7.56	2.50	6.77	4.87	8.41	6.21	0.94
0.2-0.4	1.27	0.55	26.37	0.08	1.51	0.50	1.00	0.11
0.4-0.42	0.03	0.02	6.12	0.07	0.06	0.02	0.04	0.04
0.42-0.5	0.07	0.05	3.52	0.03	0.11	0.04	0.04	0.08

LOWSSI

0-0.2	96.96	98.36	99.24	94.23	99.53	99.40	95.78	99.16
0.2-0.4	1.78	1.05	0.70	3.43	0.30	0.37	2.65	0.64
0.4-0.6	0.72	0.22	0.02	1.38	0.07	0.10	0.92	0.10
0.6-0.8	0.24	0.10	0.01	0.40	0.03	0.04	0.23	0.03
0.8-1.0	0.28	0.24	0.00	0.54	0.04	0.06	0.40	0.05

DF1 (for WSS below 1.0 Pa)

0-0.2	7.07	5.58	2.88	10.88	1.07	1.16	9.39	3.69
0.2-0.4	3.84	3.18	0.45	2.65	1.14	0.71	4.07	1.36
0.4-0.6	2.17	1.27	0.21	0.74	0.65	0.35	1.32	0.64
0.6-0.8	2.60	1.59	0.38	0.96	1.44	0.56	1.60	0.94
0.8-1.0	84.30	88.36	94.06	84.74	95.68	97.19	83.60	93.35

DF2 (for WSS above 20 Pa)

0-0.2	92.50	89.99	90.80	90.64	50.00	54.75	98.91	98.86
0.2-0.4	4.40	5.48	6.23	7.46	9.05	6.21	0.90	0.62
0.4-0.6	1.60	1.33	0.81	0.92	3.30	2.33	0.05	0.10
0.6-0.8	0.85	1.32	0.76	0.69	4.04	3.19	0.04	0.13
0.8-1.0	0.63	1.85	1.37	0.27	33.59	33.49	0.08	0.26

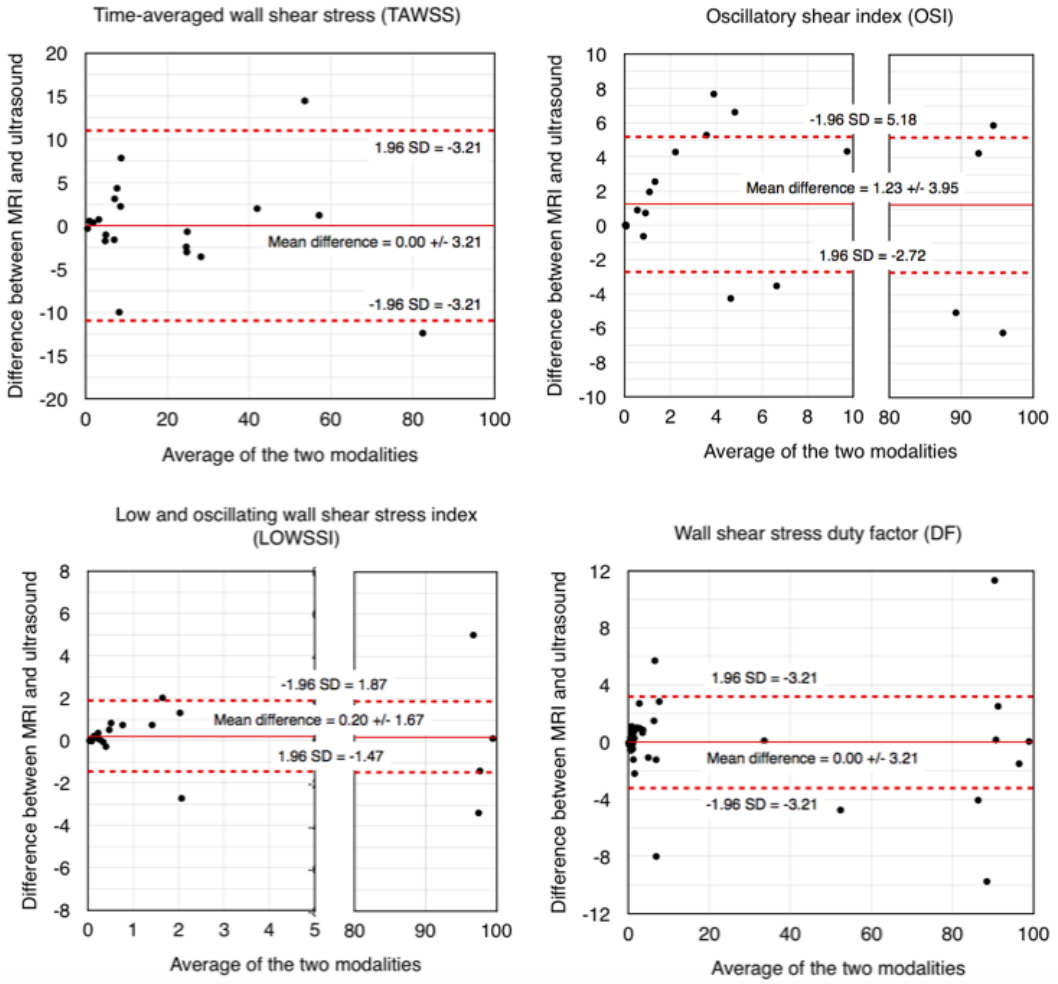

Figure 4.3: Bland-Altman plots comparing MRI and ultrasound measurements of the percentage areas associated with different ranges of TAWSS, OSI, LOWSSI and WSS duty factors in four subjects.

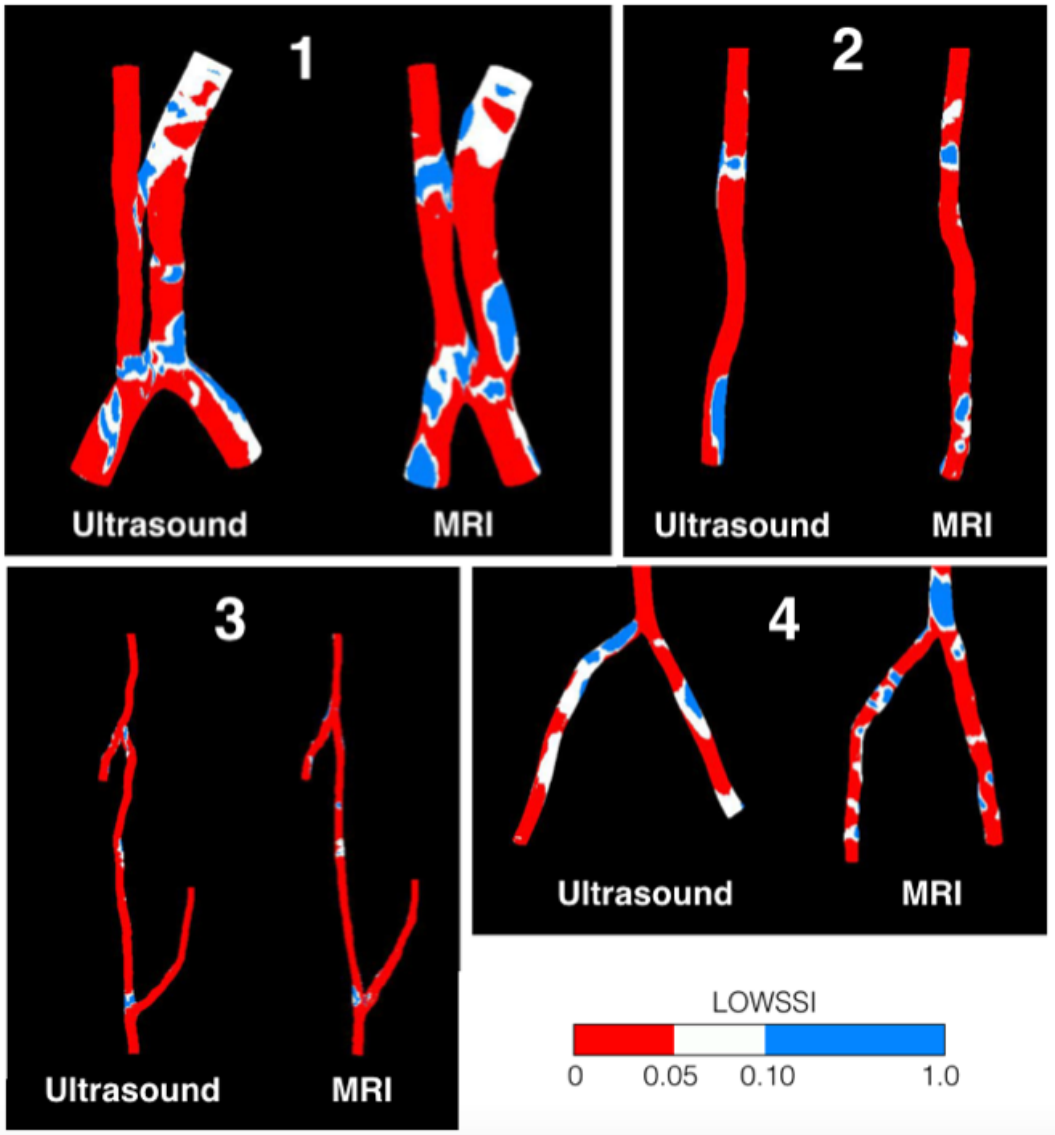

Figure 4.4: Low and oscillating wall shear stress index (LOWSSI) contours mapped on the MRI and ultrasound models of all four subjects. Numbers 1 to 4 indicate subjects 1 to 4, respectively.

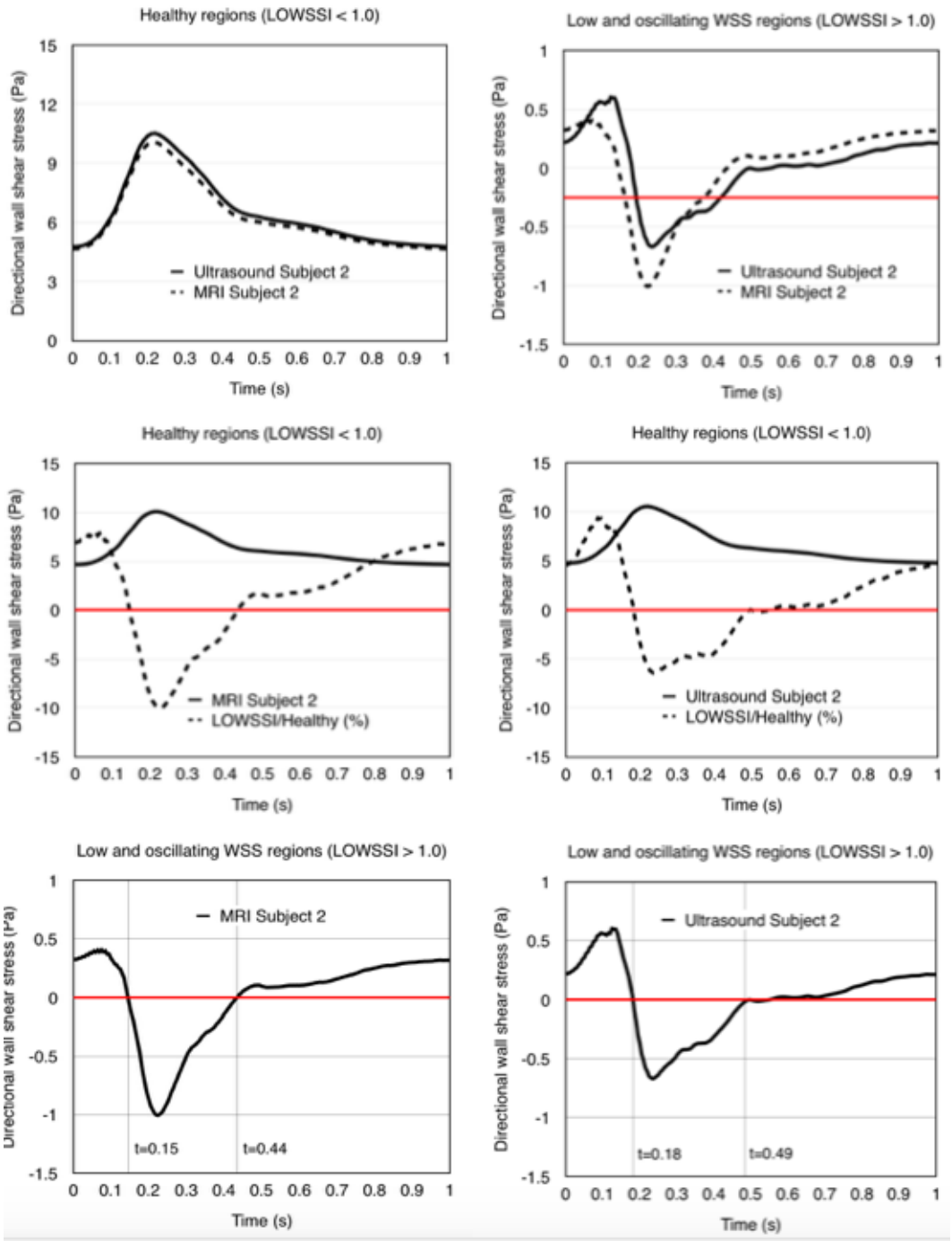

Figure 4.5: Temporal variations of surface-averaged DWSS in LOWSS, healthy regions of subject 2 and the time taken for DWSS to initiate oscillation as predicted by MRI and ultrasound.

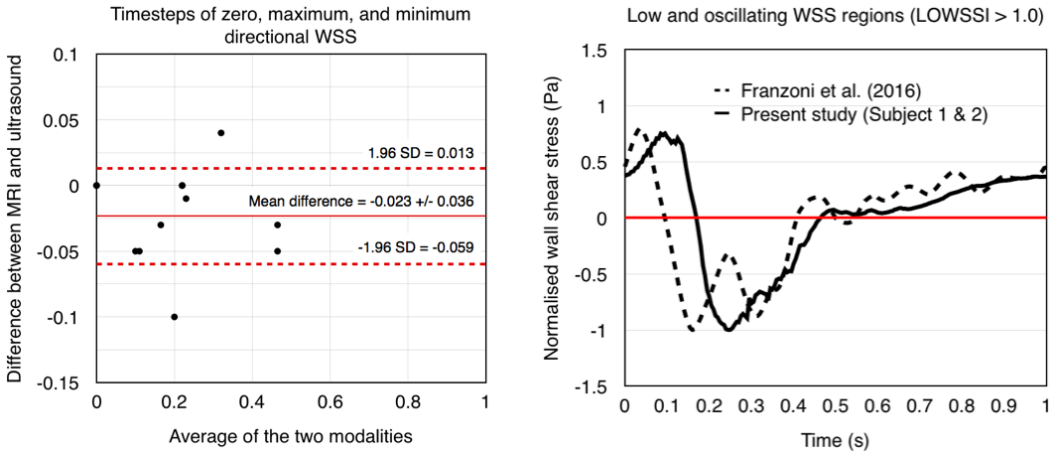

Figure 4.6: Bland-Altman plot comparing the timestep associated with zero and extreme DWSSs and the temporal variations of averaged DWSSs of subject 1 and 2 and Franzoni et al. (2016)

Table 4.6: MRI-ultrasound differences in the haematocrit (hct), discharged haematocrit (hct_D), and leukocyte volume fraction (ϵ_{WBC})

% Differences	Subject 1	Subject 2	Subject 3	Subject 4
hct	0.61%	0.90%	0.00%	0.02%
hct_D	5.92%	-1.55%	0.02%	0.01%
ϵ_{WBC}	1.56%	-0.26%	-0.63%	-2.03%

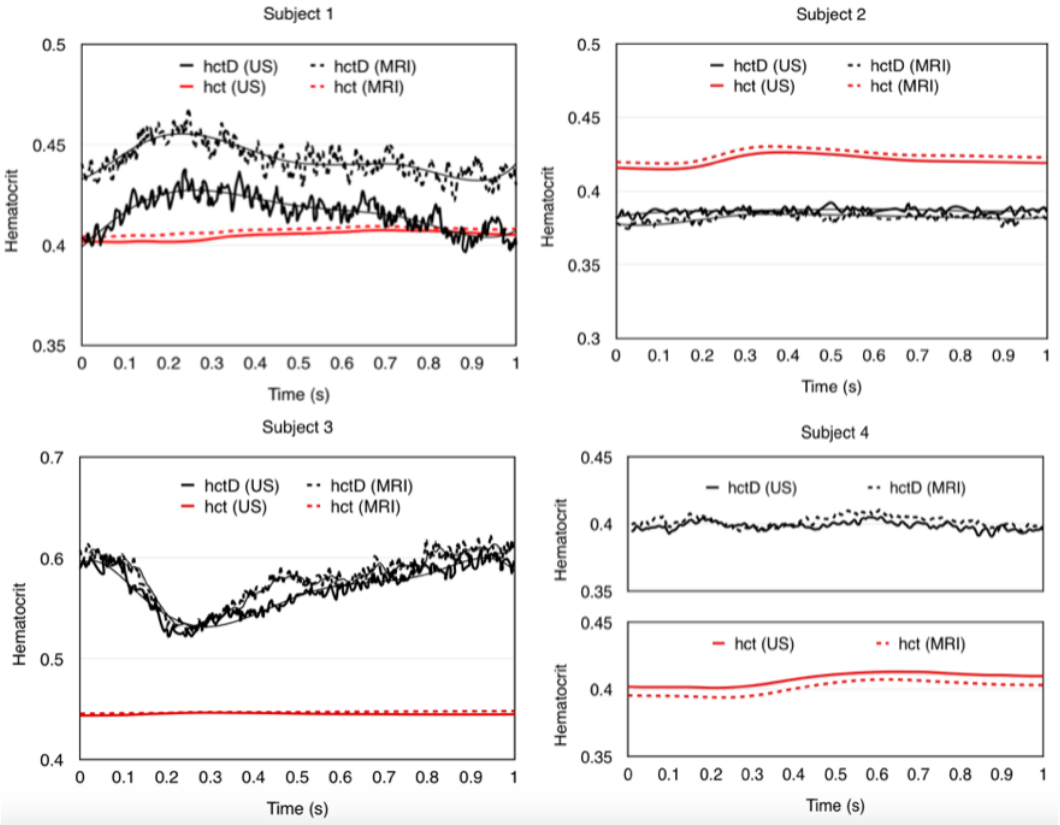

Figure 4.7: Comparison of hematocrit variations in a cardiac cycle between MRI and ultrasound.

Table 4.7: MRI-ultrasound differences in averaged velocity of erythrocytes and leukocytes.

% Differences	Subject 1	Subject 2	Subject 3	Subject 4
v_{RBC}	3.57%	-1.03%	-3.78%	2.91%
v_{WBC}	4.48%	-0.58%	-4.14%	1.52%

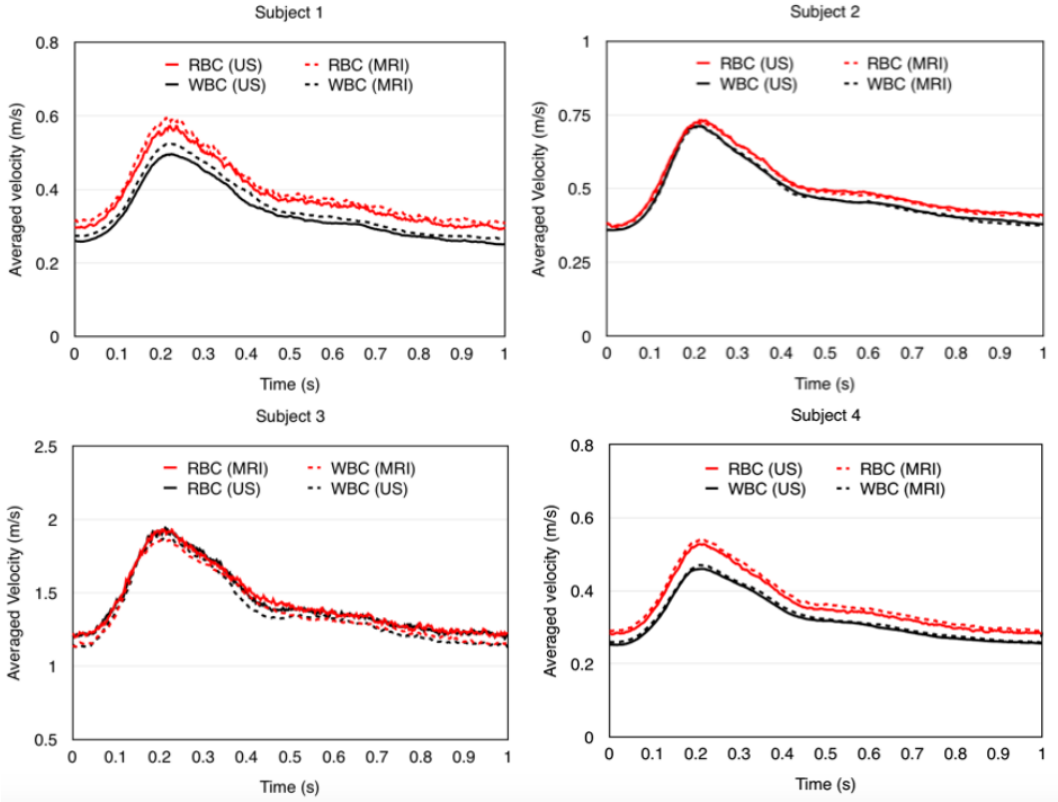

Figure 4.8: Comparison of blood cells velocity in a cardiac cycle between MRI and ultrasound

4.5 Discussion

Previous computational flow studies have rarely used ultrasound images despite their portability, affordability, and harmlessness. This is due to the moderate loss of vessel curvature and excessive imaging artifacts involved. However, this study showed that different ultrasound-derived haemodynamics were not significantly different from those derived from MRI.

Mass flow rates: Mass flow rates and their temporal variations derived from MRI and ultrasound, as shown in Table 4 and Figure 3, compared well in all four subjects, except for subject 1. This larger differences observed in subject 1 are attributed to the geometrical complications that led to flow diversion and impingement near the outlets (red point in Figure 1) of the ultrasound model. Flow impingement caused part of the I2 inflow to divert and leave the domain through outlet O1 instead of O2. As a result, approximately 45% and 74% of the total inflow left the domain through outlet O1 in the MRI and ultrasound models, respectively. However, previous studies have found a significantly larger MRI-Doppler ultrasound differences in volumetric flow rate using of up to 102% (Maier et al. 2018) and 115% (Nienmann et al. 2012). Despite this differences, the outlet flow rates predicted by the present ultrasound models are still in fair agreement with MRI (r2 = 97.7% and 87.4%). This suggests that ultrasound-based simulations can effectively predict the mass flow rate and its clinical implications such as the potentiality of successful haemodialysis.

Wall shear stresses: Differences in SAWSS predicted by all ultrasound and MRI models (Tables 5) are well below 20%, except for subject 3 where the difference reached approximately -25%. This is also reflected by the temporal variations of SAWSS in Figure 4. In most subjects, the largest SAWSS differences are observed near peak systole while the lowest difference are observed towards the end diastole. Like that of mass flow rates, overestimations of WSS by both MRI and ultrasound models are found to be independent of vessel morphology and the existence of bifurcation. In Glor et al. (2004), all eight subjects with bifurcation also presented both large and small MRI-Ultrasound

differences in spatial distributions of TAWSS. Low WSS have been correlated with atherogenic phenotype stimulation of endothelial cells (Wasserman and Topper, 2004) and thus atherosclerosis (Chaichana et al., 2011). High WSS, on the other hand, is known to cause endothelial degradation (Nakatani et al., 1991) and outward wall remodelling to maintain WSS homeostasis (McGah et al., 2014). Therefore, in this study, WSS between 1 to 7 Pa is considered healthy. Wall shear stresses below and beyond this range are interpreted according to Table 6. Percentages of surface area associated with different ranges of all four WSS parameters (Table 7) predicted by MRI and ultrasound models are in good agreement ($r2 > 0.95$). The lowest MRI-ultrasound correlation ($r2 = 0.92$) is observed in the TAWSS range of 0-7 Pa in subject 2, which is still regarded as moderate correlation (McGah et al., 2013). Bland-Altman plots in Figure 5 reveal that there is no systematic bias in the ultrasound estimation of TAWSS by both modalities. Two outliers beyond the control limits of 1.96 SD from the mean difference correspond low TAWSS in subjects 2 and 4. These outliers are found only in subjects 2 and 4. This suggests that their ultrasound models are more suitable for predicting haemodialysis patency and intimal hyperplasia due to high WSS. Two-tailed tests concluded that MRI and ultrasound predictions are statistically significant ($p < 0.05$). This indicates a strong evidence supporting the alternative hypothesis that there is a statistically significant relationship between the percentage area associated with different WSS parameters based on MRI and ultrasound.

Near-wall flow oscillations: Like TAWSS (1-7 Pa), the majority of surface areas in all four subjects are exposed to very low near-wall oscillations ($0.0 < OSI < 0.0125$). No more than 2% of the wall surface area experience high flow oscillation ($OSI > 0.42$). This is also reflected by the low LOWSSI values ($LOWSSI < 0.1$) in most regions, as shown in Table 7. These ranges of values are expected as they are typical for healthy blood vessels. In the Bland-Altman plot for OSI, outliers are mostly originated from moderate WSS oscillations ($0.0 < OSI < 0.42$) in subject 2. However, regions of high WSS oscillation ($OSI > 0.42$) (Shintani et al., 2018) can be reproduced by ultrasound images, with good agreements with MRI, for all subjects suggesting that ultrasound models are able to predict smooth muscle cells proliferation and thus intimal

hyperplasia due to oscillatory WSS (Franzoni et al., 2016). Subjects 1 and 3 are preferrable for prediction

Low and oscillating WSS: Regions of LOWSS and healthy endothelial cells are identified by the LOWSSI contours in Figure 6. In every subjects, the majority (over 99%) of the wall surfaces are not exposed to LOWSS (LOWSSI < 1.0), indicating very low possibility of intimal-hyperplasia. Therefore, the scale of the contour is bounded by 0.1, instead of 1.0 (or higher) as would have been for unhealthy cases. MRI and ultrasound predictions of the locations of non-LOWSS regions ($0.0 <$ LOWSSI < 1.0) in all subjects are in good agreement. Higher LOWSSI are mostly found immediately downstream of the bifurcations. In subject 4, LOWSS region upstream of the MRI bifurcation correspond to flow impingment after blood enters the bifurcation through a curved vessel. This vessel curvature was not fully captured during ultrasound scanning and therefore led to the underestimation of LOWSS upstream of the ultrasound bifurcation. The standard deviation from the mean LOWSSI differences was the least among all four parameters as shown by the Bland-Altman plot. Outliers correspond to low LOWSSI values in subjects 2 and 4. Nevertheless, like TAWSS, ultrasound estimation of LOWSSI was not systematically biased. Subject 3 is most preferable for the prediction of LOWSS and thus endothelial cell activation (Davies et al., 2013).

WSS duty factor: Among the four wall shear stress parameters, WSS duty factor ($0.8 <$ DF < 1.0) comparisons for WSS above 1 Pa produced the most outliers. This was observed in all subjects except for subject 3. On the other hand, only one outlier was found to be corresponding to a duty factor with a higher threshold of 20 Pa (representing risk of intimal hyperplasia due to high WSS). This may suggest that ultrasound imaging is more capable of predicting the fraction of cardiac cycle for which the vessel wall experiences high WSS and the consequent IH. The two thresholds of 1 and 20 Pa were chosen for the calculation of WSS duty factor because they represent the typical low and high WSS bounds, respectively. In all four subjects, the majority (above 80%) of the endothelial cells on the wall experiences WSS higher than 1 Pa for at least 80% of the cardiac cycle. On the contrary, no more than

2% of the wall surface area experiences WSS higher than 20 Pa for 80% of the cardiac cycle (in most subjects). This suggests that the endothelial cells experience a normal level of WSS, not too high nor too low, for the majority of the time as would be observed in healthy blood vessels.

Directional WSS variations: MRI and ultrasound predictions of directional WSS over time compare well in healthy regions and follow the temporal variation of the inlet mass flow rate profile as shown in Figure 7 and 8. In LOWSS regions, directional WSS waveforms are found to oscillate around 0 Pa as expected. The ultrasound models slightly overestimate the time taken for the averaged WSS vector to initiate the oscillations and the occurence of directional WSS extremums. However, the Bland-Altman analysis presented in Figure 9 shows that the majority of these differences are within acceptable bounds. The ultrasound-derived directional WSS waveform in LOWSS regions are found to have less fluctuations at peak systole compared to that of MRI. The WSS oscillations in both subjects 1 and 2 did not exceed 1 Pa, which is also expected in LOWSS regions. Moreover, the normalised directional WSS waveform from (Franzoni et al., 2016) and that of subjects 1 and 2 shared a common variation in time.

Blood cells distributions: Hematocrit is the volume fraction of erythrocytes suspended in the blood vessel while discharge hematocrit represents the volume fraction of red blood cells leaving through the outlets (Pozrikidis and Davis, 2013). Discharge hematocrit is determined by multiplying the hematocrit with the ratio of erythrocyte velocity and the mean blood flow velocity. Overall, the temporal variations of discharge hematocrit varies directly and inversely with that of mass flow rate (and thus SAWSS) for subjects 1 and 3, respectively. In the other two subjects, discharge hematocrit is rather constant throughout the cardiac cycle. This suggests that the risk of red blood cells adhesion may be independent of the temporal variations of WSS and mass flow rate. Instead, it is more likely to be dependent on local flow oscillations resulting from geometrical complications like those presented in subjects 1 and 3.

Towards the end diastole, the discharge hematocrit predicted by ultra-

sound models of subjects 1 and 4 becomes lower than the hematocrit for a short period of time. This means that the red blood cell velocity is lower than that of the mean blood flow during these periods. MRI-ultrasound difference in the hematocrit, leukocyte volume fraction and blood cells velocities are well below 5% in all subjects. Additionally, the erythrocyte and leukocyte velocities vary directly with the mass flow rate for all subjects. The erythrocyte velocity is generally higher than that of the leukocytes in all subjects, as expected in a normal subject. The blood cells, and also the mean blood flow, velocities in subject 3 is approximately twice higher than that of other subjects because of its smaller diameters in most regions along its long axial length.

4.6 Conclusion

Different haemodynamics derived from both MRI and ultrasound imaging have been measured and compared in four healthy subjects. The present study demonstrated the capability of ultrasound-based models in predicting temporal variations in the mass flow rate, wall shear stress parameters, and the distributions of multiphase blood cells concentration. Difference in the WSS estimations of both modalities are found to be independent of vessel morphology and, like the estimations of LOWSSI, produced no systematic bias. Additionally, the low and oscillatory wall shear stress index (LOWSSI) have proven to be useful not only in identifying LOWSS regions, but also the required increase in TAWSS to prevent LOWSS. In this case where all subjects are known to be healthy, the LOWSSI indicates the very low potential of LOWSS in these subjects. The good agreements between MRI and ultrasound measurements of these haemodynamic quantities also reflect the ability of ultrasound-based CFD in predicting intimal hyperplasia due to high wall shear stress and haemodialysis patency.

Chapter 5

Independence Studies

The sensitivity of the present results to the grid resolution and temporal discretisation have been tested. The number of elements and the timestep size used in both the aneurysm and AVF studies are justified by the independence studies presented in this chapter. The accuracy of CFD results is significantly affected by the choices of mesh and temporal resolutions. Therefore, suitable nuber of elements and timestep sizes need to be determined. The use of prism layers for wall refinement in both studies are also discussed.

Mesh generation

Multiple meshes with different grid densities were created for both aneurysm and AVF studies to find the optimal number of elements. In the aneurysm study, an unstructured polyhedal (Otani et al., 2017a) mesh was constructed with maximum element sizes of 0.137 mm, which is smaller than the ideal mesh size of 0.3 (Lee et al., 2013) and approximately 0.25 mm (Morales et al., 2013a; Otani et al., 2017b; Vali et al., 2017) previously used. Volumetric control was applied in the aneurysm sac and its bifurcation anastomosis in order to maintain element sizes of approximately 0.0397 mm and 0.0643 mm, respectively. These element sizes are in similar range (Otani et al., 2018) or even smaller (Morales et al., 2013a,b) than values used in previous studies.

For the AVF study, a polyhedral volumetric mesh (Grechy et al., 2017) was constructed with volumetric controls as it was reported to have a higher precision than that of tetrahedral meshes (McGah et al., 2014) and were used for several AVF models which required high accuracy computation of wall shear stress (Robbin et al., 2016). Volumetric control was applied at the anastomosis (Iori et al., 2015) to produce a maximum element size of 0.056 mm in anastomotic regions and sharp bends (i.e. sutures at both ends of the anastomosis and the sharp bend in the venous segment), and 0.075 mm elsewhere. These element sizes are finer than previous AVF studies (Ene-Iordache et al., 2001; Kharboutly et al., 2010; McGah et al., 2013; Iori et al., 2015; Pike et al., 2017b) and is in typical range as suggested by other studies (Bozzetto et al., 2015). Two prism layers (Ene-Iordache et al., 2015; Bozzetto et al., 2015) with thickness equal to 20% of the base size (Otani et al., 2018) were used for both the aneurysm and AVF models.

Grid independence tests

Although the mesh resolution used in the present aneurysm study is finer than those used in previous studies, grid independence tests were however performed to confirm result convergency in the case of 5 coils (packing density 21.67%). Three different grid densities corresponding to 4, 6, and 8 million elements were investigated. The aneurysm model filled with 5 coils was chosen for this test because aneurysmal flow reduction and oscillation can still be observed due to slightly insufficient coiling (Otani et al., 2017b). Seven cross-sectional planes parallel to the ostium plane were created. These planes are evenly spaced inside the coiled aneurysm. The plane-averaged velocity magnitude in each of the seven parallel planes was monitored during the fourth cardiac cycle as shown in Figure 5.1a. Seven sets of lines can be seen and each represents the plane-averaged velocity magnitude of each parallel planes 1-7. The difference between the plane-averaged velocity magnitude derived from the three meshes of 4, 6, and 8 million elements are almost identical. Therefore the three lines (with different colours representing each mesh density) in each sets of lines are very close to one another. However, the mesh

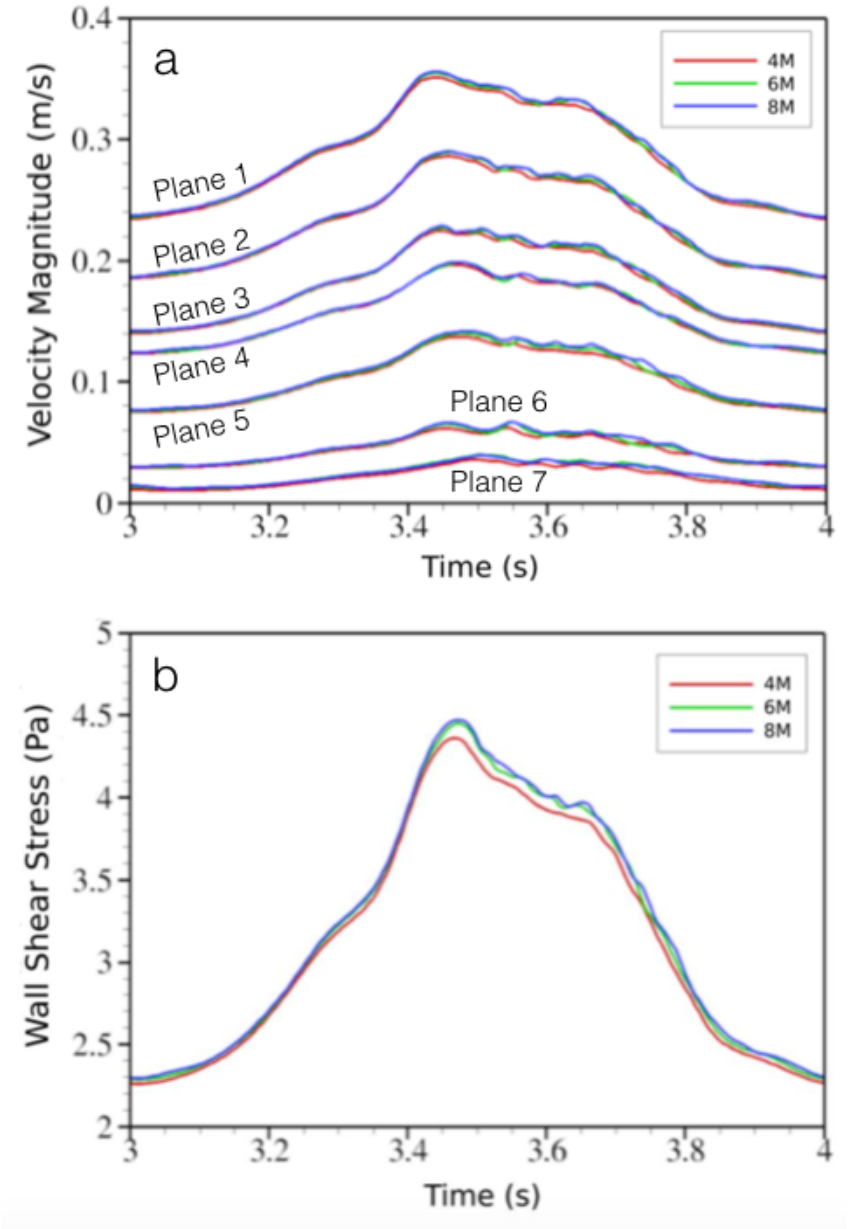

Figure 5.1: Temporal variations of (a) plane-averaged aneurysmal velocity magnitude at seven different planes 1-7 aligned parallel to the ostium plane and (b) surface-averaged WSS on the aneurysm wall for three mesh densities: 4, 6, and 8 million elements. Each mesh consisting of 4 (red), 6 (green), and 8 (blue) million elements are denoted as 4M, 6M , and 8M, respectively, during the fourth cardiac cycle. (1 seconds per 1 cardiac cycle)

with 6 million elements is found to provide a grid-independent aneurysmal velocity magnitudes. The variations of surface-averaged WSS (SAWSS) on the aneurysm wall for all three grid densities are shown in Figure 5.1b. It is again evident that the grid density of 6 million elements provides an aneurysmal wall shear stress that is sufficiently independent of further mesh refinement. Other coiled aneurysm studies (Morales et al., 2011; Otani et al., 2016, 2017a, 2018) did not explicitly report their number of elements.

The differences between the three grid densities are shown in more detail by Figure 5.2a-c. On the ostium plane (Figure 5.2a), the differences in the plane-averaged velocity magnitude between 4M-6M elements and 6M-8M elements were contained within a 1% threshold for 94% and 84% of the time in a cardiac cycle, respectively. This threshold is smaller than 5% (Morales et al., 2011) and 3% (Sharzehee et al., 2018; Otani et al., 2017b; Rayz et al., 2010, 2015) used in all previous aneurysm studies. The flow towards the mid plane (parallel to ostium) of the aneurysm was found to be less stable (Figure 5.2b) as shown by the high standard deviation. However, during the whole cardiac cycle, the difference in the mid-plane averaged velocity between 6M and 8M meshes was within a threshold difference of 5% (Morales et al., 2011). The velocity differences in the ostium plane (Figure 5.2a) and mid-plane (Figure 5.2b) between 4M-6M meshes are not significantly different to that of the 6M-8M meshes. This is also shown by the small difference between the standard deviation (S.D.) of 4M-6M grid and 6M-8M grid. The difference in SAWSS (Morales et al., 2011; Sharzehee et al., 2018) between 6M and 8M elements was maintained below 2%, lower than most studies (Rayz et al., 2010; Morales et al., 2011), for the whole cardiac cycle as shown by Figure 5.3. This difference is significantly smaller than that observed between 4M and 6M elements and resulted in the smallest mean difference among all the three parameters tested. More importantly, the differences between the 6M and 8M meshes for all parameters tested were within acceptable range used by Morales et al. (2011), the only study that previously reported a similar or higher threshold. The number of elements used in the present aneurysm study (6 million), and up to 6.5 million elements in aneurysms

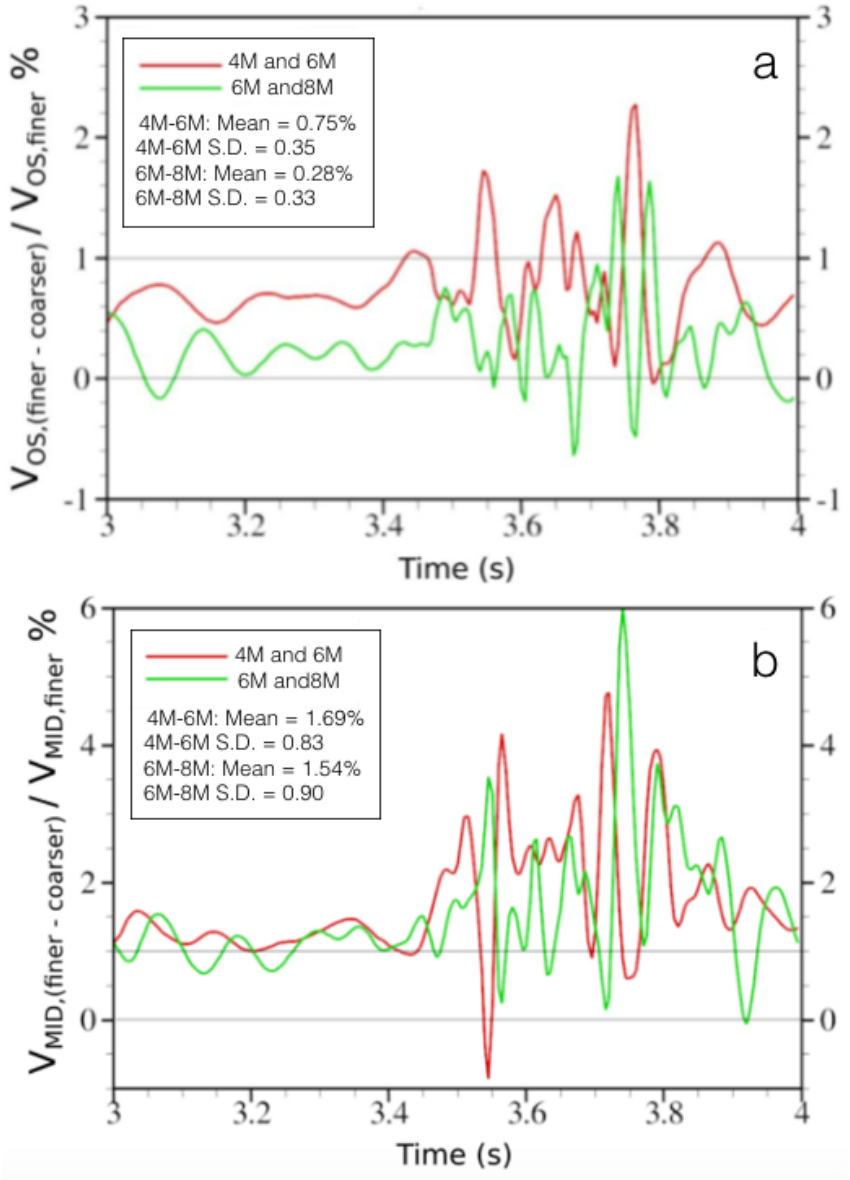

Figure 5.2: Temporal variations of the percentage differences in the plane-averaged velocity magnitude at the (a) ostium-plane and (b) plane 4 between 4 and 6 million elements mesh (red) and 6 and 8 million elements (green) mesh during the fourth cardiac cycle. (1 seconds per 1 cardiac cycle)

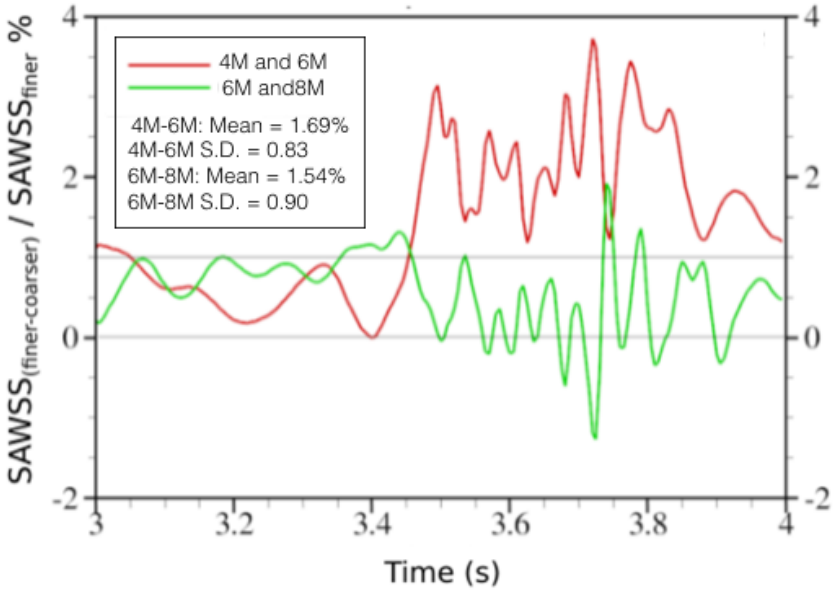

Figure 5.3: Temporal variations of the percentage differences in the surface averaged WSS between 4 and 6 million elements mesh (red) and 6 and 8 million elements (green) mesh during the fourth cardiac cycle. (1 seconds per 1 cardiac cycle)

with higher packing densities, is significantly higher compared to Vali et al. (2017); Rayz et al. (2015) and is in the same range as Morales et al. (2013a,b); Otani et al. (2017b). Although not explicitly reported, the recalculated grid densities based on image voxel sizes used in the rest of the aneurysm studies (Otani et al., 2016, 2018) were reported to be higher than 6 million, if not unknown (Morales et al., 2011; Otani et al., 2017a).

Since the volume difference between the untreated aneurysm (Volume of 1351 mm^3) and the AVF (Volume of 1413 mm^3) models is significantly small (0.07%), the same number of elements used in the aneurysm study could also be assumed for the AVF study. However, the AVF model is associated with more surface non-uniformity and sharp bends which may promote flow oscillation that could have been underestimated. Therefore, a separate study for an appropriate mesh was performed for the AVF study. The AVF geometry with bifurcation was used for the independence test to represent a scenario with extreme flow instability. The changes in velocity magnitudes (Grechy et al., 2017) during the fourth cycle at different sites that are prone to unstable

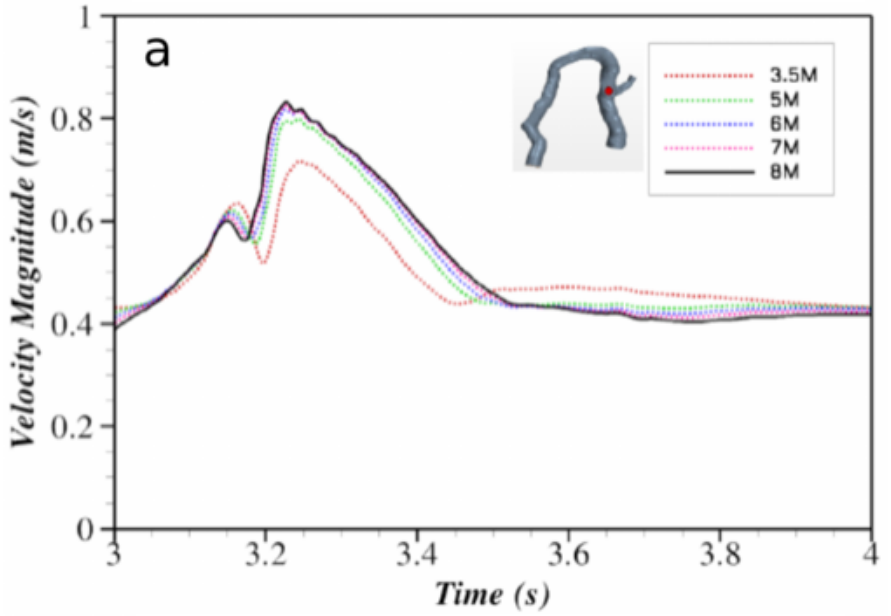
a
3.5M
5M
6M
7M
8M
Velocity Magnitude (m/s)
Time (s)
0
0.2
0.4
0.6
0.8
1
3
3.2
3.4
3.6
3.8
4

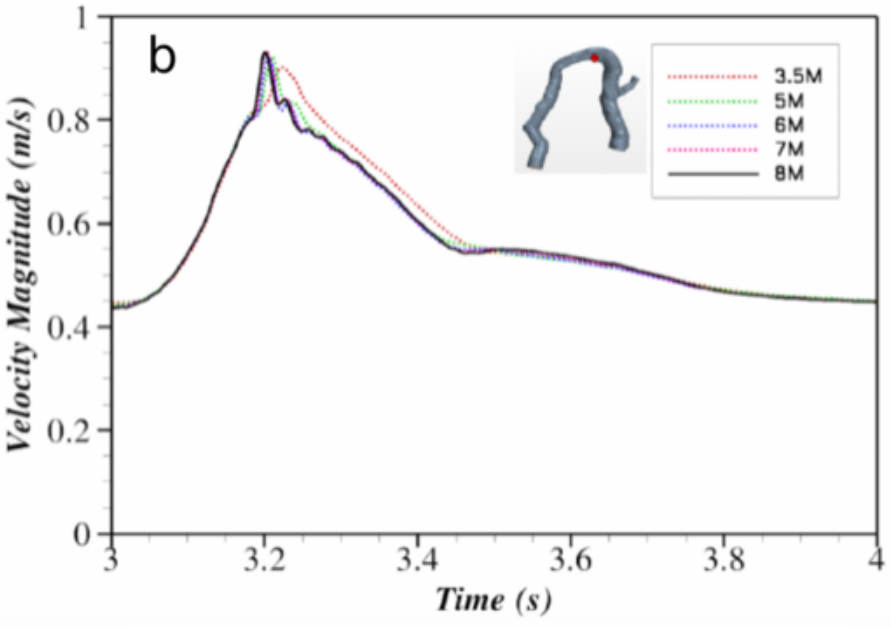
b
3.5M
5M
6M
7M
8M
Velocity Magnitude (m/s)
Time (s)
0
0.2
0.4
0.6
0.8
1
3
3.2
3.4
3.6
3.8
4

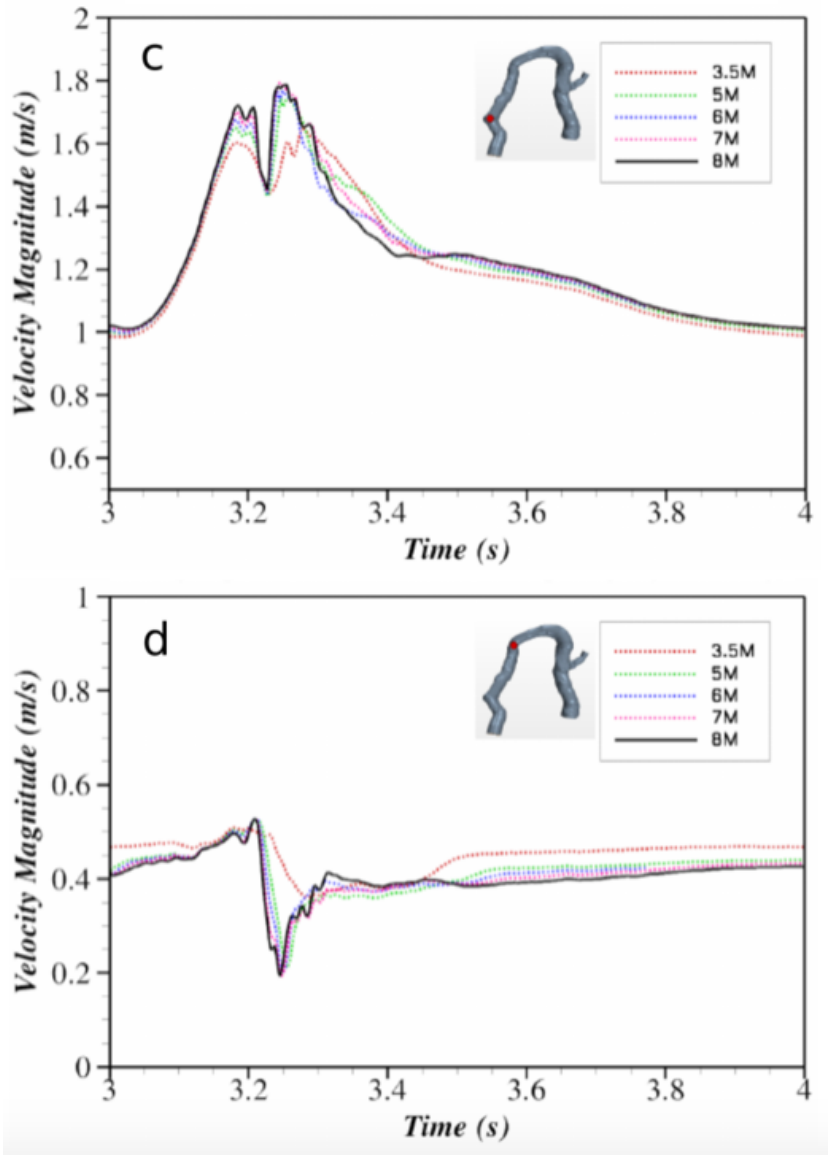

Figure 5.4: Temporal variations of velocity magnitude during the fouth cardiac cycle at (a) arterial bifurcation, (b) inner wall of the fistula entry, (c) venous bend, and (d) venous-fistula anastomosis with different grid densities of 3.5 million (red), 5 million (green), 6 million (blue), 7 million (purple), and 8 million (black) elements. (1 second per 1 cardiac cycle)

flows and vascular access failure (Ene-Iordache and Remuzzi, 2017) were used. These sites include the arterial bifurcation, the inner wall of the fistula, and the sharp bend in the vein (Caroli et al., 2013). Unlike the independence test of the aneurysm, spatially averaged data was not used for the AVF test because flow oscillations in the AVF model are expected to be higher. Five grid densities of 3.5, 5, 6, 7, and 8 million elements were investigated. Figure 5.4 shows the velocity magnitude variations at the four locations. It is evident that velocity magnitudes reach convergence at 6 million (6M) elements with approximately 1-5% difference (Ene-Iordache et al., 2015) in velocity magnitude.

Timestep size independence tests

Investigation of timestep size convergence has not been reported in any coiled aneurysm (and most untreated aneurysm) studies so far. This may be due to limited computational power or time. In the present aneurysm study, three timestep sizes (10, 5, and 2 ms/step) were tested using the grid independent mesh. It is evident from Figure 5.5 that both the spatial averaged WSS and plane-averaged velocity magnitude over the fourth cardiac cycle are converged at 5 ms/step. Therefore the timestep size of 5 ms/step was used (Torii et al., 2010; Morales et al., 2013b,a). A significantly coarser timestep size of 40 ms/step (Rayz et al., 2010; Otani et al., 2016) and 10 ms/step (Vali et al., 2017; Jahed et al., 2018) was used in previous studies, even at steady state (Otani et al., 2016). Timestep size independence tests were also performed for the AVF study. Only two previous studies (Kharboutly et al., 2007; Pike et al., 2017b) have conducted such tests for AVF models. The change in velocity magnitude over the fourth cycle at the same monitoring locations on the AVF on the grid independent mesh (Pike et al., 2017b) was investigated. Four timestep sizes of 20, 2.5, 1.25, and 0.5 ms/step were investigated. Figure 5.6 shows that a time step size of 2.5 ms/step is sufficient to provide accurate results with minimised transient instability. At the major bend in the venous segment, the flow is clearly unstable due to the immediate change in the local flow direction and presence of recirculation.

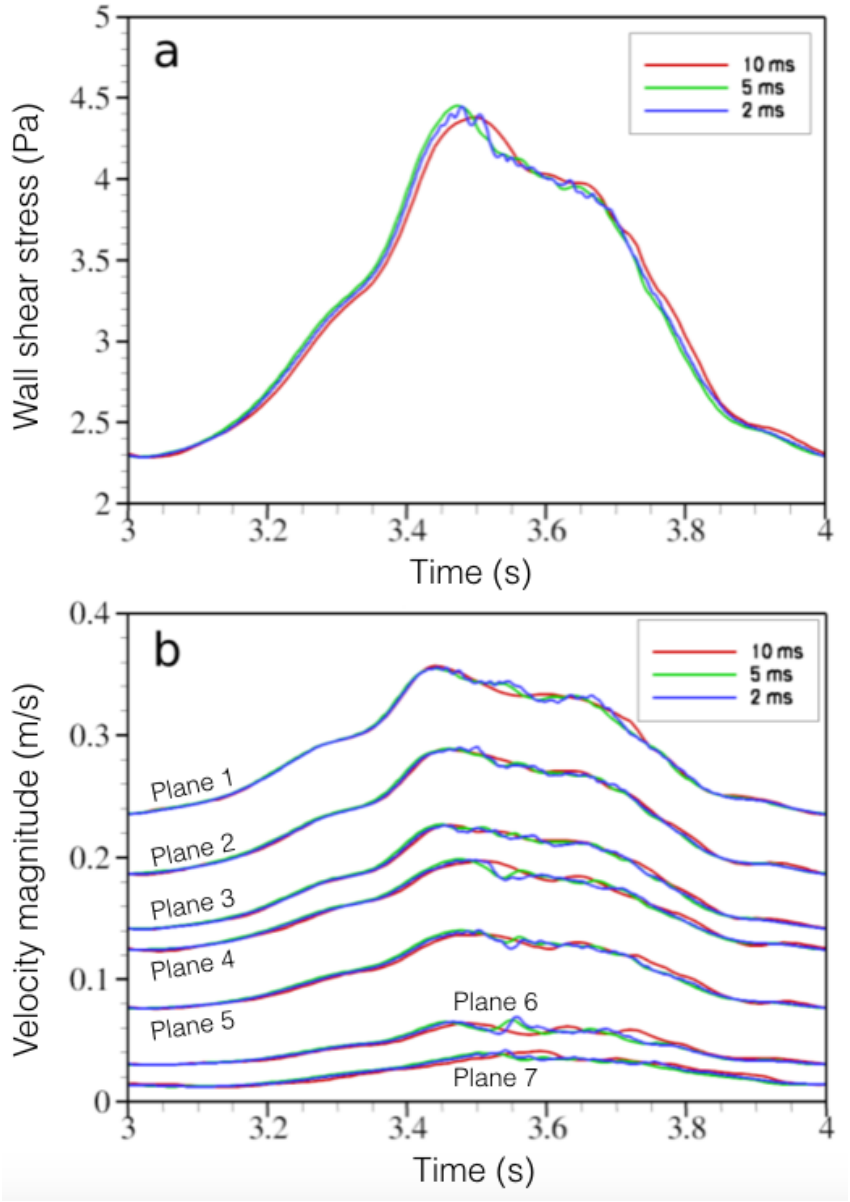

Figure 5.5: Temporal variations of the (a) spatially averaged WSS on the aneurysm wall and (b) plane-averaged velocity magnitude of the planes 1-7 inside the aneurysm at different timestep sizes of 10 ms (red), 5 ms (green), and 2 ms (blue). (1 second per 1 cardiac cycle)

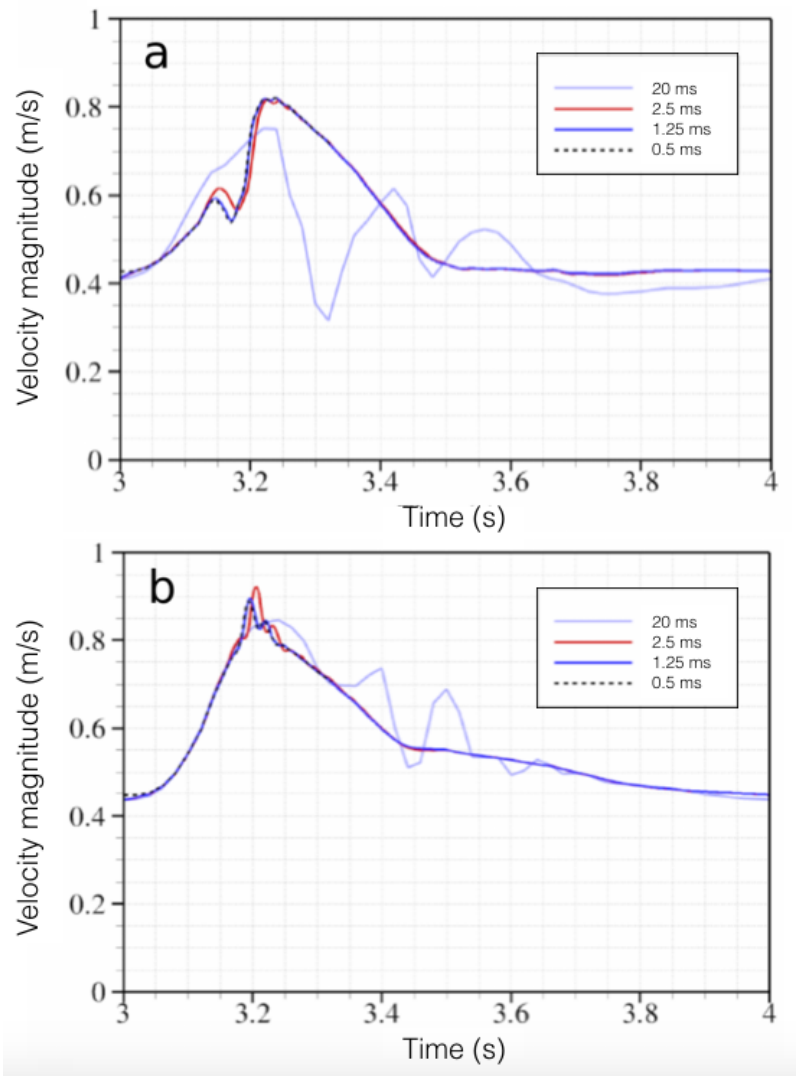
a
b
20 ms
2.5 ms
1.25 ms
0.5 ms
Velocity magnitude (m/s)
Time (s)
0
0.2
0.4
0.6
0.8
1
3
3.2
3.4
3.6
3.8
4

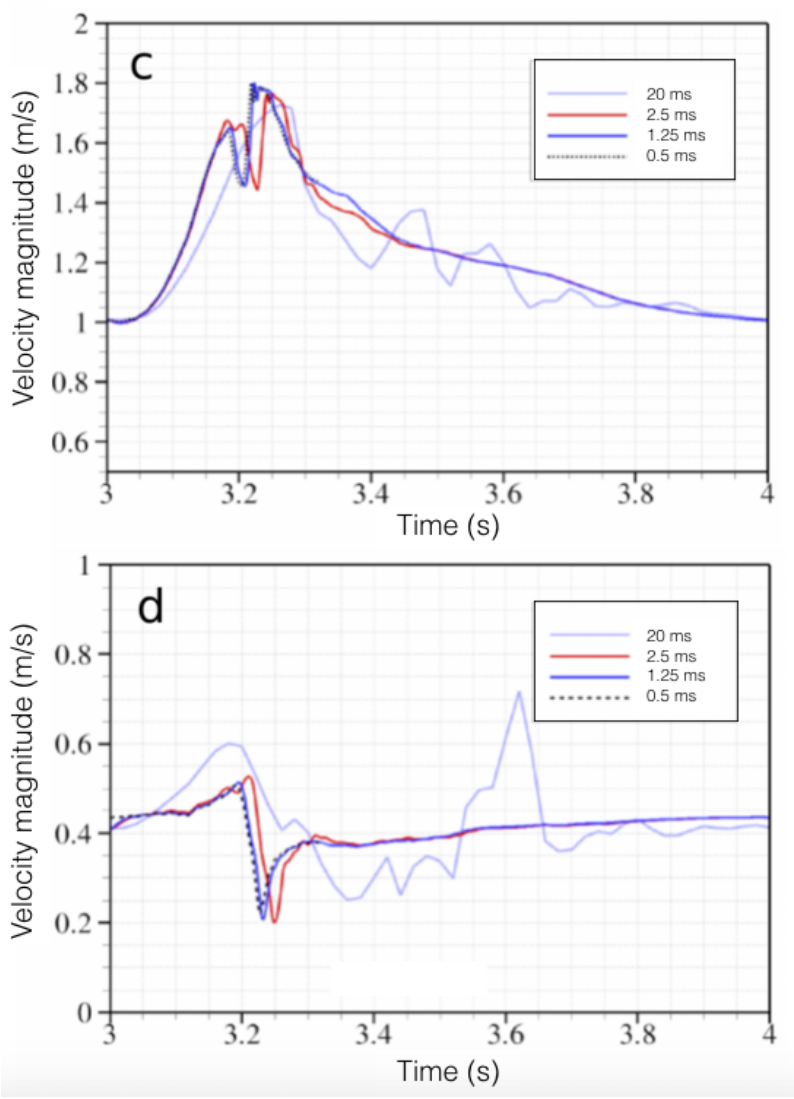

Figure 5.6: Temoral variations of the velocity magnitude during the fouth cardiac cycle at the (a) arterial bifurcation, (b) inner wall of the fistula entry, (c) venous bend, and (d) venous-fistula anastomosis, at timestep sizes of 20 ms (pale blue), 2.5 ms (red), 1.25 ms (dark blue), and 0.5 ms (black dotted). (1 second per 1 cardiac cycle)

This resulted in the incompleted convergence of the peak-systolic velocity magnitude at this bend for a timestep size of 2.5 ms/step. However, it is not ideal to use a smaller time step size of 1.25 ms/step only to change the peak velocity magnitude by a negligible amount, while a significant increase in computational cost have to be compensated. This timestep size is significantly finer than that of previous AVF studies which includes a wide range between 100 ms/step to 20 ms/step (Kharboutly et al., 2010; Ene-Iordache and Remuzzi, 2012; Jodko et al., 2014). Smaller timestep sizes were also used in previous studies (Bozzetto et al., 2015; Pike et al., 2017b) but the timestep size in the present study is converged and a finer timestep size was not required.

5.1 Independence tests for FSI cases

Grid and timestep size independence tests have also been conducted for the solid domains of both the FSI aneurysm and AVF studies. The fluid domain in both studies maintained the mesh density of 6 million elements as discussed in the previous section.

The temporal variations of wall displacement with different mesh densities (0.5, 1, and 2 million elements) and timestep sizes (10, 5, and 2.5 ms) were investigated. Figure 5.7 shows the maximum aneurysmal wall displacement variations in time during the fourth cycle. The wall displacement increased significantly after the mesh density was increased from 0.5 million element to 1 million. On the other hand, increasing the mesh density from 1 million to 2 million elements did not significantly changed the wall displacement. The wall displacement was not sensitive to the decrease in timestep size. Nevertheless, the timestep size of 5 ms was chosen as it corresponded with the timestep size used in the rigid aneurysm simulations. This timestep size has been used in most previous FSI aneurysm studies (Torii et al., 2010; Suzuki et al., 2015) and the mesh density used is in the same order of magnitude of that reported in Eken and Sahin (2017). It is clear that the mesh density of 1 million element and timestep size of 5 ms produced a wall displacement that is grid and timestep size independent and were therefore used.

The same independence tests were performed for the FSI AVF study. Figure 5.8 shows the AVF wall displacement along the circumference of a local venous cross-section. The same mesh densities of 0.5, 1, and 2 million elements and timestep sizes of 10, 5, and 2.5 ms were used for the independence tests. It is evident that the mesh density of 1 million element is most suitable as the wall displacement corresponded to it is grid independent. Although the AVF wall displacement is not sensitive to changes in timestep sizes (from 10ms to 2.5ms), a timestep size of either 5 ms or 2.5 ms is more suitable thatn 10 ms. The timestep size of 2.5 ms was used for the FSI AVF study, despite 5 ms being the the optimal choice, because it corresponded with the timestep size used in the rigid AVF study. The resulting wall displacements in both FSI studies are in the same range of that reported in previous FSI aneurysm Eken and Sahin (2017) and AVF (McGah et al., 2014; Decorato et al., 2014) studies.

To summarise, a mesh density of 6 million elements was used for both rigid aneurysm and rigid AVF studies. For both FSI aneurysm and FSI AVF studies, a mesh density of 1 million element was used for the solid domain while the fluid domain maintained a mesh density of 6 million elements. The timestep size used in both rigid and FSI aneurysm studies is 5 ms and the timestep size used in both rigid and FSI AVF studies is 2.5 ms. These combinations of mesh density and timestep size ensured results that are both grid and timestep size independent. The averaged Courant numbers in both aneurysm and AVF simulations are maintained below 1.0. Figures 5.9 and 5.10 shows the mesh of the aneurysm and AVF model,respectively.

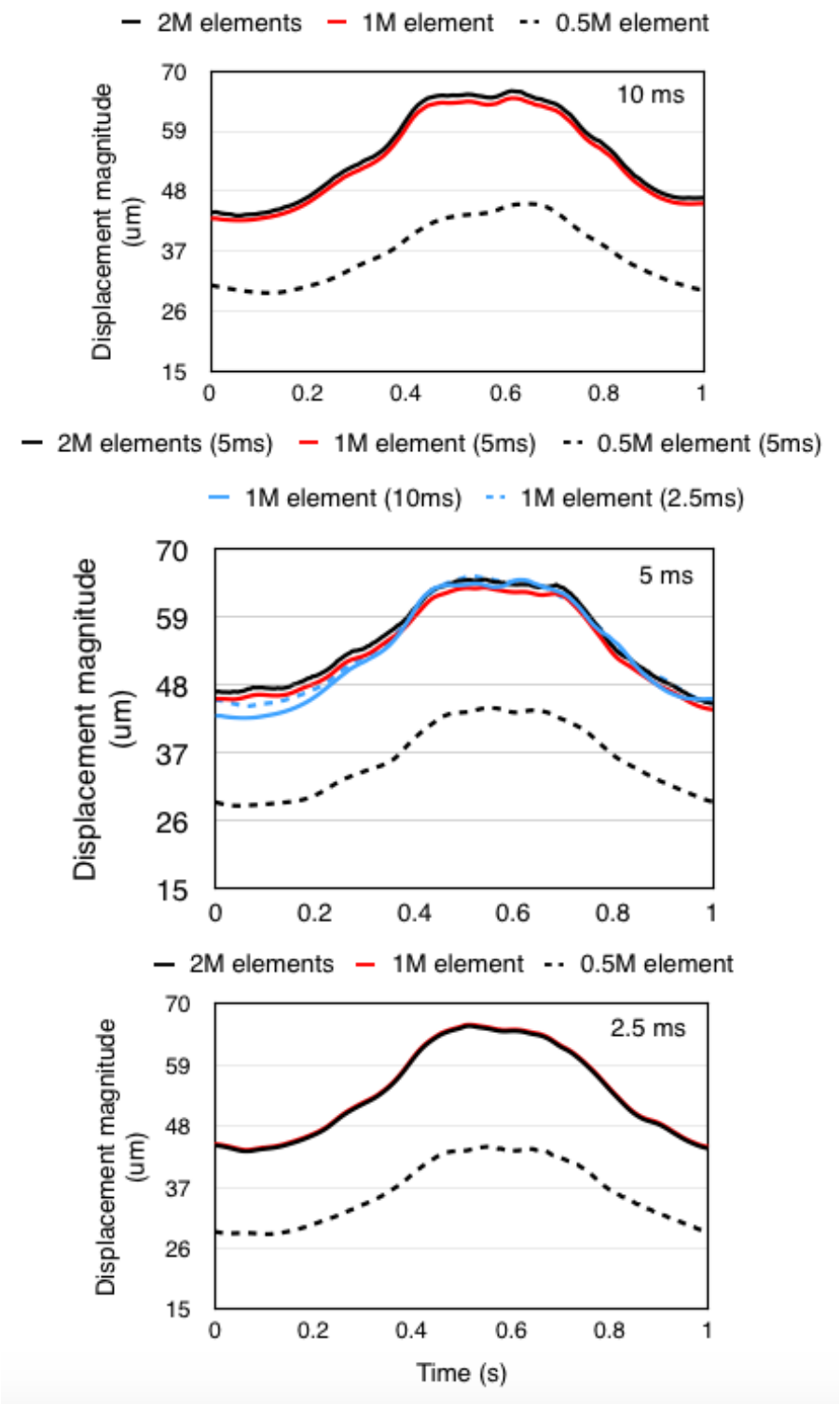

Figure 5.7: Temoral variations of the maximum aneurysmal wall displacement with different mesh densities and timestep sizes.

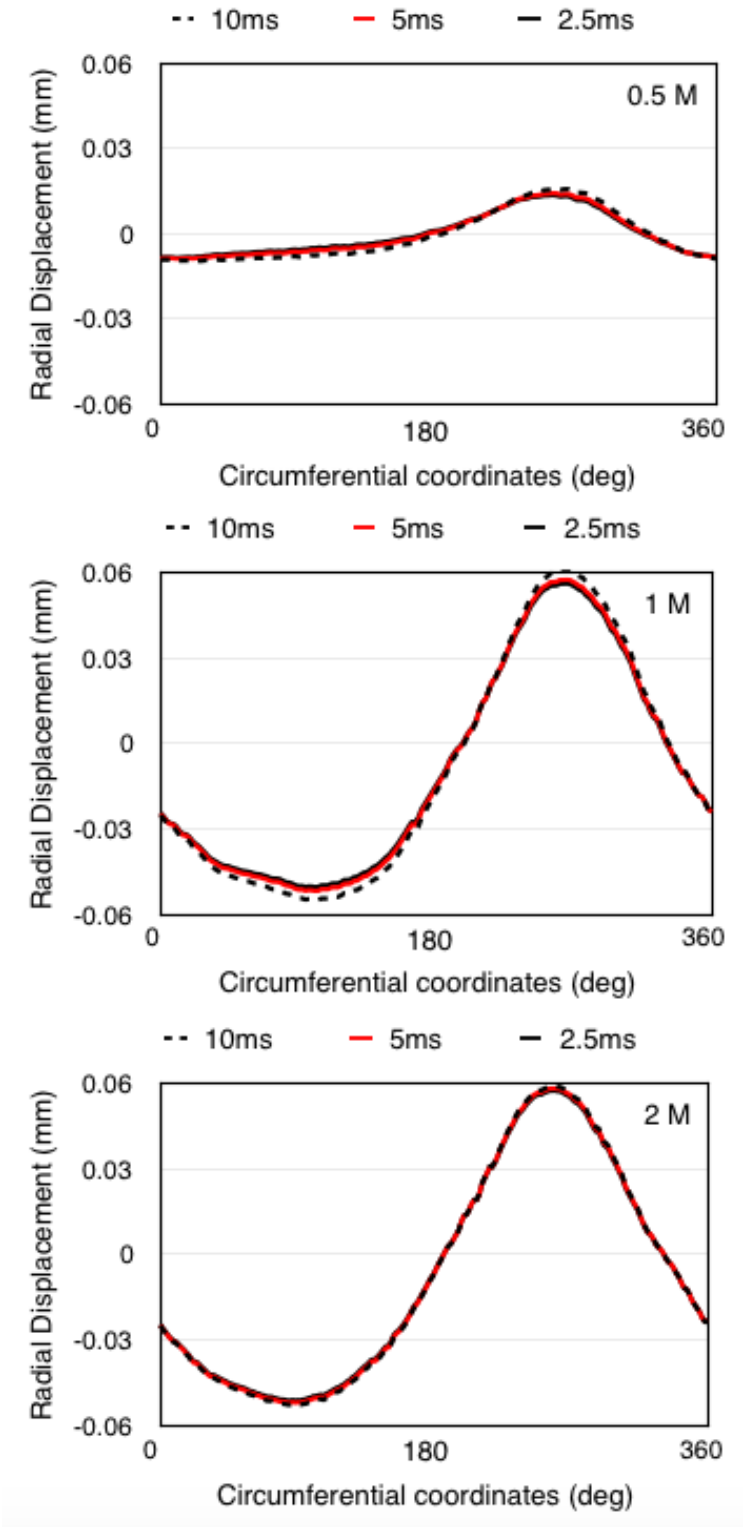

Figure 5.8: Temoral variations of a local radial displacement of the AVF wall with different mesh densities and timestep sizes.

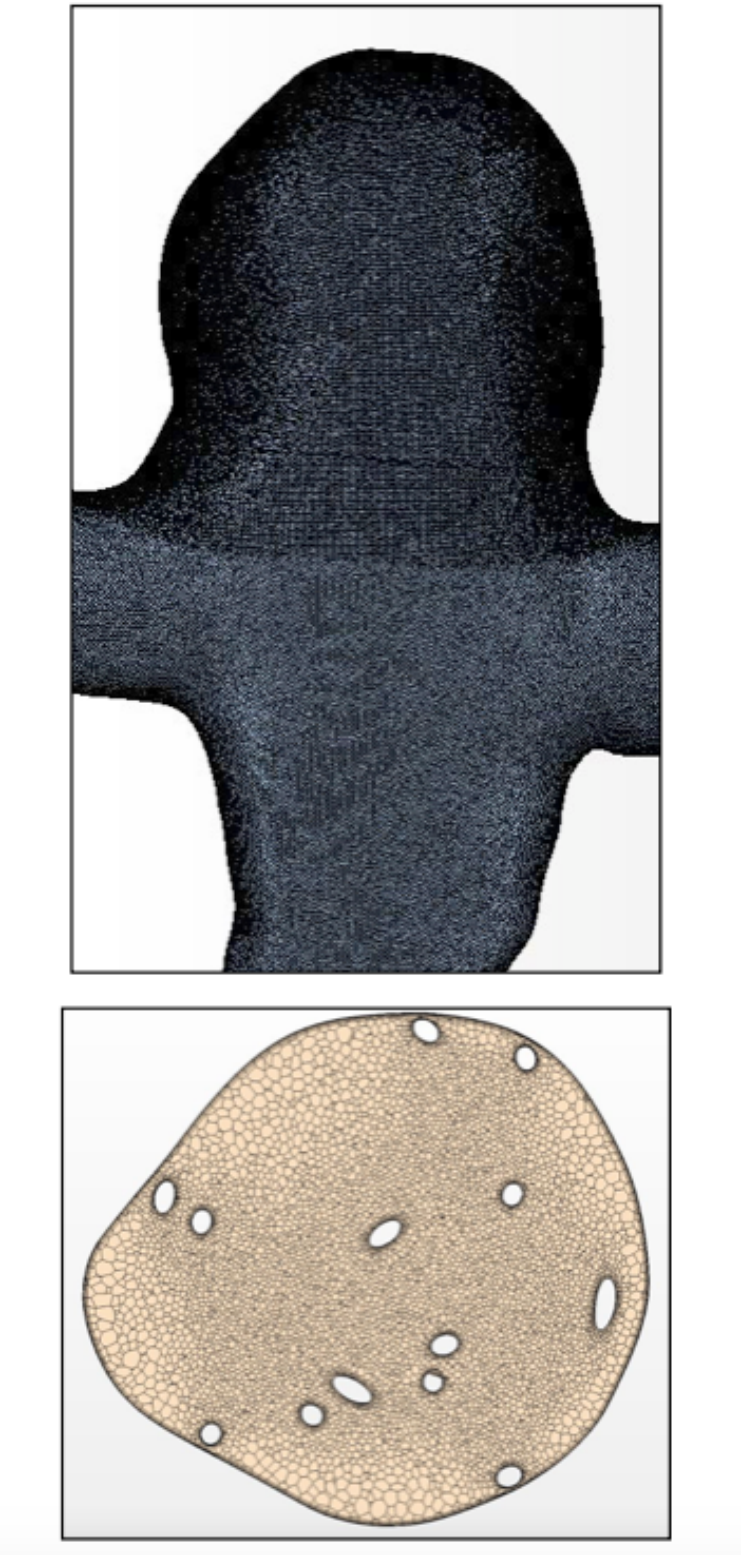

Figure 5.9: Mesh representation of the aneurysm model.

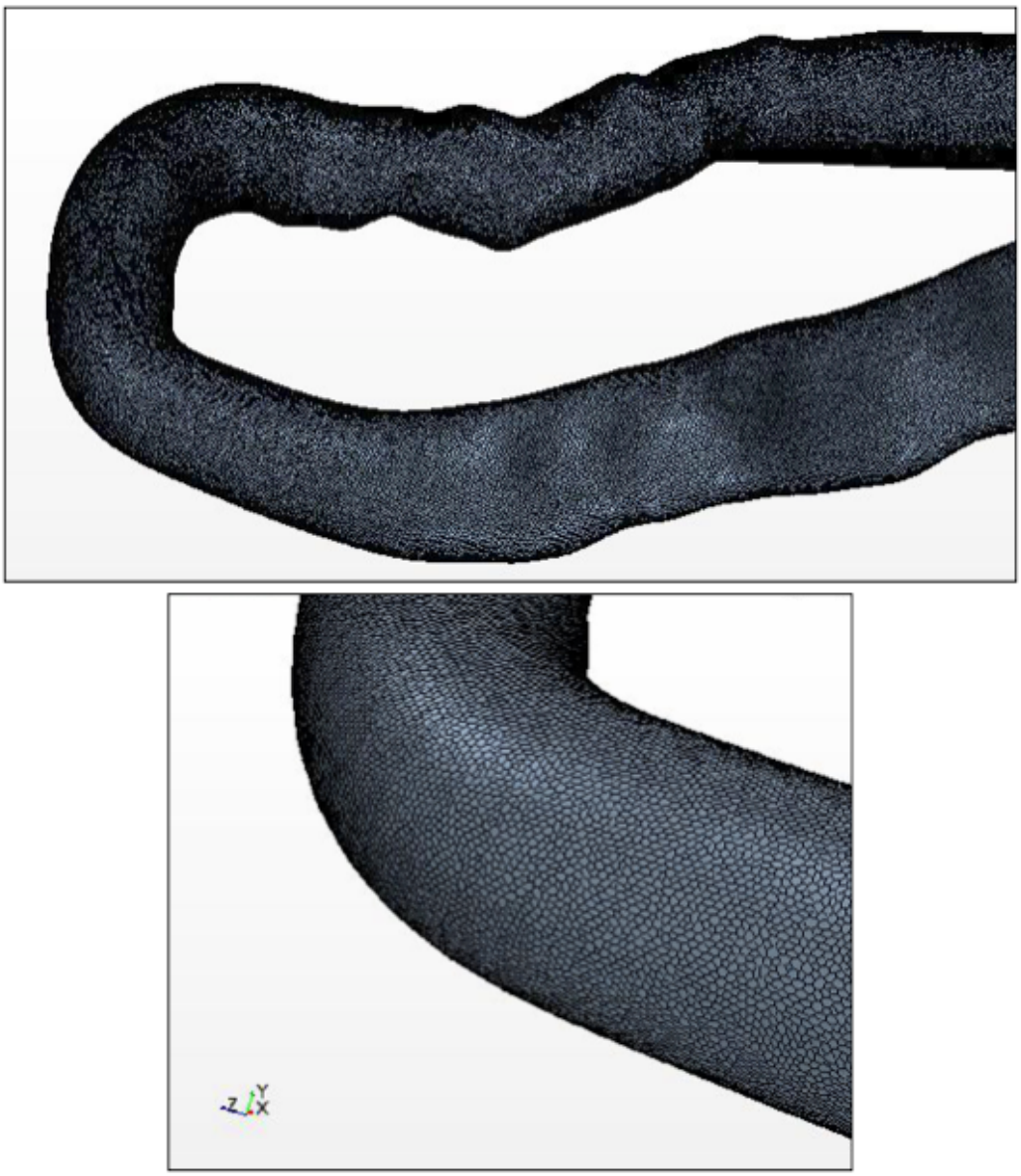

Figure 5.10: Mesh representation of the AVF model.

Chapter 6

Effects of coil packing density, leukocyte adhesion, and wall compliance on aneurysm flow reduction and recurrence

Blood velocity in a coiled cerebral aneurysm generally decrease with high coil packing density due to flow diversion (Zhou et al., 2017) and stagnation (Xiang et al., 2014). The reduction in aneurysmal velocity and WSS promotes thrombus formation, which helps with aneurysm occlusion. However, flow recanalisation can still occur, even at high packing density (Otani et al., 2018), thus re-exposing the aneurysm to risk of recurrence and rupture (Morales et al., 2011). This chapter is divided into four sections, each addressing different controversial issues regarding aneurysm rupture and recurrence.

The first section discusses changes in aneurysmal flow behaviour due to different packing densities. Eight non-Newtonian simulations (1 untreated aneurysm and 7 coiled aneurysms) have been performed. The lowest coil packing density that can supress the aneurysmal flow and wall shear stress is determined as the optimal treatment option. Temporal variations and probability distribution functions (PDF) of spatially averaged velocity magnitudes and wall shear stresses have been investigated. The effects of coil packing density on flow impingement through the coils are examined by observing the

isosurfaces of velocity magnitude. These isosurfaces also provide evidence of aneurysm recurrence at high packing density which is discussed later in the third section. A separate simulation investigating the flow in the MCA bifurcation without the aneurysm have been conducted to study the local arterial flow prior to aneurysm initiation and its relation to aneurysm growth.

The second section explores the effects of passive scalar distributions, low and oscillating wall shear stress, and coil packing density on thrombosis-induced aneurysm occlusion. Time-dependent passive scalar is added to the non-Newtonian flow in the eight simulations to study the blood residence time in coiled aneurysms with different coil packing densities. The PDF of passive scalar concentration provide information on either aneurysmal occlusion or flow recanalisation due to the coil's inability to sufficiently block the flow. Isosurfaces of the mean passive scalar concentration at different time instances and the time-density curve of passive scalar concentration of each coiling cases provide information on blood residence time and thus thrombus formation.

The third section investigates the risk of rupture and leukocyte migration in reducing the rupture risk. Aneurysmal rupture risk has been investigated by observing the near-wall flow oscillations (through OSI contours) and low and oscillating wall shear stress regions (through LOWSSI contours). The contribution of each coil inserted into the aneurysm, especially the first one, in reducing the rupture risk is shown. Leukocyte intercention, including adhesion to the aneurysm wall, in different coiling cases have been studied by discriminating the TAWSS contours based on different ranges known to correspond with certain leukocyte activity.

In the fourth section, the effects of local coil packing density, leukocyte adhesion to the wall, and wall complaince on aneurysm recurrence are shown. Aneurysm recurrence is observed when there is an abnormal increase in aneurysmal inflow despite increasing coil packing density. Increase in coil packing density have previously been understood to suppress aneurysm growth, which may consequently leads to rupture. However, blood can start to re-enter the recanalising aneurysm regardless of an increase in coil pack-

ing density. Aneurysm recurrence have been observed in the present study as shown by the velocity isosurfaces in the first section and also in Otani et al. (2018). In that previous study, aneurysm recurrence was attributed to the low coil packing density at the aneurysm neck. In the present study, the effects of local packing density of not only the neck region but the whole aneurysm dome on aneurysmal recurrence have been investigated. Additionally, FSI and multiphase simulations have been performed to further investigate aneurysm recurrence due to wall compliance andthe spatial distributions of red and white blood cells. Aneurysmal phase velocities, wall shear stress, leukocyte adhesion, and wall remodelling during aneurysm recurrence are shown.

6.1 Flow and WSS reduction

The aneurysmal volume-averaged velocity magnitude and surface-averaged wall shear stress (WSS) are to have been reduced due to coiling as shown by Figures 6.1 and 6.2, respectively. In both figures, 1C-7C denote the cases of one coil to seven coils inserted. The insertion of the first coil (represented by 1C and corresponding to a packing density of 5.07%) induced a significant flow reduction of up to 38% (t=0.7s) before the velocity continued to decrease with more coils inserted. However, an effect as large as that seen after inserting the first coil was not observed again. Reduction in both the velocity and WSS attributed to the third coil was partially larger than that of the fourth coil. This showed that the inverse relationship between coil packing density and WSS was not conserved. The velocity magnitude, and hence the WSS, attributed to the fourth coil is almost identical to that of the third coil slightly before peak systole (t=0.44s). However, exactly after peak systole, the WSS of the third coil further decreased to that of the fifth coil immediately within 20 ms. Although the inverse relationship was conserved thereafter, this behaviour was not observed in velocity reduction. The reduction in WSS became less significant after the insertion of the fifth coil. However, the insertion of two more coils after the introduction of the fifth coil further reduced the velocity and WSS by 75% and 13%, respectively. Therefore, the seventh coil, which produced a packing density of 30.35% was the optimal coiling case (Sluzewski et al., 2004; Morales et al., 2011, 2013b).

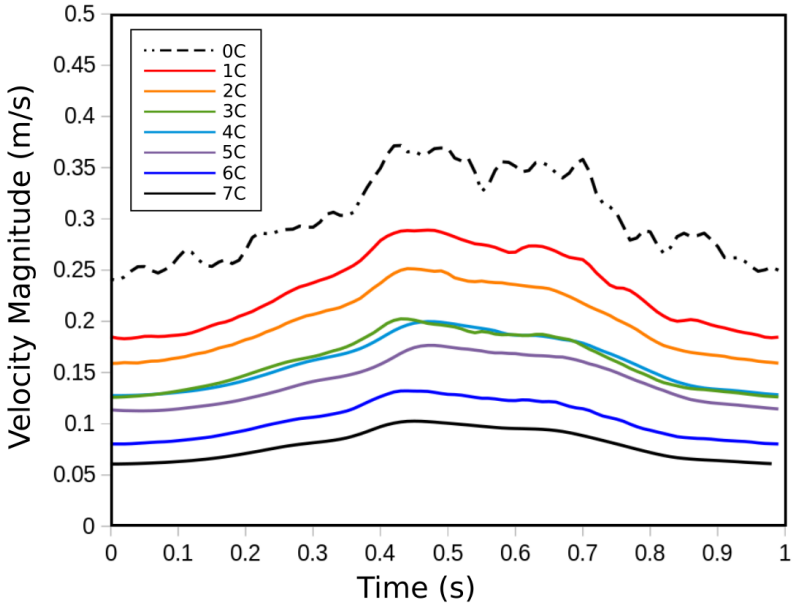

Figure 6.1: Variation of aneurysmal volume-averaged velocity magnitude with different packing densities in one cardiac cycle (1 second = 1 cycle).

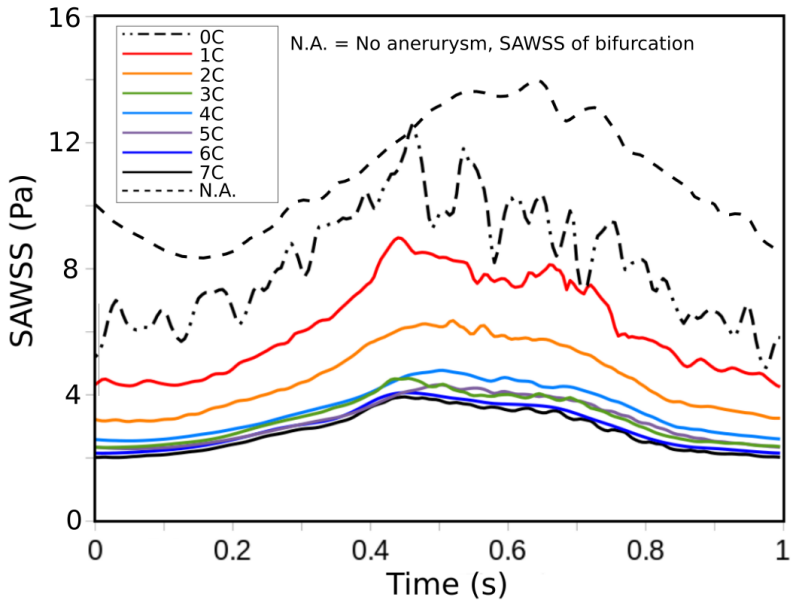

Figure 6.2: Variation of aneurysmal surface-averaged wall shear stress (SAWSS) with different packing densities in one cardiac cycle (1 second = 1 cycle). Constantly dashed line represents surface-averaged wall shear stress on the bifurcation on which the aneurysm would be initiated.

Consequently, a higher packing density was not considered (Morales et al., 2013b). Additionally, the seventh coil was the only configuration able to reduce the surface-averaged WSS back to 2.0 Pa, a typical WSS of a healthy cerebral artery (Giddens et al., 1993; Rayz et al., 2010), at peak diastole. The greatest velocity reduction due to each coil did not necessarily occurred at the peak systole, but can instead occur at any time. This suggests that velocity and WSS reduction is independent of the inflow waveform. It has also been found that the greatest WSS reduction by the first coil at peak systole is not necessarily attributed to the greatest velocity reduction (also by the first coil at t=0.77s) which occured a few milliseconds later. In other words, a packing density which reduced the aneurysmal velocity by the most significant amount may not produce the highest WSS reduction. Also, reduction in WSS may be a result of changes in other hemodynamic factors other than velocity reduction.

Relative to the untreated case, the aneurysm WSS during the insertion of the first three coils decreased dramatically as shown by the ratio of WSS of each coiling case to that of the untreated case in Figure 6.3. This represents the higher effectiveness of the coils in aneurysms with packing density lower than 13%. Low coil effectiveness translates to lowered demand for more coil and thus leads to an optimal packing density. In this case, the optimal packing density of 30.35% corresponds to 2% difference in the SAWSS ratio.

In another separate case study, the aneurysm sac was removed to represent a healthy MCA bifurcation without an aneurysm. The surface-averaged WSS over the bifurcation, which the present aneurysm would have been initiated upon, is shown by the equally dashed line in Figure 6.2 with the other coiling cases. It was observed to be higher than that of the untreated case for the whole cyclic cycle. The spatial-temporally averaged WSS on the bifurcation is 10.96 $\pm$1.8 Pa, which is 7.3 and 5.48 times larger than the normal arterial WSS and the range which initiates wall degeneration before aneurysm initiation (Humphrey and Canham, 2000). The major contributor to this abnormally high WSS on the bifurcation (Chaichana et al., 2013a) is the blood flow impingement (Torii et al., 2010; Chaichana et al., 2013a) directly from the M2 segment upstream of the bifurcation. This suggests that an abnormally

high WSS caused the initiation of this aneurysm (Zhou et al., 2017). As the aneurysm grows, the WSS decreased to the range represented by the untreated case (0C). However, the spatially-averaged WSS at the peak systole did not decrease with the rest of the cycle.

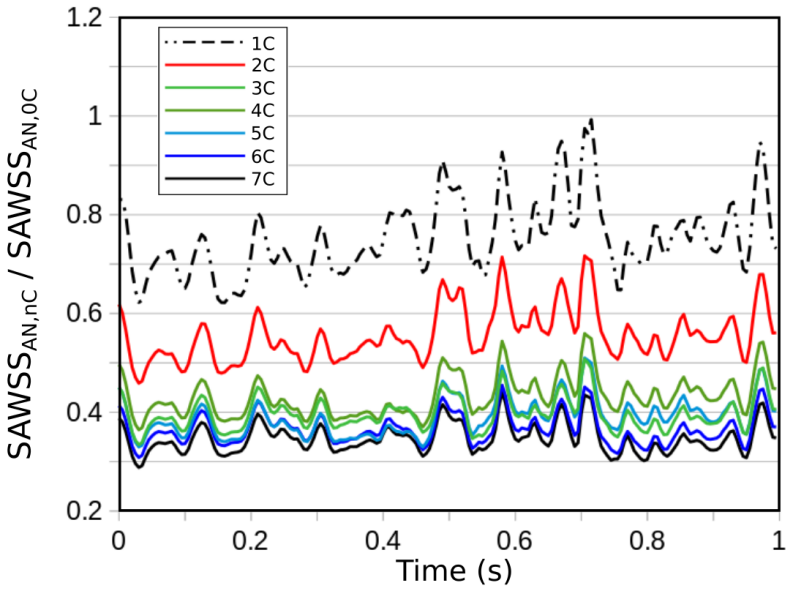

Figure 6.3: Ratio of aneurysmal surface-averaged wall shear stress (SAWSS) of each coiling cases to that of the untreated case.

Figure 6.4 shows the isosurface of the mean blood flow inside the aneurysm dome. A large vortical flow structure in the untreated aneurysm, as also observed by (Lee et al., 2013), is shown in Figure (6.4a). Flow impingement through the coils after the insertion of the first three coils has been observed as shown by Figure 6.4b). The impingement area and WSS decreased with increasing packing density. After insertion of the fourth coil (17.73%), the mean blood flow was stagnated by the coil and can no longer reach the aneurysm tip (Figure 6.4c-f). The flow penetration strength through the coils also decreased with increased packing density as observed by the significant reduction in the mean flow inside the dome. Additionally, the mean flow in the outlet arteries observed in the cases of the first three coils (Figure 6.4a-c) is absent after the insertion of the fourth coil due to flow stagnation and decreased velocity. This suggests that the coil became effective after the fourth coil is inserted as shown

in Figure 6.3, where the SAWSS ratio ceased to dramatically decrease with more coils added. The coil continued to be effective in blocking the flow, especially during peak diastole (t=0s). The local packing density near the neck region induced multi-directional flows after the seventh coil was inserted as shown by the scattered velocity distribution in Figure 6.4f. In this situation, a new local flow can be formed, which may result in a long term variation in WSS and consquently aneurysm recurrence and rupture despite high packing density (Otani et al., 2018).

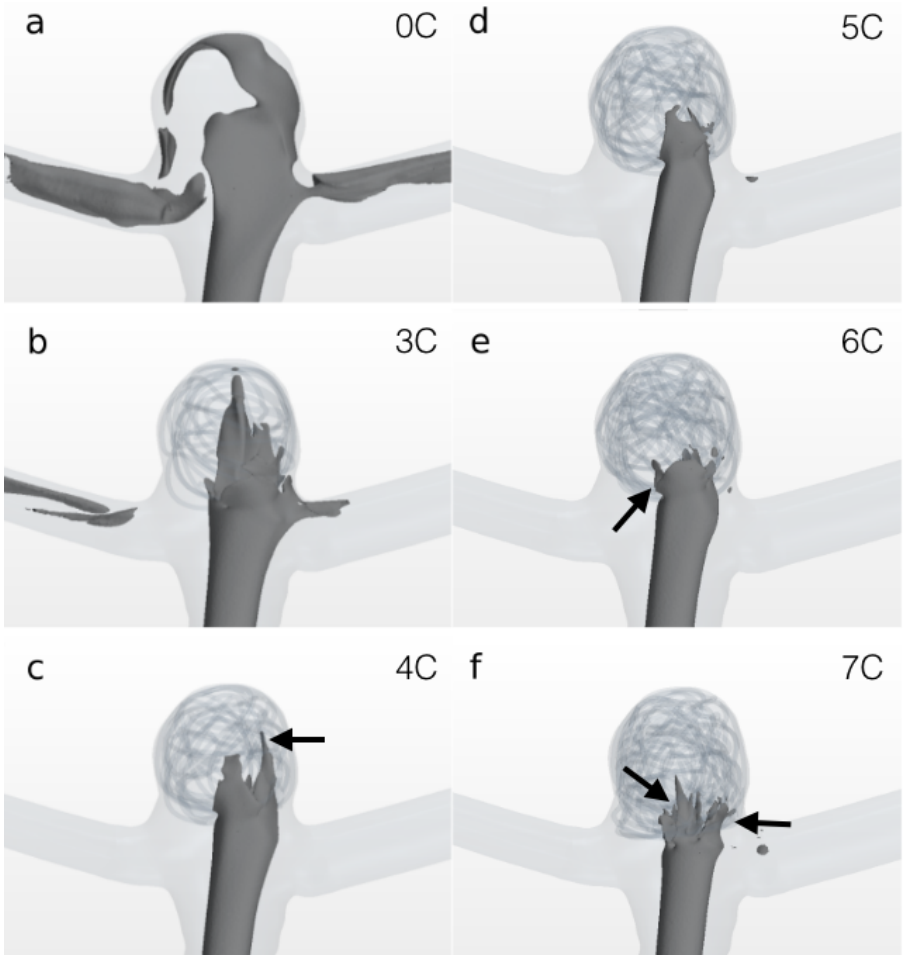

Figure 6.4: Isosurface of mean velocity (v = 0.69 m/s) in the aneurysm and proximal outlet arteries in (a) the untreated case and treated cases with (b) 3 coils, (c) 4 coils, (d) 5 coils, (e) 6 coils, and (f) 7 coils at peak systole. Arrows show regions of flow recanalisation.

The probability distribution function (PDF) of time-averaged velocity (TAVEL) normalised by its the standard deviation (SD) for the untreated case (0C), TAVEL/SD($TAVEL_{0C}$), is shown in Figure 6.5a. A high PDF value means that more of volume inside the aneurysm is filled with flows of the corresponding TAVEL and vice versa. Regions of high flow ($4.0 <$ TAVEL/SD($TAVEL_{0C}$) < 4.86) is significantly suppresed by the 6 and 7 coils. Regions of moderate flows ($1.5 <$ TAVEL/SD($TAVEL_{0C}$) < 4.86) decreased with increasing coil packing density. On the other hand, regions of very low flow (TAVEL/SD($TAVEL_{0C}$) < 0.25) increase with coil packing density as shown by Figure 6.5b. This suggests that the each coil inserted continuously reduce the aneurysmal flow, although with different rates. A significant increase in the PDF of TAVEL/SD($TAVEL_{0C}$) < 1.0 was observed upon insertion of the first coil. This suggests that the first coil is efficient in inducing low flow regions in the aneurysm. The insertion of the third coil significantly increased the regions of flow stagnation (PDF of TAVEL/SD($TAVEL_{0C}$) $= 0$), but not as efficient as the first coil. This corresponds to how efficient the first and third coils are in reducing the volume-averaged velocity magnitude (Figure 6.1) and surface-averaged wall shear stress (Figure 6.2 and 6.3). This is an evidence that aneurysmal flow stagnation significantly contributed to flow and WSS reduction. On the other hand, the insertion of the seventh coil did not increase the PDF of TAVEL/SD($TAVEL_{0C}$) < 0.5 (i.e. low flow regions). This suggests that the insertion of the sixth coil was sufficient for optimally inducing very low flows in the aneurysm.

The standard deviations of the PDF of TAVEL (normalised by that of the six coil case - 6C) about its mean value are shown by the blue bars in Figure 6.6. The red bars illustrate the difference between the normalised S.D. of the PDF of TAVEL for a coiling case and its proceeding coiling case. For example, the red bar corresponding to 4C-3C shows the difference between the normalised S.D. of the PDF of TAVEL for the 4 coil and the 3 coil cases. The difference for the 6 and 7 coil is relatively small compared to that of the other pairs of coiling cases. This negligible change in the spatial distribution of TAVEL suggested that 7 coils (packing density of 30.35%) is optimal coiling case for reducing aneurysmal flow.

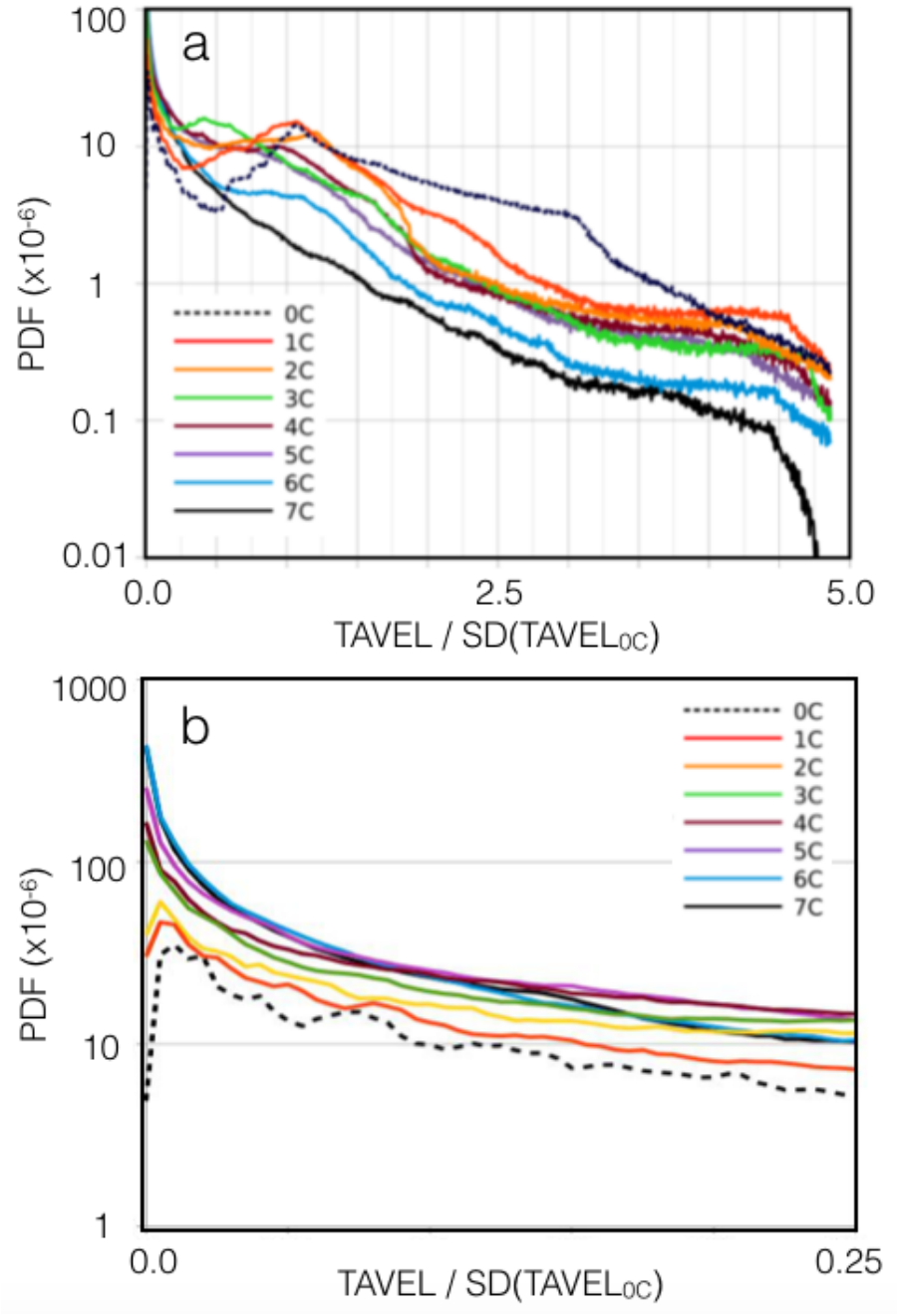

Figure 6.5: Probability distribution function (PDF) of time-averaged velocity magnitude (TAVEL) for different packing densities (0C-7C) normalsied by the standard deviation of TAVEL of the untreated case, SD($TAVEL_{0C}$), in log-scale. The horizontal axis, representing TAVEL/SD($TAVEL_{0C}$), spans (a) from 0.0 to 4.86 and (b) from 0.0 to 0.25.

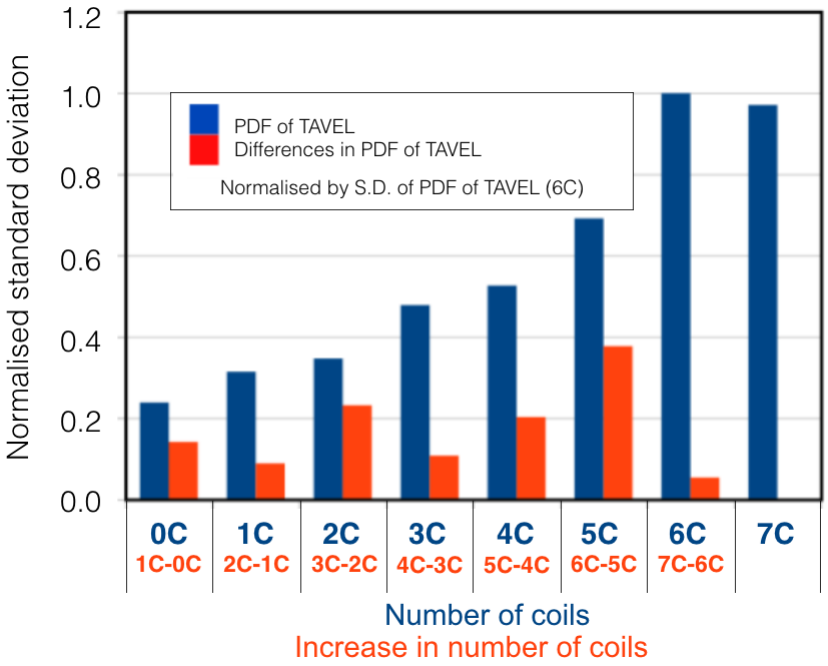

Figure 6.6: Standard deviation of the PDF of TAVEL for different packing densities and their difference from that of the preceeding coil (i.e. 2C-1C means difference between the TAVEL/SD(TAVEL$_{0C}$) of the 2 coil and 1 coil cases).

6.2 Flow occlusion and thrombus formation

A reduction in aneurysmal blood velocity and occlusion are clinically observed through the visualisation of medical contrast. The contrast are injected into an artery upstream of the region of interest and allowed to flow with the bloodstream. By looking at x-ray angiographies of these contrast, clinicans can investigate the blood flow in real time. Aneurysm occlusion is observed when the amount of contrast entering the aneurysm dome is sufficiently reduced by the blocking coils. When the local coil packing density is unable to sufficiently occlude a certain region of the aneurysm, flow recanalisation is allowed to occur. Additionally, some of the contrast that were able to penetrate through the coils may end up being accumulated inside the aneurysm dome. Blood that accumulate inside the aneurysm dome for a sufficiently long time can induce thrombosis. Therefore, thrombus formation depends on

blood residence time. If the contrast diffusion inside the coiled aneurysm can be observed, then aneurysm occlusion, blood residence time, and thrombus formation can be predicted. In computational simulations, passive scalar are used to model these contrasts. Therefore, aneurysm occlusion due to flow blockage by the coils and thrombus formation due to high blood residence time can be numerically observed. Furthermore, the distributions of passive scalar concentration can be correlated with other haemodynamic properties that cannot be obtained clinically.

Figure 6.7a shows the probability distribution function (PDF) of the normalised time-averaged passive scalar concentration (TAPS), denoted by (TAPS/SD(TAPS$_{0C}$), in different coiling cases. The first coil efficiently blocked the flow into the aneurysm as seen by the significant reduction the PDF of $1.95 <$ TAPS/SD(TAPS$_{0C}$) < 2.05. The same conclusion was made for the reduction in velocity magnitude by the first coil in Figure 6.1. This is also reflected in Figure 6.7b which shows the difference between the PDF of TAPS of a coiling case (C) and that of the preceeding case (C-1). Approximately 4.2% of the TAPS of twice its standard deviation of the untreated case is lost due to the insertion of the first coil. The introduction of additional coils following the first continue to reduce the passive scalar concentration, hence promoting aneurysm occlusion. Most coils following the first one tends to reduce the TAPS within the range of $1.90 <$ TAPS/SD(TAPS$_{0C}$) < 1.95 rather than $1.95 <$ TAPS/SD(TAPS$_{0C}$) < 2.05 observed for the first coil. This suggests that the reduction in the regions of higher passive scalar concentration is mostly attributed to the first coil while the reduction in the regions of lower passive scalar concentration is mainly attributed to the proceeding coils.

Passive scalar concentration is found to be inversely porportional to coil packing density, but the relationship is non-linear. The exception is for the cases of 4 coils and 7 coils. In these two cases, the PDF of $1.90 <$ TAPS/SD(TAPS$_{0C}$) < 1.95 increases from that of their respective preceeding cases (3 coils and 6 coils). Such increase in the PDF indicates the coil inability to occlude the aneurysm and thus allowing flow recanalisation as also shown in Figure 6.4. The recurrence in the 7 coil case (packing density of 30.35%)

is partially attributed to the inability of the fifth and sixth coils in suppresing flow recanalisation in the 4 coil case (packing density of 17.34%). It has also been reported that coil packing densities above 20% may not reduce the risk of recurrence (Greve et al., 2020). Flow recanalisation after insertion of the fourth coil can still be expected because the packing density is not very high. This increase in the PDF ($1.90 < \text{TAPS/SD}(\text{TAPS}_{0C}) < 1.95$) after the insertion of the fourth coil corresponds to the local flow recanalisation (marked by the arrow in Figure 6.4) and is slightly reflected by the volume-averaged velocity reduction (Figure 6.1 during t=0.7-0.85s). On the other hand, flow recanalisation after inserting the seventh coil is abnormal because the packing density is already high and sufficient in supressing the aneurysmal flow and wall shear stress. This increase in PDF is also corresponded to the local flow recanalisation (marked by arrow in Figure 6.4), but unlike the 4 coil case, it is not reflected by the volume-averaged velocity reduction in Figure 6.1. This suggests that the volume-averaged haemodynamics may not be able to fully capture the localised flow recanalisation, which can consequently lead to recurrence for highly packed aneurysms.

Furthermore, for the 7 coil case, a significant increase in the PDF of an even higher range of $2.0 < \text{TAPS/SD}(\text{TAPS}_{0C}) < 2.1$ has been observed as shown in Figure 6.7c. This is another strong evidence of flow recanalisation at high packing density. Although increase in the PDF of this $\text{TAPS/SD}(\text{TAPS}_{0C})$ range is also observed for other coiling cases, the increment is relatively small compared to that of the 7 coil case. Additionally, these increase in the PDF and thus flow recanalisation for the cases of 1-5 coils can be expected due to low and moderate packing density.

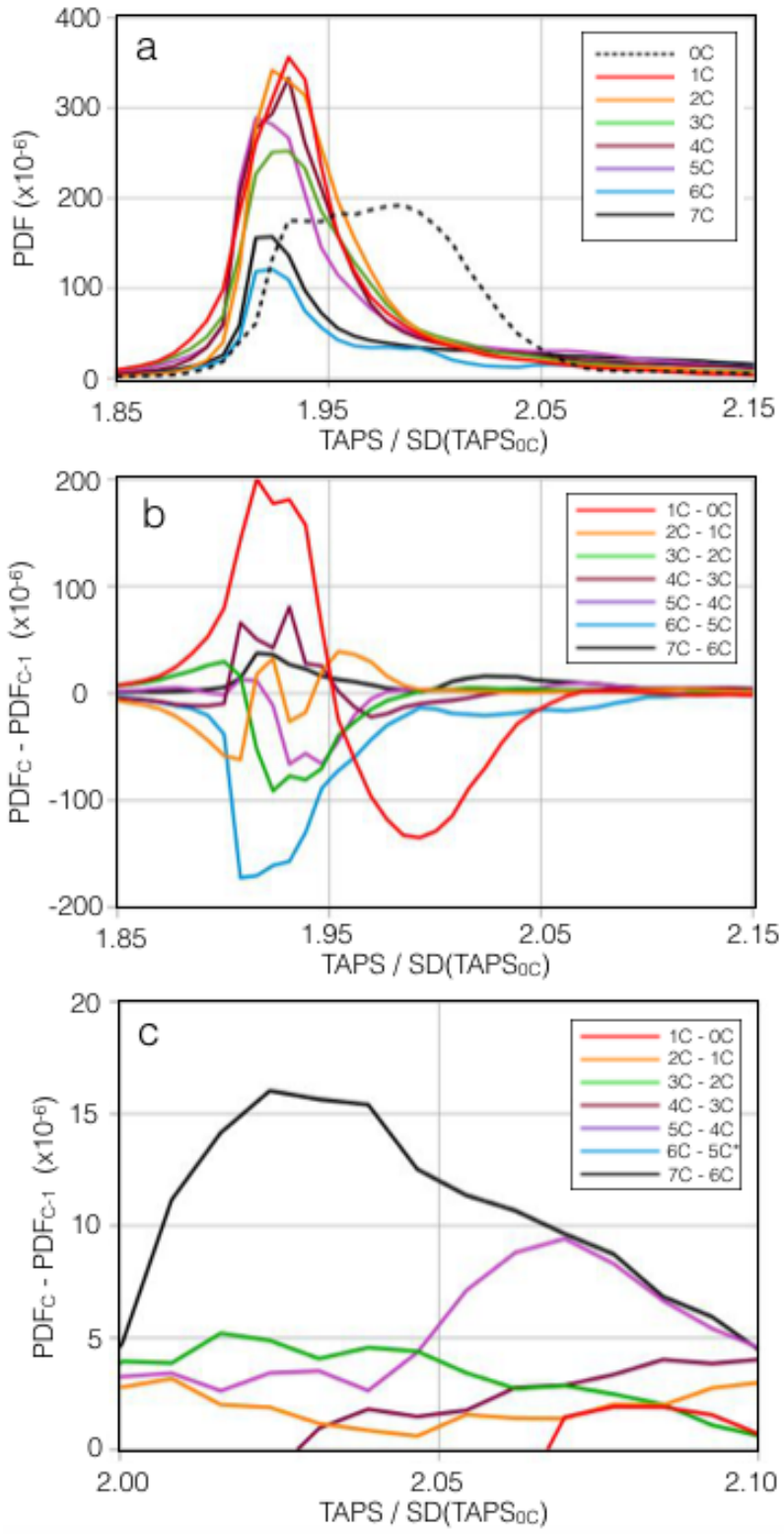

Figure 6.7: (a) Probability distribution function of time-averaged passive scalar concentration, TAPS/SD(TAPS$_{0C}$), (range 1.8 to 2.2) and the difference between the PDF of TAPS of a coiling case TAPS/SD(TAPS$_{0C,C}$) and that of the precceding coil case TAPS/SD(TAPS$_{0C,C}$) spanning (b) from. 1.85 to 2.15 and (c) 2.0 to 2.1.

The maximum PDF of TAPS in each coiling cases are shown in Figure 6.8. It has been found that the maximum PDF of TAPS is independent of coil packing density and its ability to change the PDF of TAPS of itis preceeding case. For example, the insertion of the first coil significantly decreased the PDF of TAPS (Figure 6.7b) of the untreated case. Therefore, maximum PDF of TAPS of the first coil is significantly reduced from that of the untreated case. On the other hand, the insertion of the sixth coil also significantly decreased the PDF of TAPS (Figure 6.7b) induced by the fifth coil, but its maximum PDF of TAPS is higher than that of the 5 coil case by only a small amount.

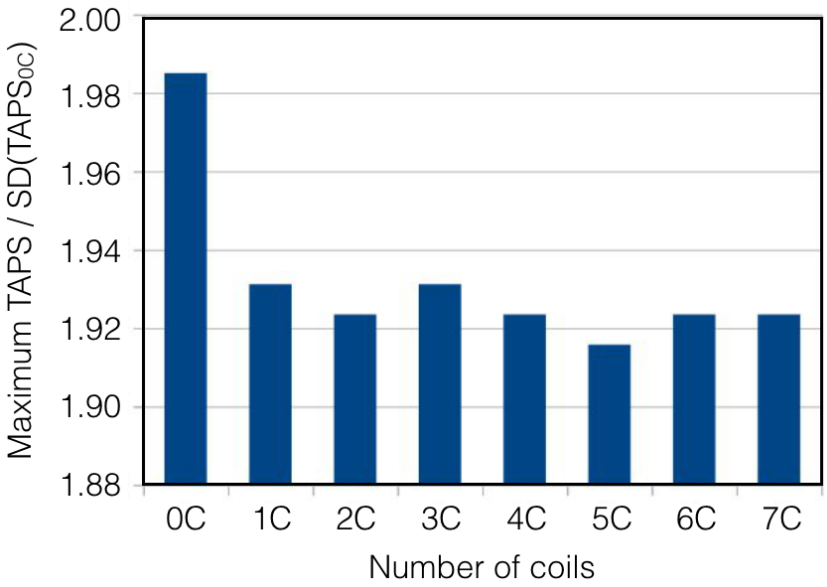

Figure 6.8: Maximum PDF of the time-averaged passive scalar concentration, TAPS/SD($TAPS_{0C}$), of each coiling case.

Blood residence time have also been investigated in each coiling cases by visualising the passive scalar transport in time. The progression of the passive scalar at three different time instances for different packing densities have been observed in Figure Figure 6.9. The figure shows the mean isosurface of passive scalar concentration of 0.8. The mean passive scalars are represented by the grey and black contours. Since the passive scalar distribution is three dimensional and the contours are two dimensional, regions that are densely packed with the mean passive scalar concentration are highlighted with slightly darker

(black) contours. Regions where the mean passive scalar concentration is less packed are highlighted in grey. Contours in the first column were captured at the time instant of t=0.32T to show the swirling vortex of passive scalar entering one side of the aneurysm and exiting the other side. At the same timestep, flow stagnation on the coils can already be observed prior to peak systole (t=0.44T) in the cases of moderate and high coil packing densities (4-7 coils). However, the scattering of the mean passive scalar profiles due to the local packing densities can be observed since the insertion of the second coil.

Nevertheless, the mean passive scalar profiles were able to reach the aneurysm tip during peak systole regardless of coil packing density as shown in the second column. This is why the figures in this column look almost the same except for that of the untreated case. The amount of the mean passive scalar in the untreated aneurysm (0 coil) is higher than those of the treated cases (1-7 coils). This suggestes that coil embolisation reduces the amount of passive scalar entering the aneurysm dome (Morales et al., 2013b). Furthermore, it has been found that the mean passive scalar profiles in low coiling cases (0-3 coils) resided in the aneurysm dome for a shorter period compared to the cases of higher packing densities (4-7 coils). This suggests that blood residence time is decreased by the insertion of the coils (Morales et al., 2013b). However, the direct relationship between the amount of passive scalar residing in the aneurysm and the coil packing density was not discussed in Morales et al. (2013b) because they did not study the effects of coil packing density on passive scalar concentration. By the time t=0.75T (75% of cardiac cycle), most of the mean passive scalar in the low coiling cases have already left the dome. The amount of passive scalar residues at t=0.77T increases with coil packing density. The insertion of the seventh coil increased the amount of mean passive scalar residue in the 6 coil case by only a small amount. Although this can be seen as the ability of seventh coil to sufficiently suprress aneurysmal flow, the increase in the passive scalar residue is a sign of aneurysm recanalisation and recurrence at a high and optimal packing density.

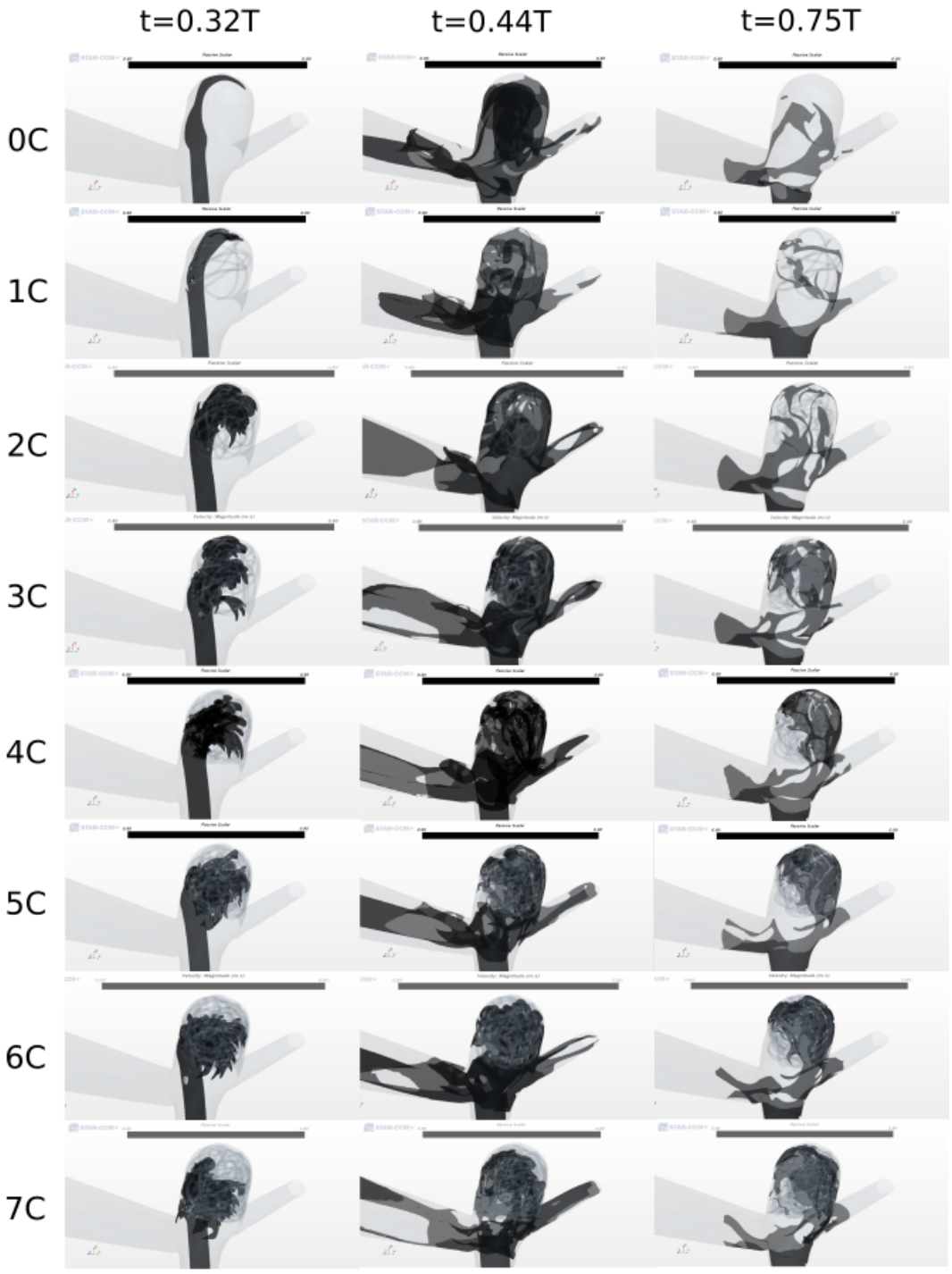

Figure 6.9: Spatial distribution of passive scalar transport inside the aneurysm and proximal outlet arteries for different packing densities at time t=0.32T, t=0.44T (peak systole), and t=0.75T where T is duration in one cardiac cycle (T=1s).

Additionally, the blood residence time inside the aneurysm for each packing density has been quantitatively investigated. A time-density curve of passive scalar at the ostium plane in each coiling case is shown in Figure 6.10a. The passive scalar took approximately 0.5 second to travel from the inlet of the 30D extension pipe and reach the ostium plane in all coiling cases. This suggests that additional coiling in the neck region (including the ostium plane) has neglibible effects on the arrival time of the passive scalar. After 1 seconds (a cardiac cycle), the passive scalar began to gradually escape the aneurysm dome.

Blood residence time is measured from the moment the passive scalar is injected to when its concentration is eventually reduced by 98% of the maximum concentration. This threshold of 0.02 is used by Rayz et al. (2010), a previous study which onvestigated blood residence time in untreated aneurysms. The longer it takes for the passive scalar to be washed out by 98%, the higher the blood residence time. There is no significant difference between the blood residence time in the aneurysms packed with 1-4 coils. It took approximately 1.39 seconds for the passive scalar at the ostium plane of these coiling cases to decrease down to the threshold of 0.02 times the maximum concentration. Blood residence time increases as the coil packing density increases. For the five, six, and seven coils cases, the blood residence timne slightly increased to 1.45, 1.46, 1.55 seconds, respectively. The highest packing density induced by the seven coils caused the longest delay in the passive scalar leaving the aneurysm. These measurements are based on the threshold of 0.02 times the maximum concentration. However, the relationship between the blood residence times induced by different packing densities did not significantly change regardless of the threshold used as illustrated by Figures 6.10b-c. Two different thresholds, 0.2 and 0.02 times the maximum concentration, were used. The highest blood residence time is always attributed to the 7 coils case (for a threshold below 0.05 times the maximum concentration). A clear and direct relationship between coil packing density and residence time can only be observed when the threshold is below 0.01.

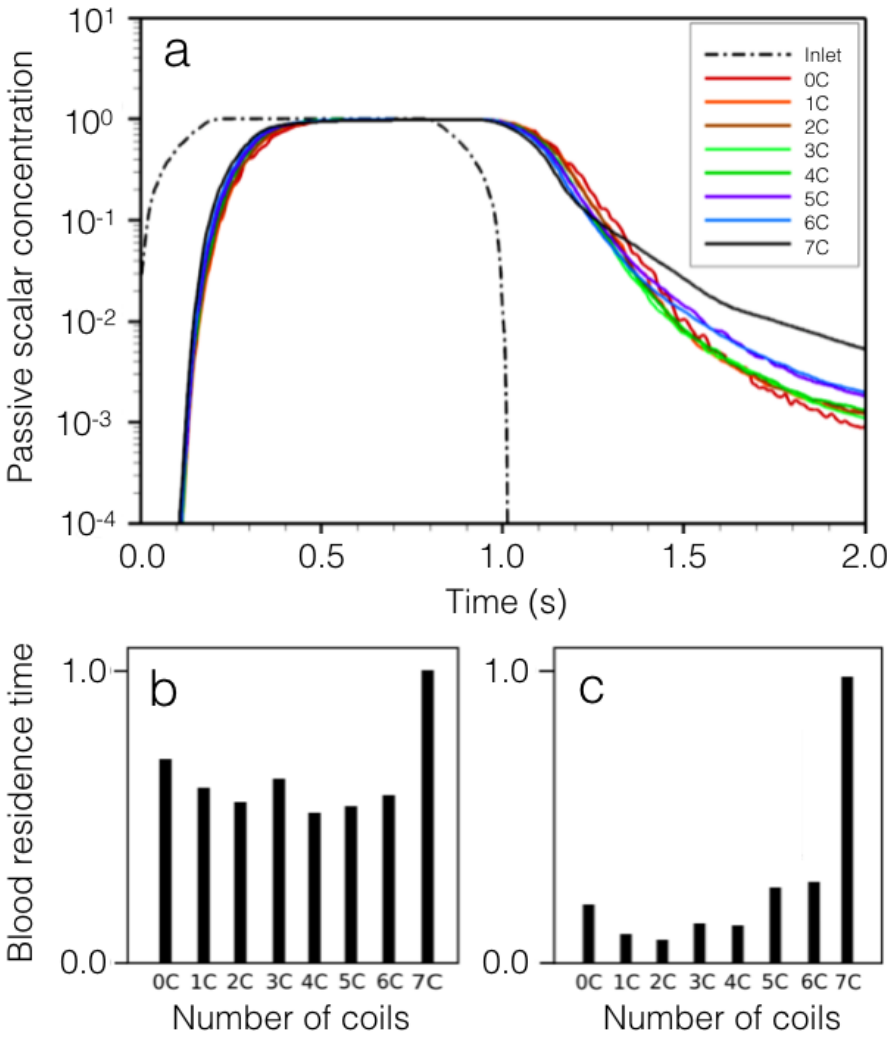

Figure 6.10: Time-density curve of passive scalar concentration on the ostium plane and blood residence time calculated using the thresholds of b. 0.2 and c. 0.02 of maximum concentration (normalised by the blood residence time of the 7 coil case).

Thrombus formation is significantly dependent on high blood residence time and low and oscillating WSS Rayz et al. (2010). The increase in blood residence time allows platelets carried by the bloodstream to accumulate (Sforza et al., 2009) and become activated (Ouared et al., 2008). Platelet activating factors are also secreted from the endothelial cells, thus activating the platelets, due to blood exposure to the foreign materials that made up the coil (Zhou et al., 2017). These activated platelets eventually form blood clots which in-

duces aneurysm occlusion. Nearby endothelial cells subjected to low WSS can also promote the production of anti-thrombotic factors that allows the blood to clot more easily. However, the aneurysm can still rupture during thrombosis. The aggregated platelets can damage the aneurysm wall and cause wall inflammation and degradation. As the aneurysm wall degrades, its critical tensile force and its ability to withstand the transmural pressure reduces and the aneurysm can rupture. In response to wall degradation, leukocytes are recruited into the aneurysm to prevent wall rupture. The rupture risk and leukocyte migration are discussed in the next section.

6.3 Rupture risk and leukocyte migration

High blood residence time and low WSS lead to thrombus formation and subsequent aneurysm occlusion. However, the aggregated platelets that forms blood clots during thrombosis can cause aneurysm wall degradation, making it vulnerable to rupture. If leukocytes cannot be recruited in time to repair the inflamed wall, then there is a high risk of rupture. If the aneurysm eventually becomes stable, a lack of leukocyte adhesion can still cause aneurysm recurrence. The risk of aneurysm rupture and leukocyte migration towards the aneurysm tip are discussed.

Near-wall flow oscillations were found to be responsible for aneurysm rupture (Zhou et al., 2017). An oscillatory shear index (OSI) greater than 0.0125 was reported to trigger the rupture of MCA aneurysms (Miura et al., 2013). Therefore, OSI contours have been plotted (Figure 6.11) to investigate potential risks of rupture in each coiling cases. Without coiling, at least three different locations on the aneurysm wall (marked by OSI $>$ 0.0125) would be at risk of rupturing. After the insertion of the first coil, the OSI and rupture risk were significantly reduced. This means that the first coil is very efficient in reducing the risk of rupture. The OSI and risk of rupture decreased with increasing packing density but in a non-linear relationship. The seventh coil significantly reduced the OSI towards the aneurysm tip, a location prone to aneurysm rupture (Zhou et al., 2017). This suggests that this last coil inserted

is able to reduce the risk of rupture.

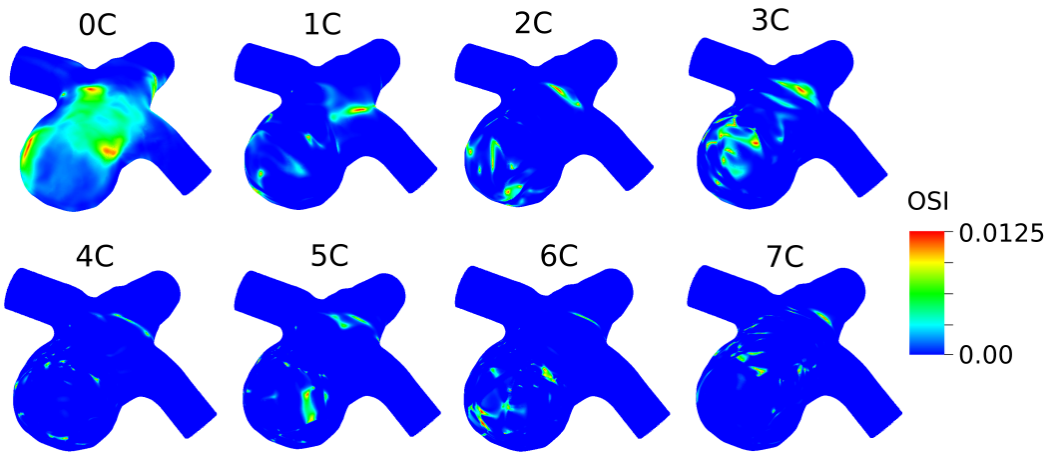

Figure 6.11: Oscillatory shear index (OSI) distributions with different packing densities.

Blood cannot reside for a long period of time in an environment of high and oscillating flow, so thrombus are usually formed in low and oscillating wall shear stress (LOWSS) regions. However, as previously explained, thrombosis and increase risk of rupture occur simultaneously. Therefore, regions of low and oscillating flows can also be prone to wall degradation and rupture (Russell et al., 2013). This suggests that high OSI cannot be the sole discriminator of aneurysm rupture. To also take account of the effects of low WSS, the low and oscillating wall shear stress index (LOWSSI) for each coiling cases are plotted as shown in Figure 6.12. For MCA aneurysms, time-averaged WSS below 2.27 Pa (Fukazawa et al., 2015) and OSI value above 0.0125 (Miura et al., 2013) were used as threshold values for the LOWSSI. Prior to coiling, high WSS was observed in the dome of the aneurysm (shown by low LOWSSI values), while LOWSS regions were mostly localised at the neck. There is a small area of LOWSS on the side where blood flow leaves the untreated aneurysm after a large vortical structure was formed (Lee et al., 2013).

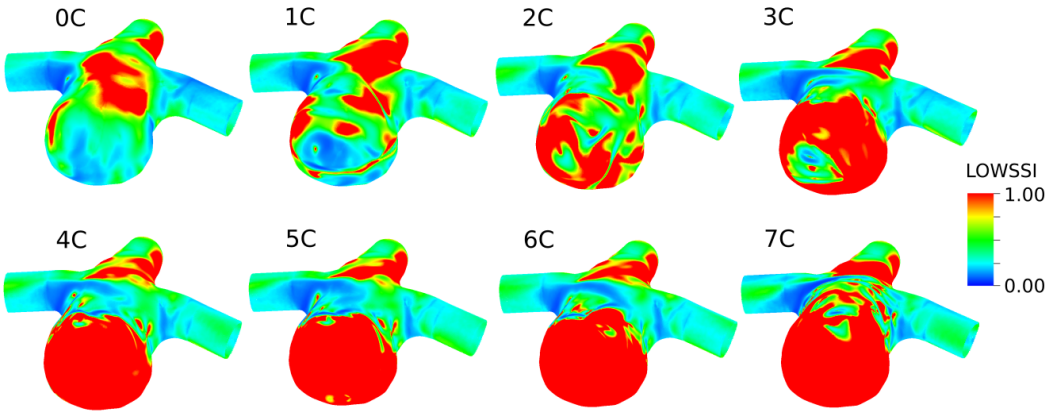

Figure 6.12: Regions of low and oscillating WSS induced by different packing densities.

As coil packing density increases, LOWSS regions started to form around the neck of the aneurysm first, before proceeding into the dome area. It was also reported in a previous study that wall degradation is initiated from the neck to continued the dome (Sadasivan et al., 2013). Unlike the regions of high OSI, the regions of LOWSS (marked by LOWSSI) increased proportionally with coil packing density. Additional coils proceeding the fourth coil did not significantly increase LOWSS regions in the aneurysm dome and its parent artery. Therefore, both thrombosis and the risk of rupture can be sufficiently reduced since the insertion of the fourth coil. Although the risk of rupture (OSI) towards the aneurysm tip is the lowest in the 7 coil case, a slight decrease in the LOWSS region (LOWSSI) was observed at the neck. This is caused by the sharp velocity distribution in the neck region of the aneurysm treated with 7 coils (Figure 6.4f). The unexpected local reduction in LOWSS area at the highest packing density is therefore understood as another risk factor for aneurysm recurrence after coiling. This also suggests that for a highly coiled aneurysm (7 coil case), high flow oscillations (OSI $>$ 0.0125) induce thrombus formation instead of aneurysm rupture at the aneurysm tip if accompanied by low wall shear stress.

Without any coil, thrombus cannot be formed in the untreated aneurysm as LOWSSI << 1.0. The confirms that coil intervention is crucial for thrombus initiation in an aneurysm. LOWSSI << 1.0 indicates that the WSS in that region of the untreated aneurysm must be above 2.27 Pa. However, lower WSS was observed at the neck and the upstream bifurcation anastomosis with three flow impingement areas as shown in Figure 6.13. Inflow impingement at the neck occured on both sides of the aneurysm. However, only the impingement point on the back side occured upon the blood inflow into the sac due to the excessive wall angulation on the opppostie side. This angled wall resulted in a biased flow direction into the aneurysm via the flat back side. After the flow exited the aneurysm, it impinged on the neck (point A) first before diverting its direction only to impinge on the bifurcation wall (point B) again.

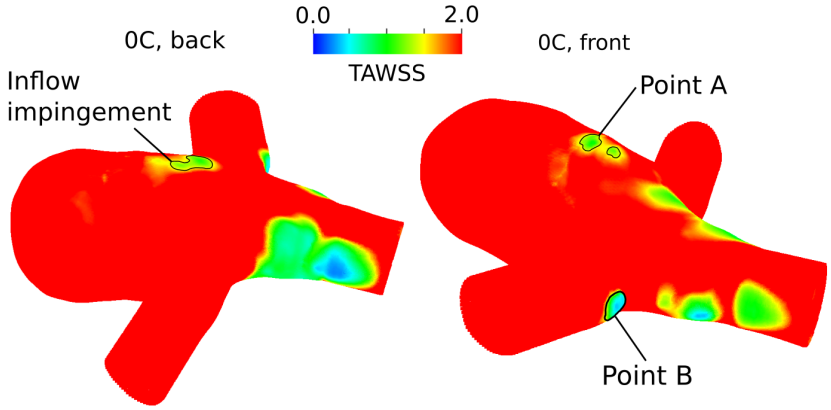

Figure 6.13: Flow impingement highlighted by abnormal low TAWSS (less than 2 Pa) region on the untreated aneurysm.

Flow impingment is further studied by investigating its relation to oscillating WSS vectors. Contours of normalised impingement ratio (NIR) on both sides of the aneurysm are shown in Figures 6.14a-b. Yellow and light blue regions indicate flow impingement while dark blue regions represent no flow impingement. Additionally, low WSS region (WSS < 1 Pa) is enclosed by the black isolines. It is shown that flow impingement induces localised reduction in WSS. The location of the highest NIR, or the strongest impingement point, oscillated at a high frequency but is bounded by this low WSS region

(black isoline). Moreover, the flow impingement point is highly correlated with the centre of WSS vector rotation as shown in Figures 6.14c-d. WSS vectors within the range of the flow impingement regions formed a rotating pattern (bounded by the pink lines) regardless of its position on the aneurysm wall.

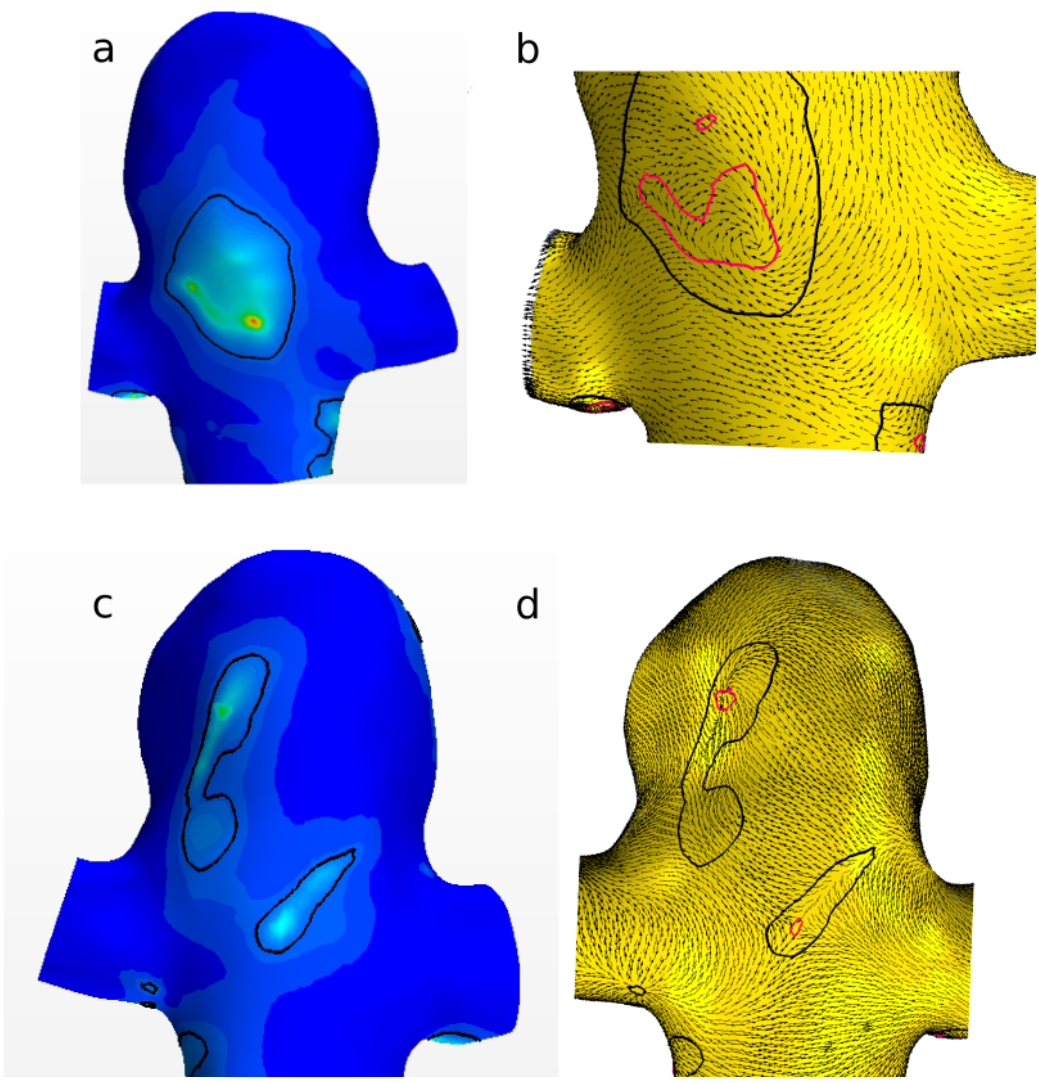

Figure 6.14: Normalised impingement ratio (NIR) on the (a) front and (b) back sides of the aneurysm and WSS vectors on the (c) front and (d) back sides of the aneurysm. Black lines enclose region of low WSS (WSS < 1 Pa) and flow impingement in both figures. Pink lines in Figure c-d enclose area of high impingement ratio (NIR > 0.1).

As thrombosis-induced wall degradation, the risk of rupture increases despite the aneurysm dome being thrombosed. In response to this wall inflammation, leukocyte are recuited into the aneurysm dome. In other words, thrombus formation and leukocyte migration are known to reduce the rupture risk. Figure 6.15 illustrates the predicted progression of leukocyte adhesion to the wall and thrombus formation. The contours of different colours represents different ranges of WSS corresponding to different levels of thrombosis and leukocyte adhesion (Rayz et al., 2010). Upon insertion of the first coil, WSS reduction below the healthy value of 1.5 Pa was observed at the bifurcation region. After the second coil was inserted, the WSS near the inflow impingement region was reduced to a value close to 0.4 Pa, which promotes leukocyte activities (Zhou et al., 2017). As the packing density increases, the dome became more prone to thrombosis (as also shown in Figure 6.12) and leukocyte aggregates gradually moved from the neck, through the coils, into the aneurysm tip. Moreover, the aggregated leukocyte started to change its shape from a hollow ring into a compact oval shape in some regions as they reaches the aneurysm tip. Leukocytes surrounded the area where thrombus is initiated as packing density is increased. Leukocytes migration and thrombus formation are shown in more detail at three locations indicated by three sets of coloured arrows.

At the location indicated by black arrows, leukocytes circled around the site of WSS reduction (5C) and aggregated into a compact shape before inducing thrombus (6C), and leaving the thrombosed site (7C). A similar pattern was observed at location indicated by the white arrow. A delayed leukocyte aggregation was observed as indicated by the green arrows, where WSS reduction and leukocyte accumulation in a ring shape was formed after insertion of the seventh coil. However, at this stage of coiling, lower possibility of thrombus formation despite an increase in leukocyte activity was observed at the dome. This suggests that there is a decrease in both thrombus formation and risk of rupture (as also shown by Figure 6.12. To the best of the author's knowledge, this study is the first to numerically investigate the relationship between leukocyte behaviour and thrombus formation in coiled aneurysms of different packing densities.

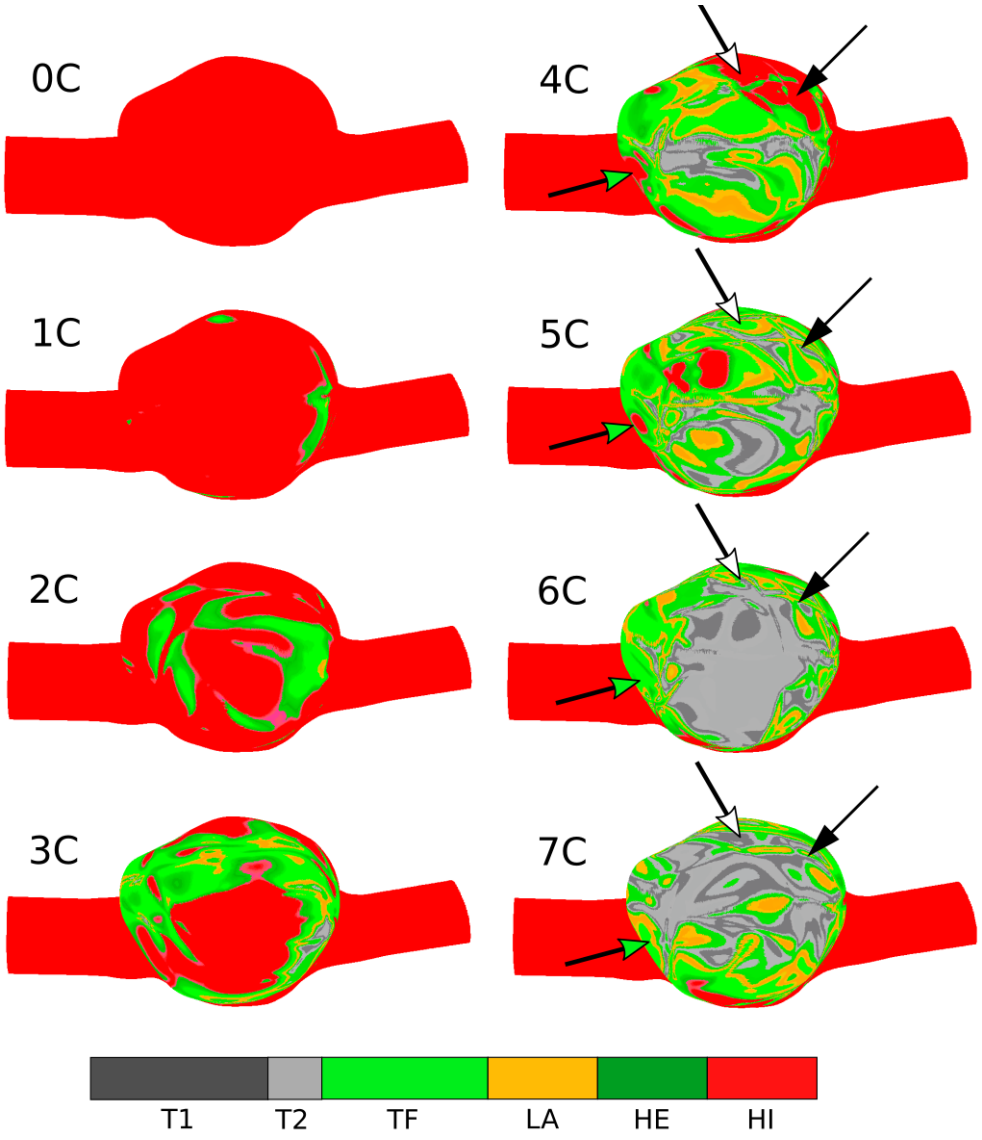

Figure 6.15: Prediction of thrombus formation and leukocyte activation based on changes in the time-averaged wall shear stresses (TAWSS) for different coiling cases. Colour labels in relation to TAWSS (Pa): HI - high WSS regions that are not prone to thrombus (TAWSS $>$ 2Pa), HE - healthy state (0.45 $<$ TAWSS $<$ 2.0Pa), LA - leukocyte adhesion (0.35 $<$ TAWSS $<$ 0.45 Pa), TF - Regions prone to thrombosis (0.2 $<$ TAWSS $<$ 0.35 Pa), T2 - thrombus induction (0.15 $<$ TAWSS $<$ 0.2 Pa), and T1- potential thrombus formation (0 $<$ TAWSS $<$ 0.15 Pa). Coloured arrows indicate locations referred to in the text.

6.4 Aneurysm recurrence

The risk of aneurysm rupture can be reduced by thrombus formation and leukocyte migration into the inflamed aneurysm wall. This can be achieved through aneurysm coiling. However, flow recanalisation can still occur even though an aneurysm is highly packed with coils. In that case, the aneurysm may regrow and recurrence can occur (Otani et al., 2018). As a result, the occluding aneurysm can again be prone to rupture. In the present study, flow recanalisation has been observed after the insertion of the seventh coil despite a high and optimal packing density. This is shown by the mean velocity magnitude isosurface in Figure 6.4 and the increase in passive scalar concentration $1.90 < \text{TAPS/SD}(\text{TAPS}_{0C}) < 2.10$ in Figure 6.7. Previous studies have observed the roles of aneurysm morphology, local coil packing density at the neck region and not anywhere else, wall shear stress, and flow velocity in aneurysm recurrence. The present study investigates the effects of local coil packing density (of the whole aneurysm sac), leukocyte adhesion, and wall complaince on aneurysm recurrence.

Since aneurysm recurrence occured after the insertion of the seventh coil, the 6 and 7 coil cases are observed. The local packing densities (LPD) along the depth of the aneurysm in both cases have been calculated and shown in Figure 6.16a. A total of 38 cross-sectional planes parallel to the ostium plane were created and evenly distributed along the depth of the aneurysm as shown in Figure 6.16b. It can clearly be observed that the LPD in the region located 0.0-2.0 mm downstream of the neck have significantly increased as a result of the insertion of the seventh coil. As new coils are inserted, the original coil can slightly move to allow the new coil to fit in as coils are considered flexible. This is why a higher local packing density is observed in the 6 coil case at some locations along the aneurysm depth (4.4, 5.0, 5.6, and 6.8mm downstream of the neck).

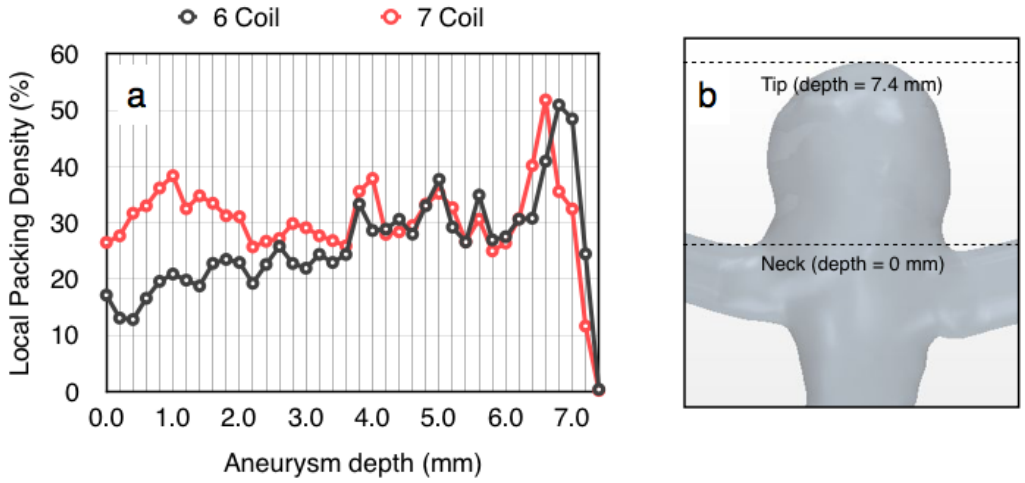

Figure 6.16: (a) Local packing densities of different cross sections along the aneurysm depth of the 6 and 7 coil case from the neck (0 mm) to the tip (7.4 mm) as shown in (b)

Local packing density

Figure 6.17 shows the cross-sectional area averaged velocity magnitude variations along the aneurysm depth during peak diastole and peak systole for both coiling cases. The averaged velocity during peak systole is always larger than that of end diastole regardless of local packing density and aneurysm depth. Averaged aneurysmal velocity in both coiling cases are compared to identify the location of recurrence during diastole and systole as shown in Figures 6.18 and 6.19, respectively. During end diastole (Figure 6.18), flow recanalisation has been observed 5.2 mm downstream of the neck, which corresponds to the decrease in the LPD at the aneurysm depths of 5.0 mm and 5.6 mm. Peak systolic flow recanalisation occur more upstream at the aneurysm depth of 4.6 mm downstream of the neck, which corresponds to the decrease in the LPD at the aneurysm depths of 4.4, 5.0, and 5.6 mm (Figure 6.19). The slight increase in LPD at 4.4 mm is more sensitive to the stronger peak systolic inflow and less sensitive to the weaker diastolic inflow. Therefore, the peak systolic recanalisation is also attributed to the lower LPD at 4.4 mm as well as that at 5.0 and 5.6 mm. At both cardiac phases, flow recurrence did not reach the aneurysm tip as it was prevented by the higher LPD of the seventh coil at aneurysm depth 6.20 - 6.65 mm.

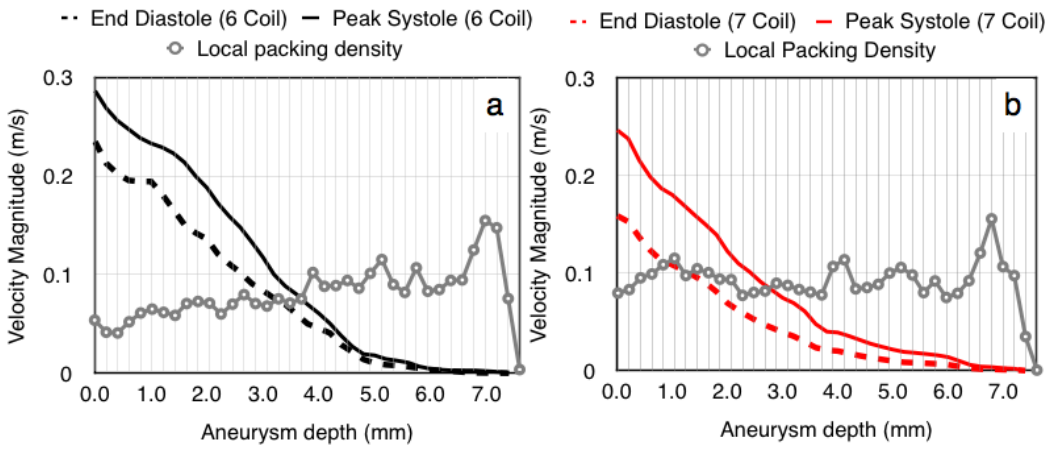

Figure 6.17: Cross-sectional area averaged velocity magnitude along aneurysm depth at end diastole (dashed) and peak systole (bold) and local packing densities (bold with symbol) of the (a) 6 and (b) 7 coil case.

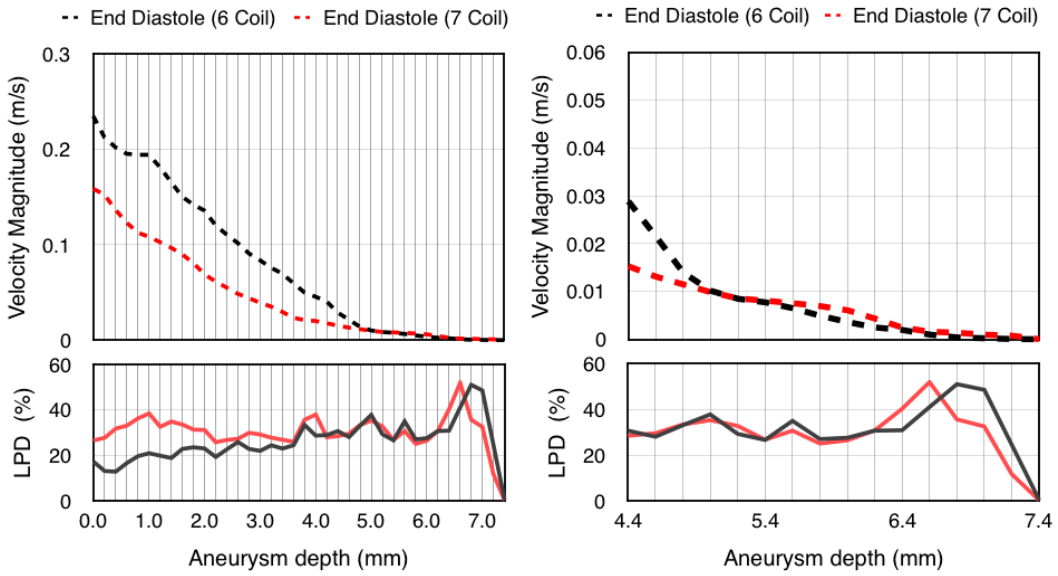

Figure 6.18: Cross-sectional area averaged velocity magnitude along aneurysm depth at end diastole of the 6 and 7 coils cases. The plot near the aneurysm tip is zoomed in as shown by the right figure.

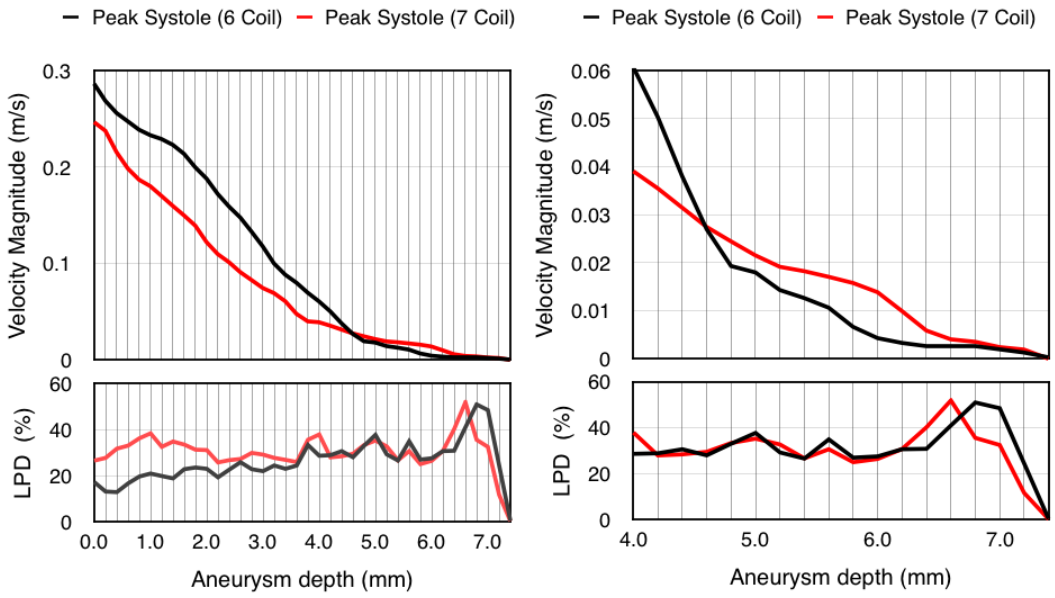

Figure 6.19: Cross-sectional area averaged velocity magnitude along aneurysm depth at peak systole of the 6 and 7 coils cases. The plot near the aneurysm tip is zoomed in as shown by the right figure.

The decrease in the LPD further downstream (6.65 - 7.40 mm) did not allow for additional flow recanalisation. This is because the flow velocity (0.002 m/s) immediately upstream of the aneurysm depth of 6.65 mm is already too low compared to 0.03 m/s at the aneurysm depth of 4.6 mm where the peak systolic flow recanalisation is initiated. The maximum increase in the averaged velocity which resulted in aneurysm recurrence at end diastole and peak systole are 0.0024 m/s (2.4 mm/s) and 0.0095 m/s (9.5 mm/s). The reduction in LPD have been observed to cause aneurysm recanalisation. Additionally, the magnitude of aneurysm recurrence is found to be dependent on the difference between the LPD of both coiling cases, the cardiac phase observed (and thus the inflow velocity) and the flow velocity immediately upstream of the recurrence location.

The flow recurrence observed in Figure 6.4 cannot be compared with that shown in Figures 6.18 and 6.19 because the former (Figure 6.4)) only shows the recanalisation of the mean flow and not that of the aneurysmal plane-averaged flow. The recanalisation of the plane-averaged velocity (Figures 6.18 and 6.19) occur further towards the aneurysm tip (aneurysm depth

= 4.6 mm) whereas that of the mean velocity (Figure 6.4) occur closer to the neck (aneurysm depth = 3.5 mm). Moreover, the flow recanalisation towards the aneurysm tip (Figures 6.18 and 6.19) is smaller in magnitude and hence not shown in the mean velocity isosurface. However, this flow recanalisation towards the aneuryy tip is observed in the passive scalar distribution for 7 coils in Figure 6.9.

Leukocyte Adhesion

Flow recanalisation and aneurysm recurrence can be observed in the 7 coil case when there is an increase in aneurysmal flow velocity, including that of the leukocyte phase. The effects of leukocyte migration and adhesion to the aneurysm wall on aneurysm recurrence has been investigated. Multiphase simulations have been performed for both coiling cases to take account of the plasma, red (RBC), and white (WBC) blood cells phases. The distribution of WBC (leukocytes) allows us to observe leukocyte adhesion to the aneurysm wall and risk of aneurysm recurrence resulting from flow recanalisation.

The change in the plane-averaged leukocyte phase velocity magnitude along the aneurysm depth is shown in Figure 6.20. Diastolic leukocyte flow recanalisation can be observed as early as 1.8 mm downstream of the neck, but significant aneurysm recurrence occured at the aneurysm depth of 3.2 mm. At peak systole, the leukocyte flow recanalisation at 1.8 mm becomes more significant and flow recanalisation downstream of this aneurysm depth is maintained. Maximum difference in the diastolic and systolic averaged leukocyte velocity between the two coiling cases occured at 3.4 mm and 4.6 mm downstream of the neck, respectively. The increase in leukocyte inflow after the insertion of the seventh coil may correspond to leukocyte migration into the aneurysm sac as a result of wall degradation due to platelet-thrombus formation as observed in Figure 6.12. Biologically, leukocyte migration is controlled by cytokines released from inflammatory endothelial cells on the aneurysm wall. However, the present CFD simulation does not take account of cell biology. Therefore, leukocyte activation by cytokines and their biological responses to the inflamed aneurysm wall are not shown. Only the increase

in leukocyte inflow into the aneurysm dome after the insertion of the seventh coil is presented. This may suggest that aneurysmal haemodynamic can independently contribute to leukocyte migration in response to thrombus-induced wall inflammation.

Additionally, flow recanalisation has previously been found to correspond with an increase in local WSS (Otani et al., 2018). In this study, regions of increased WSS is the region where the WSS of the 7 coil case is higher than that of the 6 coil case, and not necessarily the region of relatively higher WSS along the cirumference of the aneurysm in both cases. Seven planes parallel to the ostium plane were created and evenly distributed along the aneurysm depth. The WSS along the circumference of each plane 1-7 are shown in Figure 6.21. Locations along the aneurysm circumference subjected to leukocyte adhesion are shown at the bottom of each plot. The caption explains what each coloured lines represent.

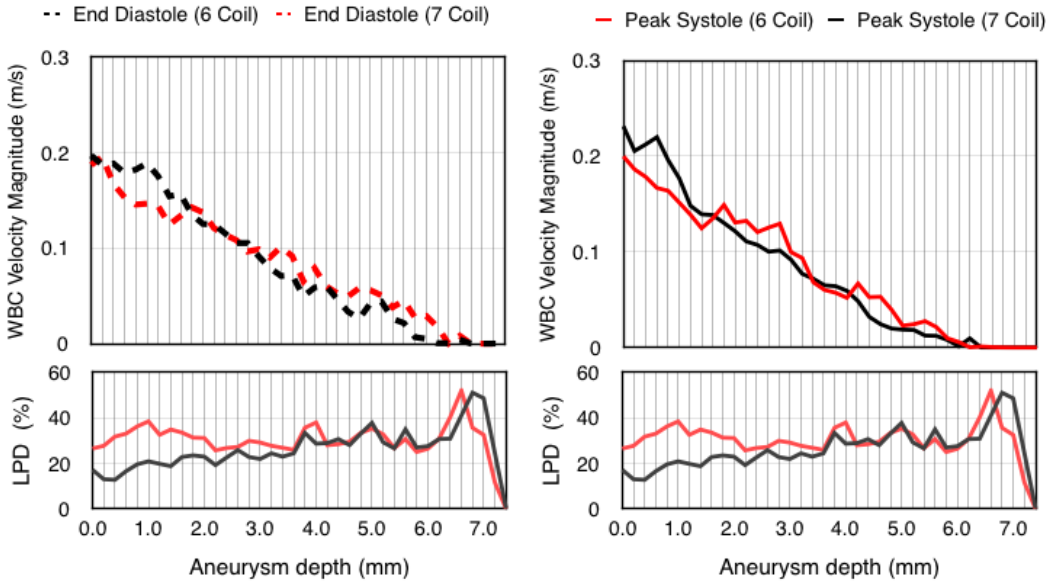

Figure 6.20: Cross-sectional area averaged velocity magnitude of white blood cells (leukocytes) along aneurysm depth at end diastole (left) and peak systole (right) of the 6 and 7 coils cases.

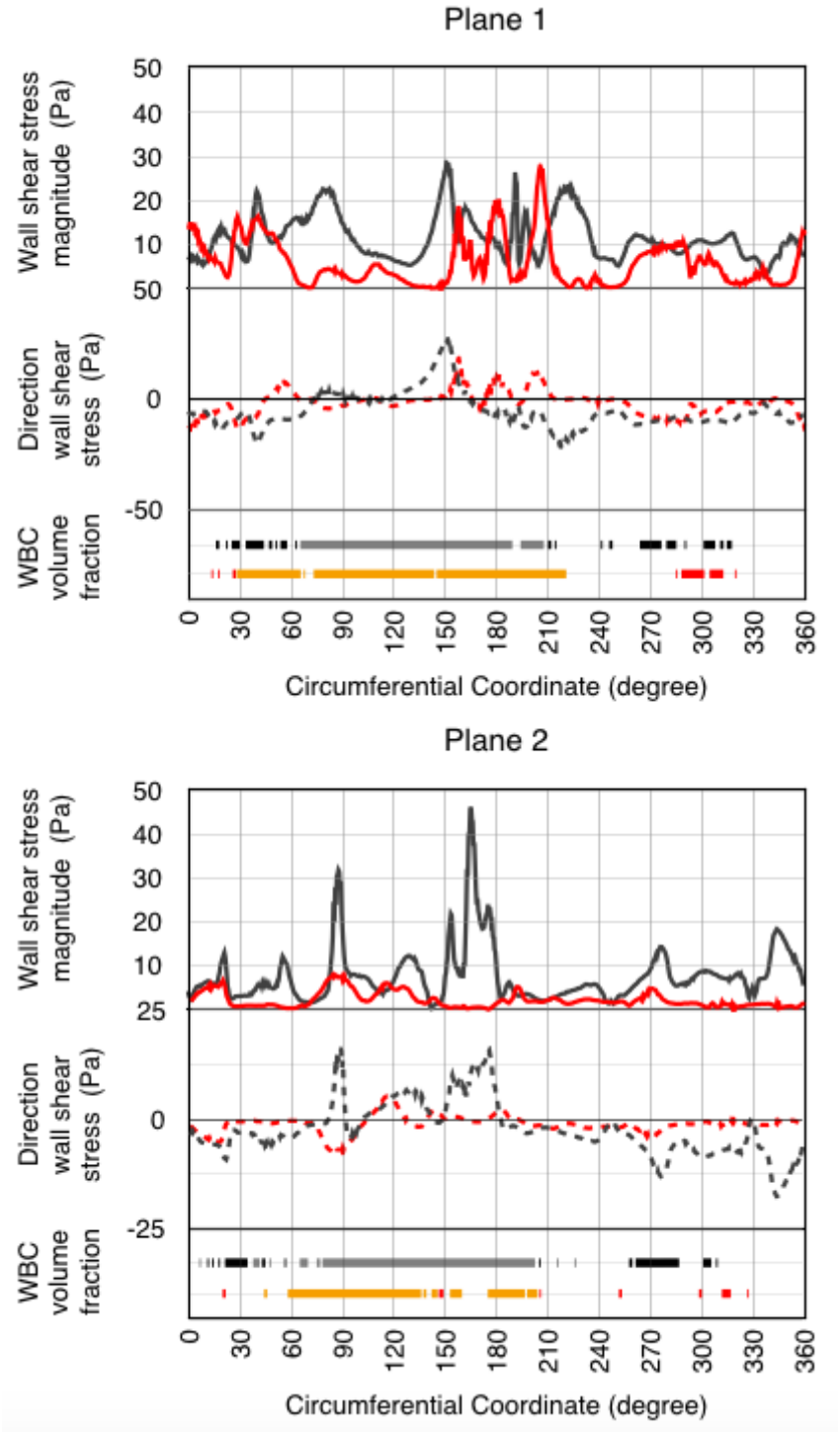
Plane 1
Wall shear stress magnitude (Pa)
50
40
30
20
10
50
Direction wall shear stress (Pa)
0
-50
WBC volume fraction
0
30
60
90
120
150
180
210
240
270
300
330
360
Circumferential Coordinate (degree)
Plane 2
Wall shear stress magnitude (Pa)
50
40
30
20
10
25
Direction wall shear stress (Pa)
0
-25
WBC volume fraction
0
30
60
90
120
150
180
210
240
270
300
330
360
Circumferential Coordinate (degree)

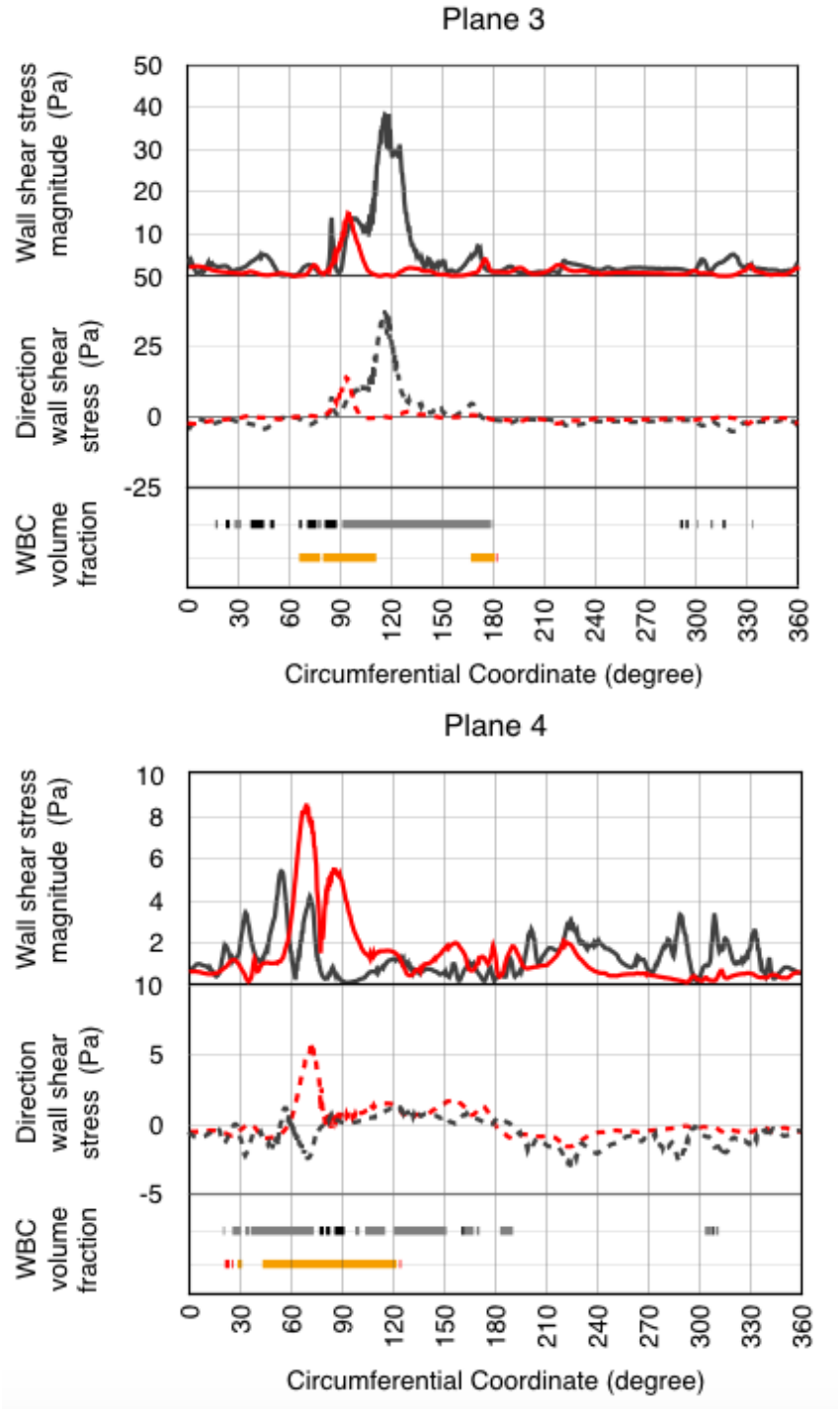
Plane 3
Wall shear stress magnitude (Pa)
50
40
30
20
10
Direction wall shear stress (Pa)
50
25
0
-25
WBC volume fraction
0
30
60
90
120
150
180
210
240
270
300
330
360
Circumferential Coordinate (degree)
Plane 4
Wall shear stress magnitude (Pa)
10
8
6
4
2
Direction wall shear stress (Pa)
10
5
0
-5
WBC volume fraction
0
30
60
90
120
150
180
210
240
270
300
330
360
Circumferential Coordinate (degree)

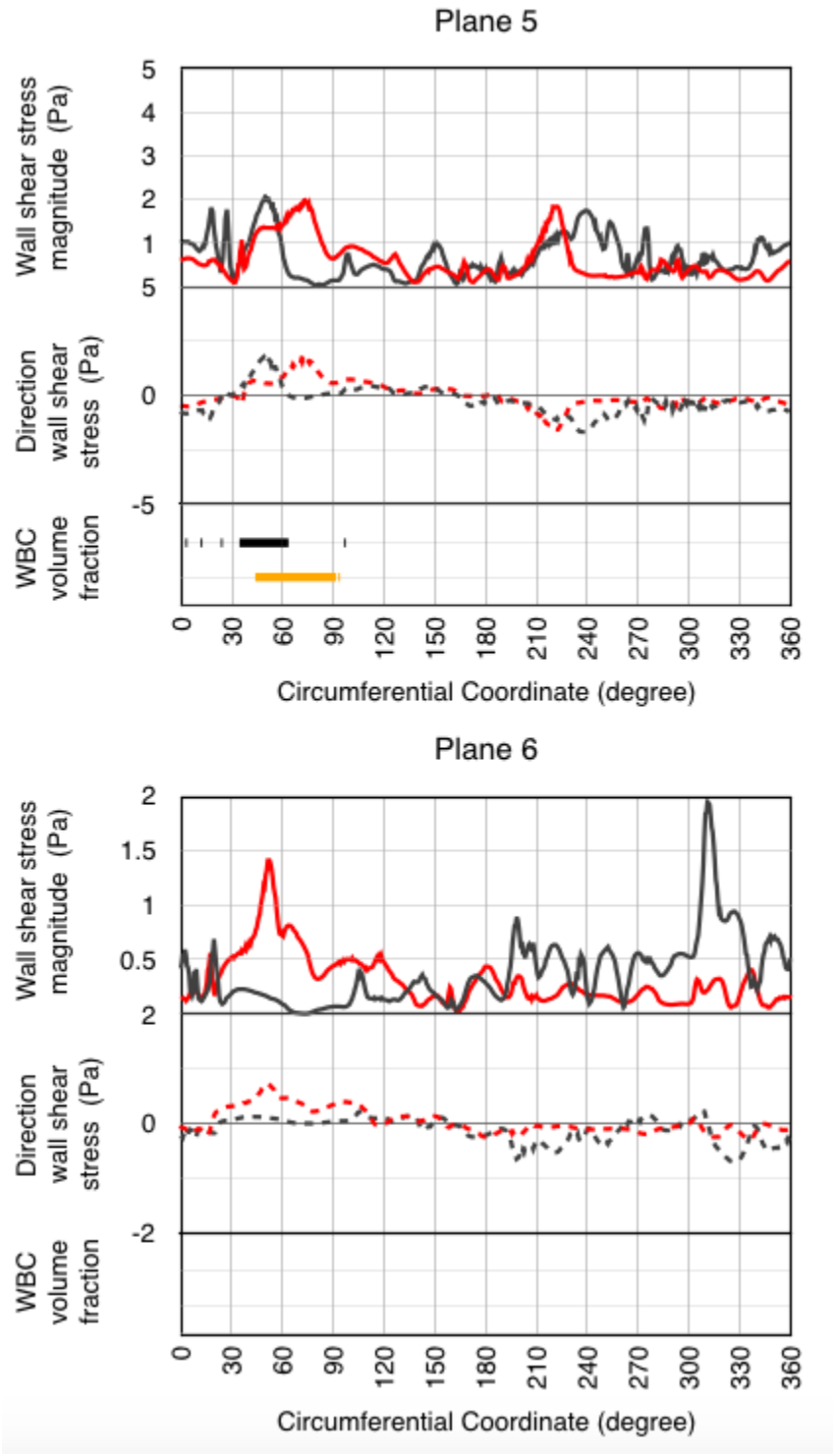
Plane 5
Wall shear stress magnitude (Pa)
5
4
3
2
1
5
Direction wall shear stress (Pa)
0
-5
WBC volume fraction
0
30
60
90
120
150
180
210
240
270
300
330
360
Circumferential Coordinate (degree)
Plane 6
Wall shear stress magnitude (Pa)
2
1.5
1
0.5
2
Direction wall shear stress (Pa)
0
-2
WBC volume fraction
0
30
60
90
120
150
180
210
240
270
300
330
360
Circumferential Coordinate (degree)

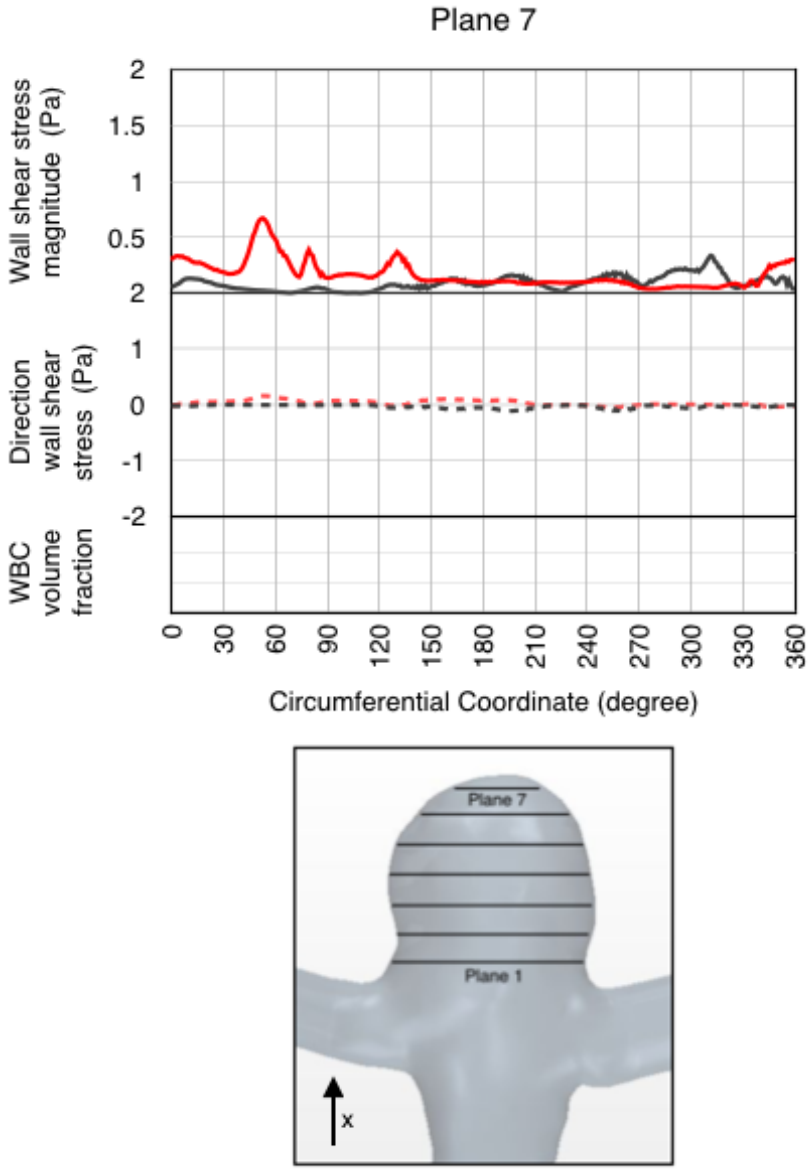

Figure 6.21: Each figure consists of three sections; Wall shear stress magnitude (bold lines in the top section), Directional wall shear stress (dashed lines in the middle section), and location of leukocyte adhesion to the wall (bold lines in the bottom section) along the circumference of cross-sectional planes 1-7 inside the aneurysm dome. Black and red lines for wall shear stresses represent the 6 and 7 coil cases, respectively. In the bottom section, grey and orange lines represent leukocyte volume fraction of 1% in the 6 and 7 coil cases. The black and red lines represent leukocyte volume fraction above % in the 6 and 7 coil cases.

The circumferential WSS in both coiling cases decreased with aneurysm depth. In planes 1-3, the circumferential WSS decreased after the insertion of the seventh coil, which is attributed to the significant increase in the LPD in this (aneurysm neck) region. However, the increase in LPD becomes insignificant downstream of plane 4 (aneurysm depth of 4.0 mm) where this trend of decreased WSS no longer applies. The increase in WSS at and downstream of plane 4 is a result of flow recanalisation observed in Figure 6.19. Although the WSS of the 7 coil case in planes 5-7 generally remained higher than that of the 6 coil case, the WSS in both cases are lower than 2 Pa. This low WSS environment contributed to the formation of thrombus in both cases as seen in Figure 6.12. The adhesion of leukocytes, especially those of WBC volume fraction above 1%, decreases with aneurysm depth. Furthermore, reduction in leukocyte adhesion has been observed after the insertion of the seventh coil. As flow recanalisation also occured towards the aneurysm tip, it is suggested that flow recanalisation is associated with a reduction in leukocyte adhesion. Towards the aneurysm tip (downstream of plane 6) where leukocyte adhesion is no longer presented, peak systolic recanalisation of leukocyte flow is also not observed. The absence of leukocyte adhesion towards the aneurysm tip (downstream of plane 6 and aneurysm depth of 6 mm) is attributed to the negligibly small averaged leukocyte phase velocity in both coiling cases rather than flow recanalisation. This suggests that flow recanalisation is associated with a reduction in leukocyte adhesion but is not necessarily associated with an absence of leukocyte adhesion. Additionally, this region of no leukocyte adhesion corresponds to the region of low WSS (WSS $<$ 2Pa) and thrombus formation. This suggests that thrombus formation towards the aneurysm tip is not attributed to leuckoyte adhesion, but is instead attributed to the platelet aggregation induced by low WSS.

The decrease in aneurysm rupture risk towards the aneurysm tip (Figure 6.11), due to increased thrombus formation, is attributed to the absence of leukocyte adhesion. Without the additional aggregation of leukocytes to the existing platelet-thrombus on the wall, the rupture risk is not increased. This absence in leukocytes may slow down the response to wall inflammation, but that is not modelled and considered in CFD simulations. The increase

in leukocyte adhesion at circumferential coordinates of 60-80 degrees in plane 5 is attributed to the local increase in high WSS in plane 4 and 5 (due to the local coil arrangement). Reduction in leukocyte adhesion is found to be corresponded with regions of reverse or low WSS as shown by the directional WSS plots. This can be observed in the circumferential coordinates of 240-280 degrees on plane 1; 10-60 and 260-300 degrees on plane 2; 110-170 degrees on plane 3; and 30-45 and 120-150 degrees on plane 4. On plane 5, the slight increase in leukocyte adhesion at 60-90 degrees corresponded with relatively higher and positive WSS. This confirms that a reduction in leukocyte adhesion corresponds to LOWSS regions where platelet-thrombus are formed. Therefore, wall inflammation associated to high rupture and recurrence risk is predicted to be corresponded to a reduction in leukocyte adhesion.

Wall compliance

The effects of wall compliance on aneurysm recurrence has also been investigated. FSI simulations have been performed for both coiling cases. The cross-sectional area averaged velocity magnitude variations along the aneurysm depth in the case of a compliant wall at end diastole and peak systole are shown in Figures 6.22 and 6.23, respectively. They are compared with that of the rigid wall case (superimposed) from Figures 6.18 and 6.19. In the neck region (aneurysm depth 0-0.8 mm), the averaged velocity in the wall compliant aneurysm is slightly higher than that of the rigid case at both time instances. However, downstream of 0.8 mm, the averaged velocity in the wall complaint aneurysm is lower. The averaged velocities in the majority of the aneurysm volume has been overestimated by the rigid wall assumption. At the aneurysm depth of 4.4 mm, the end diastolic averaged velocity in the wall complaint aneurysm with 7 coils decreased to 0.002 m/s (2 mm/s).

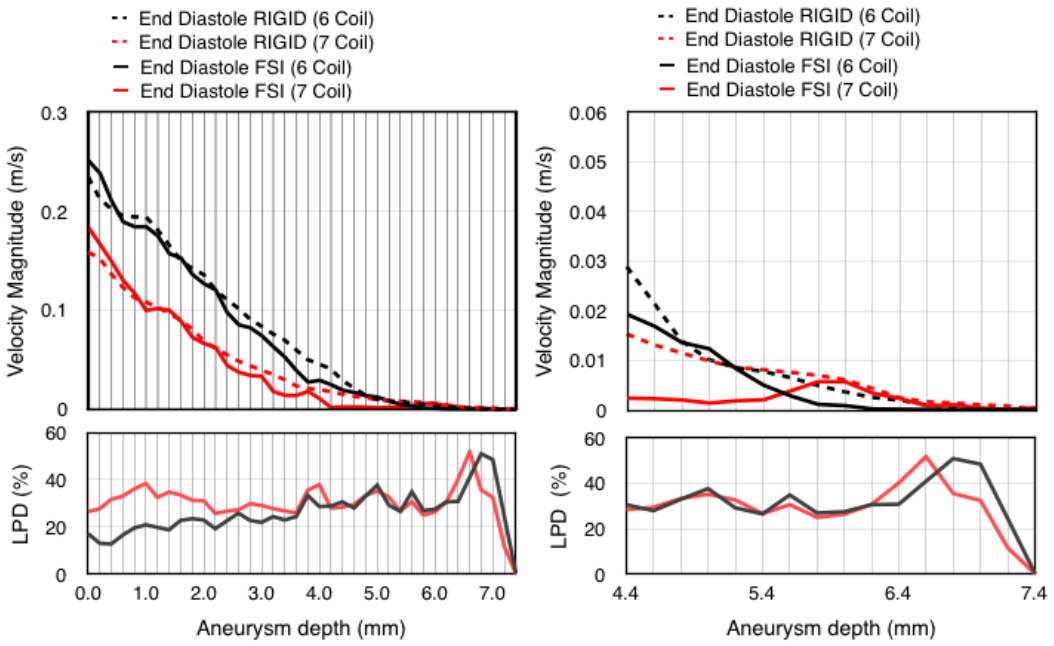

Figure 6.22: Cross-sectional area averaged velocity magnitude along aneurysm depth at end diastole of the 6 and 7 coils RIGID and FSI cases.

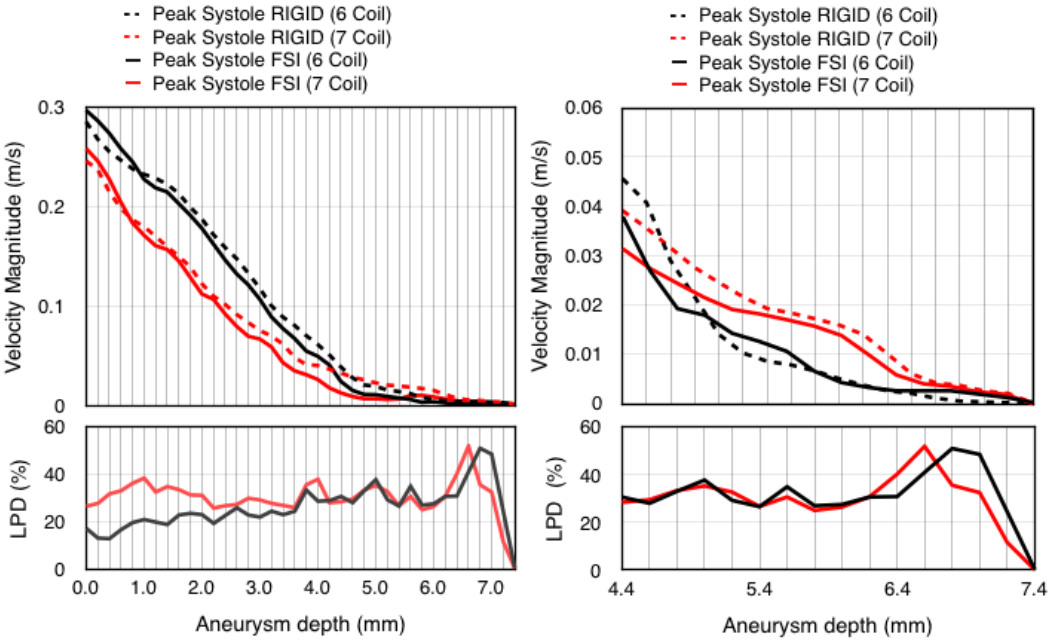

Figure 6.23: Cross-sectional area averaged velocity magnitude along aneurysm depth at peak systole of the 6 and 7 coils RIGID and FSI cases.

Diastolic flow recanalisation occur at 5.5 mm downstream of the neck, approximately at the same aneurysm depth where diastolic flow recanalisation in rigid wall is observed. However, in the wall compliant aneurysm, the magnitude of diastolic flow recanalisation is larger (0.006 m/s) due to the more significant decrease in the averaged velocity of the wall complaint case in the region between 4.8 - 5.8 mm downstream of the neck. At peak systole, the effect of wall compliance is slightly more significant compared to that of end diastole in the region upstream of the flow recanalisation, which occured at the aneurysm depth of 4.6 mm. Like that of the end diastole, the systolic flow recanalisation in the rigid wall case occured close to that of the complaint wall case at the aneurysm depth of 4.75 mm. The maximum flow recanalisation in both rigid and compliant wall cases has been observed at 6.0 mm downstream of the neck.

Radial displacement of the complaint aneurysm wall in both coiling cases are shown in Figure 6.24 with locations of leukocyte adhesion. A local cylindrical coordinate system has been created for each plane with an origin located at the centre of the plane. The radial displacement at each wall gridpoint along the circumference of the plane is measured by the distance between the centre of the plane to the respective gridpoint. An imbalance in the radial displacements of the two sides of the aneurysm has been observed. One side has a slightly larger displacement than the other and that is the side corresponding to the circumferential coordinates of 0-180 degrees (side A). On this side of the aneurysm, the radial displacement generally increased with aneurysm depth and reached up to 0.015 mm. On side B of the aneurysm (circumferential coordinates of 180-360 degrees), a slightly smaller displacement (of up to -0.009 mm) can be observed. A negative radial displacement means that the wall element is displaced closer to the aneurysm centre after one timestep. This does not necessarily means the aneurysm is being compressed. An aneurysm is subjected to expansion (or compressed) when both sides of the aneurysm has positive (or negative) displacement, respectively. If both sides have displacement vectors of opposite signs, like that of the present study, the aneurysm is translating. However, in this case, the displacement magnitude on side A (with positive radial displacement) is higher. This means that the aneurysm

is both translating and expanding on side A, signaling slight aneurysm growth.

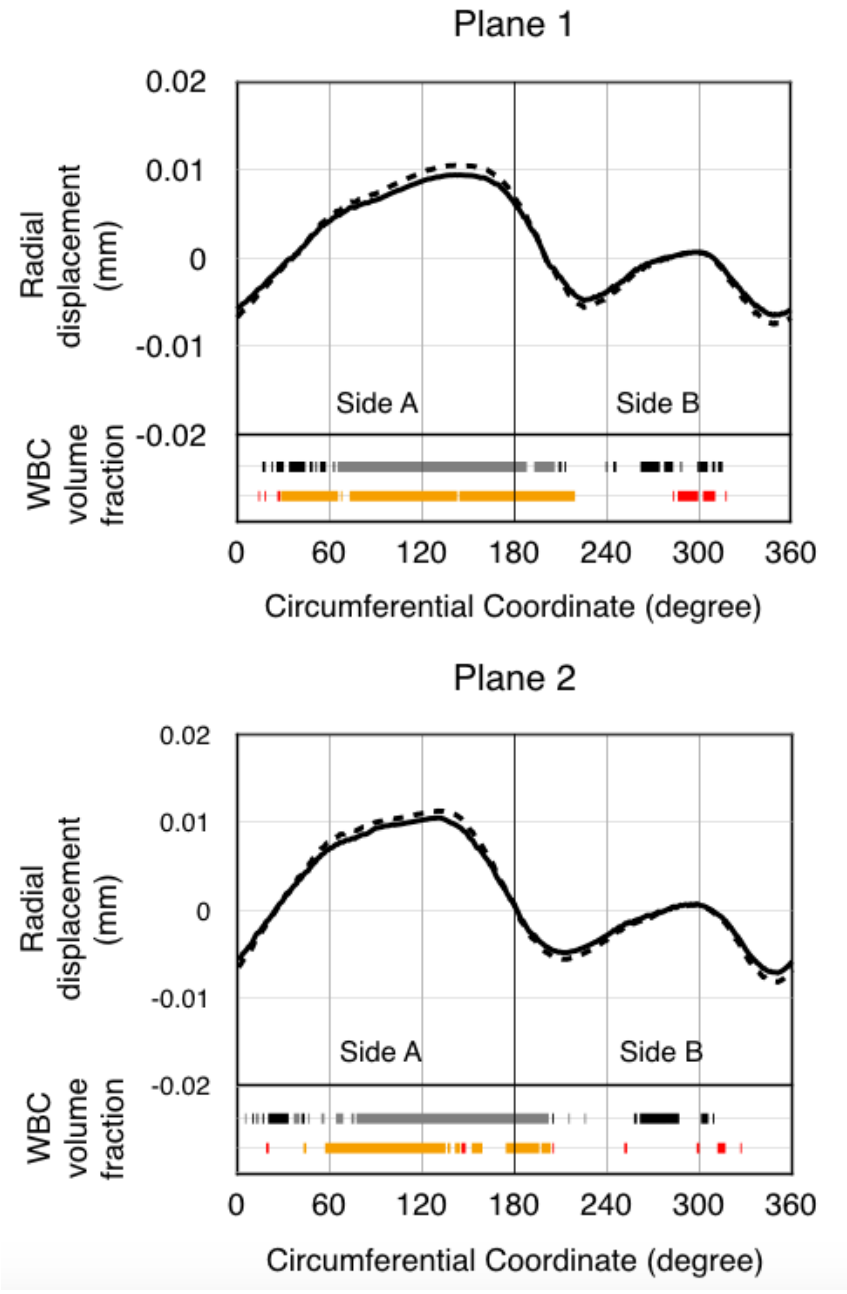

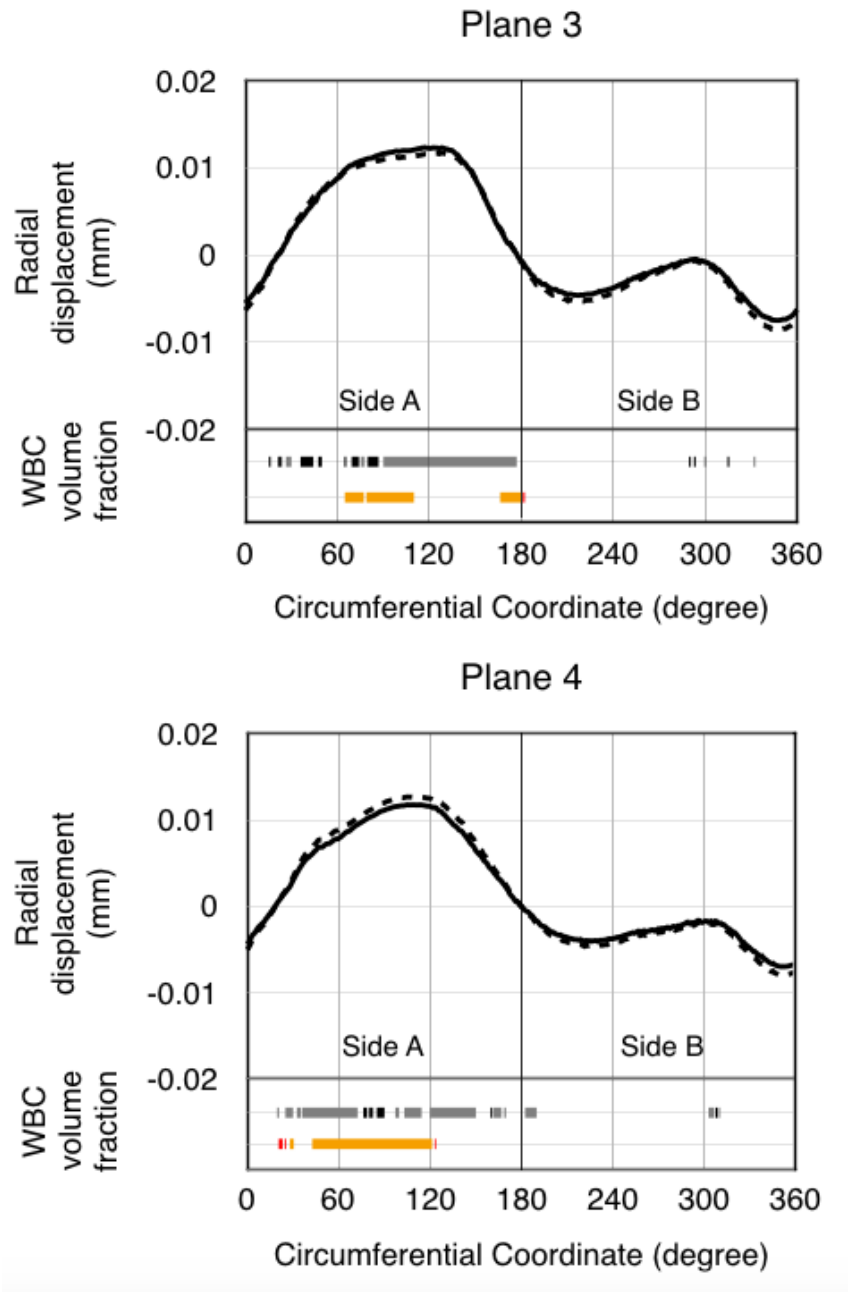
Plane 3
Radial displacement (mm)
0.02
0.01
0
-0.01
-0.02
Side A
Side B
WBC volume fraction
0
60
120
180
240
300
360
Circumferential Coordinate (degree)
Plane 4
Radial displacement (mm)
0.02
0.01
0
-0.01
-0.02
Side A
Side B
WBC volume fraction
0
60
120
180
240
300
360
Circumferential Coordinate (degree)

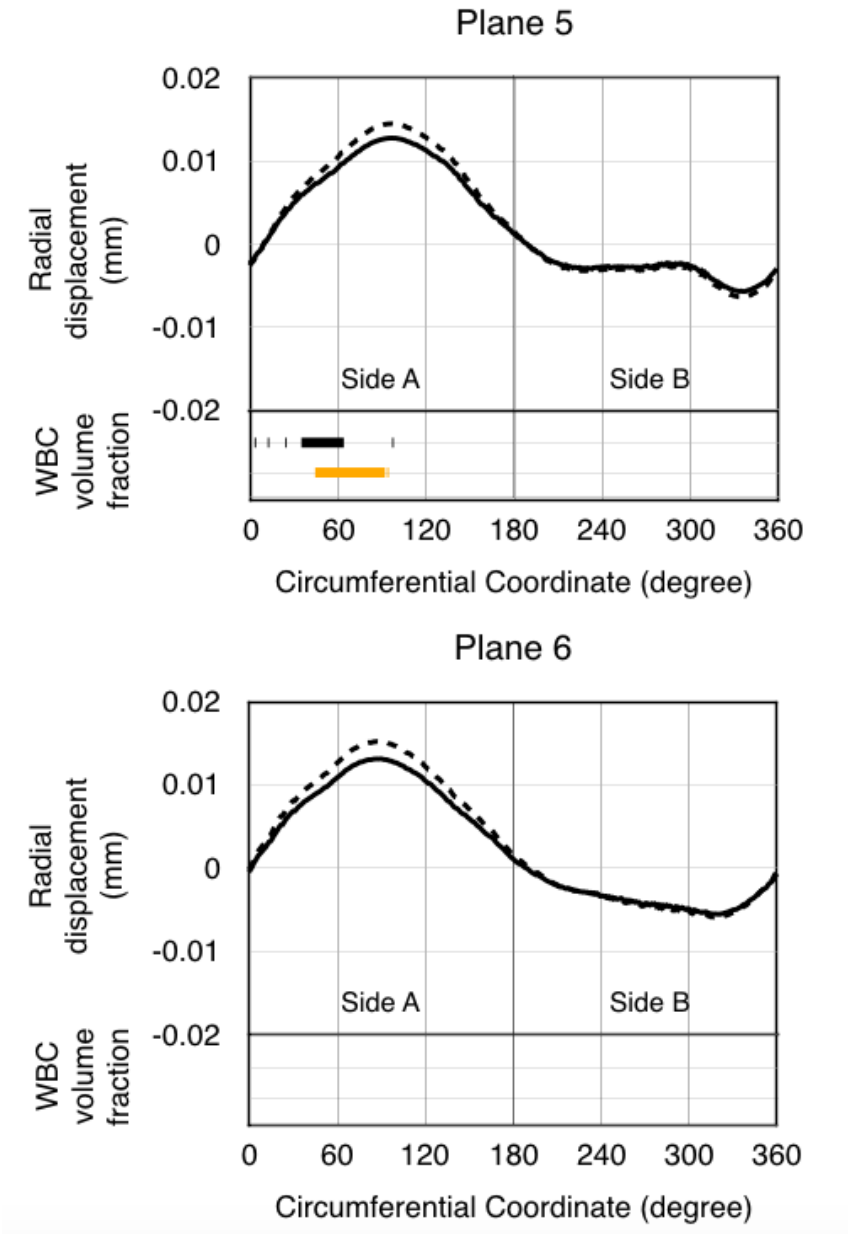
Plane 5
Radial displacement (mm)
0.02
0.01
0
-0.01
-0.02
Side A
Side B
WBC volume fraction
0
60
120
180
240
300
360
Circumferential Coordinate (degree)
Plane 6
Radial displacement (mm)
0.02
0.01
0
-0.01
-0.02
Side A
Side B
WBC volume fraction
0
60
120
180
240
300
360
Circumferential Coordinate (degree)

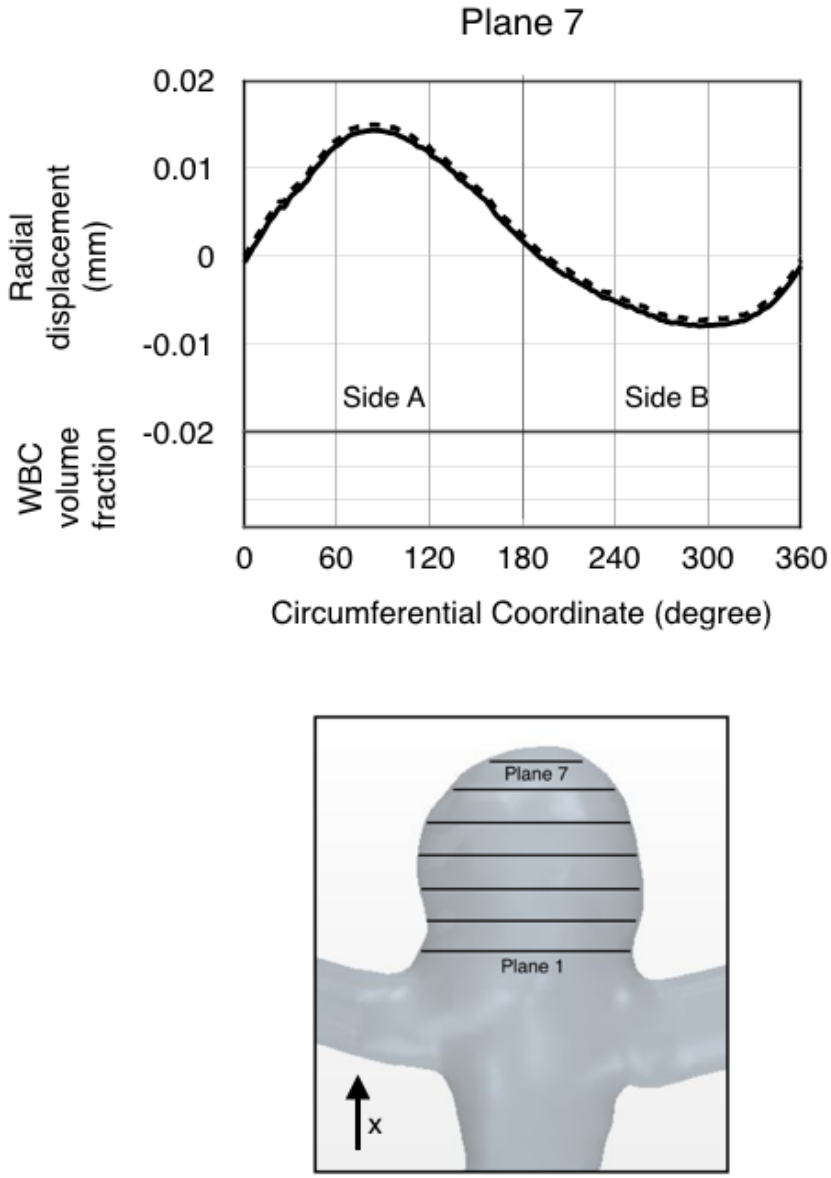

Figure 6.24: Radial displacement and location of leukocyte adhesion to the wall along the circumference of cross-sectional planes 1-7 inside the aneurysm dome with 6 (black) and 7 (red) coils.

Aneurysm recurrence has been strongly related to aneurysm regrowth . Normally as coil packing density increases, the risk of rupture and recurrence decreases due to thrombus formation. In that case, aneurysm regrowth is less likely to occur. The aneurysm radial displacement would decrease after the insertion of additional coils. On the other hand, if aneurysm recurrence exists, the aneurysm wall displacement would not be reduced (or it could be increased in the worst case) despite the insertion of additional coils.

On side A of planes 1-5, the reduction in leukocyte adhesion after the insertion of the seventh coil corresponds with identical or insignificant decrease in the aneurysm wall displacement compared to the case of 6 coils. Therefore, a reduction in leukocyte adhesion does not just signify aneurysm recurrence, but also a risk of aneurysm regrowth. An insignificantly smaller reduction in the radial displacement has been observed in plane 1 (260-280 degrees), plane 2 (10-50 and 260-290 degrees), plane 3 (20-50 and 120-170 degrees), and plane 4 (150-190 degrees) where a reduction in leukocyte adhesion was observed. On plane 5, there is a slight increase in leykocyte adhesion in the circumferential coordinates of 60-100 degrees). which corresponds to a more significant decrease in the wall displacement (no aneurysm regrowth). However, this cannot be applied to planes 6 and 7 located towards the aneurysm tips as there is no leukocyte adhesion. The most significant decrease in the radial displacement among all planes is observed in plane 6 (90 degrees). This may be associated with the the significantly reduced risk of rupture (Figure OSI) and thrombus formation at its greatest extend (Figure LOWSSI).

On side B (circumferential coordinates 180-360 degrees), aneurysm wall moved in towards the aneurysm centre. Leukocytes are predicted to adhere more densly to the wall of this side of the aneurysm (especially in the neck region) as the WBC volume fraction of the leukocyte adhesion in this region is over 1%. The increased proximity between the aneurysm wall and the coils (due to negative displacement) may contributed to such leukocyte accumulation with higher WBC volume fraction but smaller region of adhesion. As aneurysm depth increased, the two local peaks in the radial displacement gradually transformed into a single peak regardless of coiling case. There were no

significant differences in the radial displacements of both coiling cases on this side of the aneurysm. Major leukocyte adhesion on this side of the aneurysm is not observed downstream of plane 2.

Compliant coil case study

A separate simulation has been performed to study the effects of a compliant coil on aneurysmal haemodynamics. The aneurysm wall is assumed to be rigid in this case. Mechanical properties of platinum is used to model the compliant coil. Figure 6.25 shows contours of the coil displacement in the streamwise (x) and tranverse (y) directions at peak systole. Due to aneurysmal tortuosity, the blood flow preferred to enter the aneurysm and impinge the coil mass on one side rather than the other. This resulted in a higher coil displacement (in the streamwise direction) on the side subjected to flow impingement. The coil, especially in the neck region, is then displaced towards the other side of the aneurysm wall. The temporal variation of coil displacements in all three direction follows the mass flow rate waveform imposed at the inlet as shwon in Figure 6.26. This suggests that coil displacement is significantly affected by the inflow waveform. The maximum coil displacement magnitude reached up to 0.3 um. This displacement is small compared to that of the aneurysm because platinum is stiffer than arterial tissue. As this study is the first to investigate the effects of compliant aneurysmal coil, the displacement cannot be compared with previous findings. However, clinical angiography of coils inside an aneurysm showed coil displacement of the same order of magnitude (Binning et al., 2014).

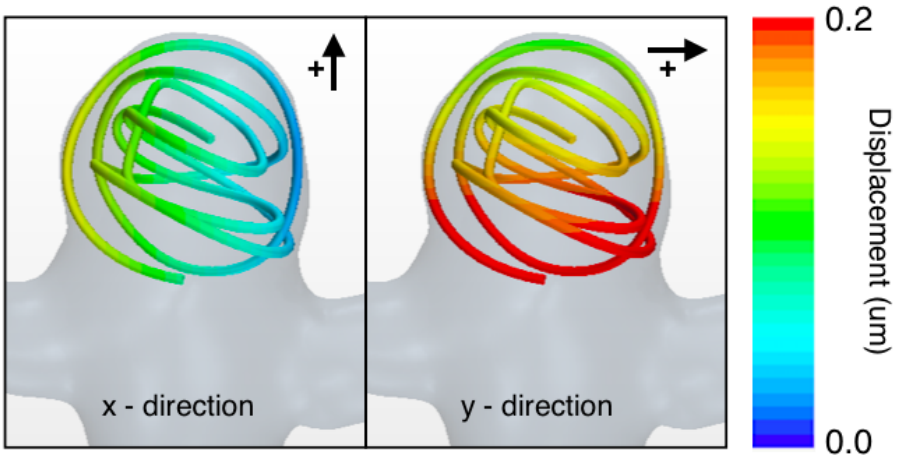

Figure 6.25: Displacement of the compliant coil in the streamwise (left) and transverse (right) directions inside the rigid-walled aneurysm at peak systole.

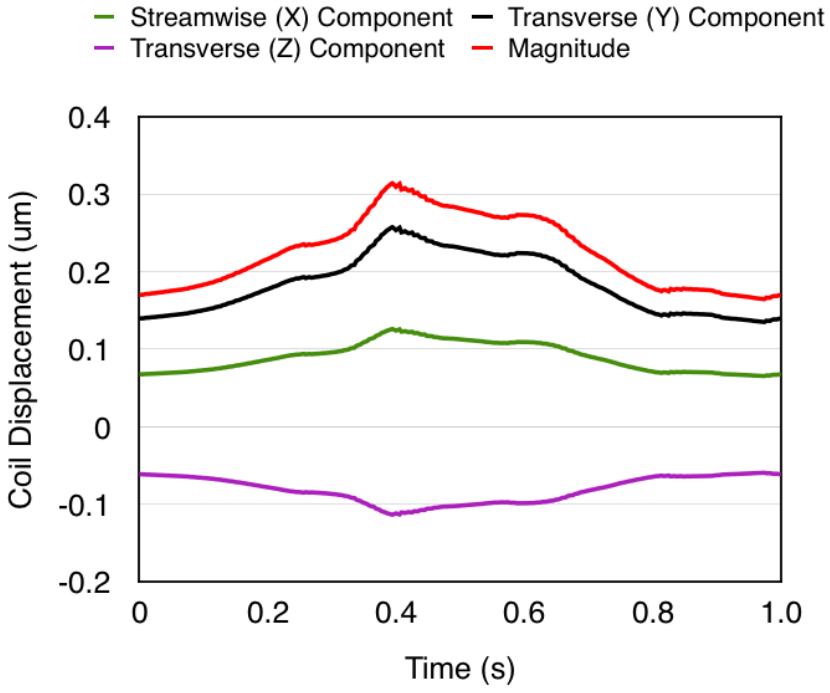

Figure 6.26: Temporal variations of coil displacements over a cardiac cycle.

The WSS on both the aneurysm wall and the coil are shown in Figure 6.27. Wall shear stress on the compliant coil is significantly smaller than that of the rigid coil as the flow energy on the compliant coil can be dissipated and converted into displacement. The maximum difference in the coil WSS between both cases (6.1 Pa) is observed at peak systole where the mean aneurysmal flow velocity is the highest.The aneurysmal WSS is smaller than that of the coil in both cases. However, the overestimation of aneurysmal WSS by the rigid coil is less significant than the overestimation of the coil WSS. The maximum difference in aneurysmal WSS between both cases is only 3.3 Pa at peak systole. This suggests that the WSS on both aneurysm and coil can be overestimated by the rigid coil and that their temporal variations follow that of the inflow waveform. The same conclusion can be made with the averaged aneurysmal velocity.

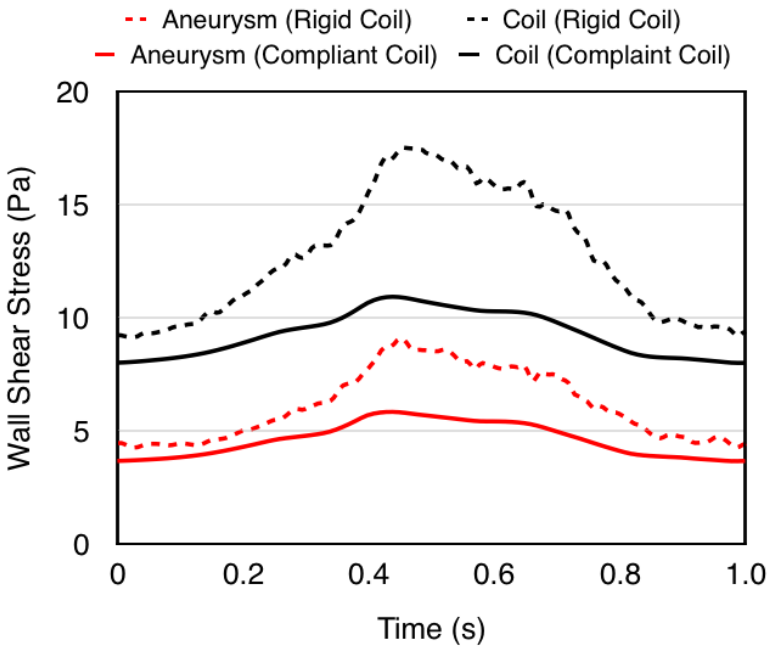

Figure 6.27: Temporal variations of wall shear stresses of the aneurysm and coil in rigid coil case and compliant coil case.

Figure 6.28 shows the plane-averaged velocity magnitude in eight different planes parallel to the ostium plane. The averaged velocity is significantly reduced in every planes as a result of compliant coil. The overestimation of averaged aneurysmal velcoity by rigid coil becomes clearer towards the aneurysm tip (plane 8).

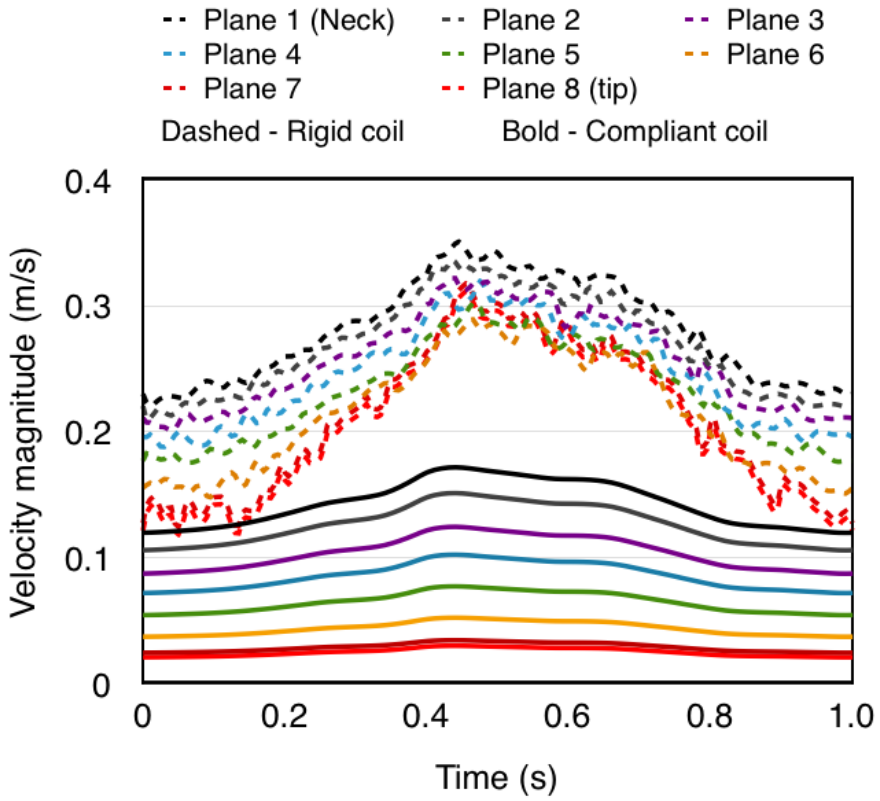

Figure 6.28: Temporal variations of plane-averaged velocity magnitude of different planes in the aneurysm in rigid coil case and compliant coil case.

Chapter 7

Effects of wall compliance and non-Newtonian haemodynamics on fistula maturation failure

Patients suffering from chronic kidney diseases require an arteriovenous fistula (AVF) that is sufficiently matured in order for haemodialysis to be carried out. However, over 50% of AVF were previously failed to mature and the underlysing mechanism is still unknown. AVF maturation failure is characterised by the inward remodelling and thickening of the vessel wall, which develops into neo-intimal hyperplastic stenosis. The assumptions of rigid vessel walls, Newtonian blood viscosity, and single-phase blood flow model in previous studies have limited our understanding on AVF wall remodelling and maturation. This chapter is divided into two sections.

The first section investigates the effects of non-Newtonian blood viscosity and wall complaince on AVF haemodynamics. Four simulations have been performed with wall conditions and blood viscosity described in Table 7.1. Different haemodynamic properties in all four cases are compared. Since low WSS promotes endothelial changes associated with AVF maturation failure, the spatial distribution of the end diastolic WSS are examined. Additionally, the present study also compares regions of flow recirculation, helicity, and other WSS derived parameters including the LOWSSI in all four cases.

Table 7.1: AVF case studies

Case	Wall condition	Blood viscosity
1	Rigid	Newtonian
2	Rigid	non-Newtonian
3	Compliant	Newtonian
4	Compliant	non-Newtonian

The second section discusses the effects of wall compliance, red blood cells viscosity, wall shear stress, von Mises stress, and flow recirculation on the remodelling of AVF walls. These haemodynamic factors are investigated in the non-Newtonian and complaint wall case (the most realistic one). Local distributions of these wall and volumetric haemodynamics are analysed to determine the mechanisms that leads to AVF maturation failure.

7.1 Non-Newtonian and wall complaint AVF

Different hemodynamic parameters in the four cases described in Table 7.1 were investigated. The spatial distributions of diastolic wall shear stress are plotted in Figure 7.1. The end diastole is chosen for investigation because it is the time instant at which low flow and WSS dominate and stenosis tends to develop. It is evident that the differences between Newtonian and non-Newtonian flow are less significant than the difference between rigid and compliant wall, especially in the arterial segment. This suggests that diastolic wall shear stress is not significantly affected by the shear-thinning property of non-Newtonian blood.

On the contrary, the overestimation (red arrows) and underestimation (blue arrows) of WSS by the rigid wall assumption at end diastole are more significant. WSS overestimation is typically observed in rigid models as the energy from the blood flow impinging into the vessel wall cannot be dissipated and converted into vessel displacement (McGah et al., 2014). This, however,

does not necessarily means that the rigid wall cannot underestimate WSS. In the present study, WSS overestimations (red arrows) were also found on arterial curvatures. Regions of WSS underestimation by rigid wall (blue arrows) have been observed, but only along the venous segment downstream of the artery exit. The arterial flow impinges the fistula wall two times; when it enters the bend and when it leaves for the vein. In the venous segment, the flow stagnation on the compliant wall is not as high as in the rigid wall case due to local damping and flow energy dissipation. Therefore, higher flow can enter the compliant vein, resulting in higher WSS at several locations on the compliant venous wall. This is shown by the venous WSS underestimation of the rigid wall marked by blue arrows in the vein. The wall thickness of the arterial and venous segments also affected the WSS overestimation. The thicker venous wall has a higher resistance to deformation, making it less compliant compared to the thinner-walled artery. If the arterial and venous walls were assumed to have the same thickness, WSS overestimation in the rigid-wall vein would be overpredicted. Nevertheless, WSS overestimation dominated the majority of the wall surface and can lead to underprediction of intimal hyperplasia due to low and oscillating WSS.

Regions of flow recirculation have been observed in all four cases as shown in Figure 7.2. There is no significant difference in the isosurface of flow recirculation regions in the Newtonian and non-Newtoninan case, except at site A where flow recirculation is slightly underestimated by the Newtonian flow. On the other hand, the effect of wall compliance on flow recirculation is clearly shown. Wall shear stress underestimation by the rigid wall at the vein entrance resulted in the overestimation of flow recircualtion at site A. The overestimation at this site is the most significant among all other sites of major differences in flow recirculation region (sites B, C, and D). The higher flow entering the compliant vein (due to smaller flow stagnation) resulted in smaller venous flow recirculation regions in the compliant wall cases. In the artery, upstream of the major flow stagnation points in the fistula, regions of flow recirculation is not affected by wall compliance. This suggests that a reduction in flow stagnation induced by wall compliance is significantly responsible for the overestimation of flow recirculation in rigid walls. Flow recirculation

is known to induce low and oscillating wall shear stress, which has been associated with intimal hyperplasia and AVF maturation failure. The rigid wall is found to have overestimated regions of flow recirculation in the AVF, especially in the venous segment where haemodialysis is performed. This means that rigid walls should not be assumed as it overestimated venous maturation failure.

Figure 7.3 shows the formation of counter-rotating vortices at the entrance to the fistula anastomosis, as also observed by Bozzetto et al. (2015). The rigid wall predicts an early formation of large counter-rotating vortices upstream of the fistula segment due to arterial curvature. Two counter-rotating vortices were formed with the clockwise and counter-clockwise rotation observed on the left and right sides of the vessel, looking towards the downstream direction. This pair of structures, also known as Dean's vortices, were also observed in the bended pipe flow downstream of the bending section (Wang et al., 2018). However, unlike in a regular pipe flow, the rotating vortices are unevenly balanced due to the patient-specific geometry. The rotation of both vortices meet at the outer wall where a higher WSS was observed. It is evident that the interaction between these vortices and the outer wall induced a high WSS. As the flow leaves the fistula, it impinges on the rigid wall while entering the vein and its downstream bend without any damping. This causes a greater deterioration in the vortical structure than that observed in the wall compliant vein. As flow impingement contributes to high WSS (Fulker et al., 2017), which consequently degrades the endothelium layer (Campa et al., 1987), the rigid wall can overpredict smooth muscle cells relaxation and thus inward remodelling in the venous segment. Inward remodelling of the vein can lead to immatured vascular access point for haemodialysis. Therefore, the rigid wall assumption can overpredict AVF maturation failure. Like that of flow recirculation, blood shear-thinning has negligible effects on AVF flow helicity.

Intimal hyperplasia and thrombosis, can lead to AVF maturation failure, are associated with low and oscillating wall shear stress (LOWSS) (Ene-Iordache and Remuzzi, 2012; Pike et al., 2017a). Stenotic development and inward wall remodelling can be expected in these regions. Therefore, the low

and oscillating wall shear stress index (LOWSSI) contours in all four cases, shown in Figure 7.4, are compared to see how AVF maturation failure is predicted in different cases. The threshold TAWSS and OSI values used for these LOWSSI contours are 0.6 Pa and 0.42, respectively (Shintani et al., 2018). Regions of low and oscillating WSS are shown in red (LOWSSI greater or equal to 1.0). It is predicted that these areas are prone to AVF maturation failure. Additionally, regions of LOWSS also correspond to locations of flow recirculation in Figure 7.2. The fistula segment (that connects the artery to the vein) is the only segment not prone to maturation failure as it has no no regions of LOWSS and this is true in all four cases. On the other hand, regions of LOWSS have been observed at arterial and venous curvatures. The rigid wall overestimated LOWSSI in the venous while most of of the arterial LOWSS regions were underestimated. The underestimation of arterial LOWSS regions by the rigid wall can be detrimental if part of the artery is occluded by unforseen stenosis development. If this happens, oxygenated blood from the artery cannot effectively reach endothelial cells downstream. With the arterial flow reduced due to a stenosis, the venous segment may fail to become matured. Non-Newtonian effects on LOWSS regions can be observed, especially in the complaint wall cases. The Newtonian assumption underestimated LOWSS region at the arterial curvature and vein entrance. However, the underestimation of LOWSSI by the Newtonian flow is less significant than that of the rigid wall. The overestimation in LOWSSI in the vein and underestimation in LOWSSI in the artery is a dangerous combination. The rigid wall assumption may misleadingly conclude that the vein needs more time to become matured and the artery is not prone to stenosis development when in fact the opposite is true. In that case, the arterial stenosis may cause downstream endothelial damage to the maturing (or matured) vein, preventing the successful maturation and haemodialysis.

Wall compliance significantly contributed to the overestimation of WSS, flow recirculation, flow helicity, and LOWSSI (in the vein). This suggests that AVF maturation failure can heavily be overestimated by the rigid wall assumption. The Newtonian flow, on the other hand, only contributed to the slight underestimation of flow recirculation and LOWSS regions in some areas.

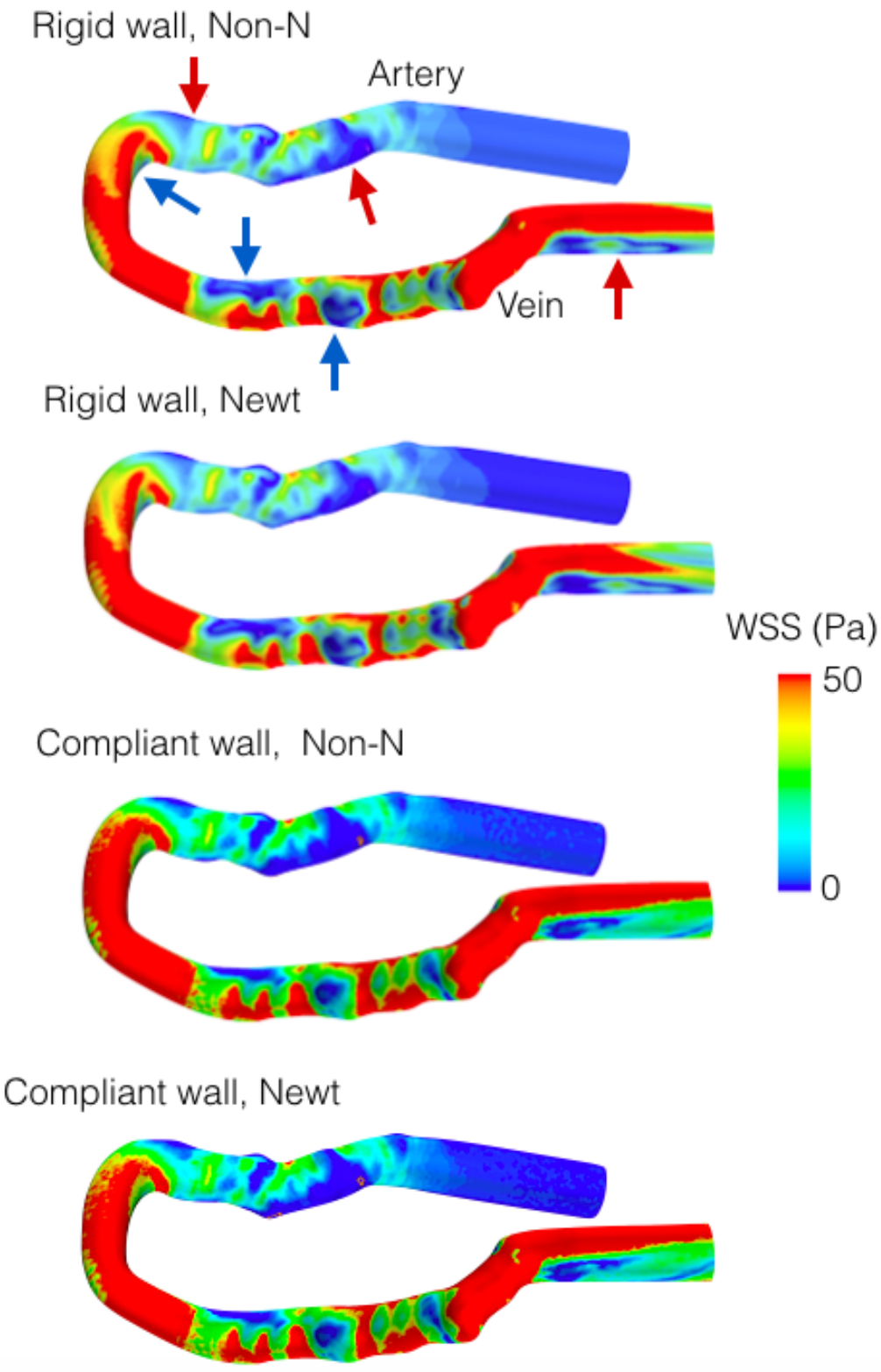
Rigid wall, Non-N
Artery
Vein
Rigid wall, Newt
WSS (Pa)
50
0
Compliant wall, Non-N
Compliant wall, Newt

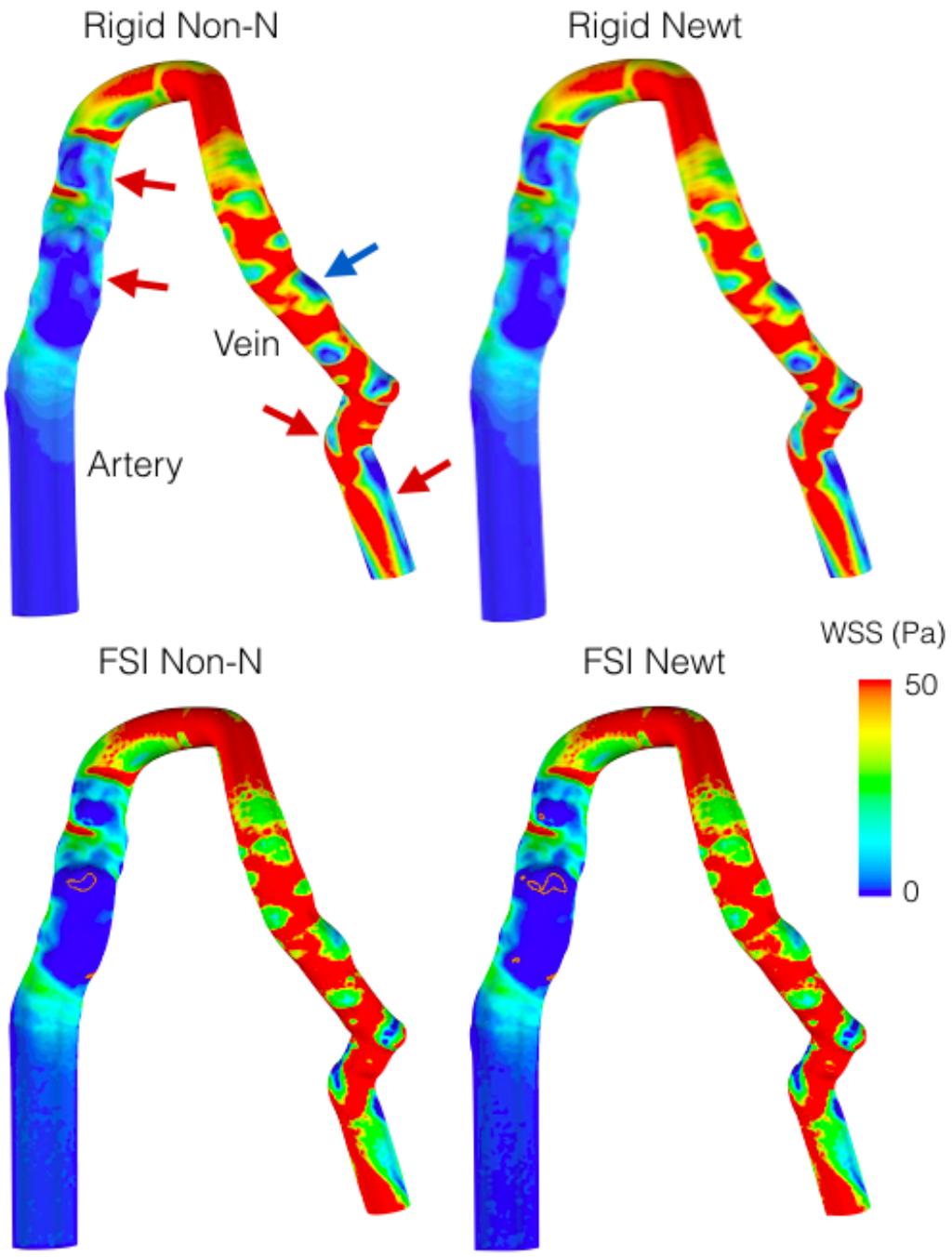

Figure 7.1: Distribution of diastolic wall shear stress in all four cases. Red and blue arrows indicate regions of major WSS overestimation and underestimation by the rigid wall assumption, respectively. White line contours encircle regions of WSS below 1 Pa.

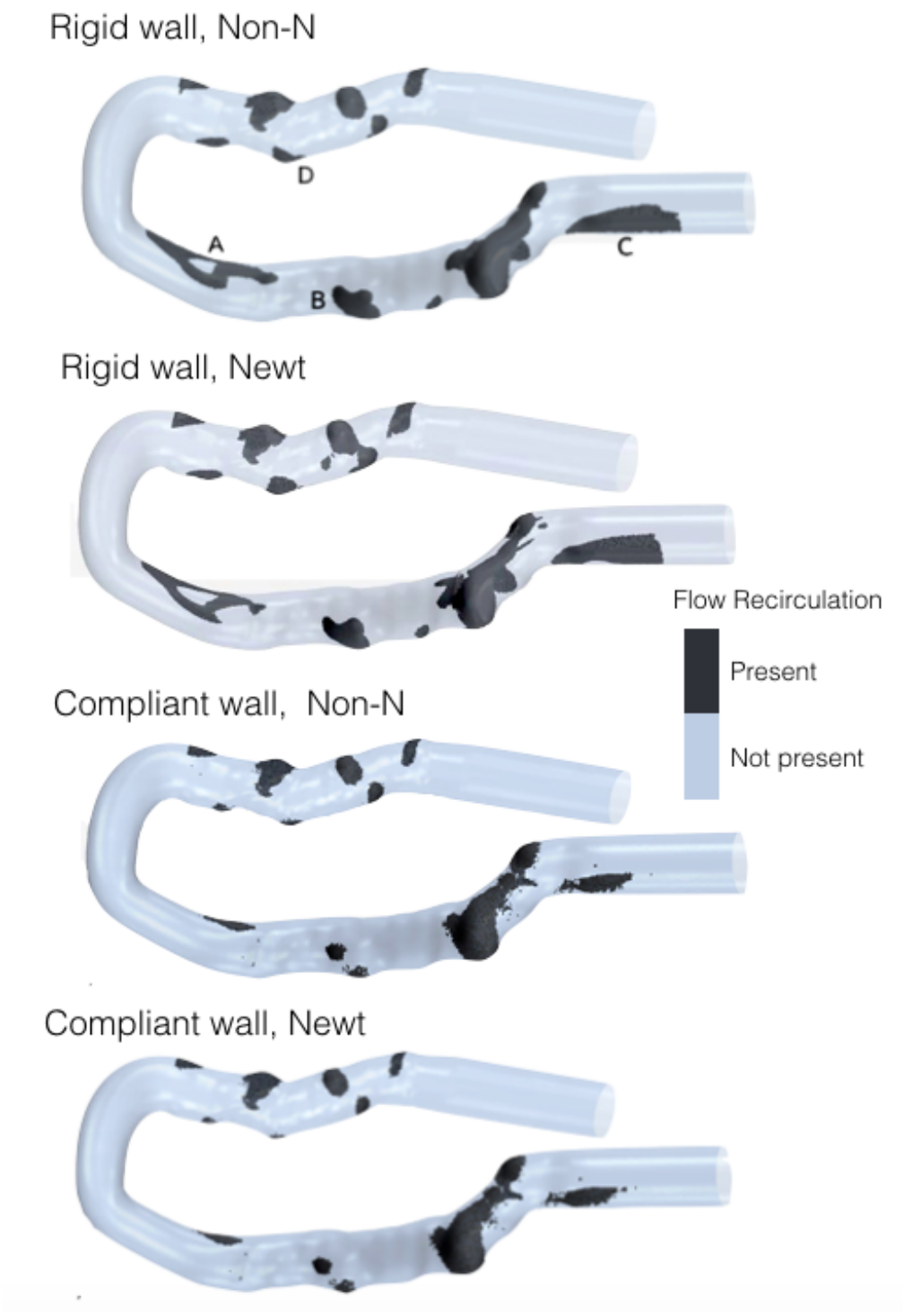

Figure 7.2: Isosurface of flow recirculation (negative streamwise velocity) in all four cases.

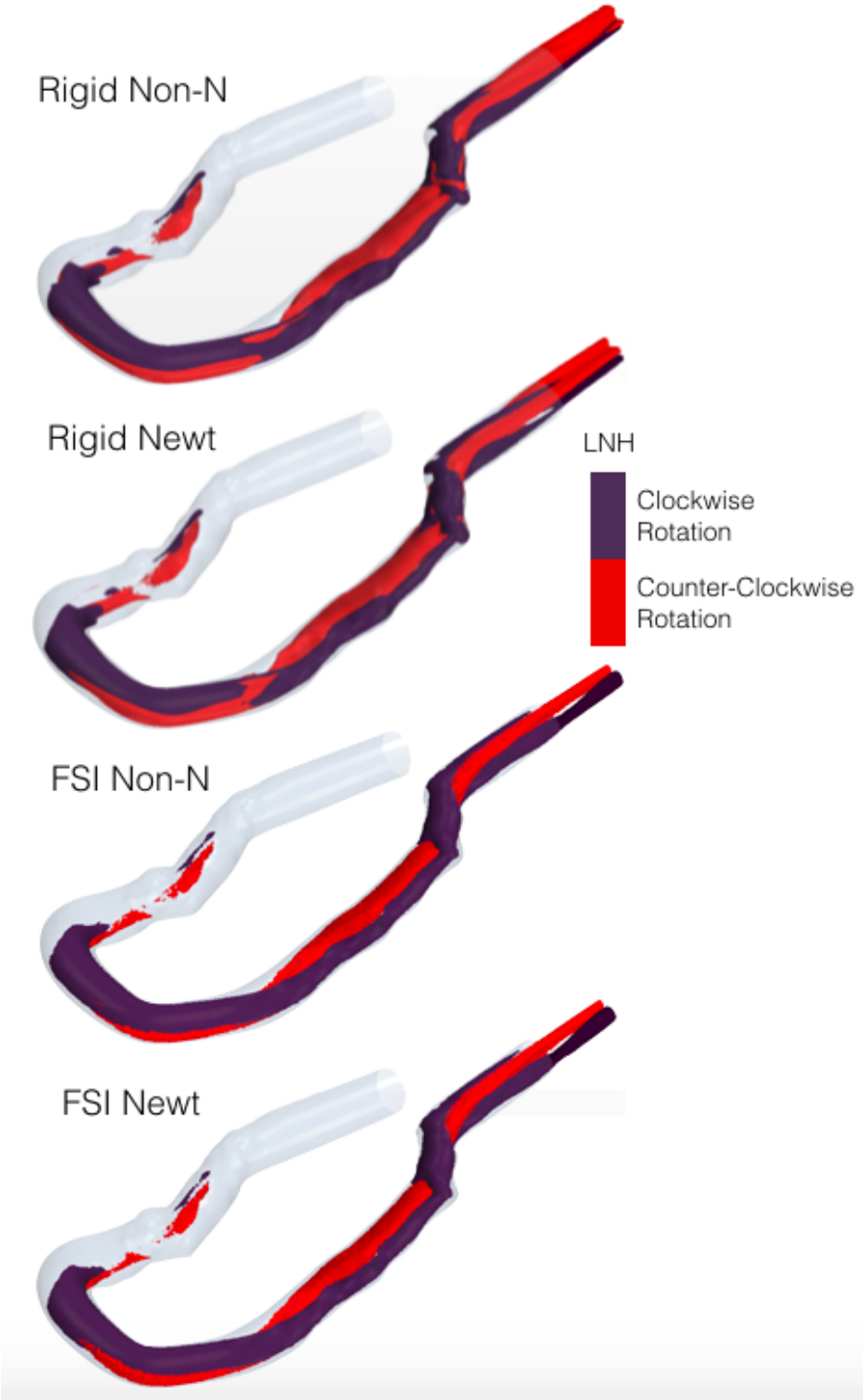

Figure 7.3: Isosurface of local normalised helicity (LNH) showing clockwise (dark purple) and anticlockwise (red) rotating vortical structures in all four cases.

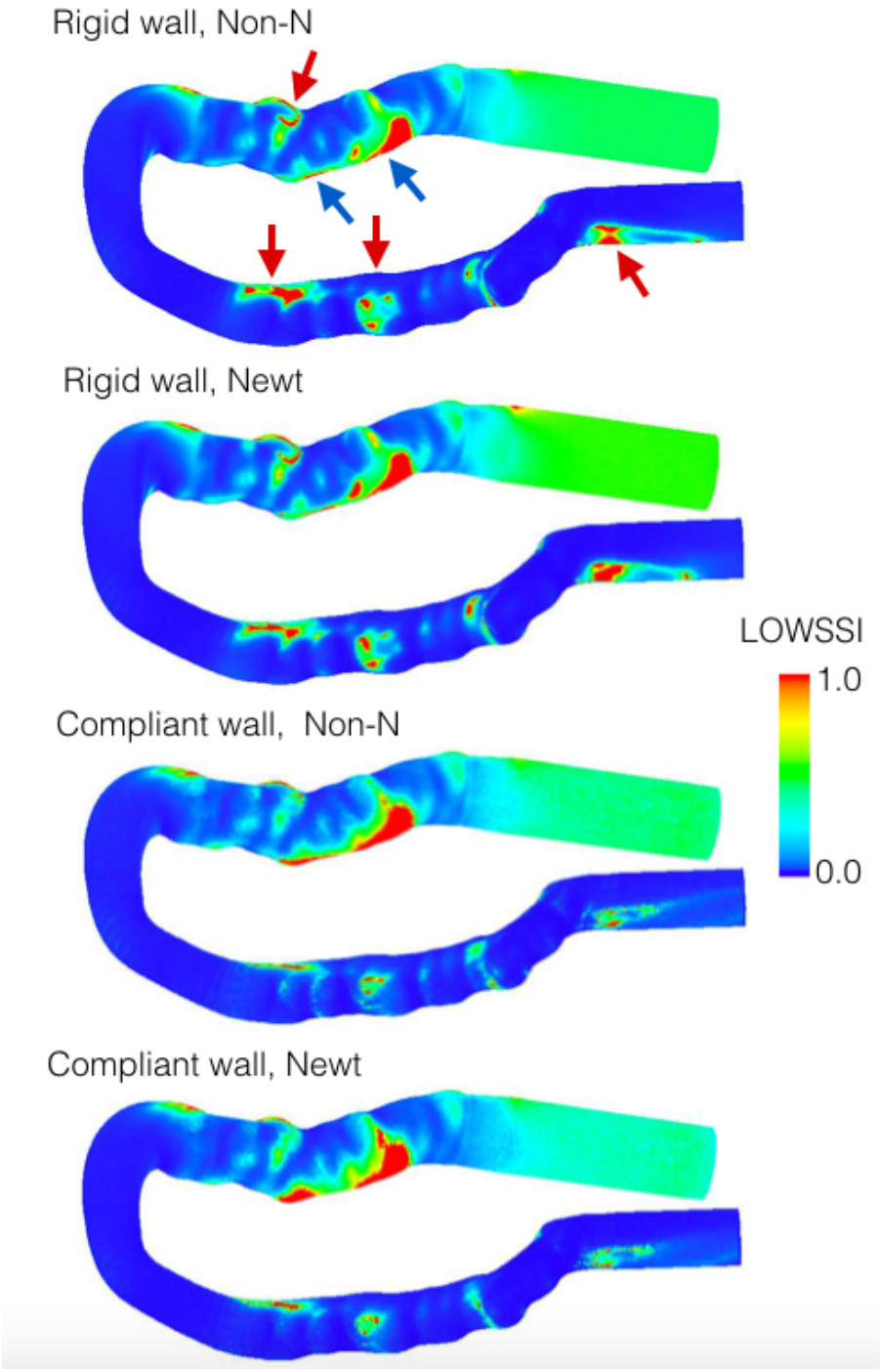
Rigid wall, Non-N
Rigid wall, Newt
Compliant wall, Non-N
Compliant wall, Newt
LOWSSI
1.0
0.0

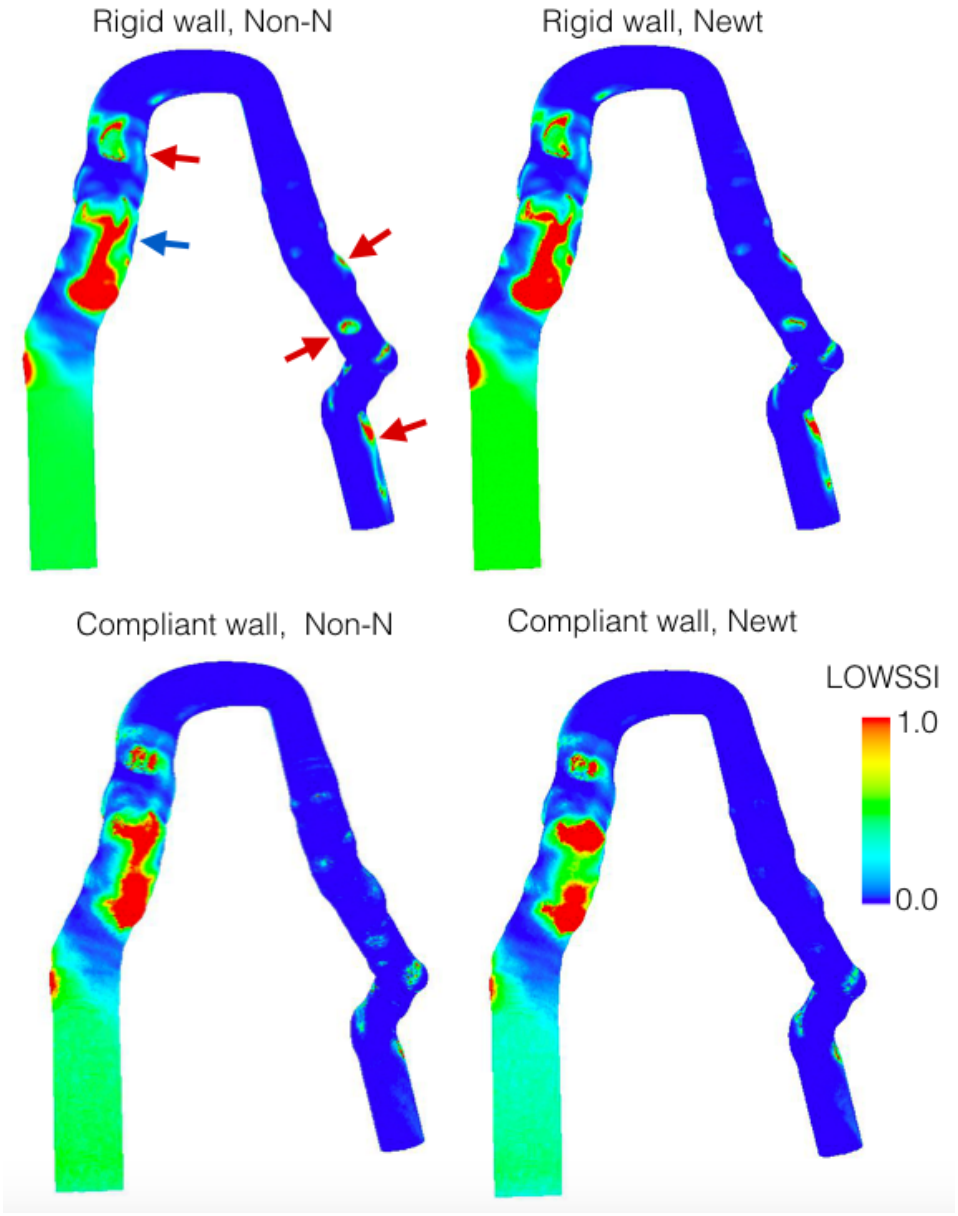

Figure 7.4: Low and oscillating wall shear stress index showing reions prone to maturation failure in all four cases. Red and blue arrows indicate regions of major WSS overestimation and underestimation by the rigid wall assumption, respectively.

Regions of LOWSS has also been underestimated by the the rigid arterial wall. Underestimation of these haemodynamic properties can result in unexpected AVF maturation failure while overestimation can cause false interpretation of haemodialysis unsuitability.

7.2 Mechanisms of maturation failure

The wall compliant and non-Newtonian AVF model is used for further investigation on the mechanism of fistula maturation failure because it provides the most realistic flow environment. The non-Newtonian blood is also modelled to consist of three phases (plasma, red and white blood cells) to take account of oxygen delivery by the red blood cells to endothelial cells on the vessel wall. Oxygen delivery is crucial for endothelial cell growth. AVF wall maturation have been investigated at six different cross sections across the model; three in the artery segment and the other three in the venous segment, as labelled in Figure 7.5. The radial wall displacements along the circumference of both the inner and outer walls determine whether the the vessel wall undergoes outward (maturation success) or inward remodelling (maturation failure). Table 7.2 explains how different ranges of radial displacements are interpretted. A positive remodelling (+) means that the wall is subjected to outward remodelling while a negative remodelling (−) means that the wall is subjected to inward remodelling. When both the outer and inner walls remodel in the same direction but at different rates, wall thickening and thinning can occur. The same thing can be observed if both wall remodel in different directions. Outward remodelling would lead to AVF maturation success while inward remodelling would result in maturation failure.

Figures 7.6 - 7.11 shows the radial wall displacement and local haemodynamic properties along the circumferences of the both the inner and outer walls of each respective cross sections (planes). Each figure consists of seven plots and a schematic structure of the lumen cross section (as seen by the flow upstream of the cross section). The quantities measured included radial wall displacement, the viscosity of the red blood cell phase (RBC), WSS magnitude, directional WSS, von Mises stress, and flow recirculation observed by

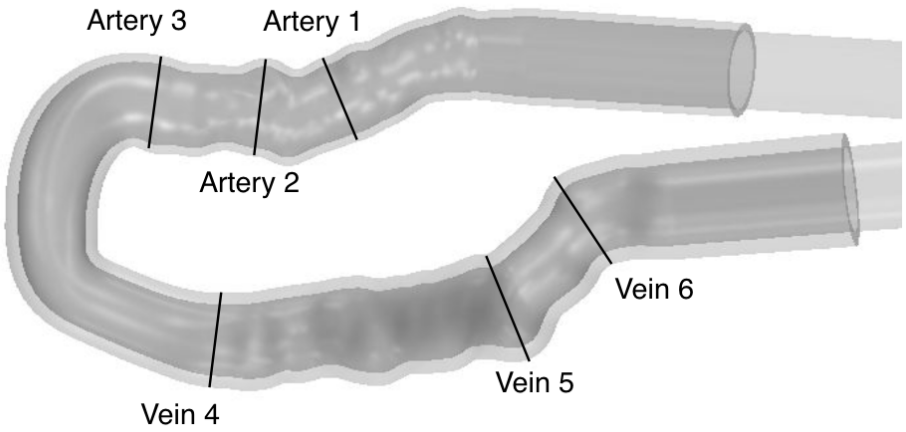

Figure 7.5: Locations of all six arterial and venous planes investigated.

Table 7.2: Radial wall displacement conditions for inward and outward wall remodelling.

Remodelling directions	Remodelling type	Possible side effects
Outer (+) / Inner (+)	Outward remodelling	Wall thickening
Outer (+/-) and Inner (+)	Outward remodelling	Wall thinning
Outer (-) / Inner (-)	Inward remodelling	Wall thinning
Outer (+/-) / Inner (-)	Inward remodelling	Wall thickening

the negative streamwise velocity. They are plotted against the circumferential coordinates (0-360 degrees).The red and black lines in the schematic structure represent the inner and outer walls. As the radial displacements and the von Mises stresses are measured on both walls, the red and black lines are used to represent their respective walls (i.e. red line in the radial displacement plot is the radial displacement of the inner wall). The RBC viscosity usually remains almost constant throughout the circumference of each plane unless there is a local accumulation of RBC. A significant increase in the local RBC viscosity, which results in RBC accumulation, is defined as at least 5% increase in the RBC viscosity from the local circumferential averaged RBC viscosity. The percentage increase in RBC viscosity at different circumferential locations of

RBC accumulation are shown in the plots. The WSS magnitude and directional WSS on the inner wall are measured. The directional WSS is the WSS in the local axial direction perpendicular the plane and the black horizontal line indicates a directional WSS of zero. Directional WSS below this line is considered oscillating WSS. The magnitude of the directional WSS determines whether it is a LOWSS or high-and-oscillating WSS. Circumferential coordinates with LOWSS correspond to the regions of LOWSSI 1.0 in Figure 7.4.The magnitude of directional WSS is independent of the WSS magnitude (in the third plot) as it only shows the WSS in the local axial direction. For example, a high WSS magnitude and a low and negative directional WSS may co-exist in the same region. This would mean that there is a presence of both high WSS and LOWSS in that region. The von Mises stresses on the inner and outer walls are proportional to the vascular injury on the endothelial cells (inner wall) and the smooth muscle cells (outer wall), respectively (Hajiali et al., 2014; Seo et al., 2018). Smooth muscle cells (SMC) are muscle cells located deeper inside the vessel wall which, in this case, represented by the outer wall. When the von Mises stress on the inner wall is higher than that of the outer wall, at a specific circumferential coordinate, it means that the endothelial cells are subjected to more vascular injury and vice versa. The local 3D flow recirculation is observed by the local streawise velocity. Negative streamwise velocities at every gridpoint on the plane are plotted in blue dots along the circumferential coordinates. The flow recirculation profile in the seventh and last plot shows how each negative streamwise velocities are distributed in the radial direction. Since each plane is not circular, the radial distance is measured from the inner wall (distance from the wall = 0 mm) to the centre of the plane instead of the other way around.

Abnormal changes in WSS promotes endothelial gene expression that stimulate wall remodelling (Sho et al., 2004). Either low WSS (Kharboutly et al., 2007) or oscillating WSS (Flores et al., 2016) can cause injury on the endothelial cells on the intimal layer (inner wall) of the vessel. The injured endothelial cells produce a substance called endothelin-1, which signals the smooth muscle cells in the media layer (outer wall) to migrate to the intimal layer (Hull et al., 2013). The migrated smooth muscle cells proliferate

(duplicate) themselves over the activated (injured) endothelial cells to protect it from further injuries (Jia et al., 2015). Smooth muscle cells proliferation leads to intimal hyperplasia (Ene-Iordache and Remuzzi, 2012), which results in either an inadequate outward wall remodelling (Humphrey, 2009) or inward wall remodelling (Rothuizen et al., 2013). Intimal hyperplasia, and thus higher risk of stenosis development, can lead to insufficient oxygen delivery to the endothelial cells by the RBC and subsequently wall maturation failure (Almasri et al., 2016).

AVF maturation is investigated at planes 1-3 of the artery (Figures 7.6 - 7.8) and planes 4-6 of the vein (Figures 7.9 - 7.11). It is evident that the arterial wall displacement (of up to 0.1 mm) is generally larger than that of the vein (up to 0.06 mm). This is due to the fact that the venous segment has a thicker wall and thus greater tolerance to wall displacement. The thicker venous wall is also responsible for the difference in von Mises in both vessels. The von Mises stresses, and thus vascular injuries, on both inner and outer walls of the venous segment are lower than those of the arterial segment. The von Mises stresses of the inner and outer walls have an inverse relationship in all planes (except for venous plane 5 and 6 as they are located at sharp bends). This means that in regions of high von Mises stress on the inner wall (more injury on the endothelial cells), the von Mises stress on the outer wall is low (less injury on the smooth muscle cells or SMC) and vice versa. Flow recirculations can be observed in LOWSS regions of both segments. Red blood cells accumulation (localised increase in the RBC viscosity) as a result of flow recirculation corresponds to outward wall remodelling due to the excess supplies of oxygen carried by the RBC to the endothelial cells on the inner wall. However, RBC accumulation at circumferential coordinate of 270 and 160 degree in the arterial plane 1 and 3 correspond to zero radial displacement (rather than positive) because they are not a result of flow recirculation. The flow recirculation at 270 degree in plane 1 is almost negligible.

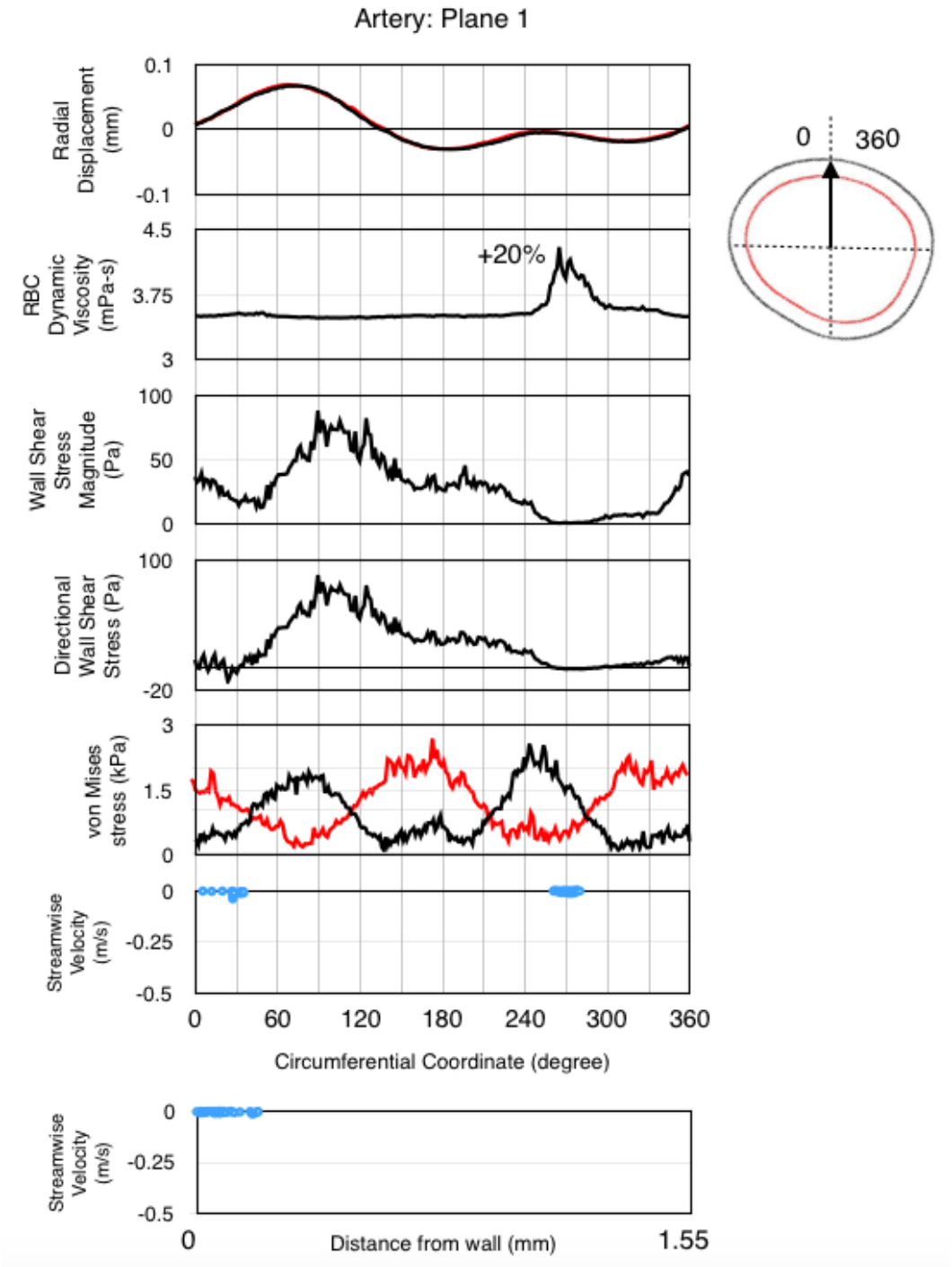

Figure 7.6: Circumferential radial displacements of the inner (red) and outer (black) walls, red blood cells viscosity, wall shear stresses, von-Mises stresses on the inner and outer walls, and flow recirculation regions (blue) on arterial plane 1.

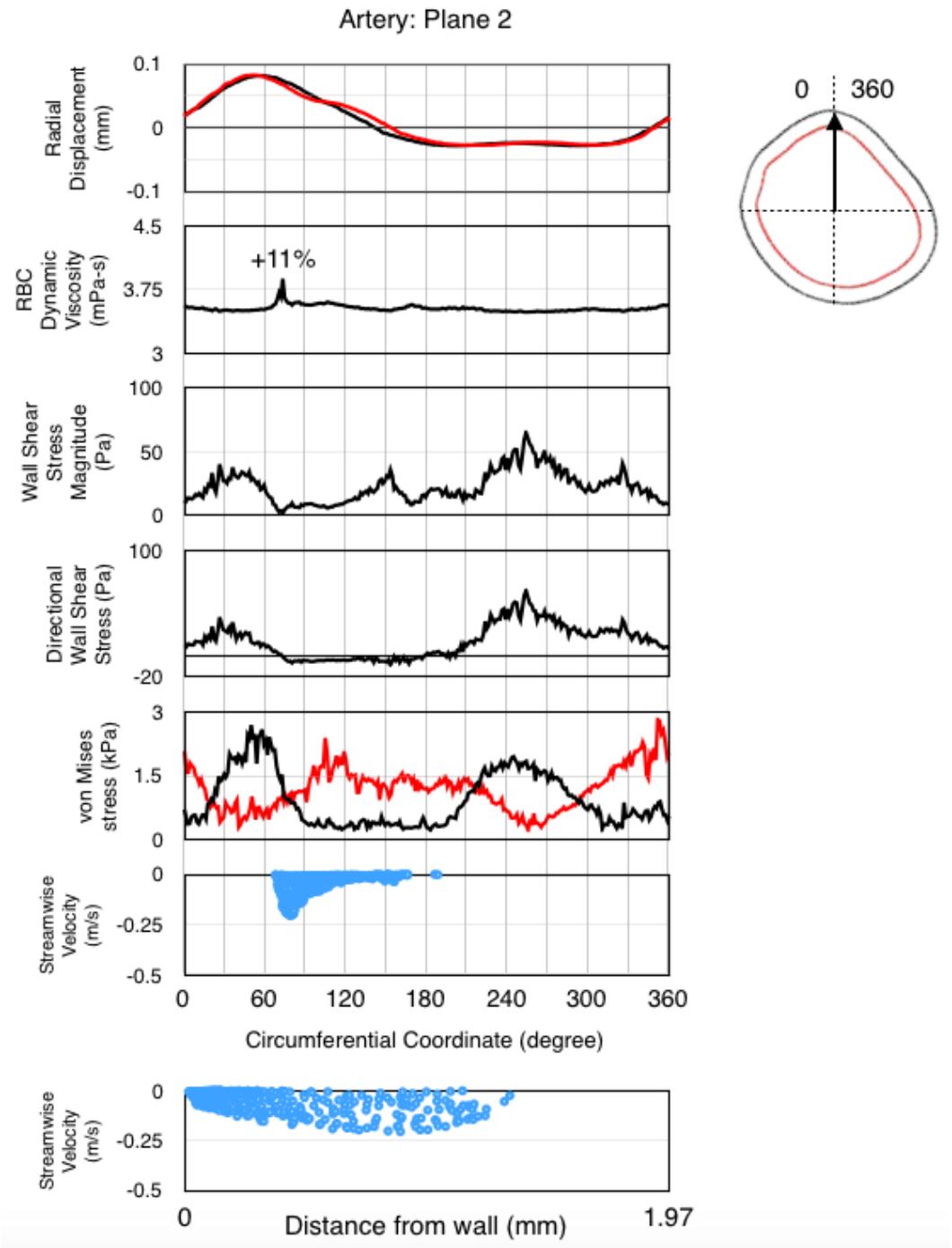

Figure 7.7: Circumferential radial displacements of the inner (red) and outer (black) walls, red blood cells viscosity, wall shear stresses, von-Mises stresses on the inner and outer walls, and flow recirculation regions (blue) on arterial plane 2.

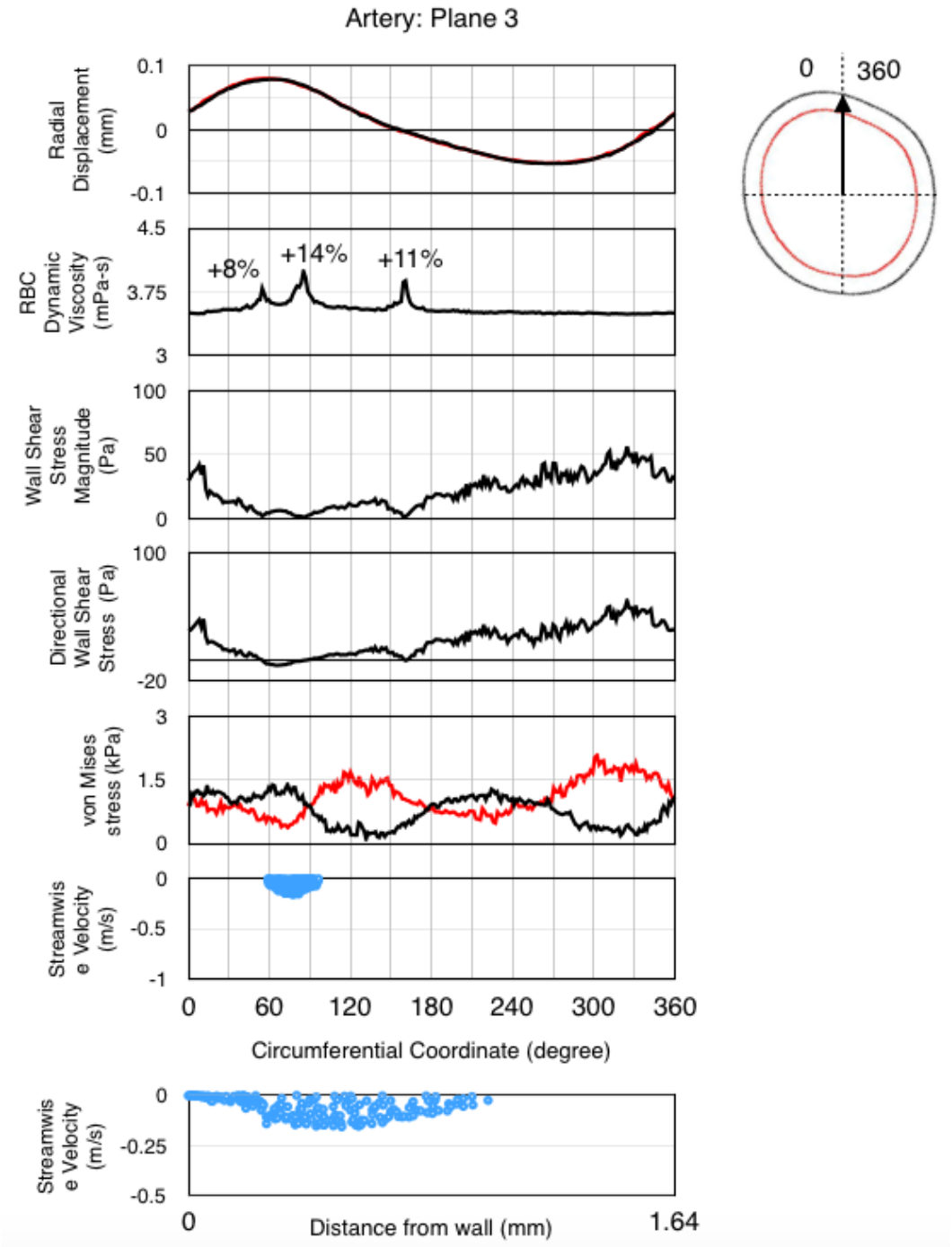

Figure 7.8: Circumferential radial displacements of the inner (red) and outer (black) walls, red blood cells viscosity, wall shear stresses, von-Mises stresses on the inner and outer walls, and flow recirculation regions (blue) on arterial plane 3.

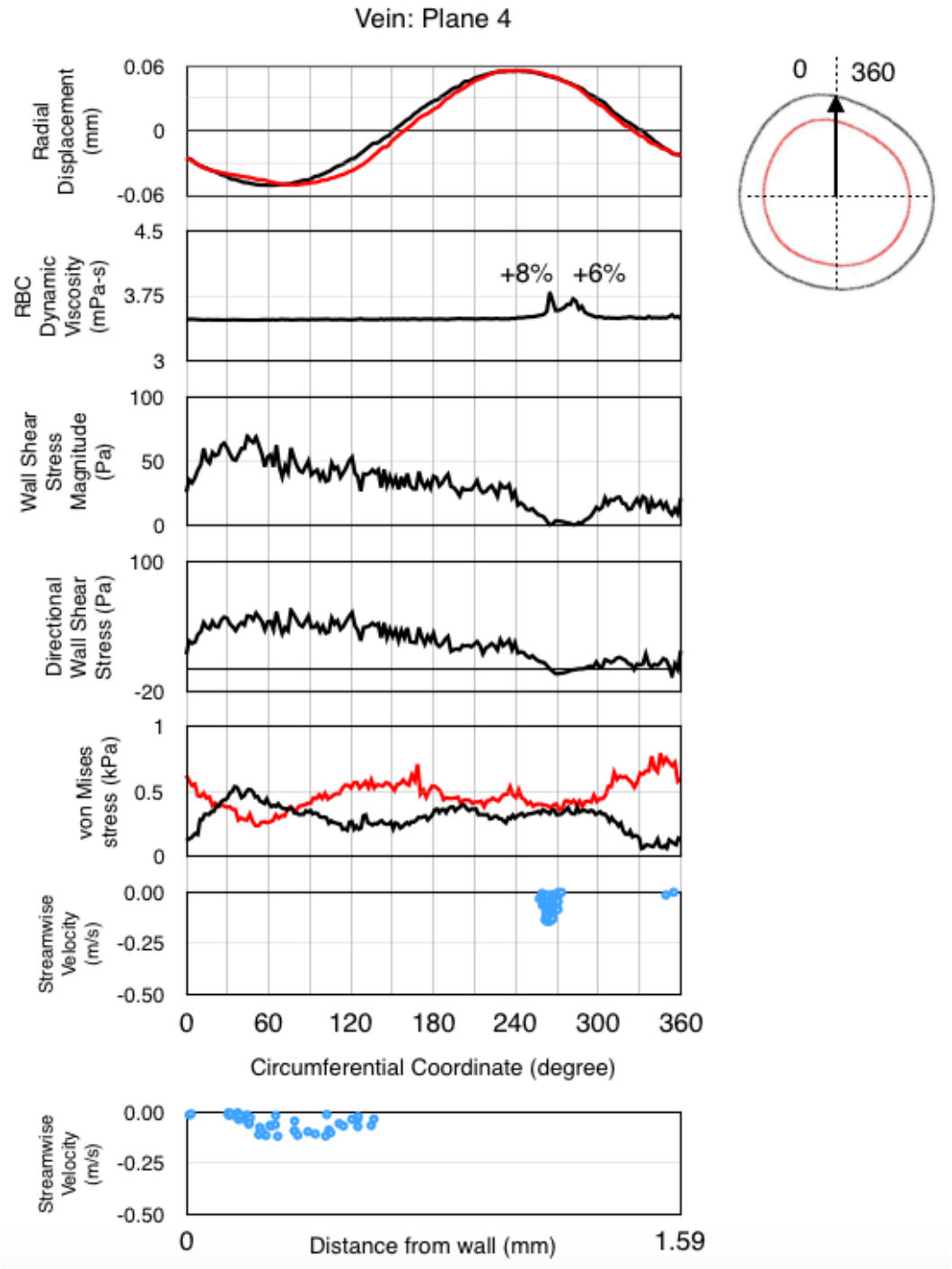

Figure 7.9: Circumferential radial displacements of the inner (red) and outer (black) walls, red blood cells viscosity, wall shear stresses, von-Mises stresses on the inner and outer walls, and flow recirculation regions (blue) on venous plane 4.

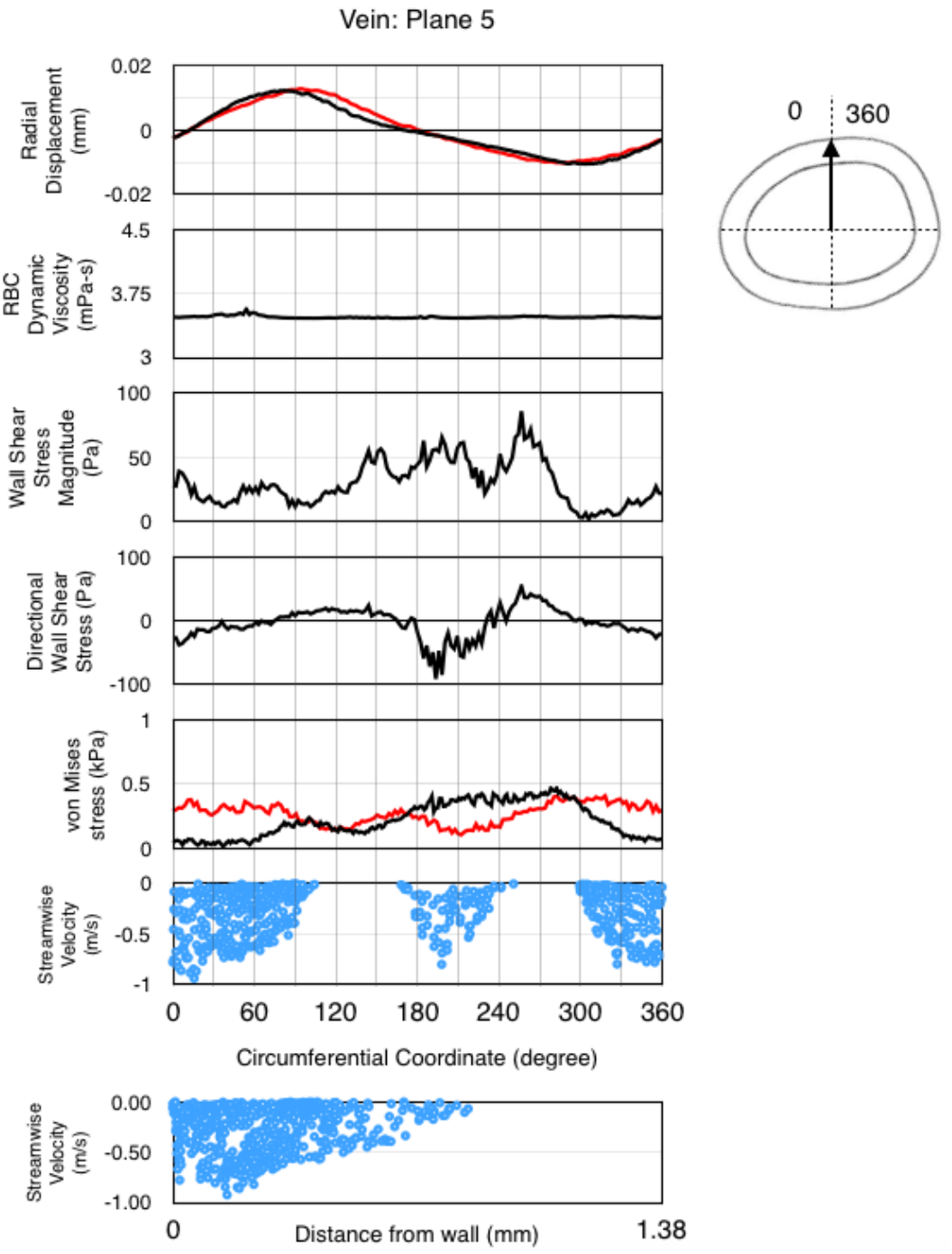

Figure 7.10: Circumferential radial displacements of the inner (red) and outer (black) walls, red blood cells viscosity, wall shear stresses, von-Mises stresses on the inner and outer walls, and flow recirculation regions (blue) on venous plane 5.

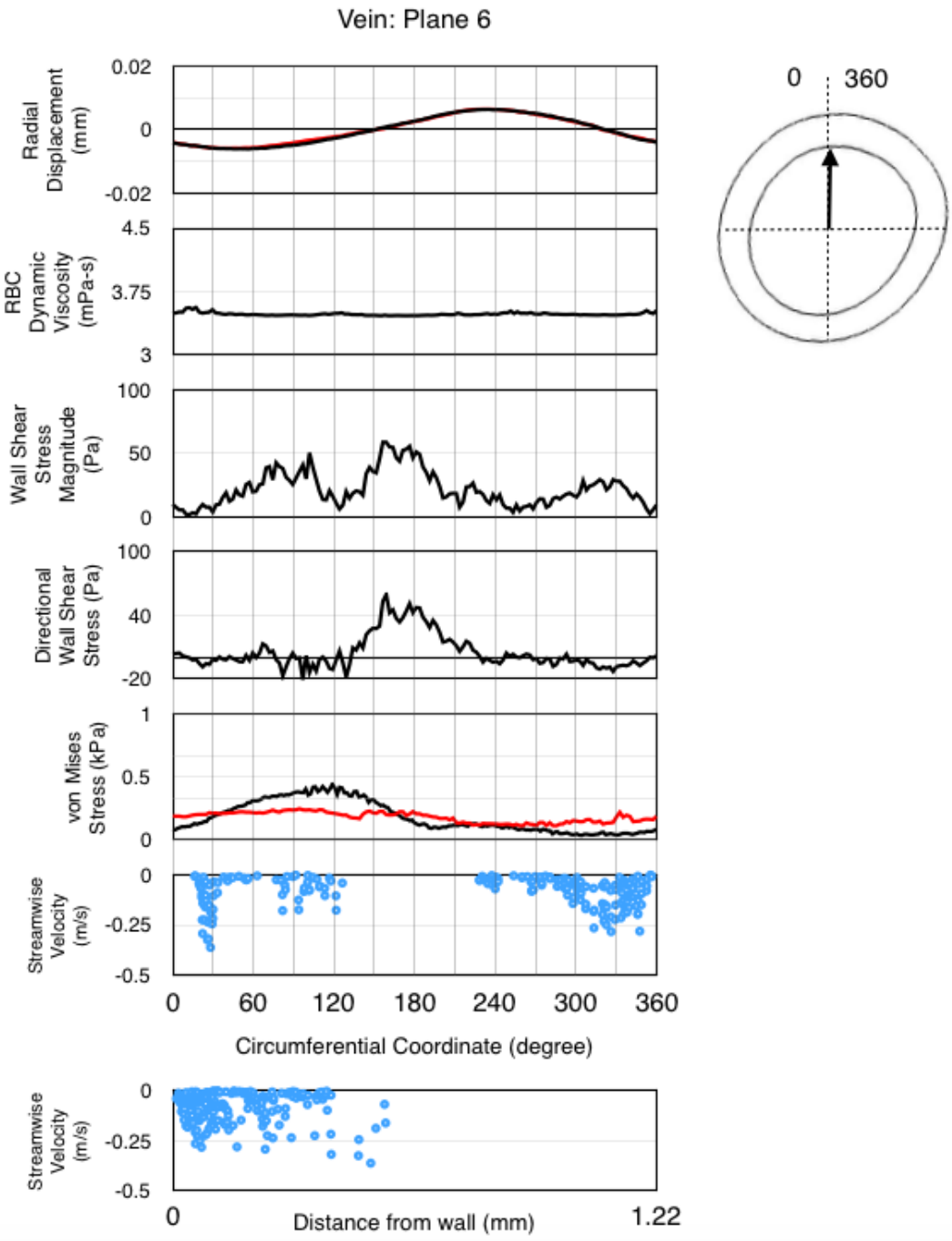

Figure 7.11: Circumferential radial displacements of the inner (red) and outer (black) walls, red blood cells viscosity, wall shear stresses, von-Mises stresses on the inner and outer walls, and flow recirculation regions (blue) on venous plane 6.

The present study have correlated AVF haemodynamics with wall remodelling that leads to intimal hyperplasia and stenosis development. It also suggests the following as mechanisms of AVF maturation failure:

1. **It was previously suggested that low WSS (Kharboutly et al., 2007) and oscillating WSS (Flores et al., 2016) independently caused endothelial cells (EC) injury. However, it has been found in the present study that both low and oscillating WSS (LOWSS) simultaneously contributed to increased EC injury (higher von Mises stress on the inner wall)**. The increase in EC injury due to LOWSS, which leads to maturation failure (inward remodelling), can be observed in the arterial plane 1 (285-360 degree). The LOWSS in the circumferential coordinates of 240-285 degrees did not increase EC injury due to RBC accumulation (20%) in the region. Local RBC accumulation supplies the endothelial cells with oxygen that is essential for growth and reduces injury. The same trend can be observed in plane 2 (80-200 degrees) with the RBC accumulation at 75 degrees decreasing the endothelial cells injury (60-80 degrees) instead of increasing it. The LOWSS in plane 3 (30-180 degrees) only increase EC injury in (90-150 degrees) when RBC accumulation is absent. Again, in plane 4, LOWSS is observed in (255-360) but EC injury only increased in (300-360) where there is no RBC accumulation. The LOWSSI in planes 5 (0-90, 300-360 degrees) and 6 (0-30, 270-360 degrees) increased the EC injury without exception regarding RBC accumulation. Note that the coordinates (180-270 degrees) in plane 5 and (60-150 degrees) in plane 6 are not subjected to LOWSS.

2. From the point above, another conclusion can be made. LOWSS without local RBC accumulation can lead to increase in EC injury. On the other hand, if RBC accumulation (above 15%) due to flow recirculation co-exists with the LOWSS, then EC injury can be reduced. Additionally, the accumulation of RBC can exhibit outward wall remodelling instead of inward remodelling despite the presence of LOWSS. This can be observed in plane 2 (60-150 degrees), plane 3 (30-150 degrees), and plane

4 (240-300 degrees). The LOWSSI at 160 degrees of plane 3 accompanied by RBC accumulation (11%) did not caused outward remodelling because the RBC accumulation is not a result of flow recirculation. **Red blood cells accumulation can decrease EC injury and may exhibit outward wall remodelling even in the presence of LOWSS. Without RBC accumulation, LOWSS would increase EC injury and exhibit inward remodelling.**

3. RBC accumulation is caused by flow recirculation and LOWSS and is associated with decrease in EC injury (and thus increase in SMC injury and von Mises stress of the outer wall instead). A local increase in the RBC viscosity (due to flow recirculation) below 15% is observed at or very proximal to the maximum radial displacement. On the other hand, a local increase in the RBC viscosity above 15% is more likely to be located further away from the maximum radial displacement or at zero radial displacement instead.

4. Flow recirculations have been corresponded with both inward and outward remodelling. However, flow recirculation can exhibit inward wall remodelling when it is associated with frequently oscillating WSS. This can be observed in plane 5 (180-240 degrees) and plane 6 (0-120 degrees). The directional WSS at these locations oscillate at a higher frequency compared to those at (60-150 degrees) in plane 2, (30-150 degrees) in plane 3, and (240-330 degrees) in plane 4 where flow recirculation led to outward remodelling. Additionally, a retrograde streamwise velocity of more than -0.3 m/s is required for inward remodelling of this AVF. **Therefore, for flow recirculation to exhibit inward wall remodelling, it must be associated with a frequently oscillating WSS and a retrograde streamwise velocity of a sufficient amount**.

5. Outward remodelling, which would lead to sucessful maturation, can cause flow recirculation that induces EC injury and maturation failure again. This can be observed at (80-150 degrees) in plane 2, (15-90 degrees) in plane 5, and (240-330 degrees) in plane 6.

6. The size (percentage of circumference) and the magnitude of flow recirculation region is directly proportional to the magnitude of LOWSS.

7. Arterial wall thinning only occur in LOWSS regions while venous wall thinning occur in high uni-directional WSS regions. Wall thinning in both segments is associated with increase in EC injury.

8. Regions of LOWSS (not necessarily associated with flow recirculation) that is in vincinity of any high uni-directional WSS ($>$ 20 Pa) can lead to outward remodelling if the EC (inner wall) is injured to the same or greater amount as the SMC (outer wall). On the other hand, regions of LOWSS with no high uni-directional WSS ($>$20) in the vincinity (up to 25% of the circumference) may exhibit inward remodelling. This does not apply for high and oscillating WSS.

9. High ($>$ 20 Pa) and oscillating WSS can also lead to inward remodelling if it is a result of flow recirculation. Therefore, inward wall remodelling is more sensitive to flow oscillatory than the magnitude of WSS.

Chapter 8

Conclusion

Haemodynamics of coiled aneurysms and arteriovenous fistulas have been investigated through CFD simulations, which have been conducted based on models reconstructed from patient-specific angiographies. The aneurysm and AVF models were acquired from CT and ultrasound scans, respectively. Coils of different packing densities were inserted into the aneurysm to study their effects on aneurysmal haemodynamics. Non-Newtonian blood viscosity, multiphase blood characteristics, and vessel wall compliance have been taken into account in both aneurysm and AVF studies. Different flow properties, including the introduced LOWSSI, were used to quantify the haemodynamics in both models. Since ultrasound images were not widely used for CFD simulations, it has therefore been validated. Good agreements between haemodynamics derived from ultrasound and MRI models confirms that ultrasound images are a safer and viable alternative to MRI. Results from both rigid-wall and compliant-wall aneurysm and AVF are independent of the mesh density and timestep size as shown by the independence tests.

The aneurysm study investigates the flow reduction, recanalisation, thrombus formation and rupture risk in a coiled cerebral aneurysm of different packing densities. The effects of local packing density, leukocyte adhesion to the wall, and wall compliance on aneurysm recurrence due to flow recanalisation have also been examined. The AVF study explores how fistula maturation failure can be misestimated by the Newtonian viscosity and rigid wall assumptions. Wall shear stress, flow reciruclation, flow helicity, and LOWSSI were

observed. The mechanisms behind maturation failure have been investigated through wall displacement, WSS, red blood cells viscosity, von-Mises stress, and flow recirculations in the non-Newtonian and wall compliant AVF model.

Aneurysmal velocity has been found to be reduced with increasing coil packing density and the first coil induced the most significant flow reduction of up to 38 %. The probability distribution function of time-averaged velocity further showed that each coil reduces the aneurysmal flow at different rates. This linear relationship between the coil packing density and surface-averaged WSS is not observed. Wall shear stress slightly increased after the insertion of the fourth coil (instead of decreasing due to flow reduction) after peak systole. The reduction in surface-averaged WSS becomes less significant after the insertion of the fifth coil, while up to seven coil is needed to sufficiently suppress the aneurysmal velocity. The seventh coil (packing density of 30.35 %) is the optimal coiling case and reduced the WSS back to the healthy value of 2.0 Pa. Moreover, velocity and WSS reduction has been found to be independent of the inflow waveform. Isosurface of the mean blood flow inside the coiled aneurysm shows not only the flow impingement and stagnation as a result of coiling, but also the mean flow recanalisation after the insertion of the fourth, sixth, and seventh coil. While the recanalisation in the 4 coil case

Without thrombosis, aneurymal flow can only be reduced but the aneurysm may not start to occlude. The distribution of contrast agent (passive scalar) in the coiled aneurysms were also investigated to study thrombus formation, which can be used to discriminate aneurysm occlusion and recurrence. Since clinicians only rely on contrast visualisation to identify aneurysmal occlusion or recurrence without any other haemodynamic data, the relationship between passive scalar distribution and aneurysmal haemodynamics presented is beneficial to the aneurysmal diagnosis and treatment. Regions of high passive scalar concentration have been reduced by the first coil, while the regions of slightly lower concentration were reduced by the proceeding coils. Like that of the aneurysmal velocity, the inverse relationship between the reduction in passive scalar concentration and coil packing density is non-linear. Passive scalar concentration increased after the insertion of the fourth and seventh

coil cases, as also evident by the flow recanalisation shown by the mean velocity isosurfaces. Although the localised flow recanalisation in the seven coil case was not captured in the volume-averaged aneurysmal haemodynamics, it is observed in the spatial distribution of passive scalar. Unlike that of the 4 coil case, this flow recanalisation in the 7 coil case is evidence of aneurysm recurrence at high packing density. By observing the time-density curves of passive scalar concentration, it was found that blood residence time increased with coil packing density after the insertion of the fifth coil. The seventh coil induced the longest blood residence time of 1.55s, and the highest probability of thrombus formation, despite its recurrence status. This suggests that the risk of aneurysm recurrence is independent of the rate of thrombosis. The stability of the aneurysm depends on what happens first - complete flow occlusion by thrombosis or aneurysm recurrence and rupture.

The risk of aneurysm rupture in each coiling cases were investigated. The effect of the first coil in reducing the overall rupture risk is significant, as shown by the great reduction in the OSI values. The seventh coil, on the other hand, is considerably effective in reducing the rupture risk towards the tip of the aneurysm, which is known to be prone to rupture. However, aneurysmal rupture risk is attributed not only to oscillatory WSS but also wall inflammation induced by platelet thrombus. Therefore, the probability of thrombus formation due to LOWSS have also been investigated. The LOWSSI served as a predicting tool for both aneurysm occlusion by thrombosis and rupture risk due to wall inflammation. The aneurysm dome gradually become filled with thrombus as coils were inserted and after the fourth coil, the majority of the dome become thrombosed. This corresponds with how the blood residence time only started to significantly increase after the insertion of the fourth coil. Like that of OSI, regions of high LOWSSI did not increase linearly with coil packing density. Flow recanalisation in the 7 coil case resulted in a slight reduction in the LOWSSI at the neck region. Nevertheless, the significant reduction in LOWSSI from the untreated case to the 7 coil case confirms that coil embolisation is crucial for thrombus initiation in the aneurysm. In response to the wall inflammation due to thrombosis, leukocytes are recruited into the aneurysm dome.

The recanalisation of the mean flow, passive scalar concentration, the increase in OSI (rupture risk), and the decrease in LOWSSI (thrombus formation on the wall) observed the neck region of the 7 coil case were evidence of aneurysm recurrence. These forms of recanalisation are partially attributed to the fact that the majority of the additional coil mass was distributed to the neck region. The effects of local coil packing density, leukocyte adhesion to the wall, and wall compliance on aneurysm recurrence were therefore investigated. Flow recanalisation can be observed in the regions of decreased local packing density at both diastolic and systolic phases. The peak systolic flow recanalisation occured more closer to the aneurysm neck as compared to that of the end diastole. On the other hand, flow recanalisation towards the aneurysm tip was not observed since the local packing densities were very high in both coiling cases. The magnitude of aneurysm recurrence has been related to the difference between the local packing density of both coiling cases, the cardiac phase in observation, and the plane-averaged velocity magnitude immediately upstream of the recurrence site. An increase in the plane-averaged velocity of up to 2.4 mm/s and 9.5 mm/s can lead to diastolic and systolic flow recanalisation, respectively.

Flow recanalisation of the leukocyte phase occured significantly closer to the aneurysm neck as compared to that of the whole blood flow. The increase in leukocyte inflow after the insertion of the seventh coil corresponds to leukocyte migration into the aneurysm dome in response to wall inflammation due to platelet-thrombus formation. This suggests that aneurysmal haemodynamics alone, without the modelling of biological cell signaling, may contributed to leukocyte migration into the inflamed aneurysm. The more significant increase in the local packing density in the neck region after the insertion of the seventh coil was more effective in reducing the circumferential wall shear stress than reducing the leukocyte adhesion in the neck region. Downstream of plane 4, the WSS started to increase after the insertion of the seventh coil, which corresponds to the region where flow recanalisation was observed. On the other hand, leukocyte adhesion significantly reduced downstream of the same plane. This indicated an association between flow recanalisation and a

reduction in leukocyte adhesion to the wall. Despite the increase in WSS, the circumferential WSS towards the aneurysm tip (planes 6-7) are oscillatory and below 2 Pa, which is low enough for the initiation of thrombus formation as seen in the LOWSSI contours. Since no leukocyte adhesion was observed towards the tip, it is suggested that thrombus formation towards the aneurysm tip was attributed to platelets aggregation rather than leukocytes. Additionally, the absence of leukocyte adhesion is not attributed to flow recanalisation, but to the negligibly small leukocyte phase velocity instead. The aneurysm rupture risk did not significantly increase, despite flow recanalisation, because there was no additional contribution to wall inflammation by the leukocytes.

Wall compliance has been found to affect aneurysm recurrence. The plane-averaged velocity in the majority of the aneurysm volume is reduced as a result of wall distensiblity. The aneurysm depth at which flow recanalisation was observed in the wall compliant case is approximately the same as that of the rigid wall case. However, the magnitude of flow recanalisation is higher in the wall compliant case. The effect of wall compliance is slightly more pronounced during peak systole as compared to the end diastole. The radial displacement around the circumferences of each aneurysmal planes are unbalanced. Slight aneurysm expansion is observed on one side of the aneurysm (side A) where the difference between the radial displacement between the two coiling cases are more significant and the majority of leukocyte adhesion took place. Aneurysm recurrence has been associated with aneurysm regrowth, which in this case is shown by the insufficient decrease in the wall displacement despite the insertion of the seventh coil. In these regions of aneurysm regrowth, reduction in leukocyte adhesion has been observed. On the contrary, increase in leukocyte adhesion after the insertion of the seventh coil has been related with a more significant decrease in the wall displacement, and thus no aneurysm regrowth. The other side of the aneurysm (side B) exhibited a smaller wall displacement, which is directed towards the aneurysm centre. Leukocyte adhesion of higher WBC volume fraction has been observed on this side and is attributed to reduction in the gap between the aneurysm wall and the coil mass. As a result, leukocyte inflow into the dome through this side of the aneurysm, and thus leukocyte adhesion to the wall, was limited.

Downstream of the aneurysm neck, the two local peaks in wall displacement transformed into a single peak, partially due to the decrease in the circumference of the observed plane. The overestimation of aneurysmal velocity and wall shear stress by the rigid wall assumption have also been observed in a separate study of a compliant coil in a rigid aneurysm.

The effects of non-Newtonian viscosity and wall compliance on AVF haemodynamics and maturation failure has been investigated. Different haemodynamic quantities were compared between four cases of Newtonian viscosity and rigid wall, Newtonian viscosity and compliant wall, non-Newtonian viscosity and rigid wall, and non-Newtonian viscosity and compliant wall. While diastolic WSS and is found to be insignificantly affected by blood shear-thinning properties, it is senstive to wall compliance. The WSS has been overestimated on arterial curvatures but underestimated along the venous segment by the rigid wall assumption. Wall thickness can affect WSS predictions as different thickness exhibit different resistance to wall deformation and thus different flow energy dissipation. The majority of the WSS was overestimated by the rigid wall assumption, which can result in the underprediction of intimal hyperplasia due to LOWSS. The non-Newtonian effect is also insignificant in the prediction of flow recirculation. However, the rigid wall assumption significantly overestimated many regions of flow recirculation as a result of the reduction in flow stagnation induced by the compliant wall. A pair of counter-rotating vortical structures observed downstream of the artery, as depicted by flow helicity, resulted in regions of high WSS and thus wall degradation, smooth muscle cells (SMC) migration, and inward remodelling. The rigid wall overestimation of WSS can be attributed to its overestimation of flow helicity. Like WSS, flow recirculation and helicity were also underestimated by the rigid wall assumption and the non-Newtonian effects on these quantities were not significant. Thrombus formation as well as intimal hyperplasia, both of which are known to lead to stenosis development, is shown by the LOWSSI contours. The rigid wall assumption overestimated LOWSSI (maturation failure) in the vein and underestimated it in the artery. In this worst case, it can be mislead that the vein is not yet matured when it actually is and stenosis may unexpectedly start to develop in the artery. Insufficient supply of oxygenated blood

to regions downstream of the stenosed artery may contribute to AVF maturation failure. The Newtonian viscosity assumption underestimated LOWSSI in both the artery and vein. The overestimation and underestimation of these haemodynamic properties, especially by the rigid wall assumption, resulted in the misinterpretation of AVF maturation failure.

The mechanisms of AVF maturation failure has been determined and discussed. The circumferential wall displacement of several arterial and venous planes identified regions of inward and outward wall remodelling. RBC viscosity, WSS magnitude, directional WSS, vom Mises stress, and flow recirculation were correlated with the local wall remodelling. It has been found that low WSS and oscillatory WSS simultaneously contributed to the increase in endothelial cell (EC) injury (inner wall von Mises stress) and thus SMC relaxation and maturation failure due to inward wall remodelling. However, EC injury can be reduced in the presence of RBC accumulation (local high RBC viscosity above 15% of the circumferentialo average value). Endothelial cells injury becomes significant when the region is subjected to LOWSS and RBC accumulation caused by flow recirculation is not present. Additionally, either RBC accumulation or nearby high uni-directional WSS can promote outward wall remodelling even if the wall is subjected to LOWSS. This may not remain true if the RBC accumulation is not attributed to flow recirculation. When the EC (inner wall) is not injured, the SMC (outer wall) is usually injured instead, causing outward wall remodelling. The maximum radial displacement corresponds to RBC accumulation associated with local increase in RBC viscosity below 15%. It has been found that flow recirculation alone cannot discriminate inward wall remodelling. It must be attributed to oscillatory WSS and be associated with a sufficiently large retrograde streamwise velocity to be able to induce the inward remodelling. By observing the six arterial and venous planes, the required retrograde streamwise velocity for this AVF model is -0.3m/s. The size and magnitude of flow recirculation is Although outward remodelling is a good sign for AVF maturity, it can still induce flow recirculation, which can again lead to inward remodelling if other conditions are satisfied. Wall thinning in both the arterial and venous segments are associated with an increased EC injury and risk of maturation failure. This has

been observed in regions of LOWSS and high uni-directional WSS in the artery and vein, respectively. The difference in the mechanism of wall thinning can be attriibuted to the difference in wall thickness in these two segment.

Bibliography

F. Abraham, M. Behr, and M. Heinkenschloss. Shape optimization in steady blood flow: A numerical study of non-newtonian effects. *Computer Methods in Biomechanics and Biomedical Engineering*, 8(2):127–137, 2005.

T. Abruzzo, G. G. Shengelaia, R. C. Dawson, D. S. Owens, C. M. Cawley, and M. B. Gravanis. Histologic and morphologic comparison of experimental aneurysms with human intracranial aneurysms. *AJNR Am J Neuroradiol*, 19(7):1309–1314, Aug 1998.

S. Ahmed, Sutalo I., H. Kavnoudias, and A. Madan. Numerical investigation of haemodynamics of lateral cerebral aneurysm following coil embolization. *Engineering Applications of Computational Fluid Mechanics*, 5:329–340, 2011.

S. M.J.M. Akherat, K. Cassel, M. Boghosian, P. Dhar, and M. Hammes. Are non-newtonian effects important in hemodynamic simulations of patients with autogenous fistula? *Journal of Biomechanical Engineering-Transactions of the Asme*, 139(4), 2017. ISSN 0148-0731. doi: 10.1115/1.4035915. URL <GotoISI>://WOS:000396214400008.

J. Almasri, M. Alsawas, M. Mainou, R. A. Mustafa, Z. Wang, K. Woo, D. L. Cull, and M. H. Murad. Outcomes of vascular access for hemodialysis: A systematic review and meta-analysis. *Journal of Vascular Surgery*, 64 (1):236–243, 2016. ISSN 0741-5214. doi: 10.1016/j.jvs.2016.01.053. URL <GotoISI>://WOS:000378562900035.

L. Andrade, A. Silva, L. Franca, L. Franca, and J. Souza. Hepatic artery aneurysm: incidental diagnosis with abdominal ultrasonography and treatment by coil embolization. *Jornal Vascular Brasileiro*, 11(3):232–235, 2012.

A. Arzani. Accounting for residence-time in blood rheology models: do we really need non-newtonian blood flow modelling in large arteries? *Journal of The Royal Society Interface*, 15(146):1–9, 2018.

A. Asif, P. Roy-Chaudhury, and G. A. Beathard. Early arteriovenous fistula failure: a logical proposal for when and how to intervene. *Clinical Journal of the American Society of Nephrology*, 1(2):332–339, 2006.

B. Astor, J. Eustace, N. Powe, M. Klag, N. Fink, and J. Coresh. Type of vascular access and survival among incident hemodialysis patients: the choices for healthy outcomes in caring for esrd study. *J Am Soc Nephrol.*, 16, 2005.

S. Baek, R. Gleason, K. Rajagopal, and J. Humphrey. Theory of small on large: potential utility in computations of fluid–solid interactions in arteries. *Comput. Methods Appl. Mech. Eng.*, 196:3070–3078, 2007.

M. Baharoglu, C. Schirmer, D. Hoit, B. Gao, and A. Malek. Aneurysm inflow-angle as a discriminant for rupture in sidewall cerebral aneurysms: morphometric and computational fluid dynamic analysis. *Stroke*, 41(7):1423–1430, Jul 2010.

Y. Bazilevs, M. C. Hsu, Y. Zhang, W. Wang, T. Kvamsdal, S. Hentschel, and J. G. Isaksen. Computational vascular fluid-structure interaction: methodology and application to cerebral aneurysms. *Biomech Model Mechanobiol*, 9(4):481–498, Aug 2010.

G. A. Beathard, E. D. Dillavou, J. S. Berns, K. A. Collins, and A. Q. Lam. Maturation and evaluation of the newly created hemodialysis arteriovenous fistula. Unpublished, 2019.

J. Bederson, I. Awad, D. Wiebers, D. Piepgras, E. Haley, T. Brott, G. Hademenos, D. Chyatte, R. Rosenwasser, and C. Caroselli. Recommendations for the management of patients with unruptured intracranial aneurysms: A Statement for healthcare professionals from the Stroke Council of the American Heart Association. *Stroke*, 31(11):2742–2750, Nov 2000.

M. Binning, Z. Hakma, and E. Veznedaroglu. Endovascular coil embolization of unruptured posterior communicating artery aneurysm. *American Association of Neurosurgeons*, 37(1), 2014.

J. M. Bland and D. G. Altman. Statistical methods for assessing agreement between two methods of clinical measurement. *The lancet*, 327(8476):307–310, 1986.

M. Boghosian, K. Cassel, M. Hammes, B. Funaki, S. Kim, X. Qian, X. Wang, P. Dhar, and J. Hines. Hemodynamics in the cephalic arch of a brachiocephalic fistula. *Medical Engineering and Physics*, 36(7):822–830, 2014.

L. Boussel, V. Rayz, C. McCulloch, A. Martin, G. Acevedo-Bolton, M. Lawton, R. Higashida, W. S. Smith, W. L. Young, and D. Saloner. Aneurysm growth occurs at region of low wall shear stress: patient-specific correlation of hemodynamics and growth in a longitudinal study. *Stroke*, 39(11): 2997–3002, Nov 2008.

J. Boyd, Buick J. M., and S. Green. Analysis of the casson and carreau-yasuda non-newtonian blood models in steady and oscillatory flows using the lattice boltzmann method. *Physics of Fluids*, 19:93–103, 2007.

M. Bozzetto, B. Ene-Iordache, and A. Remuzzi. Transitional flow in the venous side of patient-specific arteriovenous fistulae for hemodialysis. *Annals of Biomedical Engineering*, 44(8):2388–2401, 2015. ISSN 0090-6964. doi: 10.1007/s10439-015-1525-y.

M. Brescia, J. Cimino, K. Appel, and B. Hurwich. Chronic hemodialysis using venipuncture and a surgically created arteriovenous fistula. *N. Engl. J. Med.*, 275(20):1089–1092, 1966.

L. Browne, K. Bashar, P. Griffin, E. Kavanagh, S. Walsh, and M. Walsh. The role of shear stress in arteriovenous fistula maturation and failure: A systematic review. *Plos One*, 10(12), 2015.

G. Bruno, R. Todor, I. Lewis, and D. Chyatte. Vascular extracellular matrix remodeling in cerebral aneurysms. *J. Neurosurg.*, 89(3):431–440, Sep 1998.

A Buradi and A Mahalingam. Numerical simulation of pulsatile blood flow in an idealized curved section of a human coronary. *Int J Mech Prod Eng. Special Issue Sep*, pages 15–19, 2016.

G. Byrne, F. Mut, and J. Cebral. Quantifying the large-scale hemodynamics of intracranial aneurysms. *AJNR Am J Neuroradiol*, 35(2):333–338, Feb 2014.

H. Byun and K. Rhee. CFD modeling of blood flow following coil embolization of aneurysms. *Med Eng Phys*, 26:755– 61, 2004.

J. Campa, R. Greenhalgh, and J. Powell. Elastin degradation in abdominal aortic aneurysms. *Atherosclerosis*, 65(1-2):13–21, May 1987.

T. Canchi, E. Ng, S. Narayanan, and E. Finol. On the assessment of abdominal aortic aneurysm rupture risk in the Asian population based on geometric attributes. *Proc Inst Mech Eng H*, 232(9):922–929, Sep 2018.

A. Caroli, S. Manini, L. Antiga, K. Passera, B. Ene-Iordache, S. Rota, G. Remuzzi, A. Bode, J. Leermakers, F. N. van de Vosse, R. Vanholder, M. Malovrh, J. Tordoir, A. Remuzzi, and Arch Project Consortium. Validation of a patient-specific hemodynamic computational model for surgical planning of vascular access in hemodialysis patients. *Kidney International*, 84(6): 1237–1245, 2013. ISSN 0085-2538. doi: 10.1038/ki.2013.188.

CD-Adapco. Star-ccm+ tutorial.

J. Cebral and R. Lohner. Efficient simulation of blood flow past complex endovascular devices using an adaptive embedding technique. *IEEE Trans Med Imaging*, 24(4):468–476, Apr 2005.

J. Cebral and M. Raschi. Suggested connections between risk factors of intracranial aneurysms: a review. *Ann Biomed Eng*, 41(7):1366–1383, Jul 2013.

J. Cebral, M. Castro, J. Burgess, R. Pergolizzi, M. Sheridan, and C. Putman. Characterization of cerebral aneurysms for assessing risk of rupture by using patient-specific computational hemodynamics models. *AJNR Am J Neuroradiol*, 26(10):2550–2559, 2005.

J. Cebral, F. Mut, J. Weir, and C. Putman. Association of hemodynamic characteristics and cerebral aneurysm rupture. *AJNR Am J Neuroradiol*, 32(2):264–270, Feb 2011.

J. Cebral, F. Detmer, B. Chung, J. Choque-Velasquez, B. Rezai, H. Lehto, R. Tulamo, J. Hernesniemi, M. Niemela, A. Yu, R. Williamson, K. Aziz, S. Sakur, S. Amin-Hanjani, F. Charbel, Y. Tobe, A. Robertson, and J. Frosen. Local Hemodynamic Conditions Associated with Focal Changes in the Intracranial Aneurysm Wall. *AJNR Am J Neuroradiol*, 40(3):510–516, Mar 2019.

K. Cha, E. Balaras, B. Lieber, C. Sadasivan, and A. Wakhloo. Modeling the interaction of coils with the local blood flow after coil embolization of intracranial aneurysms. *J Biomech Eng*, 129(6):873–879, Dec 2007.

T. Chaichana, Z. Sun, and J. Jewkes. Computation of hemodynamics in the left coronary artery with variable angulations. *J Biomech*, 44(10):1869–1878, Jul 2011.

T. Chaichana, Z. Sun, and J. Jewkes. Computational fluid dynamics analysis of the effect of plaques in the left coronary artery. *Comput Math Methods Med*, 2012:504367, 2012.

T. Chaichana, Z. Sun, and J. Jewkes. Haemodynamic analysis of the effect of different types of plaques in the left coronary artery. *Comput Med Imaging Graph*, 37(3):197–206, Apr 2013a.

T. Chaichana, Z. Sun, and J. Jewkes. Hemodynamic impacts of left coronary stenosis: a patient-specific analysis. *Acta Bioeng Biomech*, 15(3):107–112, 2013b.

T. Chaichana, Z. Sun, and J. Jewkes. Impact of plaques in the left coronary artery on wall shear stress and pressure gradient in coronary side branches. *Comput Methods Biomech Biomed Engin*, 17(2):108–118, 2014.

N. Chalouhi, C. D. BoveNzi, V. Thakkar, J. Dressler, P. Jabbour, R. M. Starke, S. Teufack, L. F. Gonzalez, R. Dalyai, and A. S. Dumont. Long-term catheter angiography after aneurysm coil therapy: results of 209 pa-

tients and predictors of delayed recurrence and retreatment. *Journal of neurosurgery*, 121(5):1102–1106, 2014.

J. Chason and W. Hindman. Berry aneurysms of the circle of Willis; results of a planned autopsy study. *Neurology*, 8(1):41–44, Jan 1958.

Y. Cho and K. Kensey. Effects of the non-newtonian viscosity of blood on flows in a diseased arterial vessel .1. steady flows. *Biorheology*, 28(3-4):241–262, 1991.

I. Chowdhury and S. P. Dasgupta. Computation of rayleigh damping coefficients for large systems. *The Electronic Journal of Geotechnical Engineering*, 8:1–11, 2003.

B. Cornelissen, J. Schneiders, W. Potters, R. van den Berg, B. Velthuis, G. Rinkel, C. Slump, E. VanBavel, C. Majoie, and H. Marquering. Hemodynamic Differences in Intracranial Aneurysms before and after Rupture. *AJNR Am J Neuroradiol*, 36(10):1927–1933, Oct 2015.

J. Corpataux, E. Haesler, P. Silacci, H. Ris, and D. Hayoz. Low-pressure environment and remodelling of the forearm vein in Brescia-Cimino haemodialysis access. *Nephrol. Dial. Transplant.*, 17(6):1057–1062, Jun 2002.

M. R. Crompton. Mechanism of growth and rupture in cerebral berry aneurysms. *Br Med J*, 1(5496):1138–1142, May 1966.

S. L. Curtis, M. Bradley, P. Wilde, J. Aw, S. Chakrabarti, M. Hamilton, R. Martin, M. Turner, and A. G. Stuart. Results of screening for intracranial aneurysms in patients with coarctation of the aorta. *AJNR Am J Neuroradiol*, 33(6):1182–1186, Jun 2012.

M. I. Daoud, A. L. Alshalalfah, F. Awwad, and M. Al-Najar. Freehand 3d ultrasound imaging system using electromagnetic tracking. pages 1–5, 2015.

A. Dardik, L. Chen, J. Frattini, H. Asada, F. Aziz, F. A. Kudo, and B. E. Sumpio. Differential effects of orbital and laminar shear stress on endothelial cells. *J. Vasc. Surg.*, 41(5):869–880, May 2005.

P. F. Davies, M. Civelek, Y. Fang, and I. Fleming. The atherosusceptible endothelium: endothelial phenotypes in complex haemodynamic shear stress regions in vivo. *Cardiovascular research*, 99(2):315–327, 2013.

A. de Villiers, A. McBride, B. Reddy, T. Franz, and B. Spottiswoode. A validated patient-specific fsi model for vascular access in haemodialysis. *Biomechanics and Modeling in Mechanobiology*, 17(2):479–497, 2018. ISSN 1617-7959. doi: 10.1007/s10237-017-0973-8.

F. de Vocht, J. Wilen, K. H. Mild, L. E. van Nierop, P. Slottje, and H. Kromhout. Health effects and safety of magnetic resonance imaging. *Journal of medical systems*, 36(3):1779–1780, 2012.

I. Decorato, Z. Kharboutly, T. Vassallo, J. Penrose, C. Legallais, and A-V. Salsac. Numerical simulation of the fluid structure interactions in a compliant patient-specific arteriovenous fistula. *International Journal for Numerical Methods in Biomedical Engineering*, 30(2):143–159, 2014.

J. Degroote and J. Vierendeels. Multi-solver algorithms for the partitioned simulation of fluid–structure interaction. *Computer Methods in Applied Mechanics and Engineering*, 200(25-28):2195–2210, 2011.

J. M. Dolan, H. Meng, F. J. Sim, and J. Kolega. Differential gene expression by endothelial cells under positive and negative streamwise gradients of high wall shear stress. *Am. J. Physiol., Cell Physiol.*, 305(8):C854–866, Oct 2013.

H. Drexler and B. Hornig. Endothelial dysfunction in human disease. *J. Mol. Cell Cardiol*, 31:51–60, 1999.

S. Drost, N. Alam, J. G. Houston, and D. Newport. Review of experimental modelling in vascular access for hemodialysis. *Cardiovascular Engineering and Technology*, 8(3):330–341, 2017.

A. Eken and M. Sahin. A parallel monolithic approach for fluid-structure interaction in a cerebral aneurysm. *Computers and Fluids*, 153:61–75, 2017.

H. E. Ellamushi, J. P. Grieve, H. R. Jager, and N. D. Kitchen. Risk factors for the formation of multiple intracranial aneurysms. *J. Neurosurg.*, 94(5): 728–732, May 2001.

A. Elsharkawy, M. Leheka, M. Niemela, R. Billon-Grand, H. Lehto, R. Kivisaari, and J. Hernesniemi. A new, more accurate classification of middle cerebral artery aneurysms: computed tomography angiographic study of 1,009 consecutive cases with 1,309 middle cerebral artery aneurysms. *Neurosurgery*, 73(1):94–102, Jul 2013.

B. Ene-Iordache and A. Remuzzi. Disturbed flow in radial-cephalic arteriovenous fistulae for haemodialysis: low and oscillating shear stress locates the sites of stenosis. *Nephrology Dialysis Transplantation*, 27(1):358–368, 2012.

B. Ene-Iordache and A. Remuzzi. Blood flow in idealized vascular access for hemodialysis: A review of computational studies. *Cardiovascular Engineering and Technology*, 8(3):295–312, 2017.

B. Ene-Iordache, L. Mosconi, G. Remuzzi, and A. Remuzzi. Computational fluid dynamics of a vascular access case for hemodialysis. *Journal of Biomechanical Engineering-Transactions of the Asme*, 123(3):284–292, 2001.

B. Ene-Iordache, L. Cattaneo, G. Dubini, and A. Remuzzi. Effect of anastomosis angle on the localization of disturbed flow in side-to-end fistulae for haemodialysis access. *Nephrology Dialysis Transplantation*, 28(4):997–1005, 2013.

B. Ene-Iordache, C. Semperboni, G. Dubini, and A. Remuzzi. Disturbed flow in a patient-specific arteriovenous fistula for hemodialysis: Multidirectional and reciprocating near-wall flow patterns. *Journal of Biomechanics*, 48(10): 2195–2200, 2015.

P. Evegren, J. Revstedt, and L. Fuchs. Pulsating flow and mass transfer in an asymmetric system of bifurcations. *Computers and Fluids*, 49:46–61, 2011.

A. Fedorov, R. Beichel, J. Kalpathy-Cramer, J. Finet, J.-C. Fillion-Robin, S. Pujol, C. Bauer, D. Jennings, F. Fennessy, M. Sonka, J. Buatti, S. Aylward, J. V. Miller, S. Pieper, and R. Kikinis. 3d slicer as an image computing platform for the quantitative imaging network. *Magnetic Resonance Imaging*, 30(9):1323–1341, 2012.

S. P. Ferns, M. E. Sprengers, W. J. van Rooij, G. J. Rinkel, J. C. van Rijn, S. Bipat, M. Sluzewski, and C. B. Majoie. Coiling of intracranial aneurysms: a systematic review on initial occlusion and reopening and retreatment rates. *Stroke*, 40(8):e523–529, Aug 2009.

M. F. Fillinger, J. Racusin, R. K. Baker, J. L. Cronenwett, A. Teutelink, M. L. Schermerhorn, R. M. Zwolak, R. J. Powell, D. B. Walsh, and E. M. Rzucidlo. Anatomic characteristics of ruptured abdominal aortic aneurysm on conventional CT scans: Implications for rupture risk. *J. Vasc. Surg.*, 39 (6):1243–1252, Jun 2004.

J. Flores, J. Alastruey, and E. C. Poiré. A novel analytical approach to pulsatile blood flow in the arterial network. *Annals of Biomedical Engineering*, 44 (10):3047–3068, 2016.

M. D. Ford, N. Alperin, S. H. Lee, D. W. Holdsworth, and D. A. Steinman. Characterization of volumetric flow rate waveforms in the normal internal carotid and vertebral arteries. *Physiol Meas*, 26(4):477–488, Aug 2005.

L. Formaggia, J. Gerbeau, F. Nobile, and A. Quarteroni. On the coupling of 3d and 1d navier–stokes equations for flow problems in compliant vessels. *Computer methods in applied mechanics and engineering*, 191(6-7):561–582, 2001.

M. Franzoni, I. Cattaneo, B. Ene-Iordache, A. Oldani, P. Righettini, and A. Remuzzi. Design of a cone-and-plate device for controlled realistic shear stress stimulation on endothelial cell monolayers. *Cytotechnology*, 68(5): 1885–1896, 2016.

J. Frosen, A. Piippo, A. Paetau, M. Kangasniemi, M. Niemela, J. Hernesniemi, and J. Jaaskelainen. Remodeling of saccular cerebral artery aneurysm wall is associated with rupture: histological analysis of 24 unruptured and 42 ruptured cases. *Stroke*, 35(10):2287–2293, Oct 2004.

W. Fu and A. Qiao. Analysis of fluid structure interaction based on patient-specific internal carotid aneurysm model. *IEEE*, 2011.

K. Fukazawa, F. Ishida, Y. Umeda, Y. Miura, S. Shimosaka, S. Matsushima, W. Taki, and H. Suzuki. Using computational fluid dynamics analysis to characterize local hemodynamic features of middle cerebral artery aneurysm rupture points. *World Neurosurg*, 83(1):80–86, Jan 2015.

S. Fukuda, N. Hashimoto, H. Naritomi, I. Nagata, K. Nozaki, S. Kondo, M. Kurino, and H. Kikuchi. Prevention of rat cerebral aneurysm formation by inhibition of nitric oxide synthase. *Circulation*, 101(21):2532–2538, May 2000.

D. Fulker, A. Simmons, and T. Barber. Computational model of the arterial and venous needle during haemodialysis. *J Biomech Eng.*, 2017.

P. Gaetani, F. Tartara, V. Grazioli, F. Tancioni, L. Infuso, and R. Rodriguez Baena. Collagen cross-linkage, elastolytic and collagenolytic activities in cerebral aneurysms: a preliminary investigation. *Life Sci.*, 63(4): 285–292, 1998.

S. Gallas, A. Pasco, J. P. Cottier, J. Gabrillargues, J. Drouineau, C. Cognard, and D. Herbreteau. A multicenter study of 705 ruptured intracranial aneurysms treated with Guglielmi detachable coils. *AJNR Am J Neuroradiol*, 26(7):1723–1731, Aug 2005.

D. Gallo, D. Steinman, P. Bijari, and U. Morbiducci. Helical flow in carotid bifurcation as surrogate marker of exposure to disturbed shear. *Journal of Biomechanics*, 45(14):2398–2404, 2012.

A. J. Gauden, P. M. Phal, and K. J. Drummond. Mri safety; nephrogenic systemic fibrosis and other risks. *Journal of Clinical Neuroscience*, 17(9): 1097–1104, 2010.

A. Gee, R. Prager, G. Treece, and L. Berman. Engineering a freehand 3d ultrasound system. *Pattern Recognition Letters*, 24(4-5):757–777, 2003.

I. L. Geenen, F. F. Kolk, D. G. Molin, A. Wagenaar, M. G. Compeer, J. H. Tordoir, G. W. Schurink, J. G. De May, and M. J. Post. Nitric oxide resistance reduces arteriovenous fistula maturation in chronic kidney disease in rats. *PloS One*, 11(1):1–17, 2016.

D. G. Genek, C. T. Altay, T. Unek, A. Sifil, M. Secil, and T. Camsari. Can primary failure of arteriovenous fistulas be anticipated? *Hemodialysis International*, 19(2):296–305, 2015.

E. Georgakarakos, C. V. Ioannou, Y. Kamarianakis, Y. Papaharilaou, T. Kostas, E. Manousaki, and A. N. Katsamouris. The role of geometric parameters in the prediction of abdominal aortic aneurysm wall stress. *Eur J Vasc Endovasc Surg*, 39(1):42–48, Jan 2010.

D. P. Giddens, C. K. Zarins, and S. Glagov. The role of fluid mechanics in the localization and detection of atherosclerosis. *J Biomech Eng*, 115(4B): 588–594, Nov 1993.

F. J. H. Gijsen, E. Allanic, F. N. van de Vosse, and J. D. Janssen. The influence of the non-newtonian properties of blood on the flow in large arteries: unsteady flow in a 90 degrees curved tube. *Journal of Biomechanics*, 32(7): 705–713, 1999a.

F. J. H. Gijsen, F. N. van de Vosse, and J. D. Janssen. The influence of the non-newtonian properties of blood on the flow in large arteries: steady flow in a carotid bifurcation model. *Journal of Biomechanics*, 32(6):601–608, 1999b.

F. P. Glor, B. Ariff, L. A. Crowe, A. D. Hughes, P. L. Cheong, S. A. Thom, P. R. Verdonck, D. N. Firmin, D. C. Barratt, and X. Y. Xu. Carotid geometry reconstruction: a comparison between mri and ultrasound. *Medical physics*, 30(12):3251–3261, 2003.

F. P. Glor, B. Ariff, A. D. Hughes, L. A. Crowe, P. R. Verdonck, D. C. Barratt, S. A. Thom, D. N. Firmin, and X. Y. Xu. Image-based carotid flow reconstruction: a comparison between mri and ultrasound. *Physiological measurement*, 25(6):1495, 2004.

L. Grechy, F. Iori, R. W. Corbett, S. Shurey, W. Gedroyc, N. Duncan, C. G. Caro, and P. E. Vincent. Suppressing unsteady flow in arterio-venous fistulae. *Physics of Fluids*, 29(10), 2017.

T. Greve, M. Sukopp, M. Wostrack, E. Burian, C. Zimmer, and B. Friedrich. Initial raymond–roy occlusion classification but not packing density defines risk for recurrence after aneurysm coiling. *Clinical Neuroradiology*, pages 1–9, 2020.

C. Groden, B. Eckert, T. Ries, E. N. Probst, T. Kucinski, and H. Zeumer. Angiographic follow-up of vertebrobasilar artery aneurysms treated with detachable coils. *Neuroradiology*, 45(7):435–440, Jul 2003.

R. J. Gusic, R. Myung, M. Petko, J. W. Gaynor, and K. J. Gooch. Shear stress and pressure modulate saphenous vein remodeling ex vivo. *J Biomech*, 38 (9):1760–1769, Sep 2005.

M. Gutierrez, P. Pilon, S. Lage, L. Kopel, and S. Carvalho, R. amd Furuie. Automatic measurement of carotid diameter and wall thickness in ultrasound images. *Computing in Cardiology*, 29:359–362, 2002.

Z. Hajiali, M. Dabagh, and P. Jalali. A computational model to assess post-stenting wall stresses dependence on plaque structure and stenosis severity in coronary artery. *Mathematical Problems in Engineering*, 2014, 2014.

H. C. Han. The theoretical foundation for artery buckling under internal pressure. *J Biomech Eng*, 131(12):124501, Dec 2009.

H. C. Han. Twisted blood vessels: symptoms, etiology and biomechanical mechanisms. *J. Vasc. Res.*, 49(3):185–197, 2012.

H. C. Han, J. K. Chesnutt, J. R. Garcia, Q. Liu, and Q. Wen. Artery buckling: new phenotypes, models, and applications. *Ann Biomed Eng*, 41(7):1399–1410, Jul 2013.

A. Hara, N. Yoshimi, and H. Mori. Evidence for apoptosis in human intracranial aneurysms. *Neurol. Res.*, 20(2):127–130, Mar 1998.

A. Harloff, T. Zech, F. Wegent, C. Strecker, C. Weiller, and M. Markl. Comparison of blood flow velocity quantification by 4d flow mr imaging with ultrasound at the carotid bifurcation. *American Journal of Neuroradiology*, 34(7):1407–1413, 2013.

T. Hatakeyama, H. Shigematsu, and T. Muto. Risk factors for rupture of abdominal aortic aneurysm based on three-dimensional study. *J. Vasc. Surg.*, 33(3):453–461, Mar 2001.

C. M. He and M. R. Roach. The composition and mechanical properties of abdominal aortic aneurysms. *J. Vasc. Surg.*, 20(1):6–13, Jul 1994.

X. He and D. N. Ku. Pulsatile flow in the human left coronary artery bifurcation: average conditions. *J Biomech Eng*, 118(1):74–82, Feb 1996.

Y. He, Y. T. Shiu, D. B. Pike, P. Roy-Chaudhury, A. K. Cheung, and S. A. Berceli. Comparison of hemodialysis arteriovenous fistula blood flow rates measured by doppler ultrasound and phase-contrast magnetic resonance imaging. *Journal of vascular surgery*, 68(6):1848–1857, 2018.

J. H. G. Helthuis, S. Bhat, T. P. C. van Doormaal, R. K. Kumar, and A. van der Zwan. Proximal and distal occlusion of complex cerebral aneurysms - implications of flow modeling by fluid-structure interaction analysis. *Operative Neurosurgery*, 15(2):217–230, 2018.

H. A. Himburg, D. M. Grzybowski, A. L. Hazel, J. A. LaMack, X. M. Li, and M. H. Friedman. Spatial comparison between wall shear stress measures and porcine arterial endothelial permeability. *American Journal of Physiology-Heart and Circulatory Physiology*, 286(5):H1916–H1922, 2004.

Y. Hirashima, M. Kurimoto, M. Kubo, and S. Endo. Blade crossing of a pure titanium clip applied to a cerebral aneurysm–case report. *Neurol. Med. Chir. (Tokyo)*, 42(3):123–124, Mar 2002.

Y. Hoi, H. Meng, S. H. Woodward, B. R. Bendok, R. A. Hanel, L. R. Guterman, and L. N. Hopkins. Effects of arterial geometry on aneurysm growth: three-dimensional computational fluid dynamics study. *J. Neurosurg.*, 101 (4):676–681, Oct 2004.

A. L. Hoppe, M. L. Raghavan, and D. M. Hasan. Comparison of the association of sac growth and coil compaction with recurrence in coil embolized cerebral aneurysms. *PLoS One*, 10(4), 2015.

K. Hoshina, E. Sho, M. Sho, T. K. Nakahashi, and R. L. Dalman. Wall shear stress and strain modulate experimental aneurysm cellularity. *J. Vasc. Surg.*, 37(5):1067–1074, May 2003.

W. Huberts, S. G. H. Heinen, N. Zonnebeld, D. A. F. van den Heuvel, Jppm de Vries, J. H. M. Tordoir, D. R. Hose, T. Delhaas, and F. N. van de Vosse. What is needed to make cardiovascular models suitable for clinical decision support? a viewpoint paper. *Journal of Computational Science*, 24:68–84, 2018.

J. E. Hull, B. V. Balakin, B. M. Kellerman, and D. K. Wrolstad. Computational fluid dynamic evaluation of the side-to-side anastomosis for arteriovenous fistula. *J. Vasc. Surg.*, 58(1):187–193, Jul 2013.

J. D. Humphrey. Coupling haemodynamics with vascular wall mechanics and mechanobiology to understand intracranial aneurysms. *International journal of computational fluid dynamics*, 23(8):569–581, 2009.

J. D. Humphrey and P. B. Canham. Structure, mechanical properties and mechanics of intracranial saccular aneurysms. *Journal of Elasticity and the Physical Science of Solids*, 61:49–81, 2000.

J. D. Humphrey and C. A. Taylor. Intracranial and abdominal aortic aneurysms: similarities, differences, and need for a new class of computational models. *Annu Rev Biomed Eng*, 10:221–246, 2008.

F. Iori, L. Grechy, R. W. Corbett, W. Gedroyc, N. Duncan, C. G. Caro, and P. E. Vincent. The effect of in-plane arterial curvature on blood flow and oxygen transport in arterio-venous fistulae. *Physics of Fluids*, 27(3), 2015.

M. Jahed, F. Ghalichi, and M. Farhoudi. Fluid-structure interaction of patient-specific Circle of Willis with aneurysm: Investigation of hemodynamic parameters. *Biomed Mater Eng*, 29(3):357–368, 2018.

L. Jia, L. H. Wang, F. Wei, H. B. Yu, H. Y. Dong, B. Wang, Z. Lu, G. J. Sun, H. Y. Chen, J. Meng, B. Li, R. N. Zhang, X. Q. Bi, Z. Wang, H. Y. Pang, and A. L. Jiang. Effects of wall shear stress in venous neointimal hyperplasia of arteriovenous fistulae. *Nephrology*, 20(5):335–342, 2015.

J. Jiang and C. Strother. Computational fluid dynamics simulations of intracranial aneurysms at varying heart rates: a "patient-specific" study. *Journal of biomechanical engineering*, 131(9), 2009.

L. Jing, J. Fan, Y. Wang, H. Li, S. Wang, X. Yang, and Y. Zhang. Morphologic and Hemodynamic Analysis in the Patients with Multiple Intracranial Aneurysms: Ruptured versus Unruptured. *PLOS ONE*, 10(7):e0132494, 2015.

D. Jodko, D. Obidowski, P. Reorowicz, and K. Jozwik. Simulations of the blood flow in the arterio-venous fistula for haemodialysis. *Acta of Bioengineering and Biomechanics*, 16(1):69–74, 2014.

D. Jodko, D. Obidowski, P. Reorowicz, and K. Jozwik. Blood flows in end-to-end arteriovenous fistulas: Unsteady and steady state numerical investigations of three patient-specific cases. *Biocybernetics and Biomedical Engineering*, 37(3):528–539, 2017. ISSN 0208-5216. doi: 10.1016/j.bbe.2017.05.006.

B. M. Johnston, P. R. Johnston, S. Corney, and D. Kilpatrick. Non-newtonian blood flow in human right coronary arteries: steady state simulations. *Journal of Biomechanics*, 37(5):709–720, 2004.

L. Jou and G. Britz. Correlation Between Aneurysm Size and Hemodynamics in One Individual with Multiple Small Intracranial Aneurysms. *Cureus*, 8 (7):e683, Jul 2016.

L. D. Jou, G. Wong, B. Dispensa, M. T. Lawton, R. T. Higashida, W. L. Young, and D. Saloner. Correlation between lumenal geometry changes and hemodynamics in fusiform intracranial aneurysms. *AJNR Am J Neuroradiol*, 26(9):2357–2363, Oct 2005.

L. D. Jou, D. H. Lee, H. Morsi, and M. E. Mawad. Wall shear stress on ruptured and unruptured intracranial aneurysms at the internal carotid artery. *AJNR Am J Neuroradiol*, 29(9):1761–1767, Oct 2008.

J. Jung and A. Hassanein. Three-phase cfd analytical modeling of blood flow. *Medical engineering & physics*, 30(1):91–103, 2008.

J. Jung, R. W. Lyczkowski, C. B. Panchal, and A. Hassanein. Multiphase hemodynamic simulation of pulsatile flow in a coronary artery. *Journal of biomechanics*, 39(11):2064–2073, 2006.

N. M. Kakalis, A. P. Mitsos, J. V. Byrne, and Y. Ventikos. The haemodynamics of endovascular aneurysm treatment: a computational modelling approach for estimating the influence of multiple coil deployment. *IEEE Trans Med Imaging*, 27(6):814–824, Jun 2008.

Y. Kaku, H. Watarai, J. Kokuzawa, T. Tanaka, and T. Andoh. Treatment of cerebral aneurysms: surgical clipping and coil embolization. *Interv Neuroradiol*, 13 Suppl 1:68–72, Mar 2007.

A. Kamiya, R. Bukhari, and T. Togawa. Adaptive regulation of wall shear stress optimizing vascular tree function. *Bulletin of mathematical biology*, 46(1):127–137, 1984.

A. Kamiya, J. Ando, M. Shibata, and H. Masuda. Roles of fluid shear stress in physiological regulation of vascular structure and function. *Biorheology*, 25(1-2):271–278, 1988.

K. Kataoka, M. Taneda, T. Asai, A. Kinoshita, M. Ito, and R. Kuroda. Structural fragility and inflammatory response of ruptured cerebral aneurysms. A comparative study between ruptured and unruptured cerebral aneurysms. *Stroke*, 30(7):1396–1401, Jul 1999.

Z. Kharboutly, M. Fenech, J. M. Treutenaere, I. Claude, and C. Legallais. Investigations into the relationship between hemodynamics and vascular alterations in an established arteriovenous fistula. *Medical Engineering and Physics*, 29(9):999–1007, 2007. ISSN 1350-4533.

Z. Kharboutly, V. Deplano, E. Bertrand, and C. Legallais. Numerical and experimental study of blood flow through a patient-specific arteriovenous fistula used for hemodialysis. *Medical Engineering and Physics*, 32(2):111–118, 2010. ISSN 1350-4533. doi: 10.1016/j.medengphy.2009.10.013.

S. Kondo, N. Hashimoto, H. Kikuchi, F. Hazama, I. Nagata, and H. Kataoka.

Apoptosis of medial smooth muscle cells in the development of saccular cerebral aneurysms in rats. *Stroke*, 29(1):181–188, Jan 1998.

J. Krejza, M. Arkuszewski, S. E. Kasner, J. Weigele, A. Ustymowicz, R. W. Hurst, B. L. Cucchiara, and S. R. Messe. Carotid artery diameter in men and women and the relation to body and neck size. *Stroke*, 37(4):1103–1105, Apr 2006.

D. N. Ku, D. P. Giddens, C. K. Zarins, and S. Glagov. Pulsatile flow and atherosclerosis in the human carotid bifurcation. positive correlation between plaque location and low oscillating shear stress. *Arteriosclerosis: An Official Journal of the American Heart Association, Inc.*, 5(3):293–302, 1985.

I. Langen and R. Sigbjornsson. Dynamisk analyse av konstruksjoner: Dynamic analysis of structures. 1979.

A. Lauric, J. Hippelheuser, A. D. Cohen, L. M. Kadasi, and A. M. Malek. Wall shear stress association with rupture status in volume matched sidewall aneurysms. *J Neurointerv Surg*, 6(6):466–473, Jul 2014.

A. Y. Lee, A. Sanyal, Y. Xiao, R. Shadfan, and H. C. Han. Mechanical instability of normal and aneurysmal arteries. *J Biomech*, 47(16):3868–3875, Dec 2014.

C. J. Lee, Y. Zhang, H. Takao, Y. Murayama, and Y. Qian. A fluid-structure interaction study using patient-specific ruptured and unruptured aneurysm: the effect of aneurysm morphology, hypertension and elasticity. *J Biomech*, 46(14):2402–2410, Sep 2013.

S. W. Lee and D. A. Steinman. On the relative importance of rheology for image-based cfd models of the carotid bifurcation. 2007.

J. J. Leermakers, A. S. Bode, A. Vaidya, F. M. van der Sande, S. M. Evers, and J. H. Tordoir. Cost-effectiveness of vascular access for haemodialysis: arteriovenous fistulas versus arteriovenous grafts. *Eur J Vasc Endovasc Surg*, 45(1):84–92, Jan 2013.

D. F. Leotta, J. F. Primozich, K. W. Beach, R. O. Bergelin, R. E. Zierler, and D. E. Strandness. Remodeling in peripheral vein graft revisions: Serial study with three-dimensional ultrasound imaging. *Journal of Vascular Surgery*, 37 (4):798–807, 2003.

M. R. Levitt, M. C. Barbour, S. Rolland du Roscoat, C. Geindreau, V. K. Chivukula, P. M. McGah, J. D. Nerva, R. P. Morton, L. J. Kim, and A. Aliseda. Computational fluid dynamics of cerebral aneurysm coiling using high-resolution and high-energy synchrotron X-ray microtomography: comparison with the homogeneous porous medium approach. *J Neurointerv Surg*, 9(8), Aug 2017.

S. Lindemann, N. D. Tolley, D. A. Dixon, T. M. McIntyre, S. M. Prescott, G. A. Zimmerman, and A. S. Weyrich. Activated platelets mediate inflammatory signaling by regulated interleukin 1β synthesis. *The Journal of cell biology*, 154(3):485–490, 2001.

J. Liu, L. Jing, C. Wang, Y. Zhang, and X. Yang. Recanalization, regrowth, and delayed rupture of a previously coiled unruptured anterior communicating artery aneurysm: a longitudinal hemodynamic analysis. *World Neurosurg*, 89:5–726, May 2016.

Q. Liu and H. C. Han. Mechanical buckling of artery under pulsatile pressure. *J Biomech*, 45(7):1192–1198, Apr 2012.

P. W. Longest and C. Kleinstreuer. Numerical simulation of wall shear stress conditions and platelet localization in realistic end-to-side arterial anastomoses. *J Biomech Eng*, 125(5):671–681, Oct 2003.

TF. Luscher and FC. Tanner. Endothelial regulation of vascular tone and growth. *Am. J. Hypertens*, 6, 1993.

I. L. Maier, S. Hofer, A. A. Joseph, K. D. Merboldt, Z. Tan, K. Schregel, M. Knauth, M. Bahr, M. N. Psychogios, and J. Liman. Carotid artery flow as determined by real-time phase-contrast flow mri and neurovascular ultrasound: A comparative study of healthy subjects. *European journal of radiology*, 106:38–45, 2018.

A. M. Malek, S. L. Alper, and S. Izumo. Hemodynamic shear stress and its role in atherosclerosis. *Jama*, 282(21):2035–2042, 1999.

M. Malovrh. Expansion of blood volume increases the primary patency rate of arteriovenous fistulas for hemodialysis in patients with critical arterial quality. *Therapeutic Apheresis and Dialysis*, 13(4):345–349, 2009.

L. G. Margolin. Introduction to "an arbitrary lagrangian-eulerian computing method for all flow speeds". *Journal of Computational Physics*, 135(2): 198–202, 1997.

P. M. McGah, D. F. Leotta, K. W. Beach, J. J. Riley, and A. Aliseda. A longitudinal study of remodeling in a revised peripheral artery bypass graft using 3d ultrasound imaging and computational hemodynamics. *Journal of Biomechanical Engineering-Transactions of the Asme*, 133(4):10, 2011.

P. M. McGah, D. F. Leotta, K. W. Beach, R. E. Zierler, J. J. Riley, and A. Aliseda. Hemodynamic conditions in a failing peripheral artery bypass graft. *Journal of Vascular Surgery*, 56(2):403–409, 2012. ISSN 0741-5214. doi: 10.1016/j.jvs.2012.01.045. URL `<GotoISI>://WOS:000307160400016`.

P. M. McGah, D. F. Leotta, K. W. Beach, R. E. Zierler, and A. Aliseda. Incomplete restoration of homeostatic shear stress within arteriovenous fistulae. *Journal of Biomechanical Engineering-Transactions of the Asme*, 135 (1), 2013.

P. M. McGah, D. F. Leotta, K. W. Beach, and A. Aliseda. Effects of wall distensibility in hemodynamic simulations of an arteriovenous fistula. *Biomechanics and Modeling in Mechanobiology*, 13(3):679–695, 2014.

R. Mehri, C. Mavriplis, and M. Fenech. Red blood cell aggregates and their effect on non-newtonian blood viscosity at low hematocrit in a two-fluid low shear rate microfluidic system. *PLoS One*, 13(7), 2018.

B. Melka, M. Gracka, W. Adamczyk, M. Rojczyk, A. Golda, A. J. Nowak, R. A. Bialecki, and Z. Ostrowski. Multiphase simulation of blood flow within main thoracic arteries of 8-year-old child with coarctation of the aorta. *Heat and Mass Transfer*, 54(8):2405–2413, 2018.

S. Menashi, J. S. Campa, R. M. Greenhalgh, and J. T. Powell. Collagen in abdominal aortic aneurysm: typing, content, and degradation. *J. Vasc. Surg.*, 6(6):578–582, Dec 1987.

H. Meng, Z. Wang, Y. Hoi, L. Gao, E. Metaxa, D. D. Swartz, and J. Kolega. Complex hemodynamics at the apex of an arterial bifurcation induces vascular remodeling resembling cerebral aneurysm initiation. *Stroke*, 38(6): 1924–1931, Jun 2007.

G. Metry, R. Adhikarla, D. Schneditz, C. Ronco, and N. W. Levin. Effect of changes in the intravascular volume during hemodialysis on blood viscoelasticity. *Indian Journal of Nephrology*, 21(2):95–100, 2011.

R. K. Middleton, G. M. Lloyd, M. J. Bown, N. J. Cooper, N. J. London, and R. D. Sayers. The pro-inflammatory and chemotactic cytokine microenvironment of the abdominal aortic aneurysm wall: a protein array study. *Journal of Vascular Surgery*, 45:574–80, 2007.

K. Misaki, H. Takao, T. Suzuki, K. Nishimura, I. Kan, I. Yuki, T. Ishibashi, M. Yamamoto, and Y. Murayama. Estimated pretreatment hemodynamic prognostic factors of aneurysm recurrence after endovascular embolization. *Technology and Health Care*, 25(5):843–850, 2017.

Y. Miura, F. Ishida, Y. Umeda, H. Tanemura, H. Suzuki, S. Matsushima, S. Shimosaka, and W. Taki. Low wall shear stress is independently associated with the rupture status of middle cerebral artery aneurysms. *Stroke*, 44(2):519–521, Feb 2013.

H. G. Morales, M. Kim, E. E. Vivas, M. C. Villa-Uriol, I. Larrabide, T. Sola, L. Guimaraens, and A. F. Frangi. How do coil configuration and packing density influence intra-aneurysmal hemodynamics? *AJNR Am J Neuroradiol*, 32(10):1935–1941, 2011.

H. G. Morales, A. Geers, I. Larrabide, and J. M. Macho. Comparison of two techniques of endovascular coil modeling in cerebral aneurysms using CFD. *IEEE*, pages 1935–1941, 2012.

H. G. Morales, I. Larrabide, A. J. Geers, M. L. Aguilar, and A. F. Frangi. Newtonian and non-Newtonian blood flow in coiled cerebral aneurysms. *J Biomech*, 46(13):2158–2164, Sep 2013a.

H. G. Morales, I. Larrabide, A. J. Geers, L. San Roman, J. Blasco, J. M. Macho, and A. F. Frangi. A virtual coiling technique for image-based aneurysm models by dynamic path planning. *IEEE Trans Med Imaging*, 32(1):119–129, Jan 2013b.

H. G. Morales, O. Bonnefous, A. J. Geers, O. Brina, V. M. Pereira, L. Spelle, J. Moret, and I. Larrabide. Does arterial flow rate affect the assessment of flow-diverter stent performance? *American Journal of Neuroradiology*, 37 (12):2293–2298, 2016.

L. Moreno, F. Calderas, G. Sanchez-Olivares, L. Medina-Torres, A. Sanchez-Solis, and O. Manero. Effect of cholesterol and triglycerides levels on the rheological behavior of human blood. *Korea-Australia Rheology Journal*, 27 (1):1–10, 2015.

A. M. Mortimer, B. Steinfort, K. Faulder, and T. Harrington. Delayed infarction following aneurysmal subarachnoid hemorrhage: Can the role of severe angiographic vasospasm really be dismissed? *J Neurointerv Surg*, 8 (8):802–807, Aug 2016.

T .M. Mubita, L. R. Rojas-Solorzano, and J. B. Moreno. A multiphase approach to model blood flow in micro-tubes. pages 235–247, 2014.

A. Nader-Sepahi, M. Casimiro, J. Sen, and N. D. Kitchen. Is aspect ratio a reliable predictor of intracranial aneurysm rupture? *Neurosurgery*, 54(6): 1343–1347, Jun 2004.

T. K. Nakahashi, K. Hoshina, P. S. Tsao, E. Sho, M. Sho, J. K. Karwowski, C. Yeh, R. B. Yang, J. N. Topper, and R. L. Dalman. Flow loading induces macrophage antioxidative gene expression in experimental aneurysms. *Arterioscler. Thromb. Vasc. Biol.*, 22(12):2017–2022, Dec 2002.

H. Nakatani, N. Hashimoto, Y. Kang, N. Yamazoe, H. Kikuchi, S. Yamaguchi,

and H. Niimi. Cerebral blood flow patterns at major vessel bifurcations and aneurysms in rats. *J. Neurosurg.*, 74(2):258–262, Feb 1991.

A. Narracott, S. Smith, and P. et al. Lawford. Development and validation of models for the investigation of blood clotting in idealized stenoses and cerebral aneurysms. *J Artif Organs*, 8:56–62, 2005.

M. N. Ngoepe, B. D. Reddy, D. Kahn, C. Meyer, P. Zilla, and T. Franz. A numerical tool for the coupled mechanical assessment of anastomoses of ptfe arterio-venous access grafts. *Cardiovascular Engineering and Technology*, 2 (3):160–172, 2011.

A. K. Niemann, J. Udesen, S. Thrysoe, J. V. Nygaard, E. T. Frund, S. E. Petersen, and J. M. Hasenkam. Can sites prone to flow induced vascular complications in a-v fistulas be assessed using computational fluid dynamics? *Journal of Biomechanics*, 43(10):2002–2009, 2010.

A. K. Niemann, S. Thrysoe, J. V. Nygaard, J. M. Hasenkam, and S. E. Petersen. Computational fluid dynamics simulation of a-v fistulas: from MRI and ultrasound scans to numeric evaluation of hemodynamics. *J Vasc Access*, 13(1):36–44, 2012a.

A. K. Niemann, S. Thrysoe, J. V. Nygaard, J. M. Hasenkam, and S. E. Petersen. Computational fluid dynamics simulation of a-v fistulas: From mri and ultrasound scans to numeric evaluation of hemodynamics. *Journal of Vascular Access*, 13(1):36–44, 2012b.

Z. Ostrowski, B. Melka, W. Adamczyk, M. Rojczyk, A. Golda, and A. J. Nowak. Cfd analysis of multiphase blood flow within aorta and its thoracic branches of patient with coarctation of aorta using multiphase euler-euler approach. In *Journal of Physics: Conference Series*, volume 745, 2016.

T. Otani, S. Li, S. Wada, and T. et. al. Shigematsu. A Computational Approach for Blood Flow Analysis in the Densely Coiled Cerebral Aneurysm. *IEEE International Conference on Bioinformatics and Bioengineering*, pages 342–345, 2016.

T. Otani, S. Li, M. Hirata, and S. Wada. Computational Study of the Non-Newtonian Effect of Blood on Flow Stagnation in a Coiled Cerebral Aneurysm. *Journal of the Society of Rheology, Japan*, 45(5), 2017a.

T. Otani, S. Li, T. Shigematsu, T. Fujinaka, M. Hirata, T. Ozaki, and S. Wada. Computational study for the effects of coil configuration on blood flow characteristics in coil-embolized cerebral aneurysm. *Med Biol Eng Comput*, 55 (5):697–710, May 2017b.

T. Otani, T. Shindo, S. Li, M. Hirata, and S. Wada. Effect of Local Coil Density on Blood Flow Stagnation in Densely Coiled Cerebral Aneurysms: A Computational Study Using a Cartesian Grid Method. *J Biomech Eng*, 140(4), Apr 2018.

C. Ou, W. Huang, M. Yuen, and Y. Qian. Hemodynamic modeling of leukocyte and erythrocyte transport and interactions in intracranial aneurysms by a multiphase approach. *Journal of biomechanics*, 49(14):3476–3484, 2016.

R. Ouared, B. Chopard, B. Stahl, D. A. Rufenacht, H. Yilmaz, and G. Courbebaisse. Thrombosis modeling in intracranial aneurysms: a lattice boltzmann numerical algorithm. *Computer Physics Communications*, 179(1-3):128–131, 2008.

A. C. Pearson, D. Nagelhout, R. Castello, C. R. Gomez, and A. J. Labovitz. Atrial septal aneurysm and stroke: a transesophageal echocardiographic study. *J. Am. Coll. Cardiol.*, 18(5):1223–1229, Nov 1991.

S. J. Peerless and C. G. Drake. Management of aneurysms of the posterior circulation. *Neurological Surgery*, 3:1715–1763, 1982.

G. Pennati, L. Socci, S. Rigano, S. Boito, and E. Ferrazzi. Computational patient-specific models based on 3-d ultrasound data to quantify uterine arterial flow during pregnancy. *IEEE transactions on medical imaging*, 27 (12):1715–1722, 2008.

K. Perktold and G. Rappitsch. Computer simulation of local blood flow and vessel mechanics in a compliant carotid artery bifurication model. *Journal of Biomechanics*, 28(7):845–856, 1995.

D. Pike, Y. Shiu, M. Somarathna, L. Guo, T. Isayeva, J. Totenhagen, and T. Lee. High resolution hemodynamic profiling of murine arteriovenous fistula using magnetic resonance imaging and computational fluid dynamics. *Theoretical Biology and Medical Modelling*, 14(1):1–17, 2017a.

D. Pike, Y. T. Shiu, M. Somarathna, L. Guo, T. Isayaeva, J. Totenhagen, and T. Lee. High resolution hemodynamic profiling of murine arteriovenous fistula using magnetic resonance imaging and computational fluid dynamics. *Theoretical Biology and Medical Modelling*, 14(1):1–17, 2017b.

C. Pozrikidis and J. M. Davis. Blood flow through capillary networks. *Transport in Biological Media. Elsevier*, 2013.

M. Rahman, J. Smietana, E. Hauck, B. Hoh, N. Hopkins, A. Siddiqui, E. I. Levy, H. Meng, and J. Mocco. Size ratio correlates with intracranial aneurysm rupture status: a prospective study. *Stroke*, 41(5):916–920, May 2010.

V. L. Rayz, L. Boussel, L. Ge, J. R. Leach, A. J. Martin, M. T. Lawton, C. McCulloch, and D. Saloner. Flow residence time and regions of intraluminal thrombus deposition in intracranial aneurysms. *Ann Biomed Eng*, 38(10): 3058–3069, Oct 2010.

V. L. Rayz, A. Abla, L. Boussel, J. R. Leach, G. Acevedo-Bolton, D. Saloner, and M. T. Lawton. Computational modeling of flow-altering surgeries in basilar aneurysms. *Ann Biomed Eng*, 43(5):1210–1222, May 2015.

A. Ribeiro, O. Husson, N. Drey, I. Murray, K. May, J. Thurston, and W. Oyen. Ionising radiation exposure from medical imaging–a review of patient's (un) awareness. *Radiography*, 26(2):25–30, 2020.

G. J. Riccardello, A. R. Changa, F. Al-Mufti, I. P. Singh, C. Gandhi, M. Roman, and C. J. Prestigiacomo. Hemodynamic impingement and the initiation of intracranial side-wall aneurysms. *Interv Neuroradiol*, 24(3):288–296, Jun 2018.

W. A. Riley, R. W. Barnes, G. W. Evans, and G. L. Burke. Ultrasonic measurement of the elastic modulus of the common carotid artery. The Atherosclerosis Risk in Communities (ARIC) Study. *Stroke*, 23(7):952–956, Jul 1992.

G. J. Rinkel, M. Djibuti, A. Algra, and J. van Gijn. Prevalence and risk of rupture of intracranial aneurysms: a systematic review. *Stroke*, 29(1): 251–256, Jan 1998.

M. L. Robbin, T. Greene, A. K. Cheung, M. Allon, S. A. Berceli, J. S. Kaufman, M. Allen, P. B. Imrey, M. K. Radeva, Y. T. Shiu, H. R. Umphrey, and C. J. Young. Arteriovenous fistula development in the first 6 weeks after creation. *Radiology*, 279(2):620–629, 2016.

R. Ross. Atherosclerosis–an inflammatory disease. *N. Engl. J. Med.*, 340(2): 115–126, Jan 1999.

T. C. Rothuizen, C. Wong, P. H. Quax, A. J. van Zonneveld, T. J. Rabelink, and J. I. Rotmans. Arteriovenous access failure: more than just intimal hyperplasia? *Nephrol. Dial. Transplant.*, 28(5):1085–1092, May 2013.

P. Roy-Chaudhury, L. M. Spergel, A. Besarab, A. Asif, and P. Ravani. Biology of arteriovenous fistula failure. *Journal of Nephrology*, 20(2):150–163, 2007.

J. H. Russell, N. Kelson, M. Barry, M. Pearcy, D. F. Fletcher, and C. D. Winter. Computational fluid dynamic analysis of intracranial aneurysmal bleb formation. *Neurosurgery*, 73(6):1061–1069, 2013.

H. S. Ryou, S. Kim, S. W. Kim, and S. W. Cho. Construction of healthy arteries using computed tomography and virtual histology intravascular ultrasound. *Journal of biomechanics*, 45(9):1612–1618, 2012.

C. Sadasivan, D. J. Fiorella, H. H. Woo, and B. B. Lieber. Physical factors effecting cerebral aneurysm pathophysiology. *Annals of biomedical engineering*, 41(7):1347–1365, 2013.

T. S. Safavi, N. Fatouraee, and E. Soleimani. Quantification of blood flow velocity of the internal carotid artery: A comparison between phase-contrast mri and doppler ultrasound. In *2017 24th National and 2nd International Iranian Conference on Biomedical Engineering (ICBME)*, pages 330–333.

W. I. Schievink. Intracranial aneurysms. *N. Engl. J. Med.*, 336(1):28–40, Jan 1997.

C. M. Schirmer and A. M. Malek. Wall shear stress gradient analysis within an idealized stenosis using non-newtonian flow. *Neurosurgery*, 61(4):853–863, 2007.

C. M. Schirmer and A. M. Malek. Critical influence of framing coil orientation on intra-aneurysmal and neck region hemodynamics in a sidewall aneurysm model. *Neurosurgery*, 67:1692–702, 2010.

T. W. Secomb. Hemodynamics. *Comprehensive Physiology*, 6(2):975–1003, 2016.

T. Seo, G. Shin, and D. Kim. The study of abdominal aortic aneurysm rupture risk using fluid-structure interaction. *International Journal of Applied Engineering Research*, 13(8):6183–6187, 2018.

D. M. Sforza, C. M. Putman, and J. R. Cebral. Hemodynamics of Cerebral Aneurysms. *Annu Rev Fluid Mech*, 41:91–107, Jan 2009.

A. Shamloo, M. A. Nejad, and M. Saeedi. Fluid-structure interaction simulation of a cerebral aneurysm: Effects of endovascular coiling treatment and aneurysm wall thickening. *J Mech Behav Biomed Mater*, 74:72–83, 10 2017.

M. Sharzehee, S. S. Khalafvand, and H. C. Han. Fluid-structure interaction modeling of aneurysmal arteries under steady-state and pulsatile blood flow: a stability analysis. *Comput Methods Biomech Biomed Engin*, 21(3):219–231, Feb 2018.

B. Sheng, D. Wu, J. Yuan, S. Xu, Z. Li, J. Dong, N. Lai, and X. Fang. Hemodynamic characteristics associated with paraclinoid aneurysm recurrence in patients after embolization. *Frontiers in Neurology*, 10, 2019.

S. Shenoy. Surgical anatomy of upper arm: what is needed for AVF planning. *J Vasc Access*, 10(4):223–232, 2009.

Y. Shintani, K. Iino, Y. Yamamoto, H. Kato, H. Takemura, and T. Kiwata. Analysis of computational fluid dynamics and particle image velocimetry

models of distal-end side-to-side and end-to-side anastomoses for coronary artery bypass grafting in a pulsatile flow. *Circulation Journal*, 82(1):110–117, 2018.

E. Sho, M. Sho, K. Hoshina, H. Kimura, T. K. Nakahashi, and R. L. Dalman. Hemodynamic forces regulate mural macrophage infiltration in experimental aortic aneurysms. *Exp. Mol. Pathol.*, 76(2):108–116, Apr 2004.

M. Sho, E. Sho, T. M. Singh, M. Komatsu, A. Sugita, C. Xu, H. Nanjo, C. K. Zarins, and H. Masuda. Subnormal shear stress-induced intimal thickening requires medial smooth muscle cell proliferation and migration. *Exp. Mol. Pathol.*, 72(2):150–160, Apr 2002.

M. Shojima, M. Oshima, K. Takagi, R. Torii, M. Hayakawa, K. Katada, A. Morita, and T. Kirino. Magnitude and role of wall shear stress on cerebral aneurysm: computational fluid dynamic study of 20 middle cerebral artery aneurysms. *Stroke*, 35(11):2500–2505, Nov 2004.

M. Sigovan, V. Rayz, W. Gasper, H. F. Alley, C. D. Owens, and D. Saloner. Vascular remodeling in autogenous arterio-venous fistulas by mri and cfd. *Annals of Biomedical Engineering*, 41(4):657–668, 2013.

M. Sluzewski, W. J. van Rooij, G. Rinkel, and D. Wijnalda. Endovascular treatment of ruptured intracranial aneurysms with detachable coils: Long-term clinical and serial angiographic results. *Radiology*, 227(3):720–724, 2003.

M. Sluzewski, W. J. van Rooij, M. J. Slob, J. O. Bescos, C. H. Slump, and D. Wijnalda. Relation between aneurysm volume, packing, and compaction in 145 cerebral aneurysms treated with coils. *Radiology*, 231(3):653–658, Jun 2004.

M. Sobkowiak, W. Wolanski, M. Zimny, M. Gzik, and W. Kaspera. Analysis of an impact of hemodynamic parameters in relation to variable morphometric features of the middle cerebral artery (mca). pages 200–209, 2018.

J. V. Soulis, T. M. Farmakis, G. D. Giannoglou, , and G. E. Louridas. Wall

shear stress in normal left coronary artery tree. *Journal of Biomechanics*, 39(4):742–749, 2006.

P. C. Sousa, F. T. Pinho, M. A. Alves, and M. S. N. Oliveira. A review of hemorheology: Measuring techniques and recent advances. *Korea-Australia Rheology Journal*, 28(1):1–22, 2016. ISSN 1226-119X. doi: 10.1007/s13367-016-0001-z. URL <GotoISI>://WOS:000371374900001.

W. E. Stehbens. Etiology of intracranial berry aneurysms. *J. Neurosurg.*, 70 (6):823–831, Jun 1989.

H. J. Steiger. Pathophysiology of development and rupture of cerebral aneurysms. *Acta Neurochir Suppl (Wien)*, 48:1–57, 1990.

H. J. Steiger, R. Aaslid, S. Keller, and H. J. Reulen. Strength, elasticity and viscoelastic properties of cerebral aneurysms. *Heart Vessels*, 5(1):41–46, 1989.

P. Sun, C. Zhang, R. Lan, and L. Li. Monolithic arbitrary lagrangian–eulerian finite element method for a multi-domain blood flow–aortic wall interaction problem. pages 60–74, 2020.

Z. Sun and Y. Cao. Multislice CT angiography assessment of left coronary artery: correlation between bifurcation angle and dimensions and development of coronary artery disease. *Eur J Radiol*, 79(2):e90–95, Aug 2011.

J. Suzuki and H. Ohara. Clinicopathological study of cerebral aneurysms. Origin, rupture, repair, and growth. *J. Neurosurg.*, 48(4):505–514, Apr 1978.

T. Suzuki, H. Takao, T. Suzuki, Y. Kambayashi, M. Watanabe, K. Shinohara, H. Fujiwara, S. Nakazato, M. Watanabe, and C. Dahmani. Fluid structure interaction analysis reveals facial nerve palsy caused by vertebral-posterior inferior cerebellar artery aneurysm. *Computers in biology and medicine*, 66: 263–268, 2015.

L. L. Swystun and P. C. Liaw. The role of leukocytes in thrombosis. *The Journal of the American Society of Hematology*, 128(6):753–762, 2016.

K. Takizawa, J. Christopher, T. E. Tezduyar, and S. Sathe. Space–time finite element computation of arterial fluid–structure interactions with patient-specific data. *International Journal for Numerical Methods in Biomedical Engineering*, 26(1):101–116, 2010.

D. Tang, C. Yang, G. Canton, Z. Wu, T. Hatsukami, and C. Yuan. Correlations between carotid plaque progression and mechanical stresses change sign over time: a patient follow up study using MRI and 3D FSI models. *Biomed Eng Online*, 12:105, Oct 2013.

C. L. Taylor, Z. Yuan, W. R. Selman, R. A. Ratcheson, and A. A. Rimm. Cerebral arterial neurysm formation and rupture in 20,767 elderly patients: hypertension and other risk factors. *Journal of Neurosurgery*, 83:812–819, 1995.

L. L. Teunissen, G. J. Rinkel, A. Algra, and J. van Gijn. Risk factors for subarachnoid hemorrhage: a systematic review. *Stroke*, 27(3):544–549, Mar 1996.

T. E. Tezduyar, S. Sathe, T. Cragin, B. Nanna, B. S. Conklin, J. Pausewang, and M. Schwaab. Modelling of fluid–structure interactions with the space–time finite elements: Arterial fluid mechanics. *International Journal for Numerical Methods in Fluids*, 54(6-8):901–922, 2007.

Y. Tobe, T. Yagi, and Y. Iwabuchi. Combined analysis of pathology and hemodynamics of human unruptured cerebral aneurysm with thin-walled region. *ASME, 2013*.

Y. Tobe, T. Yagi, and Y. Iwabuchi. Relationship between pathology and hemodynamics of human unruptured cerebral aneurysms. *IFMBE*, pages 44–47, 2014.

R. Torii, M. Oshima, T. Kobayashi, K. Takagi, and T. E. Tezduyar. Fluid–structure interaction modeling of aneurysmal conditions with high and normal blood pressures. *Computational Mechanics*, 38(4-5):482–490, 2006.

R. Torii, M. Oshima, T. Kobayashi, K. Takagi, and T. Tezduyar. Fluid–structure interaction modeling of blood flow and cerebral aneurysm:

Significance of artery and aneurysm shapes. *Comput. Methods Appl. Mech. Engrg.*, 198:3613–3621, 2009.

R. Torii, M. Oshima, T. Kobayashi, K. Takagi, and T. Tezduyar. Influence of wall thickness on fluid–structure interaction computations of cerebral aneurysms. *Int. J. Numer. Meth. Biomed. Engng.*, 26:336–347, 2010.

H. Ujiie, H. Tachibana, O. Hiramatsu, A. L. Hazel, T. Matsumoto, Y. Ogasawara, H. Nakajima, T. Hori, K. Takakura, and F. Kajiya. Effects of size and shape (aspect ratio) on the hemodynamics of saccular aneurysms: a possible index for surgical treatment of intracranial aneurysms. *Neurosurgery*, 45(1):119–129, Jul 1999.

H. Ujiie, Y. Tamano, K. Sasaki, and T. Hori. Is the aspect ratio a reliable index for predicting the rupture of a saccular aneurysm? *Neurosurgery*, 48 (3):495–502, Mar 2001.

T. Uno, K. Misaki, I. Nambu, A. Yoshikawa, T. Kamide, N. Uchiyama, and M. Nakada. Prediction of internal carotid artery aneurysm recurrence by pressure difference at the coil mass surface. *Neuroradiology*, pages 1–10, 2020.

A. Valencia and F. Solis. Blood flow dynamics and arterial wall interaction in a saccular aneurysm model of the basilar artery. *Comput. Struct.*, 84: 1326–1337, 2006.

A. Valencia, H. Morales, R. Rivera, E. Bravo, and M. Galvez. Blood flow dynamics in patient-specific cerebral aneurysm models: the relationship between wall shear stress and aneurysm area index. *Med Eng Phys*, 30(3): 329–340, Apr 2008.

A. Vali, A. A. Abla, M. T. Lawton, D. Saloner, and V. L. Rayz. Computational Fluid Dynamics modeling of contrast transport in basilar aneurysms following flow-altering surgeries. *J Biomech*, 50:195–201, 01 2017.

J. van Gijn and G. J. Rinkel. Subarachnoid haemorrhage: diagnosis, causes and management. *Brain*, 124(Pt 2):249–278, Feb 2001.

Application. VisibleBody. Human anatomy atlas. 2019.

Vorp. Biomechanics of abdominal aortic aneurysm. *Journal of Biomechanics*, 40(9):1887–1902, 2007.

J. M. Wakeling and B. M. Nigg. Modification of soft tissue vibrations in the leg by muscular activity. *Journal of applied physiology*, 90(2):412–420, 2001.

H. Wan, G. Lu, L. Huang, L. Ge, Y. Jiang, G. Li, X. Leng, J Xiang, and X. Zhang. Hemodynamic effect of the last finishing coils in packing the aneurysm neck. *Frontiers in Neurology*, 11, 2020.

Z. Wang, R. Orlu, P. Schlatter, and Y. M. Chung. Direct numerical simulation of a turbulent 90 bend pipe flow. *International Journal of Heat and Fluid Flow*, 73:199–208, 2018.

S. M. Wasserman and J. N. Topper. Adaptation of the endothelium to fluid flow: in vitro analyses of gene expression and in vivo implications. *Vasc Med*, 9(1):35–45, Feb 2004.

P. N. Watton, Y. Ventikos, and G. A. Holzapfel. Modelling the growth and stabilization of cerebral aneurysms. *Math Med Biol*, 26(2):133–164, Jun 2009.

B. Weir. Patients with small, asymptomatic, unruptured intracranial aneurysms and no history of subarachnoid hemorrhage should be treated conservatively: against. *Stroke*, 36(2):410–411, Feb 2005.

J. W. Weisel. Enigmas of blood clot elasticity. *Science*, 320(5875):456–457, 2008.

J. Wen, K. Liu, K. Khoshmanesh, W. Jiang, and T. Zheng. Numerical investigation of haemodynamics in a helical-type artery bypass graft using non-newtonian multiphase model. *Computer methods in biomechanics and biomedical engineering*, 18(7):760–768, 2015.

E. L Wilson. Static and dynamic analysis of structures (4th edition). *Computers and Structures, Inc*, 2004.

J. Xiang, V. M. Tutino, K. V. Snyder, and H. Meng. CFD: computational fluid dynamics or confounding factor dissemination? The role of hemodynamics in intracranial aneurysm rupture risk assessment. *AJNR Am J Neuroradiol*, 35(10):1849–1857, Oct 2014.

X. Xie, Y. Wang, H. Zhu, H. Zhou, and J. Zhou. Impact of coronary tortuosity on coronary blood supply: a patient-specific study. *PLoS ONE*, 8(5):e64564, 2013.

K. Yamamoto, C. D. Protrack, G. Kuwahara, M. Tsuneki, T. Hashimoto, M. R. Hall, R. Assi, K. E. Brownson, T. R. Foster, H. Bai, M. Wang, J. A. Madri, and A. Dardik. Disturbed shear stress reduces klf2 expression in arterial-venous fistulae in vivo. *Physiological Reports*, 3(3):1–13, 2015.

F. Yilmaz, A. I. Kutlar, and M. Y. Gundogdu. Analysis of drag effects on pulsatile blood flow in a right coronary artery by using eulerian multiphase model. *Korea-Australia rheology journal*, 23(2):89, 2011.

G. Zhou, Y. Zhu, Y. Yin, M. Su, and M. Li. Association of wall shear stress with intracranial aneurysm rupture: systematic review and meta-analysis. *Sci Rep*, 7(1):5331, 07 2017.